

**AN INVESTIGATION INTO THE
EFFICIENCY OF SYSTEMS FOR CIR-
CULATING REFRIGERANT
THROUGH EVAPORATORS IN THE
ICE-MAKING PLANT AT THE ERPM
GOLD MINE**

Steven Katzeff

A research report submitted to the Faculty of Engineering and the Built Environment, University of the Witwatersrand, Johannesburg, in partial fulfilment of the requirements for the degree of Master of Science in Engineering.

Johannesburg 2011

DECLARATION

I declare that this research report is my own unaided work. It is being submitted to the Degree of Master of Science to the University of the Witwatersrand, Johannesburg. It has not been submitted before for any degree or examination to any other University.

.....
...

.....day of..... 2011

ABSTRACT

Although comparisons of relative energy efficiency and cost effectiveness for small gas and mechanically pumped liquid overfeed refrigeration systems (arrangements) have been performed, no such comparison has been reported for large batch type ice-making systems. The ice-making plant at the Far East Vertical Shaft, East Rand Proprietary Mines (ERPM) Ltd, South Africa, which produced¹ ice in a batch-type process for cooling its underground workings, utilizes cold flash gas to pump liquid refrigerant to and through its ice-building evaporators. Each of this plant's three operating units manufactured up to 1000 tons of ice per day to adequately cool this gold mine's underground workings. For one unit of this plant, this investigation models the functioning of the existing 'cold gas' pumping arrangement, supported by test data. It then investigates, through similar modelling, a more conventional 'hot gas' pumping arrangement, and two possible mechanically pumped arrangements for this unit, functioning under similar conditions. The models provide a thermodynamically meaningful comparison of the different liquid overfeed refrigerant pumping arrangements, principally in terms of their energy efficiency and electrical cost effectiveness. They predict that under similar operating conditions, the current cold gas pumping arrangement is more energy efficient and electrically cost effective than both hot gas and *conventionally* mechanically pumped arrangements. This agrees with the suggestions and conclusions of previous investigations performed on smaller refrigeration systems. However, compared to a theoretical *fully* mechanically pumped arrangement, the existing cold gas pumped system is predicted to incur larger unproductive refrigeration demand and higher annual electrical operating cost.

¹ Underground operations at the mine were suspended on 31 October 2008.

For my dear mother,

Rubina Katzeff

ACKNOWLEDGEMENTS

I would like to acknowledge my supervisor, Dr. Michael Bailey-McEwan, for his guidance, support and assistance.

I would also like to acknowledge my wife Rosie for her continuous support.

CONTENTS.....Page

DECLARATION.....	2
ABSTRACT.....	3
ACKNOWLEDGEMENTS.....	5
LIST OF FIGURES.....	15
LIST OF TABLES.....	21
LIST OF SYMBOLS AND NOMENCLATURE.....	23
1. INTRODUCTION	30
1.1. Overview: Refrigeration Systems of Ice.....	30
1.2. Introduction to Liquid Overfeed Systems (Arrangements).....	32
1.2.1. Hot and Cold Gas Pumped Arrangements	33
1.2.2. Mechanically Pumped Arrangements	34
1.2.3. Brief Introduction to the Operating ERPM Plant.....	35
1.2.4. Brief Overview of the Development of Gas Pumped Liquid Overfeed Systems	35
1.2.5. Overview of this Investigation	38
2. LITERATURE SURVEY: KEY FEATURES OF LIQUID OVERFEED PUMPING ARRANGEMENTS.....	40
2.1. Efficiencies of Differently Pumped Liquid Overfeed Arrangements	41
2.1.1. Advantages of Liquid Overfeed Arrangements and using Ammonia as the Refrigerant for such Systems.....	41
2.1.2. Refrigerant Recirculation Ratio	41
2.1.3. Mechanically and Gas Pumped Systems	42
2.2. Comparative Efficiencies of Differently Pumped Liquid Overfeed Systems, an Investigation by Lorentzen and Baglo ⁽⁶⁾	44
2.3. An Investigation of Gas Powered Liquid Recirculation Compared To Mechanical Pumps by Wright ⁽¹¹⁾	46
2.3.1. Controlled Pressure Receiver System	47

2.4. A Note on Stationary Processes in Batch Cycling of Batch Refrigeration Systems	49
3. THE ICE MAKING PLANT AT ERPM, LTD	52
3.1. Background: Design, Layout and Description	52
3.1.1. Units in the Ice Plant	53
3.1.2. Control System for Ice Production.....	53
3.1.3. The Plate Ice Making Unit 5	54
3.2. Operation of Ice-Making Modules pf Unit 5 of Plant.....	55
3.2.1. The Processes at the Pumper Drums.....	61
3.2.2. The Process at the Evaporator during Ice Building	62
3.2.3. The Processes at the Accumulator and the Compressor	62
3.2.4. The Process at the Evaporator during the Warming and Re-Cooling Sub-Period of the Harvesting Period.....	63
4. REASON FOR THE STUDY	65
5. OVERVIEW OF METHODOLOGY	66
6. OBJECTIVES OF THE STUDY	67
7.THEORETICAL MODELLING OF EXISTING AND ALTERNATIVE BATCH ICE-MAKING ARRANGEMENTS IN ERPM'S PLANT	68
7.1 Key Concepts when Modelling the Different Possible Operating Arrangements of the Plant.....	68
7.1.1. Liquid Overfeed Arrangements	68
7.1.2. Productive and Unproductive Refrigeration Demand.....	69
7.2 Productive and Unproductive Refrigeration Demands of Thermodynamic Processes in Ice-Making Systems with Different Refrigerant Liquid Overfeed Pumping Arrangements.....	70
7.2.1 Productive and Unproductive Refrigeration Demands.....	70
7.2.2 Avoidable and Unavoidable Unproductive Refrigeration Demands.....	71

7.2.3	Simplified Control-Volume Thermodynamic Analysis of Gas and Mechanically Pumped Arrangements.....	72
7.2.4	Refrigerant Pumping by Cold Gas.....	79
7.3	Configurations of the Different Operating Arrangements.....	81

8. MODELLING OF PRODUCTIVE AND UNPRODUCTIVE

REFRIGERATION DEMANDS FOR DIFFERENTLY PUMPED LIQUID

OVERFEED ARRANGEMENTS.....	86
8.1. Productive and Unproductive Refrigeration Demands Directly Related to Ice Building.....	87
8.1.1. URDs and PRDs at the Evaporator during the Ice Building Period.....	91
8.1.2. PRD of Cooling the Incoming Make-Up Feed Water at the Pre-Chiller.....	92
8.2. Control Volume Energy Balances to Predict the URDs at the Evaporator during the Harvesting Period.....	94
8.2.1 The Warming Sub-Period.....	94
8.2.2 The Re-Cooling Sub-Period.....	102
8.3. Control Volume Energy Balances to Predict the URDs at the Accumulator.....	107
8.3.1 URDS at the Accumulator during the Transient Period.....	112
8.3.2 URDs at the Accumulator during the Complete Ice Building and Shedding Cycle of One Module.....	114
8.4. Control Volume Energy Balance to Predict the URDs at the Filling Pumper Drum.....	116
8.4.1 URDs at the Filling Pumper Drum.....	118
8.4.2 URD of Re-Cooling the Upper Portion of Circulating Liquid at the Pumping Pumper Drum.....	120
8.5. Total PRD and URD for the Cold Gas Pumped Arrangement Per Module.....	121
8.5.1 Total PRD Per Module for all Pumping Arrangements.....	121
8.5.2 Total URD Per Module for the Cold Gas Pumped Pumping Arrangement.....	121

8.6.	Predicting the Average Recirculation Ratio and Compressor Work Input for the Operating Cold Gas Pumped System Per Module	121
8.6.1	Predicting the Average Recirculation Ratio for the Operating CGPS	121
8.6.2	Predicting the Average Electrical and Mechanical Compressor Work Input for the Operating CGPS	124
8.7.	Total URD for the Hot Gas Pumped Arrangement Per Module	124
8.7.1	URDs at the Accumulator for the HGPS.....	125
8.7.2	URDs at the Filling Pumper Drum r for the HGPS.....	127
8.7.3	URD of Re-Cooling the Upper Portion of Circulating Liquid at the Pumping Pumper Drum for the HGPS.....	128
8.7.4	Total URD for the HGPS.....	129
8.8.	Total URD for the Mechanically Pumped Arrangement Per Module.....	129
8.8.1	URD of Re-Cooling the Circulated Liquid at the Mechanical Pump	130
8.8.2	Total URD for the MPS.....	132
8.9.	Total URD for a Fully Mechanically Pumped Arrangement Per Module	132
8.9.1	Total URD for the MPS.....	134
8.10.	Comparison of Results for the Four Arrangements	135
8.10.1	Results for Different Average Recirculation Ratios.....	135
8.10.2	Results for Different Evaporator Pressures.....	143
8.10.3	Results and Comparison of the URDs for each Arrangement.....	148
8.11.	Operating Cost Analysis for the Different Pumping Arrangements	155
8.11.1	Results for Different Average Recirculation Ratios.....	155
8.12	Remark: Accuracy of Predicted URDs and COPs.....	159
9.	HEAT TRANSFER MODEL TO CORROBORATE THE AVERAGE RECIRCULATION RATIO AND MASS FLOW RATE PREDICTED BY THE MODEL OF SECTION 8	163
9.1.	Heat Transfer Model during the Ice Building Period.....	164

9.1.1. Brief Overview of the Heat Transfer Correlations used to Predict the Refrigerant Side Convective Boiling Heat Transfer Coefficient	169
9.1.2. Predicting the Layer of Ice Built during the Ice Building Period	174
9.2. Heat Transfer Model during the Warming Sub-Period of the Harvesting Period	184
9.2.1. Predicting the Evaporator Steel Temperature Distribution during the Warming Sub-Period.....	186
9.2.2. Predicting the Temperature reached by the Melted Ice Layer at the end of the Warming Sub-Period.....	187
9.2.3 Predicting the Melted Ice Layer Thickness.....	190
9.2.4 Predicting the Mass Flow Rate of Harvesting Gas during the Warming Sub-Period.....	191
9.2.5 Predicting the Refrigerant Side Convective Condensing Heat Transfer Coefficient	193
10. CONCLUSIONS.....	202
11. SUGGESTIONS FOR FURTHER WORK	210
12. REFERENCES.....	212
APPENDICES	216
APPENDIX A1	216
P&I and P-h Diagrams of the Cold Gas and Mechanically Pumped Arrangements of Unit 5 of the ERPM Plant	216
A1.1 The Cold Gas Pumped Arrangement.....	218
A1.2 Mechanically Pumped Arrangement.....	219

APPENDIX A2	220
Model Developed to Predict the Amount of Liquid Ammonia Remaining in an Evaporator Module at the End of the Ice Building Period.....	220
APPENDIX A3	225
Calculations for Predicting the Free Stream Film Velocity of the Falling Water over the Evaporator Plates during the Ice Building Period.....	225
APPENDIX A4	228
Model to Predict the Time Required by the Fully Mechanically Pumped Arrangement to Recharge the Evaporator Plates after Harvesting	228
A4.1 Required Recharge Pump Mechanical Input Power.....	229
A4.2 Vessel and Piping Design for the FMPS.....	232
APPENDIX A5	236
A Brief Investigation, for Purpose of Comparison to the Shah and Nusselt Correlations, of Convective Condensing Heat Transfer Correlations for Flow in Horizontal Tubes.....	236
A5.1 The Dobson and Chato ⁽³⁶⁾ Correlation	236
A5.2 The Jaster and Krosky ⁽³⁷⁾ Correlation	237
A5.3 The EES ⁽³⁷⁾ Correlation.....	237
APPENDIX A6	240
Presentation of Test Data Obtained from Testing at the ERPM Ice Making Plant	240
A6.1 Electrical Meter Readings for the Compressor and the Rate per kWh	241
A6.2 Water and Ice Quantities Measured at the Plant	242
A6.3 Data at the Evaporators	243
A6.4 Data at the Pumper Drums	248
A6.5 Data at the Accumulator.....	254
A6.6 Data at the Condensed Liquid Receiver.....	255
A6.7 Data at the Compressor	256

A6.8 Comparison of the Theoretical and Actual Timing Diagram/Pumping Schedule.....	258
APPENDIX A7	261
Measured Operating Parameters and List of Facilities and Testing Equipment for the Test Days at the ERPM Ice Making Plant	261
A7.1 Component List.....	261
A7.2 Schedule of Gauges.....	262
A7.3 Sample of Recording Data Sheets.....	265
APPENDIX A8	270
Dimensions and Volumes of the Pumper Drum and Accumulator at the ERPM Plant, and Predicting the URD due to the Interaction of Pumping Gas and Cold Circulating Refrigerant.....	270
A8.1 Dimensions of the Pumper Drum and Accumulator at the ERPM Plant ...	270
A8.2 Gas Pumping Process: Predicting the URD due to the Interaction of Pumping Gas and Cold Liquid Refrigerant Being Pumped.....	272
A8.2.1 Predicting the Initial Volume of Liquid in the Pumper Drum	273
A8.2.2 Predicting the Final Volume of Liquid in the Pumper Drum.....	275
A8.2.3 Predicting the Mass and Temperature of the Upper Portion of.....	
Pumped Liquid in the Pumping Pumper Drum.....	278
A8.2.4 Predicting the Temperature of the Upper Pumped Layer for the.....	
Hot Gas Pumped Arrangement	280
APPENDIX A9.....	284
Sizing the Mechanical Pump for the Mechanically Pumped System.....	284
APPENDIX A10	290
Analyses to Support Predictions of the Models of Sections 8 and 9	290
A10.1 Sensitivity Analysis to Support the Predicted Temperature of Liquid that is Expelled and Warmed by Harvesting Gas at the Beginning of the Warming Sub-Period from Section 8.2.1.....	290
A10.2 Sensitivity Analysis to Support the Assumed Percentage of Liquid Trapped behind the Level Regulating Valve at the Beginning of the Re-Cooling Sub-Period of Section 8.2.2	291

A10.3 Mass Rate Balance to Predict the Mass Flow Rate of Refrigerant Built-Up in the Evaporator during Ice Building.....	292
APPENDIX A11	294
Sample Calculation to Support the Model of Section 8.....	294
A11.1 Productive and Unproductive Refrigeration Demands	296
Directly Related to Ice Building	296
A11.1.1 URDs and PRDs at the Evaporator during the Ice Building Period.....	297
A11.1.2 The Warming Sub-Period.....	298
A11.1.3 The Re-Cooling Sub-Period	300
A11.2 URDs at the Accumulator during the Transient Period.....	303
A11.2.1 URDs at the Accumulator during the Complete Ice Building and Shedding Cycle of One Module.....	304
A11.2.2 URDs at the Filling Pumper Drum.....	306
A11.2.3 URD of Re-Cooling the Upper Portion of Circulating Liquid at the Pumping Pumper Drum.....	307
A11.3 Total PRD and URD for the Cold Gas Pumped.....	
Arrangement Per Module	308
A11.3.1 Total PRD Per Module for all Pumping Arrangements.....	308
A11.3.2 Total URD Per Module for the Cold Gas Pumped Arrangement.....	309
A11.4 Predicting the Average Recirculation Ratio and Compressor Work Input for the Operating Cold Gas Pumped System Per Module	309
A11.4.1 Predicting the Average Recirculation Ratio for the Operating CGPS...309	
A11.4.2 Predicting the Average Electrical and Mechanical Compressor Work Input for the Operating CGPS.....	312
A11.5 Total URD for the Hot Gas Pumped Arrangement Per Module	313
A11.5.1 URDs at the Accumulator for the HGPS.....	313
A11.5.2 URDs at the Filling Pumper Drum for the HGPS.....	315
A11.5.3 URD of Re-Cooling the Upper Portion of Circulating Liquid at the Pumping Pumper Drum for the HGPS.....	316
A11.5.4 Total URD for the HGPS.....	317
A11.6 Total URD for the Mechanically Pumped Arrangement Per Module.....	318

A11.6.1 Total URD for the MPS.....	319
A11.7 Total URD for a Fully Mechanically Pumped Arrangement Per Module	319
A11.7.1 Total URD for the FMPS.....	320
A11.8 Comparison of Results for the Pumping Arrangements	320
A11.8.1 Total PRD and URD for the Four Pumping Arrangements.....	320
A11.8.2 COP for the Four Pumping Arrangements.....	322
A11.9 Operating Cost Analysis for the Different Pumping Arrangements	324
 APPENDIX A12.....	 325
Sample Calculation to Support the Model of Section 9.	325
A12.1 Heat Transfer Model during Ice Building.....	326
A12.1.1 The Shah Correlation.....	328
A12.1.2 The Gungor-Winterton Correlation.....	330
A12.1.3 Predicting the Layer of Ice Built during the Ice Building Period	332
A12.2 Heat Transfer Model during the Warming Sub-Period of the Harvesting Period.....	334
A12.2.1 Predicting the Evaporator Steel Temperature Distribution during the Warming Sub-Period.....	334
A12.2.2 Predicting the Temperature reached by the Melted Ice Layer at the end of the Warming Sub-Period.....	336
A12.2.3 Predicting the Mass Flow Rate of Harvesting Gas during the Warming Sub-Period.....	338
A12.2.4 Predicting the Refrigerant Side Convective Condensing Heat Transfer Coefficient.....	340
 APPENDIX A13.....	 345
Analysis to Prove the Simplified Control-Volume Thermodynamic Analysis of Gas and Mechanically Pumped Arrangements in Section 7.2.3.....	345

LIST OF FIGURES.....	Page
Figure 1.1 A diagram of a simplified plate batch ice making machine, based on Senatore ⁽⁴⁾	30
Figure 1.2 Schematic diagram of a simple gas pumped liquid overfeed arrangement.....	33
Figure 1.3 Schematic diagram of a simple mechanically pumped overfeed arrangement.....	34
Figure 1.4 Diagram of the “Cycle Center” liquid overfeed refrigeration system ⁽¹⁰⁾	37
Figure 2.1 Control pressure recirculation system (CPR) from Wright ⁽¹¹⁾	48
Figure 3.1 Timing diagram of Unit 5 of the of the ERPM plant for a full ice making cycle of 15 minutes.....	58
Figure 3.2 Magnified timing diagram for First Half (0 - 450 seconds) if Ice Building and Shedding Cycle.....	59
Figure 3.3 Magnified timing diagram for Second Half (450 - 900 seconds) of Ice- Building and Shedding Cycle.....	60
Figure 3.4 Control volume of Unit 5 of the ERPM plant.....	63
Figure 7.1 Diagram of a simple cold and hot gas pumped liquid overfeed arrangement.....	72
Figure 7.2 Diagram of a simple cold pumped system during pumping.....	75
Figure 7.3 Interior of pumper drum during pumping.....	75
Figure 7.4 (repeated) Diagram of a simple cold gas pumped system during pumping.....	79
Figure 8.1 Control Volume: Evaporator Plates and Manifolds (Ice Building)	88
Figure 8.2 Control Volume: Pre-Chiller	92
Figure 8.3 Control Volume: Evaporator Plates and Manifolds (Warming Sub- Period).....	94
Figure 8.4 Temperature before level regulating valve, T12 versus time for all tests performed at the plant	100
Figure 8.5 Magnified portion of Figure 8.3 to illustrate the method used to obtain the change in temperature of the expelled liquid	101

Figure 8.6 Control Volume: Evaporator Plates and Manifolds (Re-Cooling Sub-Period).....	102
Figure 8.7 Control Volume: Accumulator Drum.....	107
Figure 8.8 Temperature at the accumulator drum for the first test at the ERPM plant.....	113
Figure 8.9 Diagram of the pumper drum showing level control sensors.....	115
Figure 8.10 Control Volume: Pumper Drum { 1 } When Filling	116
Figure 8.11 Wall temperature of pumper drum 1 for the second test at the ERPM plant.....	119
Figure 8.12 Control Volume: Mechanical Pump and Piping	130
Figure 8.13 Recharge/discharge vessels and pump for the fully mechanically pumped arrangement.....	133
Figure 8.14 Percentage URD of total refrigeration demand per module versus average recirculation ratio for one ice building and shedding cycle of 15 minutes	136
Figure 8.15 Magnified scale of Figure 8.14 above	136
Figure 8.16 Total refrigeration demand per module per 15 minute ice building and shedding cycle versus average recirculation ratio.....	138
Figure 8.17 COP per module versus average recirculation ratio over a complete 15 minute ice building and shedding cycle.....	140
Figure 8.18 Percentage URD of total refrigeration demand per module over one ice building and shedding cycle versus saturated evaporator temperature during ice building. Average recirculation ratio is maintained constant at 5.	145
Figure 8.19 Total refrigeration demand per module versus evaporator temperature at an average recirculation ratio of five.....	147
Figure 8.20 COP per module versus evaporator temperature at an average recirculation ratio of five.....	148
Figure 8.21 Total refrigeration demand per module for the four pumping arrangements over a complete ice building and shedding period	149
Figure 8.22 Percentage that each individual URD comprises of the total URD per module for the four pumping arrangements.....	150

Figure 8.23 Total URD per module for the four pumping arrangements	151
Figure 8.24 Total URD per module ignoring $Q_{URD[E]}$ and $\Delta H_{r,s[E]}$	153
Figure 8.25 Annual electrical operating cost for the four pumping arrangements versus average recirculation ratio.....	159
Figure 9.1 Linearised temperature profile for ice being built on one side of an evaporator plate. The actual temperature profile within the ice layer is shown in dashed lines, and the entire system is treated as a control volume. Adapted from Senatore's Fig. 4.3, p. 28 ⁽⁴⁾	166
Figure 9.2 Front and top view of evaporator plates with dimensions and details of the channels within which the refrigerant flows.	167
Figure 9.3 Wall mid-point temperature versus time at the beginning of the re- cooling sub-period.....	176
Figure 9.4 Refrigerant side convective boiling heat transfer coefficients versus inverse of quality (average recirculation ratio x_l) The average recirculation ratio of 5 predicted for the operating ERPM plant is shown in dashed lines.	178
Figure 9.5 Thickness of ice built versus time at an average recirculation ratio of five.....	180
Figure 9.6 Ice thickness built during an ice building period of 13,5 minutes versus refrigerant side convective boiling heat transfer coefficient.....	182
Figure 9.7 Thickness of ice built during the ice building period of 13,5 minutes versus average recirculation ratio for the different heat transfer coefficients. The average recirculation ratio of 5 predicted for the operating ERPM plant is shown as a dashed line.	183
Figure 9.8 Linear temperature distribution in the built up ice layer at the beginning of the warming sub-period	185
Figure 9.9 Temperatures of the inner and outer evaporator steel wall versus time during harvesting, assuming that the outside of the plate is insulated adiabatically by the ice layer.....	187

Figure 9.10 Temperature distribution of the control volume at the evaporator during the warming sub-period, including the melted ice layer at temperature $T_{L.m.har}$ (ignoring the natural convection effect of the ambient air at T_{∞})....	188
Figure 9.11 Temperature of the melted ice layer during the warming sub-period	189
Figure 9.12 Convective condensing heat transfer coefficients versus harvesting time.....	196
Figure 9.13 Ice melted thickness versus harvesting time for the predicted vertical-tube film condensation heat transfer coefficients.....	197
Figure 9.14 Ice melted thickness versus harvesting time assuming that ice is melted for only half of the total harvesting time of 90 seconds.....	199
Figure A1.1 Detailed P & I diagram of Unit 5 of ERPM Plant, showing placement of pressure gauges and temperature sensors	217
Figure A1.2 P-h diagram of refrigerating cycle in Unit 5 with its cold gas pumping arrangement (based on Figure 7.1)	218
Figure A1.3 P-h diagram of refrigerating cycle in the mechanically pumped system of Unit 5, based on Figure 7.2 above	219
Figure A2.1 Flow of ammonia within a channel of the evaporator plate.....	220
Figure A2.2 Fractional liquid content of evaporator channels versus velocity ratio at various average recirculation ratios.....	223
Figure A2.3 Areas occupied by liquid and vapour, predicted by equation (12), throughout the length of the evaporator channels. The actual channel cross sectional area is shown dashed.....	224
Figure A3.1 Diagram of one water distributor above the evaporator.....	225
Figure A4.1 Recharge/discharge vessels and pump for the fully mechanically pumped arrangement.....	228
Figure A4.2 Time required to recharge the evaporator plates vs. number of pipes of equal diameter connected to the evaporator module.....	234
Figure A4.3 Control Volume for Fully Mechanically Pumped System: The recharge/discharge vessels and basic positions and dimensions.....	235

Figure A5.1 Convective condensing heat transfer coefficients versus harvesting time for horizontal and vertical tubes.....	239
Figure A6.1 Refrigerant Pressure at Top and Bottom of Evaporator Plates.....	243
Figure A6.2 Refrigerant Pressures at Evaporator and Pumper Drums, Test 2 Run 1	244
Figure A6.3 Surface Temperatures at Evaporator Bottom Ports: Liquid Inlet and Liquid Outlet.....	244
Figure A6.4 Surface Temperatures at Evaporator Bottom Ports: Liquid Inlet and Liquid Outlet, Test 1 Run 1	245
Figure A6.5 Surface Temperatures at Evaporator Top Ports: Warm Gas Inlet and Liquid-Vapour Outlet.....	246
Figure A6.6 Surface Temperatures at Top, Middle and Bottom of Evaporator Plate	247
Figure A6.7 Temperature at the Level Regulating Control Valve of the Evaporator	247
Figure A6.8 Pumper Drum Pressures (Test 1).....	248
Figure A6.9 Pumper Drum Pressures (Test 1).....	249
Figure A6.10 Pressures and Surface Temperatures (magnified to show effect) at Pumper Drum 1 (Test 2, Run 1).....	249
Figure A6.11 Temperatures at Pumper Drum 1 (Test 2, Run 1).....	250
Figure A6.12 Pressures at Pumper Drum 1 (Tests 1 and 2).....	251
Figure A6.13 Pressures at Pumper Drum 2 (Tests 1 and 2).....	251
Figure A6.14 Pumper Drum and Accumulator Pressures.....	252
Figure A6.15 Surface Temperatures of Liquid Outlet of Pumper Drum 1.....	253
Figure A6.16 Accumulator Pressure for the 1 st Test.....	254
Figure A6.17 Accumulator Temperatures for the 1 st Test.....	254
Figure A6.18 Condensed Liquid Receiver Temperatures for both Tests.....	255
Figure A6.19 Compressor Inlet Pressure.....	256
Figure A6.20 Compressor Outlet Pressure.....	257
Figure A6.21 Compressor Inlet Temperature.....	257
Figure A6.22 Compressor Outlet Temperature.....	258

Figure A6.23 Overlay Plot of Theoretically Predicted (denoted TH) and Actually Measured (denoted ACT) Pumper Drum and Evaporator Pressures during a Harvesting Period of One Module.....	260
Figure A8.1 Volume of Shell of Pumper Drum showing the actual length, and the idealized length of the tube and hemispheres.....	270
Figure A8.2 Volume of Shell of Accumulator Drum showing the actual length, and the idealized length of the tube and hemispheres.....	271
Figure A8.3 Level control sensors of Pumper Drum.....	272
Figure A8.4 Idealised cylindrical pumper drum.....	273
Figure A8.5 Cross-sectional area occupied by the liquid in the pumper drum at the start of pumping.....	274
Figure A8.6 Geometrical partitioning of area occupied by the liquid at the start of pumping (denoted by the hatched and dashed areas).....	274
Figure A8.7 Area occupied by the liquid in the pumper drum at the end of pumping.....	275
Figure A8.8 Geometrical partitioning of area occupied by the liquid at the end of pumping (denoted by the hatched and dashed areas).....	276
Figure A8.9 Recorded Temperatures at Liquid Outlet of Pumper Drum 1.....	278
Figure A8.10 Magnification of Figure A8.9 to show one peak temperature of Test 2, Run 1.....	279
Figure A8.11 Control Volume showing areas occupied by the Residual and Upper Pumped Liquid Layers in the Pumper Drum for the CGPS.....	281
Figure A9.1 Control Volume: Mechanical Pump and Piping.....	285
Figure A9.2 Splitter Manifold feeding modules.....	287
Figure A9.3 Moody Diagram ⁽³⁹⁾	289
Figure A13.1 Cold Gas Pumped System: Processes during Pumping in the Pumper Drum.....	346
Figure A13.2 Interior of pumper drum during pumping.....	347
Figure A13.3 Control Volume: Throttle valve at the entrance to the pumper drum. ⁽⁴⁵⁾	348

LIST OF TABLES.....	Page
Table 3.1 Definition of periods during the ice making cycle for Unit 5 of the ERPM plant.....	56
Table 3.2 Pumping schedule for the two pumper drums of Unit 5.....	57
Table 3.3 Timed processes in the pumper drum and in the evaporator modules..	58
Table 8.1 Pressure recorded at the ERPM plant (Absolute, $P_{atm} = 83,5$ kPa).....	144
Table 8.2 Percentage of total URDs for the four pumping arrangements over a complete ice building and harvesting period, at ERPM operating conditions and at an average recirculation ratio of 5.....	151
Table 8.3 Annual electrical power consumption and cost for the different pumping arrangements, at an average recirculation ratio of 5. Annual cost rounded to nearest R1,000.....	157
Table 9.1 Refrigerant side convective boiling heat transfer coefficients at an average recirculation ratio of 5.....	179
Table 9.2 Parameters predicted from the heat transfer model during ice building at an average recirculation ratio of 5.....	181
Table 9.3 Convective condensing heat transfer coefficients and corresponding thickness of melted ice layer.....	198
Table 9.4 Convective condensing heat transfer coefficients thickness of melted ice for a harvesting time of 45 seconds.....	199
Table 10.1 Key performance quantities measured at the plant.....	203
Table 10.2 (continued) Key performance quantities measured at the plant.....	204
Table A5.1 Convective condensing heat transfer coefficients for flow in horizontal tubes, based on an average recirculation ratio of 5.....	238
Table A6.1 Recorded data for the 2 nd test at the electrical power usage meters..	241
Table A6.2 Industrial kWh tariffs (>132 kV) from Eskom ⁽²⁵⁾ for the period 2010- 2011.....	242
Table A6.3 Water and ice quantities measured at the plant.....	242

Table A7.1 Table of testing apparatus and positions for tests performed at the ERPM plant.....	264
Table A7.2 Definition of periods during the ice making cycle for Unit 5 of the ERPM plant.....	268
Table A7.3 Pumping schedule for the two pumper drums of Unit 5.....	269
Table A9.1 Dimensions of piping measured at the ERPM plant.....	284
Table A10.1 Sensitivity analysis: effect on total percentage URD of the assumed time required to expel the remaining refrigerant in the module at the beginning of the warming sub-period.....	291
Table A10.2 Sensitivity analysis predicting the change in URD per module as a percentage of total refrigeration demand if the volume of liquid trapped behind the level regulating valve at the beginning of the re-cooling sub-period is varied from 0 – 5 %. Average recirculation ratio is five....	292
Table A11.1 Variables used in the sample calculation of Section 8.....	294
Table A11.2 Comparison of the results for the four pumping arrangements.....	321
Table A11.3 Comparison of the COP for the four pumping arrangements.....	323
Table A11.4 Annual electrical power consumption and cost for the different pumping arrangements, at an average recirculation ratio of 5. Annual cost rounded to nearest R1,000.....	324
Table A12.1 Variables used in the sample calculation of Section 9.....	325
Table A12.2 Mid-point steel wall temperatures.....	333
Table A12.3 Parameters predicted from the heat transfer model during ice building.....	334
Table A12.4 Inner and outer wall temperatures at the end of the harvesting period	335
Table A12.6 Convection condensing heat transfer coefficients and corresponding thickness of melted ice layer.....	343
Table A12.7 Convective condensing heat transfer coefficients thickness of melted ice for a harvesting time of 45 seconds	343
Table A13.1 Variables used in the analysis presented below.....	345

LIST OF SYMBOLS AND NOMENCLATURE

Variable	Description	Units
a	Area	m^2
$a_{[E]chl}$	Cross-sectional area of one channel of an evaporator plate	m^2
B_i	Biot number	
Bo	Boiling number; Shah ⁽²⁶⁾	
c	Specific heat	$kJ/kg.C$
C	Coefficient used in the one-term approximation of the Fourier series for transient heat conduction	
$CGPS$	Cold gas pumped system	
Co	Boiling convection number; Shah ⁽²⁶⁾	
Co_{har}	Condensing convection number; Shah ⁽²⁹⁾	
COP	Coefficient Of Performance	
d, D	Diameter of pipe, channel or vessel/drum	m
E	Enhancement factor; Gungor et. al ⁽²⁸⁾	
E_{cv}	Internal energy of a control volume	kJ
$f_{[PI]}$	Constant friction factor of piping	
F_o	Fourier number	
$F_{rl[E]chl}$	Fractional refrigerant liquid content of the evaporator channel.	
$FMPS$	Fully mechanically pumped system	
g	Acceleration due to gravity	m/s^2
G	Mass flow per unit area (mass flux)	$kg/m^2.s$
h	Specific enthalpy	kJ/kg
h_{sf}	Latent heat of ice formation	kJ/kg
h'_r	Refrigerant side convective boiling heat transfer coefficient	$W/m^2.^0C$
h'_l	Superficial heat transfer coefficient of the liquid phase only; Shah ⁽²⁹⁾	$W/m^2.^0C$
h'_w	Water-side Convection heat transfer coefficient	$W/m^2.^0C$
$h'_{r.har}$	Refrigerant side convective condensing heat transfer coefficient during the harvesting process	$W/m^2.^0C$
$h'_{2ph[EES]}$	Local two-phase convective boiling heat transfer coefficient predicted by Engineering Equation Solver (software) ⁽³⁴⁾	$W/m^2.^0C$
h'_l	Heat transfer coefficient assuming all mass to be flowing as liquid; Shah ⁽²⁶⁾	$W/m^2.^0C$
$h'_{2ph[EES]\{c\}}$	Local two-phase convective condensing heat transfer coefficient in horizontal tubes, predicted by Engineering Equation Solver (software) ⁽³⁷⁾	$W/m^2.^0C$
$h'_{l\{c\}}$	Heat transfer coefficient assuming all mass to be flowing as liquid; Shah ⁽²⁹⁾	$W/m^2.^0C$

Variable	Description	Units
$h'_{2ph[Sh]}$	Local two-phase convective boiling heat transfer coefficient; Shah ⁽²⁶⁾	W/m ² . ⁰ C
h'_p	Pool boiling convection heat transfer coefficient	W/m ² . ⁰ C
$h'_{2ph[Sh][c]}$	Modified local two-phase convective condensing heat transfer coefficient; Shah ⁽²⁹⁾	W/m ² . ⁰ C
$h'_{2ph[D\&C][c]}$	Local two-phase convective condensing heat transfer coefficient in horizontal tubes; Dobson and Chato ⁽³⁶⁾	W/m ² . ⁰ C
$h'_{2ph[J\&K][c]}$	Local two-phase convective condensing heat transfer coefficient in horizontal tubes; Jaster and Krosky ⁽³⁷⁾	W/m ² . ⁰ C
$h'_{2ph[G]}$	Local two-phase convective boiling heat transfer coefficient; Gungor et. al ⁽²⁸⁾	W/m ² . ⁰ C
$h_{2ph[Nu][c]}$	Nusselt two-phase convective condensing heat transfer coefficient; Johnson ⁽²⁷⁾	W/m ² . ⁰ C
$\bar{h}'_{2ph[Sh][c]}$	Mean local two-phase convective condensing heat transfer coefficient; Shah ⁽²⁹⁾	W/m ² . ⁰ C
h_{fg}	Difference in enthalpy for saturated vapour and saturated liquid conditions	kJ/kg
ΔH_r	An enthalpy gain of flowing refrigerant	kJ
$\Delta \bar{H}_r$	A temporary enthalpy gain of flowing refrigerant due to an inherent refrigerating process	kJ
$H'_{[P]}$	Head developed by mechanical pump	m
$HGPS$	Hot gas pumped system	
k	Thermal conductivity	W/m. ⁰ C
kWh	Kilowatt hour	kWh
$K_{[PI]}$	Minor loss coefficient of piping	
$l_{[PI]}$	Length of piping	m
L	Length	m
$L_{[E]chl}$	Length of the evaporator channel	m
L_c	Characteristic length	m
L'	Idealised length of the cylindrical portion of the pumper drum and accumulator	m
L''	Idealised length of the cylinder of the pumper drum incorporating the entire volume of the pumper drum	m
m_m	Molecular weight	g/mol
m	Mass	kg
\dot{m}	Mass flow rate	kg/s
MPS	Mechanically pumped system	
n	Number of plates per module	
Nu	Nusselt number	
P	Pressure	kPa
PRD	Productive refrigeration demand, any load directly associated with ice making	kJ
Pr	Prandtl number	

Variable	Description	Units
Q	Heat transfer across the boundary of a control volume	kJ
Q_{PRD}	Productive refrigeration demand arising from heat transfer across the boundary of a control volume	kJ
Q_{PRD}	Unproductive refrigeration demand arising from heat transfer across the boundary of a control volume	kJ
\dot{q}	Heat flux	W/m ²
\dot{Q}_{cv}	Net rate of energy transfer by heat across the boundary of a control volume	W
\dot{Q}	Heat flow	kW
$r_{[PD]}$	Radius of the pumper drum	m
Re	Reynolds number	
S	Suppression factor; Gungor et. al ⁽²⁸⁾	
t	time	s
$t_2 - t_1$	Unless otherwise stated, denotes the time interval between the beginning and end of a period	s
T	Temperature	⁰ C
T_{sat}	Saturated temperature	⁰ C
u	Internal energy	kJ/kg
U	Internal energy of a control volume	kJ
$\Delta \hat{U}$	Temporary change in internal energy due to an inherent refrigerating process	kJ
URD	Unproductive refrigeration demand, any load not directly associated with ice making	kJ
V	Volume	m ³
V_i	Velocity at the inlet of the control volume	m/s
V_o	Velocity at the outlet of the control volume	m/s
$V_{[ACC]}$	Internal volume of the accumulator drum	m ³
$V_{[PD]}$	Internal volume of the pumper drum	m ³
\dot{V}	Volumetric flow rate	m ³ /s
\dot{v}	Velocity	m/s
\dot{v}_∞	Velocity of the falling water at the evaporator plate during ice building	m/s
$w_{[E]}$	Width of one plate of the evaporator	m
\dot{W}	Power	kW
\dot{W}_{cv}	Net rate of energy transfer by work across the boundary of a control volume	W
W	Energy input by work across the boundary of a control volume	kJ
$\dot{W}_{[CR]elec}$	Electrical shaft power input into the compressor	kW
$\dot{W}_{[P]elec}$	Electrical shaft power input into the pump	kW
$\dot{W}_{[CR]mech}$	Mechanical shaft power input into the compressor	kW

Variable	Description	Units
$\dot{W}_{[P]mech}$	Mechanical shaft power input into the pump	kW
x'	Refrigerant quality	
x	Instantaneous refrigerant recirculation ratio	
\bar{x}	Average refrigerant recirculation ratio	
x_I	Average refrigerant recirculation ratio, same as \bar{x}	
$x_{r[E]o}$	Quality at the outlet of the evaporator	
X_{tt}	Turbulent-turbulent Lockhart Martinelli parameter	
y	Thickness	m
y_I	Thickness of the ice layer	m
y_s	Thickness of steel	m
z	Height	m
z_i	Height at the inlet of the control volume	m
z_o	Height at the outlet of the control volume	m

Subscripts

Subscript	Description
$2ph$	Two-phase
atm	Atmospheric conditions
$[ACC]$	{referring to} The accumulator
$[ACC-PD]$	From the accumulator to the pumper drum
$[ACC-P]$	From the accumulator to the mechanical pump
$build$	Parameters associated with the ice building process
b	Built (as in ice built)
$\{c\}$	{referring to} Condensation, or the condensing process
$[C]$	{referring to} The condenser
chl	Parameters associated with the channel of the plate inside which refrigerant circulates
$[CR]$	{referring to} The compressor
$circ[PD-E]$	Circulating (e.g. circulation of liquid between pumper drum and evaporator during pumping period of the pumper drum). Referring to the interaction of pressurising gas and the upper portion of colder circulating liquid refrigerant in the pumper drum
$cont[E-ACC]$	Parameters associated with warm harvesting gas in contact with the cold liquid refrigerant at the beginning of the warming sub-period
$\{CGPS\}$	The cold gas pumped system
$[DV-RV]$	From discharge vessel to recharge vessel
$[DV]$	{referring to} The discharge vessel of the fully mechanically pumped system
$\{e\}$	{referring to} Evaporation
$elec$	{referring to} Electrical work input
$[E]$	{referring to} The evaporator

<i>Subscript</i>	Description
<i>[E-ACC]</i>	From the evaporator to the accumulator
<i>[E-DV]</i>	From the evaporator to the discharge vessel
E_{cv}	Sum of the internal, kinetic and gravitational potential energies of the mass contained within a control volume
<i>EES</i>	Engineering Equation Solver (software)
<i>[EX&p]</i>	{referring to} The expansion valve and its piping
<i>{FMPS}</i>	The fully mechanically pumped system
<i>h</i>	{referring to} The horizontal pipes of the MPS
<i>har</i>	{referring to} The harvesting process
<i>har.1 ...har.3</i>	1 st ... 3 rd harvesting load
<i>heat[ACC]</i>	Parameters associated with vented pressurising gas from the pumping pumper drum heating up the accumulator at the end of the pumping period of that pumper drum
<i>heat[PD]</i>	Parameters associated with pressurising gas heating up the pumper drum during the pumping period of that pumper drum
<i>{HGPS}</i>	The hot gas pumped system
<i>i</i>	Inlet
<i>.i</i>	Inner (e.g. layer or thickness)
<i>I</i>	Ice
<i>I.b</i>	Parameters associated with the ice layer during ice building
<i>I.i</i>	Parameters associated with the inner layer of ice built
<i>I.o</i>	Parameters associated with the outer layer of ice built
<i>I.m</i>	Ice melted, or melting
<i>I.m.har</i>	Parameters associated with the melted ice layer during the harvesting process
<i>I.req</i>	Ice required
<i>l</i>	Liquid (subcooled or saturated)
<i>(l,v)</i>	Two-phase mixture
<i>mech</i>	{referring to} Mechanical work input
<i>mod</i>	Parameters associated with the evaporator plates of one module
<i>{MPS}</i>	The mechanically pumped system
<i>o</i>	Outlet
<i>.o</i>	Outer (e.g. layer)
<i>PRD</i>	Productive Refrigeration Demand
<i>[PRC]</i>	The water pre-chiller
<i>[PI]</i>	{referring to} Piping
<i>[P]</i>	The mechanical pump
<i>[P-E]</i>	From the mechanical pump outlet to evaporator inlet
<i>[PD+]</i>	Parameters associated with the pressurised [pumping] pumper drum during the pumping period
<i>[PD-]</i>	Parameters associated with the de-pressurised pumper drum during the filling period
<i>[PD-E]</i>	From the pumper drum to the evaporator
<i>[PD]</i>	The pumper drum
<i>rfl</i>	The (re)filling process at the pumper drum

<i>Subscript</i>	Description
<i>rl</i>	Parameters associated with the liquid state of the refrigerant
<i>rv</i>	Parameters associated with the vapour state of the refrigerant
<i>r</i>	Refrigerant
<i>r.har</i>	{referring to} the refrigerant during the harvesting period
[<i>REC</i>]	The condensed liquid receiver
[<i>REC-E</i>]	From the condensed liquid receiver to the evaporator
<i>RL</i>	The residual layer in the pumper drum
<i>rech</i>	{referring to} The recharge pipe attached to each evaporator plate in the fully mechanically pumped system
<i>req</i>	Required (e.g. ice required)
[<i>RV</i>]	{referring to} The recharge vessel of the fully mechanically pumped system
<i>s</i>	Steel parameters of the evaporator plates
<i>sat</i>	Saturation / saturated
{ <i>sc</i> }	Subcooled ice layer
<i>trap[E]</i>	Parameters associated with trapped liquid and vapour in the modules that is vented to the accumulator at the beginning of the re-cooling sub-period
<i>UPL</i>	The upper pumped layer in the pumper drum
<i>URD</i>	Unproductive Refrigeration Demand
<i>v</i>	Vapour (saturated or superheated)
<i>vent[PD-ACC]</i>	Parameters associated with the venting of gas from the pumper drum to the accumulator
<i>vent[(PD+)-ACC]</i>	Parameters associated with the venting of gas from the pressurised pumping pumper drum to the accumulator
<i>vent[(PD-)-ACC]</i>	Parameters associated with the venting of gas from the depressurised pumper drum to the accumulator
<i>w</i>	Water (liquid)
<i>w.i</i>	Water inlet
<i>w.o</i>	Water outlet

Greek Variables

<i>Greek Variable</i>	Description	Units
ρ	Density	kg/m ³
η	Efficiency	
η_m	Motor efficiency	
$\eta_{[P]}$	Pump efficiency	
μ	Dynamic Viscosity	kg/m.s
θ	Velocity ratio of average velocities within the plate channel	
ψ	$h'_{2ph[Sh]} / h'_1$	
ψ_{har}	$h'_{2ph[Sh]\{c\}} / h'_1$	

<i>Greek Variable</i>	Description	Units
ψ_{bs}	Value of ψ in the bubble suppression regime based on, and at various values of Co	
ψ_{cb}	Value of ψ in the convective boiling regime based on, and at various values of Co	
α	Thermal diffusivity	m^2/s
ξ	Coefficient used in the one-term approximation of the Fourier series for transient heat conduction	
δ_w	Film layer thickness of water flowing down one evaporator plate	mm
ν	Specific Volume	m^3/kg
ν_w	Kinematic viscosity of water	m^2/s
β	Plate inclination angle	$^\circ$
Γ_n	Liquid feed rate per unit width	$kg/m.s$
φ, θ, β	Angles	rad

1. INTRODUCTION

1.1.Overview: Refrigeration Systems of Ice

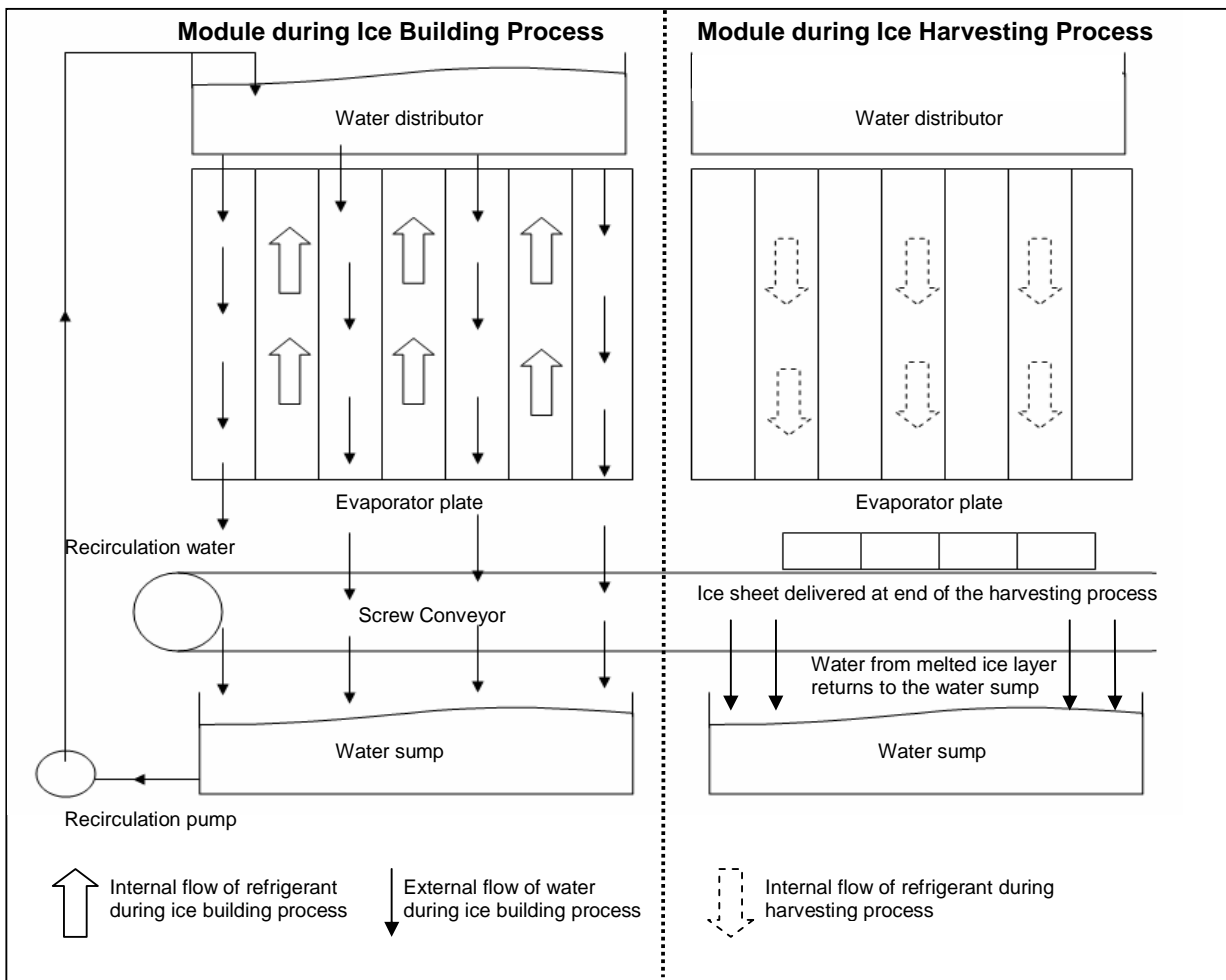


Figure 1.1 A diagram of a simplified plate batch ice making machine, based on Senatore⁽⁴⁾

“Ice can be made in either continuous or batch-type processes, depending on the form of ice desired and the principle(s) of operation of the machine making such ice.”⁽²⁾ Most mines in South Africa use batch-type processes to produce ice. “Two classes of suitable ice are single-phase solid pieces of irregular, finite size, termed particulate ice, and near homogenous ice-water mixtures termed binary or slurry ice.”⁽²⁾ “With ice the latent heat of melting as well as the warming of the melted

ice water is available for cooling and per kilogram ice has approximately five times the cooling effect of chilled water.”⁽⁹⁾ Thus ice is ideal for efficient cooling applications in mines at depths below 3000 m.^{(18) & (47)}

Figure 1.1 above shows a simplified arrangement of a plate batch ice making machine. This produces finite-size, particulate ice – difficult to make in continuous processes. The maximum production rate of such particulate ice is achieved by optimising the duration of the ice-making cycle, consisting of an ice making process and a harvesting process. During ice making, refrigerant at temperatures below the solidification temperature of water runs upwards within channels inside the steel plates. Water flows along the outside of the plates via gravity, and solidifies on the plate wall. Plates are mounted vertically in rows and are connected to common refrigerant and water sources. The layer of ice built on each plate continues to grow until the heat flux through the plate decreases sufficiently to unacceptably slow further solidification.

During the harvesting process, once the desired thickness of ice is formed, hot refrigerant liquid or vapour displaces the cold liquid refrigerant. The ice layer in contact with the plate wall melts, and the ice sheet slides off the plate via gravity. Once the ice sheet has fallen off the plate, cold refrigerant enters the channels and the process of ice making recommences. “The ice can vary in thickness but is generally about 6 mm thick.”⁽¹⁸⁾

“The concept of sending ice down a shaft dates back to about 1976 when the Chamber of Mines of South Africa first considered it.”⁽¹⁸⁾ A major advantage of using ice in mine cooling is that “the amount of water to be sent down in the form of ice and subsequently pumped out of a mine can be reduced to between 10 and 20 % of that required when employing a conventional machine producing 4°C

water on surface without an energy recovery system. This implies a five to ten fold reduction in energy consumption associated with pumping to surface.”⁽¹⁸⁾

Senatore⁽⁴⁾ succinctly outlines the thermodynamic disadvantages of particulate ice-making by a batch process and the need to identify sensitive parameters in mitigating these disadvantages.

“The major disadvantages of the use of particulate ice as a cooling medium are:

1. The high power consumption resulting from the necessity of low evaporator temperatures which in turn lead to low coefficients of performance.
2. The inherent inefficiencies, namely the harvesting process.”⁽⁴⁾ These inefficiencies are discussed in detail in Section 8. below.

“The cost effectiveness of ice systems depends largely on the capital and operating costs involved,”⁽⁴⁾ with the main objective to obtain a maximum ice making yield at the lowest possible operating costs. “It is essential to know what parameters or factors are sensitive in the process so as to facilitate an increase in the ice making capacity, efficiency. A greater understanding of the process will assist the design engineer in developing or improving the ice machines and the ice making process.”⁽⁴⁾

1.2. Introduction to Liquid Overfeed Systems (Arrangements)

The basic operation of gas and mechanically pumped liquid overfeed arrangements is presented below. The operating ERPM plant is then briefly introduced, followed by a brief overview of the development of liquid overfeed systems.

Evaporators flooded by liquid overfeed systems have an advantage over dry-expansion evaporators in that the greatest wetting of interior tube surfaces, and consequently highest possible heat transfer rate, are obtained. These systems are fed from an accumulator or surge drum that serves as a liquid reservoir from which the liquid refrigerant is pumped or circulated (usually via gravity) through the evaporators. The accumulator serves to eliminate any flash gas from entering the evaporator, as well as preventing any liquid from entering the compressor. High recirculation ratios of up to 7 to 1 can be obtained (seven times as much liquid is circulated as can be vapourised, in which case the returning refrigerant mixture is composed of six parts liquid and one part vapour).

1.2.1. Hot and Cold Gas Pumped Arrangements

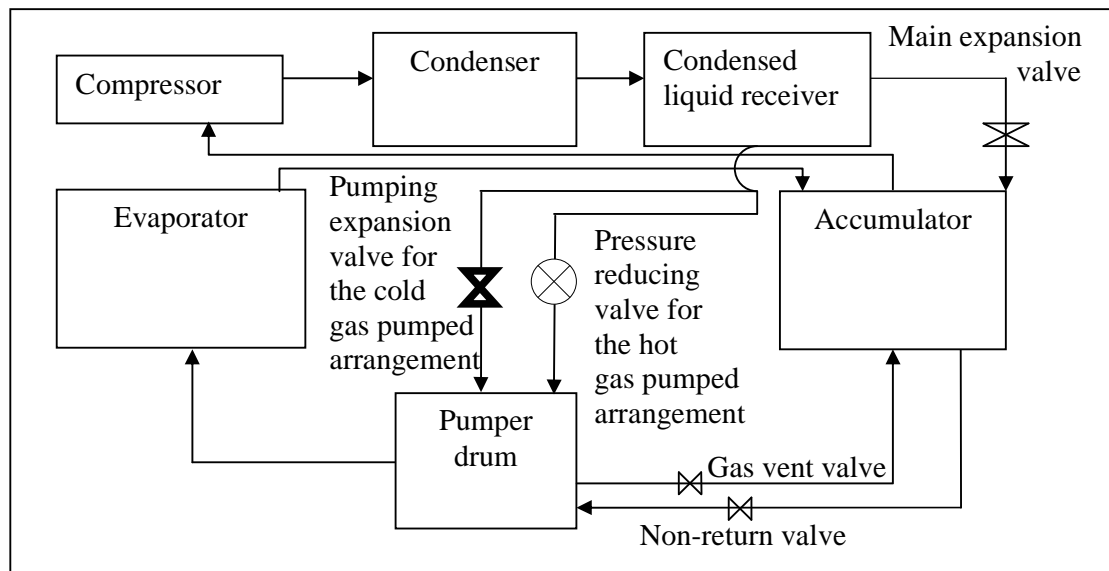


Figure 1.2 Diagram of a simple cold and hot gas pumped liquid overfeed arrangement

From Figure 1.2 above, for a *hot* gas pumped arrangement, high pressure gas from the high pressure receiver² pressurizes the pumper drum and feeds liquid refrigerant to and through the evaporator. The two-phase mixture at the exit of the evaporators then passes into the accumulator, where it is separated into saturated

² For smaller hot gas pumped arrangements, hot gas directly from the compressor outlet is used to pressurize the pumper drum.

liquid and vapour. Liquid in the accumulator fills the pumper drum before its next pumping period, whilst the vapour is drawn into the compressor. Any pressurising gas remaining in the pumper drum at the end of its pumping period is vented to the accumulator.³

For a *cold* gas pumped arrangement, essentially the same pumping process occurs as described above, except saturated liquid from the high pressure⁴ receiver expands across the expansion valve (shown in bold in Figure 1.2 above) to pressurize the liquid in the pumping pumper drum. Section A1.1 of Appendix A1 presents a P-h diagram for a cold gas pumped arrangement.

1.2.2. Mechanically Pumped Arrangements

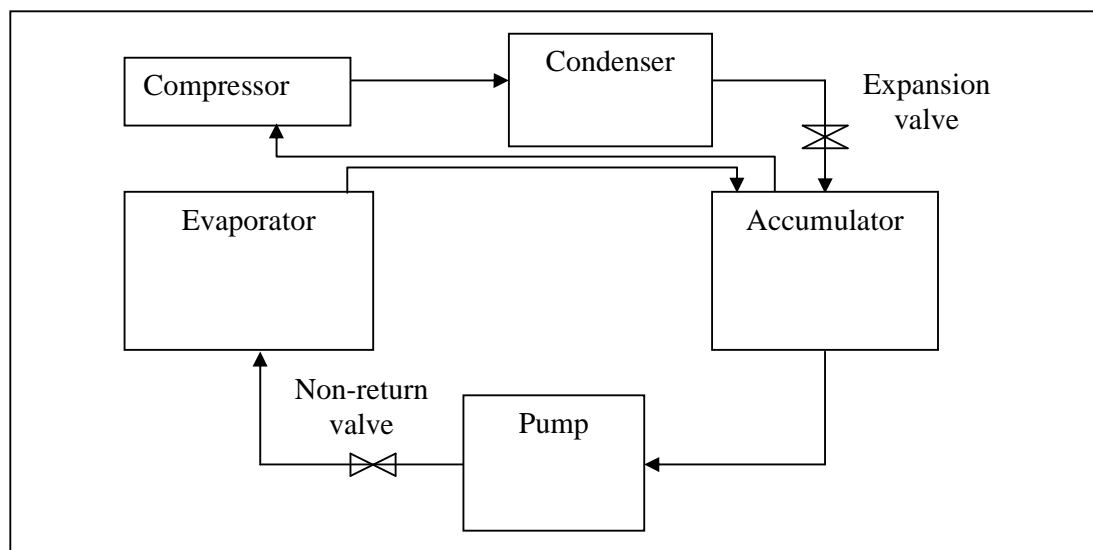


Figure 1.3 Schematic diagram of a simple mechanically pumped overfeed arrangement

From Figure 1.3 above, liquid refrigerant is circulated to and through the evaporator using a mechanical pump, which is fed from the accumulator. The two-phase mixture at the exit of the evaporators then passes into the accumulator, where it is separated into saturated liquid and vapour. Liquid in the accumulator

³ The gas vent line to the accumulator, regulated by a controlled valve, is opened during venting and filling of the pumper drum.

⁴ Usually a condensed liquid receiver for the cold gas pumped arrangement.

feeds the pump whilst the vapour is drawn into the compressor. Section A1.2 of Appendix A1 presents a P-h diagram for a mechanically pumped arrangement.

1.2.3. Brief Introduction to the Operating ERPM Plant

Underground operations at East Rand Proprietary Mines (ERPM) Ltd were suspended on 31 October 2008, however, all the work described in this research report took place whilst the mine was still operational.

The wholly South African designed surface plant at ERPM's Far East Vertical Shaft, consists of six ice-making units, each comprising multiple evaporators (ice makers), a screw compressor package, multiple condensers and a cooling tower. In total, the plant is capable of producing 6000 tons of ice in a 24 hour day. "Traditionally, deep level mines have used chilled water produced on surface or underground for their cooling requirements, however, as mines go deeper the pumping costs and piping systems required make the use of chilled water less economical." ⁽⁹⁾ The refrigeration capacity for each unit (at the time of writing of this report, three of the six units were in operation) is provided by Howden type WRV-510 screw compressors, which are driven by 1700 kW motors. Four of the units utilise unique vertical shell and tube type evaporators, with a liquid defrost ice making system, whilst two units utilise plate evaporators and warm refrigerant gas as the harvesting medium. A more detailed description of the plant and its operations is provided in Section 3.1. below.

1.2.4. Brief Overview of the Development of Gas Pumped Liquid Overfeed Systems

The gas pumped liquid overfeed system of the ERPM ice making plant is based on the overfeed system first designed in the late 1950's by Jack Watkins, who "developed his liquid line transfer concept further into what he called a 'Cycle

Center,' using high pressure gas to recirculate the liquid refrigerant.⁽¹⁰⁾” Shown in Figure 1.4 below, this involved controlling a liquid level in an accumulator. The following is a description of operation of the “Cycle Center” design.

The liquid, flash cooled to suction temperature through the expansion valve at the inlet to the accumulator would alternately fill the two pumper drums mounted below the accumulator. The pumper drums alternately being pressurized by discharge gas, reduced in pressure from the compressor outlet, would thus feed its volume of cold liquid to and through the evaporators. Non-return valves ensure that the pressurized pumper drum does not feed its liquid back into the accumulator. The cycle center is thus a liquid recirculation system using high pressure gas from the compressor outlet.

“In 1972, Watkins patented the concept of recirculating the liquid by use of flash gas. Instead of pressurizing the “pumper” with high pressure gas, high pressure warm liquid would be introduced into the trap.⁽¹⁰⁾”⁵ The difference between a hot and cold gas pumped arrangement is illustrated in Figure 1.2 above, where instead of using hot gas from the condenser to pressurise the pumper drum, flash gas, generated at the expansion valve between the condenser and the pumper drum, pressurises the drum.

The flash gas generated as the liquid enters the “pumper [drum]” displaces the liquid in the “pumper”, this liquid being the feed to the evaporators. Using flash gas for such pumping, as opposed to warmer high pressure gas, “represents energy savings compared to the original concept, as the flash gas, reintroduced to the compressor suction after the pumper drum cycles back to the “fill” cycle, would represent no penalty to the operating cost of the system.”⁽¹⁰⁾ This is because the

⁵ The “trap” referred to here is a vessel that is filled with liquid from the accumulator and is then pushed through to a secondary vessel that circulates the liquid through the evaporators. Section 2.2 below describes a plant utilising a “dump trap”.

use of flash gas to pressurise a drum and circulate liquid refrigerant through the evaporators is essentially thermodynamically “free”; the last step of the reduction of condensed liquid down to evaporating pressure does useful internal work in pumping the liquid to and through the evaporators⁶. A more detailed description of the operation of the ERPM plant and its similarities to the system described above is provided in Section 3. below.

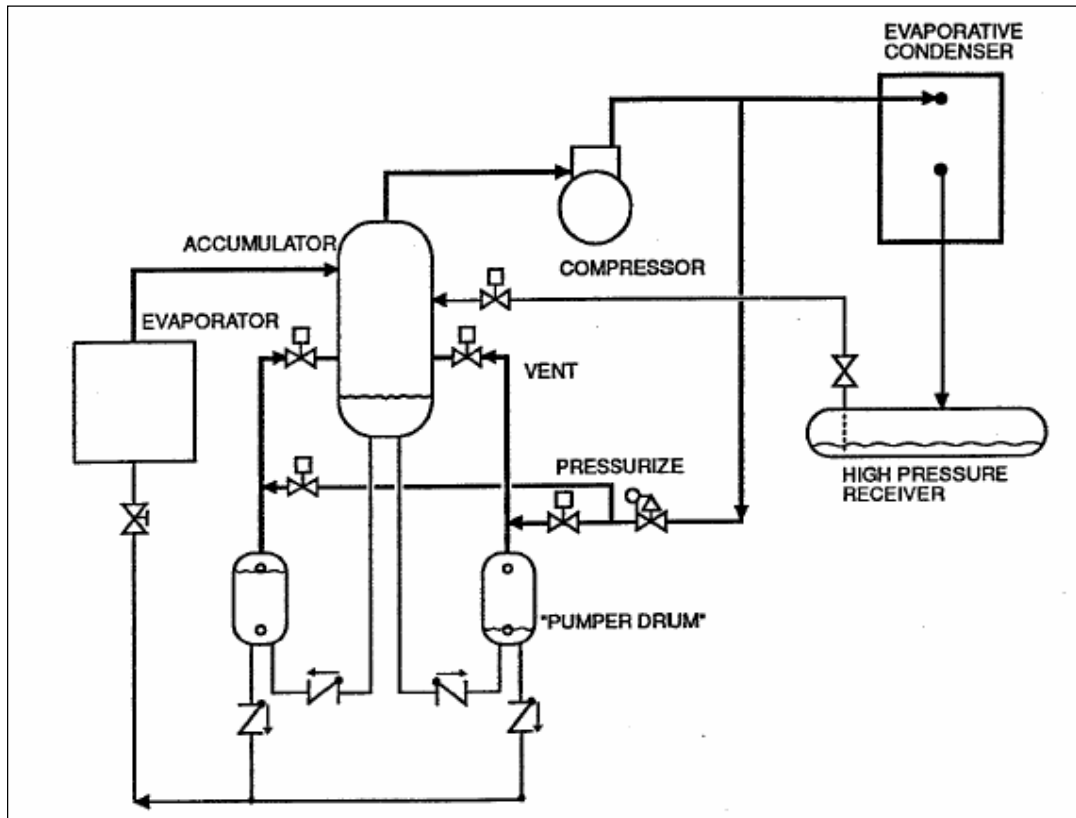


Figure 1.4 Diagram of the “Cycle Center” liquid overfeed refrigeration system⁽¹⁰⁾

⁶ The concept that using flash gas to pump the liquid refrigerant to the evaporators is thermodynamically “free” is expanded on in Section 7.2 below.

1.2.5. Overview of this Investigation

A brief overview of the topics discussed in each section of this investigation is presented below.

Section 2 presents a literature review of three articles from (i) ASHRAE,⁽⁵⁾ (ii) Lorentzen and Baglo⁽⁶⁾ and (iii) Wright.⁽¹¹⁾ All three articles investigate the relative energy efficiency and cost effectiveness of small (relative to the ERPM plant) gas and mechanically pumped liquid overfeed arrangements. The suggestions and conclusions of these articles form the basis on which the results of the theoretical models developed in Sections 8. and 9. are compared. Finally, an overview of current methods of theoretically modelling the stationary processes in batch cycling refrigeration systems is presented, and their relevance to the theoretical models of this investigation are discussed.

Section 3 introduces the ice making plant at ERPM. The plant's background, design and layout, as well as the operating processes of Unit 5 of the plant are described in detail. A timing diagram and a pumping schedule are presented to illustrate when the different processes of the ice making cycle occur.

Section 4 discusses the reason for and the scope of this investigation, and discusses what contribution this study aims to make to advancing engineering knowledge on the subject of batch-type ice making.

Section 5 outlines the methodology that is used to develop the theoretical models of the mechanically and gas pumped liquid overfeed arrangements. Areas of analysis where significant comparisons can be made between the different

pumping systems are identified as key modelling parameters for Section 8. Section 6 then lists the objectives of the study.

Section 7 outlines the fundamental basis of theoretically modeling the different pumping arrangements. It also expands on some vital concepts mentioned in the introductory chapters (Sections 1-5). The method of comparing the energy efficiency and electrical cost effectiveness of the different arrangements is also introduced in this section.

Section 8. develops the theoretical model of productive and unproductive refrigeration demands for the different pumping arrangements. It predicts, based on test data from the existing cold gas pumped ERPM plant, the average recirculation ratio and consequently the mass flow rate through the evaporators. By predicting this performance quantity, models of a hot gas and two possible mechanically pumped arrangements, operating under the same operating conditions (pressures and temperatures) as well as performance quantities (average recirculation ratio and mass flow rate), are developed. All productive and important unproductive refrigeration demands are included in these models, which then allows for the energy efficiency and electrical cost effectiveness of the four models to be compared under similar operating conditions.

In Section 9., heat transfer models during the ice building and shedding periods are developed to provide an independent method of corroborating the average recirculation ratio and mass flow rate predicted in Section 8.

Section 10. discusses the results of the theoretical models of Sections 8. and 9., and compares them to the conclusions and suggestions of the three articles reviewed in Section 2. Conclusions are therefore drawn regarding the relevance of these articles to large batch-type ice making plants. Finally in Section 11. suggestions for further work are proposed.

2. LITERATURE SURVEY: KEY FEATURES OF LIQUID OVERFEED PUMPING ARRANGEMENTS

This Section presents a critical review of one overview and two studies that are relevant to this investigation. Statements from the literature are reviewed on the relative merits of gas and mechanically pumped arrangements, however, one key objective of this investigation is to predict whether these statements are true for large batch-type plants such as ERPM.

ASHRAE⁽⁵⁾ (pp. 1,1 - 1,9) introduces the concept of hot gas and mechanically pumped liquid overfeed systems and lists the advantages and disadvantages of both pumping arrangements.

Lorentzen and Baglo⁽⁶⁾ then compare the operational efficiencies of a hot gas pumped recirculation system with that of a mechanically pumped system. They also suggest that a cold gas pumped arrangement, operated at high recirculation ratios, would be even more energy efficient than a mechanically pumped arrangement.

Finally, Wright⁽¹¹⁾ compares the efficiencies of cold and hot gas as well as mechanically pumped arrangements and concludes that the cold gas pumped system, operating at low recirculation ratios (2:1) would be more energy efficient than its mechanically pumped counterpart.

Later, in Sections 8. and 9., the predictions of the models therein are compared to those in these three key pieces of literature. Conclusions drawn therefrom are discussed in Section 10.

2.1. Efficiencies of Differently Pumped Liquid Overfeed Arrangements

2.1.1. Advantages of Liquid Overfeed Arrangements and using Ammonia as the Refrigerant for such Systems

In general, there are many advantages that a liquid overfeed system offers over dry expansion type systems, including:

- high system efficiency
- reduced operating expenses
- lower energy costs
- fewer operating hours. ⁽⁵⁾

“Ammonia has a relatively high latent heat of vaporization, so for equal heat removal, much less ammonia mass must be circulated compared to halocarbons. ⁽⁵⁾” Thus ammonia is a most suitable refrigerant for overfeed systems.

2.1.2. Refrigerant Recirculation Ratio

In a liquid overfeed system, the recirculation ratio is the mass ratio of liquid pumped to the evaporator over the amount of vapour present at the outlet of the evaporator; with the amount of liquid vapourised based on the latent heat for the refrigerant. The optimum recirculation ratio at the outlet of the evaporator for both gas and mechanically pumped arrangements “will always be one of great and varied discussion.”⁽¹¹⁾ “For each evaporator, there is an ideal circulating rate for every loading condition that will result in the minimum temperature difference and the best evaporator efficiency.”⁽⁵⁾ It appears that it is safer to “overcirculate”, with a mechanically pumped circulation ratio of 5 and that of a single gas pump

(which uses one pumper drum to circulate the liquid) of 2⁽¹¹⁾, “however, the selection of recirculation rate is much more critical for a gas pressure recirculation system than it is for a mechanical pump when considering the energy required to operate.⁽¹¹⁾”

Although high recirculation ratios are advantageous from a heat transfer perspective, for a mechanically pumped arrangement, “high circulation rates (and subsequently higher mass flow rates through the evaporator) can cause excessively high pressure drops through evaporators and wet return lines.⁽⁵⁾” For a gas pumped system, a higher recirculation ratio, which increases the mass flow rate through the evaporators, results in the warm pressurising gas coming into contact with a greater volume of circulating liquid at the pumper drum. This interaction results in an *unproductive refrigeration demand* of re-cooling the warmed liquid. To decrease this interaction, lower recirculation ratios are favoured for gas pumped arrangements.⁽⁵⁾

2.1.3. Mechanically and Gas Pumped Systems

When comparing mechanically pumped to equivalent hot gas pumped overfeed arrangements, several factors must be considered. The added setup cost of the pump, the possibly large Net Positive Suction Head required, as well as maintenance costs, may offset any achievable increase in efficiency. If the pump inlet pressure is not more than double the specified net positive suction pressure, and velocity is higher than 0,9 m/s, cavitation may occur. It is also generally good practice to use 2 pumps, one operating and one standby.⁽⁵⁾

“A mechanical pump can be used to pump the gas with no effect on evaporator performance.”⁽⁵⁾ The above statement forms part of the fundamental assumptions considered when modelling and comparing the two pumping arrangements in this

investigation. “Gas-operated systems must, however, maintain the condensing pressure within a much smaller range to pump the liquid and maintain the required overfeed rate.⁽⁵⁾” Referring to Figure 1.4 above, a gas pumped arrangement, where pumping power is supplied by hot gas at condenser pressure, usually utilises two pumper drums, alternating between filling and pumping throughout the refrigeration cycle. As “hot” gas from the condenser is used to pressurise the pumper drum and circulate the cold liquid refrigerant to the evaporators, the difference in pressure between the condenser and the evaporator must be kept as small as possible to minimise the unproductive refrigeration demand resulting from this interaction, whilst at the same time maintaining a large enough pressure difference to fulfill the pumping requirements. To compensate for this unproductive refrigeration demand (to be hereafter referred to in this investigation as URD), it is necessary to increase the recirculation ratio through the evaporator, whilst at the same time, minimising the resulting increase in URD at the pumper drums. Thus, optimising the recirculation ratio for gas pumped arrangements is more critical – and complicated - than for their mechanically pumped counterparts.

When analysing and modelling the two different classes of pumping arrangements (gas and mechanical) in Section 8. below, it is assumed that since the plant has been designed for cold gas pumping (the worst case of gas pumping, with the lowest pressure differential between the pressurising gas and the liquid being pumped), it is capable, with negligible change in condensing conditions, of recirculating liquid by either mechanical or hot gas pumping.

ASHRAE⁽⁵⁾ concludes that “gas pumped systems offer no advantage over their mechanically pumped counterparts when the overall capital and operational costs of both systems are compared.”⁽⁵⁾ Although this statement may be true for continuous-process overfeed systems, whether the above statements also apply to

large batch type ice making plants, in particular that of the ERPM facility, is one objective of this investigation as outlined in Section 6 below.

A further disadvantage of using hot condenser gas as the medium of pumping cold liquid refrigerant through the evaporators as opposed to a mechanical pump, is that it requires additional compressor volume, from which no useful refrigeration is obtained, and consumes 4-10 % more of the compressor power to maintain the refrigerant flow.⁽⁵⁾ This is due to the interaction of the hot gas and cold liquid at the pumper drum mentioned above, and since all URDs manifest themselves as commensurate quantities of refrigerant vapour arriving at the accumulator, and hence at the compressor inlet to be compressed, more compressor power is required for hot gas pumped arrangements to compensate for the increased URDs. Predicting whether this implies preferential use of mechanical pumps in all overfeed systems is one of the objectives of this investigation as outlined in Section 6 below.

ASHRAE⁽⁵⁾ briefly mentions using high-pressure liquid to produce flash gas as the medium of pumping liquid refrigerant through the evaporators, but does not investigate the relative efficiencies of such an arrangement. Lorentzen and Baglo,⁽⁶⁾ and Wright⁽¹¹⁾ reviewed below, both however suggest that using flash gas as the pumping medium would result in the most energy efficient of all pumping arrangements.

2.2. Comparative Efficiencies of Differently Pumped Liquid Overfeed Systems, an Investigation by Lorentzen and Baglo⁽⁶⁾

Lorentzen and Baglo⁽⁶⁾ compared the operational efficiencies of a hot gas pumped recirculation system with that of a mechanically pumped system. The URD of the gas pumped system, resulting primarily from the transport of heat from the

condenser side to the evaporator side during pumping, varied with the design of the pumping system, operating temperatures and recirculation ratio “n”. The nomenclature below is that of Lorentzen and Baglo⁽⁶⁾ and is different to this report’s nomenclature.

For the gas pumped system: $N_g = N_c = (Q_0 + Q_{lost}) / (\eta_e \cdot K_{th})$

For the mechanically pumped system: $N_m = N_c + N_p = N_p + (Q_0 + 860 \cdot N_p) / (\eta_e \cdot K_{th})$

Where:

N_g and N_m is the power consumption of the gas pumped and mechanically pumped system respectively, in kW.

Q_0 = refrigeration capacity, kcal/h.

Q_{lost} = unproductive refrigeration demand of the system, kcal/h.

N_c = compressor power, kW.

N_p = pump power, kW.

η_e = total efficiency of compressor.

K_{th} = theoretical specific refrigeration capacity, kcal/kWh.

The above formulae were derived from First Law thermodynamic principles, based on data collected for a 10,000 kcal/h hot gas and a mechanically pumped system at an evaporating and condensing temperature of -20 °C and 20 °C respectively. Data was obtained using both a forced and a still air cooler as the evaporator. It was discovered that higher circulation ratios improved heat transfer, as would be expected with increased surface wetting. However, “the circulation ratio should not be higher than necessary to secure efficient distribution and heat transfer.”⁽⁶⁾

Lorentzen and Baglo’s⁽⁶⁾ experimental results with the forced air cooler (the difference with still air coolers was less marked) showed that the mechanically

pumped system at an optimal recirculation ratio of six yielded a 4,5 % power saving over the gas pumped system at its optimal circulation ratio of two.⁽⁶⁾ “The conventional gas pump system gives a considerable loss of refrigeration capacity and power per kcal produced, compared to a mechanical pump system.”⁽⁶⁾ Although these authors’ statements apply to continuous-process overfeed systems, their validity for other types of overfeed systems, in particular that of the ERPM facility, is one objective of this investigation as outlined in Section 6 below.

Lorentzen and Baglo⁽⁶⁾ then describe a system whereby the URD (Q_{lost}) associated with the gas pumped system could be significantly reduced. If flash gas from the throttling process is used to pressurise a vessel that would in turn pump the liquid refrigerant through the evaporator, the URD associated with hot gas pumped systems can be significantly reduced, “as only the normal throttling loss is utilised to activate the pump.”⁽⁶⁾ Lorentzen and Baglo⁽⁶⁾ propose that at high recirculation ratios, power consumption for such a “loss-free”⁽⁶⁾ system would be even lower than a mechanically pumped system. The suggestion of higher energy efficiency and subsequently lower power consumption for cold gas pumped systems over mechanically pumped systems is a key objective of this investigation, as outlined in Section 6 below.

2.3. An Investigation of Gas Powered Liquid Recirculation Compared To Mechanical Pumps by Wright⁽¹¹⁾

In an article comparing the performance of gas and mechanically pumped overfeed arrangements for a “120 ton, two-stage, -40° F load”⁽¹¹⁾, one of the gas pumped arrangements investigated shows similarities to the operating system at the ERPM facility. The following is a description of this “cold” gas pumped plant of Wright⁽¹¹⁾, shown in Figure 2.1 below.

2.3.1. Controlled Pressure Receiver System

In a constant pressure liquid recirculation system (referred to as a CPR system), liquid from the condenser outlet is fed to a controlled pressure receiver (CPR), where it is flash cooled down to liquid circulating pressure, which is usually 1,5-2,5 bar above compressor suction pressure.⁽¹¹⁾ The pressurised CPR circulates liquid through the evaporator, with the overfed liquid and vapour returned to the accumulator.

Wright⁽¹¹⁾ describes the CPR system as follows: “The accumulator in a CPR system will remain essentially empty as the overfed liquid is drained by gravity from the accumulator into the transfer vessel, referred to as a “Dump Trap” or “Liquid Transfer Unit,” LTU for simple reference. Liquid flows into the LTU through a low pressure drop inlet check valve, while the displaced gas is vented back to the accumulator through a 3-way solenoid valve. When the LTU is full, a float switch initiates the transfer cycle by switching the 3-way valve from its “vent” position to the “pressurize” position, connected to a higher pressure source of “transfer gas”. The transfer gas is regulated to a minimum pressure adequate to push the liquid refrigerant out of the LTU and over to the CPR through the outlet check valve. The cold liquid is returned to the bottom of the CPR where it mixes with a portion of the make-up liquid and is recirculated back out to the evaporators.”⁽¹¹⁾

Similarities between the CPR system and the flash gas pumped system of the ERPM plant are evident in the method of circulating the liquid through the evaporator. Both systems use flash gas, throttled down from the condenser to an intermediate ‘pumping’ pressure, to pressurise a vessel that circulates the liquid.

When comparing the CPR system to a mechanically pumped system, “it is observed that for 3:1 recirculation rates, the mechanical pump system may consume only 25% to 50% of the energy of a gas pressure recirculation system, but at 2:1 recirculation rate it is much closer, and, in fact, if designed and operated

correctly, a gas pressure recirculation system at -20F suction may operate at lower energy cost than a mechanical pump at the same recirculation rate (2:1), and even lower if the pump is operated at their more common recirculation rates of 4:1 to 6:1.”⁽¹¹⁾

Both Lorentzen and Baglo⁽⁶⁾ and Wright⁽¹¹⁾⁷ conclude that conventional (“hot”) gas pumped arrangements are less energy efficient and therefore less cost effective when compared to their mechanically pumped counterparts. However, Wright’s⁽¹¹⁾ conclusion that lower recirculation ratios would favour the “cold” gas pumped system over the mechanically pumped arrangements disagrees with the suggestion of Lorentzen and Baglo⁽⁶⁾, who recommend higher recirculation ratios for such systems. As mentioned above and elaborated on in Section 6 below, the test plant of Wright⁽¹¹⁾ more closely resembles that of the ERPM plant.

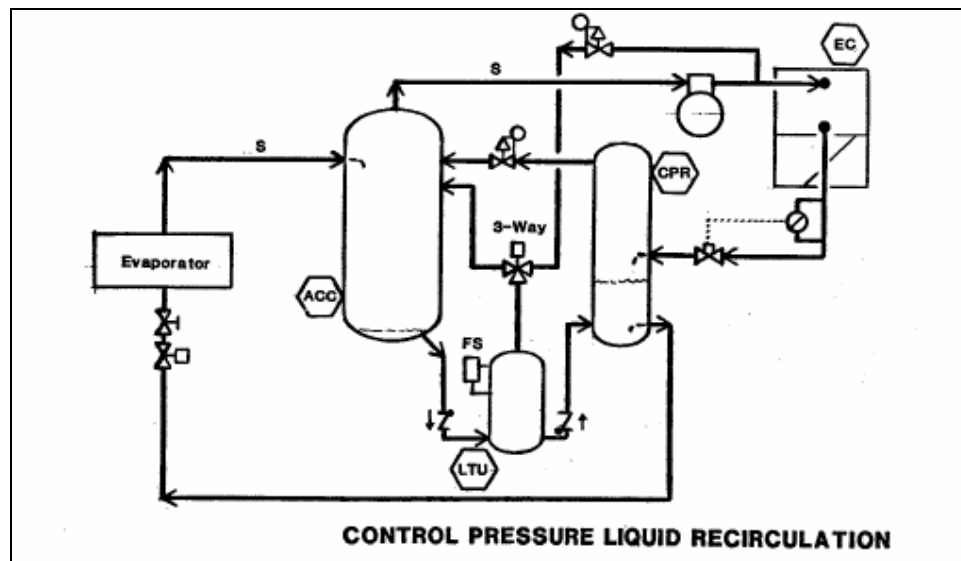


Figure 2.1 Control pressure recirculation system (CPR) from Wright⁽¹¹⁾

⁷ Wright⁽¹¹⁾ compares both “cold” and “hot” gas pumped arrangements.

2.4. A Note on Stationary⁸ Processes in Batch Cycling of Batch Refrigeration Systems

“The experimental investigation of any refrigeration system is usually very complicated, mainly due to the financial costs and the large number of variables involved. The use of numerical models can reduce the costs and also facilitate understanding the phenomena related to the problem.”⁽²²⁾ These models are useful tools for “design and performance evaluation of refrigeration systems.”⁽²⁰⁾

There is an abundance of academic literature, two examples of which are described below, on dynamic and steady state modelling of heat pumps and various refrigeration systems. The field of knowledge is narrower where specific configurations of refrigeration systems are concerned, and even more limited when modelling large industrial systems, especially batch-type ice making systems such as the one found at ERPM. The following brief investigation of current analysis methodologies to model steady state, dynamic, stationary and non-stationary performance of refrigeration systems will serve as a general background of, and introduction to, the theoretical models developed in Sections 7, 8 and 9.

Khan and Zubair⁽²⁰⁾ simulated the working of an actual vapor-compression system in which “evaporator capacity is varied by changing the mass flow rate of the refrigerant, while keeping the inlet chilled-water temperature as constant.”⁽²⁰⁾ This model accounted for “irreversibilities existing due to the finite temperature difference in the heat exchangers as well as the losses due to non isentropic compression and expansion in the compressor and expansion valve of the system, respectively.”⁽²⁰⁾ Khan and Zubair⁽²⁰⁾ observed that the efficiency of the system decreases with increasing refrigeration capacity owing to the irreversibilities mentioned above. Heat exchanger irreversibilities “dominate at high evaporator

⁸ Oxford English Dictionary⁽⁴¹⁾: *Stationary*: Meaning “**d.** *Statistics*: Applied to a series of observations that has attained equilibrium, so that the expected value of any function of a section of it is independent of the time for which it has been running.”

capacities and that due to the non-isentropic compression and expansion are significant at low evaporator capacities.”⁽²⁰⁾ The dependence of some irreversibilities on evaporating temperature was observed by Wright⁽¹¹⁾ for a system similar to that of the ERPM plant as described in Section 2.3 above.

Browne and Bansal⁽²¹⁾ utilised “a thermal capacitance approach for specific state variables”⁽²¹⁾ which “accounts for the change in heat transfer coefficients throughout the heat exchangers”⁽²¹⁾ to improve the accuracy of the model. The model requires only those parameters readily available to the engineer i.e. the condenser and chilled water temperatures, and outputs include COP “as well as states of the refrigerant throughout the refrigeration cycle with respect to time.”⁽²¹⁾ This method of modelling, which utilises accessible operating parameters from testing⁹ to predict other inaccessible performance quantities of the system¹⁰, is applied in this investigation to model the operating ERPM plant, as described in Section 8.

A significant point culled from both these models is that machines in the field usually operate away from design conditions under part-load conditions. “This generally results in a decrease in the coefficient of performance and hence electrical costs are greater than necessary.”⁽²¹⁾ Manufacturers’ catalogues rarely predict the performance of these chilling machines during start up and other transient operations, thus these models fill in the gap where manufacturer’s data is sparse, especially in the area of online fault detection, optimal control analysis and diagnostics. “Steady state models are useful under many conditions although under strongly dynamic conditions that are often seen in real-life operation, these models can become unacceptably inaccurate.”⁽²¹⁾ The complex nature of even simple chilling systems makes dynamic simulation very difficult.

Whereas water chilling is a continuous process, normally steady, ice making in batch-type processes is inherently unsteady, with the highest load apparent at the

⁹ Such as pressures and temperatures .

¹⁰ Such as mass flow rates of refrigerant, average recirculation ratios and heat transfer coefficients.

beginning of the ice building process, and decreasing due to thickening ice slowing down heat transfer. "...the unsteadiness of the batch process, and the need to even this out-make the refrigerant circuits of such machines considerably more complex than those of machines employing continuous processes."⁽²⁾ Large ice plants such as the ERPM facility utilise multiple modules of plates or tubes operating successively in order to "even out the unsteady refrigerating load as much as possible."⁽²⁾ The batch-type ice making cycle of the ERPM plant can be described as stationary, in that the non-steady processes such as the ice building or harvesting periods¹¹ are repetitive and systematic. The staggered operation of all 8 modules of Unit 5, as shown in the timing diagram of Figure 3.1, governs when the different processes commence and conclude and allows for maximum smoothing of load on the compressor. As such, aspects of the stationary processes of the plant, such as the harvesting process, can be modelled, as they are repetitive and can be predicted to occur within a known time frame (every 13,5 minutes of ice building is followed by harvesting for 1,5 minutes).

Both the investigations of Khan and Zubair⁽²⁰⁾ and Browne and Bansal⁽²¹⁾ used test rigs that incorporated mass flow rate meters. Knowledge of the mass flow rate, especially through the evaporators, is crucial when validating a theoretical model of the system, as "prediction of the refrigerant distribution within the cycle is a difficult task requiring accurate knowledge of the void fraction in the heat exchangers."⁽²¹⁾ Installing invasive measuring equipment such as flow meters at the ERPM plant was prohibited for safety reasons, and for this reason, predicting the mass flow rate and average recirculation ratio through the evaporators of the ERPM plant are key objectives of this investigation, as outlined in Section 6 below. Without reliable predictions of these important performance quantities, no model of the system can be validated. Therefore two different models, the refrigeration demand model developed in Section 8. and the heat transfer model developed Section 9. serve to predict and corroborate (between these two models) the mass flow rate and average recirculation ratio at the evaporators of the ERPM plant.

¹¹ Described in detail in Section 3. below.

3. THE ICE MAKING PLANT AT ERPM, LTD

3.1. Background: Design, Layout and Description

The following description of the ERPM mine and ice plant is based on the paper by Hemp⁽⁴²⁾. As mentioned in Section 1.2.3, underground operations at the mine were suspended on 31 October 2008.

“East Rand Proprietary Mines Ltd (ERPM) is a gold mine situated in Boksburg, east of Johannesburg.” Underground refrigeration plants, the first of their kind in South Africa, were installed, with a total capacity of 29,000 kW. However, the dramatic increase in the gold price during 1979/1980 demanded that an additional shaft be commissioned. At the time of writing, the Far East Vertical shaft (serviced by the ice plant), at a maximum depth of 3157 m below surface, and with an additional cooling load of 18 MW, presented “considerable ventilation and cooling problems.” Three alternative cooling schemes were compared, and the investigation revealed that the capital and operating cost of an underground plant “was marginally less than that of an ice scheme, and the cost of the surface water chilling scheme was considerably higher.” As an underground plant would limit any further increase in cooling capacity, as well as complicate installation and maintenance, it was decided to proceed with the ice plant - despite the increased capital and operating costs, as well as the complexity of the control system required.

Using “well established methods” of ice production, Bronsair (Pty) Ltd. won the tender for a 6000 ton per day ice making plant, which at a design inlet water temperature of 18⁰ C, constituted 31,4 MW of cooling - “more than double the mine’s (current) cooling capacity (of 29 MW).” The plant consists of six separate 1000 ton per day units, four of which use “tube icemakers” and the remaining two use “plate icemakers.”

3.1.1. Units in the Ice Plant

As Hemp's paper⁽⁴²⁾ was written before the plate ice makers were installed, he proceeds to describe the tube ice-making arrangement for the first four 1000 ton per day units. The ice building and harvesting periods last for 13,5 and 1,5 minutes respectively. "Each plant has a single screw compressor which is direct driven by a four pole 1800 kW¹² motor. Vertical shell and tube condensers are used, with a packed induced draught cooling tower cooling the circulating condenser water." Pumper drums circulate cold liquid ammonia through the tube icemakers to build the ice, with harvesting achieved by "passing warm liquid ammonia from the high pressure receiver through the icemakers." In Units 5 and 6,¹³ pumper drums likewise pump cold liquid ammonia to the plate ice-makers to build the ice, but harvesting is achieved by pressurising the plates with warm gas from the condensed liquid receiver. In each unit, a hopper, placed below the evaporators, collects the ice that has been shed during the harvesting period, and a screw conveyor discharges the collected ice "onto one of the two feed conveyor belts which cover the length of the icemaker building." A separate shell and tube water pre-chiller chills the incoming water, utilising the economiser port on the compressor.

3.1.2. Control System for Ice Production

The ice is transported from the "icemaker building" to four pipes in the Far East vertical shaft, which deliver the ice to four cooling sites below the surface. The ice is used to "cool water to a temperature very close to 0° C", and the cold water is used "for various cooling processes, depending on the site." "The water resulting from the melted ice will not be pumped directly out of the mine, but will first be

¹² Based on Worthington-Smith & Brouwer⁽¹³⁾, the compressor plate ice makers are driven by 1700 kW motors.

¹³ Unit 6 has never been commissioned.

used to supply some or all of the service water requirements in this area of the mine.”

An advanced control system has been implemented at the plant that matches the ice production at the surface to the total demand at the four cooling sites below ground. This is achieved by modifying the evaporator temperature via slide valve control at the compressors. Higher evaporating temperatures could be achieved that would result in the plant operating at 75 % of its rated production. Another method of controlling ice production is by stopping “individual 1000 tons per day ice plants.” This change in ice production is achieved through ultrasonic level detectors at the cooling sites below ground, which matches ice production to cooling demand.

At the time of writing Hemp’s paper,⁽⁴²⁾ Unit 5 of the ice making plant had not been commissioned. This investigation focuses on Unit 5, and as such, a brief summary of the differences between the plate ice-maker and the tube ice-maker - as described above by Hemp⁽⁴²⁾ is presented below.

3.1.3. The Plate Ice Making Unit 5

This investigation focuses on Unit 5 of the ice plant, which was modified by Worthington-Smith & Brouwer⁽¹³⁾ to utilise plate-type evaporators. The advantages of plate-type evaporators over tube-type evaporators include:⁽¹³⁾

1. Heat transfer area increases from 1600 m² to 2200 m².⁽¹³⁾
2. Evaporator temperature rises from -10° C to -7° C.⁽¹³⁾
3. Condensing temperature decreases from 33° C-31° C.⁽¹³⁾
4. The overall metal mass is reduced, leading to improved heat transfer between the refrigerant and water.⁽¹³⁾
5. Ice breakers and stirrers are not required under this configuration.⁽¹³⁾

3.2. Operation of Ice-Making Modules of Unit 5 of Plant

All units of this plant utilise flash gas refrigerant pumping – based on the method suggested by Lorentzen and Baglo⁽⁶⁾ and Watkins (as described in Wright^(10,11)), and reviewed in Sections 2.2 and 2.3 above – to eliminate the unproductive refrigeration demand associated with hot gas pumped systems.

Figure A1.1 of Appendix A1 shows a detailed plant diagram of Unit 5 of this plant, and Figure 3.1 below shows the timing diagram for this unit. This diagram shows not only the pumping schedules (those of the pumper drums), but the ice-building and harvesting periods of each module. From Figure 3.1, although one full ice building and harvesting cycle of one module lasts for 15 minutes (900 seconds), the schedule effectively repeats itself every 450 seconds, as shown in the magnified timing diagrams of Figure 3.2 and Figure 3.3 below. Table 3.1 and Table 3.2 below summarise the different periods illustrated in the timing diagram and pumping schedule respectively (both are shown in Figure 3.1). All information is based on data obtained from testing at the plant, as well as from Worthington-Smith & Brouwer⁽¹³⁾ and Rankin.⁽¹⁴⁾ Where timed events are uncertain, they are indicated in italics. Those timed processes that are illustrated in the timing diagram and pumping schedule are repeated in Table 3.3.

Table 3.1 Definition of periods during the ice making cycle for Unit 5 of the ERPM plant

Elapsed time (s)	Period length (s)	Name of period	Valve operations	Intended events during operation
10	10	Re-cooling sub-period (Depressurizing of evaporator after harvesting period)	Controlled valve between evaporator and accumulator opens fully.	Evaporator returns to ice-building temperature before ice building commences.
820	810	Ice-building period	Different controlled valves opened and closed.	Cold ammonia liquid circulated through module, entering as liquid and leaving as 4 parts liquid and 1 part gas on average (as predicted in Sections 8. and 9.).
830	10	Liquid transfer period	Harvesting gas controlled valve opens.	Hot gas from condenser pushes liquid to accumulator.
900	70	Warming sub-period	Harvesting gas controlled valve opens.	Hot ammonia gas from condenser warms steel module to melt the inner ice layer.

Table 3.2 Pumping schedule for the two pumper drums of Unit 5

Elapsed time (s)	Period length (s)	Name of period	Valve operations	Intended events during operation
20	20	Pumper drum #1 depressurises during changeover period from pumping to filling	Controlled valve open between pumper drum and accumulator.	Pumper drum vents pressurising harvesting gas to accumulator.
150	130	Re-filling period of pumper drum #1	Controlled valve open between pumper drum and accumulator.	Pumper drum receives full charge from, whilst venting displaced gas to, the accumulator.
170	20	Pumper drum #2 pressurises during changeover period from filling to pumping	Pressure reducing valve open between pumper drum and condensed liquid receiver.	Pumper drum is pressurised by flash gas and starts to pump liquid to evaporators.
300	130	Pumping period of pumper drum #2	Pressure reducing valve open between pumper drum and condensed liquid receiver.	Pumper drum pumps liquid to and through evaporators.

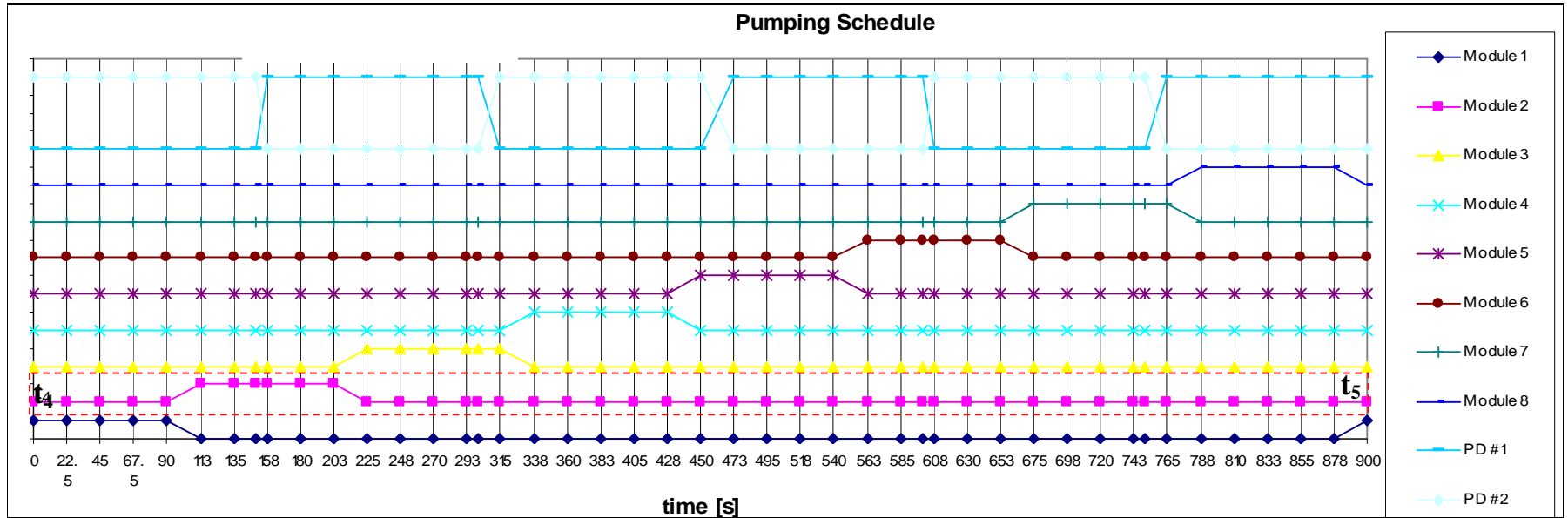


Figure 3.1 Timing diagram of Unit 5 of the ERPM plant for a full ice making cycle of 15 minutes

Table 3.3 Timed processes in the pumper drum and in the evaporator modules

Timed Processes in the Pumper Drums	Time [s]
Pumping Time	130 (2½ min)
Venting of Pumping Pumper Drum	20 (⅓ min)
Filling of Pumper Drum	130 (2½ min)
Changeover from Filling to Pumping	20 (⅓ min)

Timed Processes in Evaporator Modules	Time [s]
Changeover from Ice Building to Harvesting	10
Warming Sub-Period of Harvesting Period	70
Venting to Accumulator during Re-Cooling Sub-Period	10
Ice Building Period	810
Period from Beginning of Ice Building of One Module to Changeover Period of the Next Module	22.5

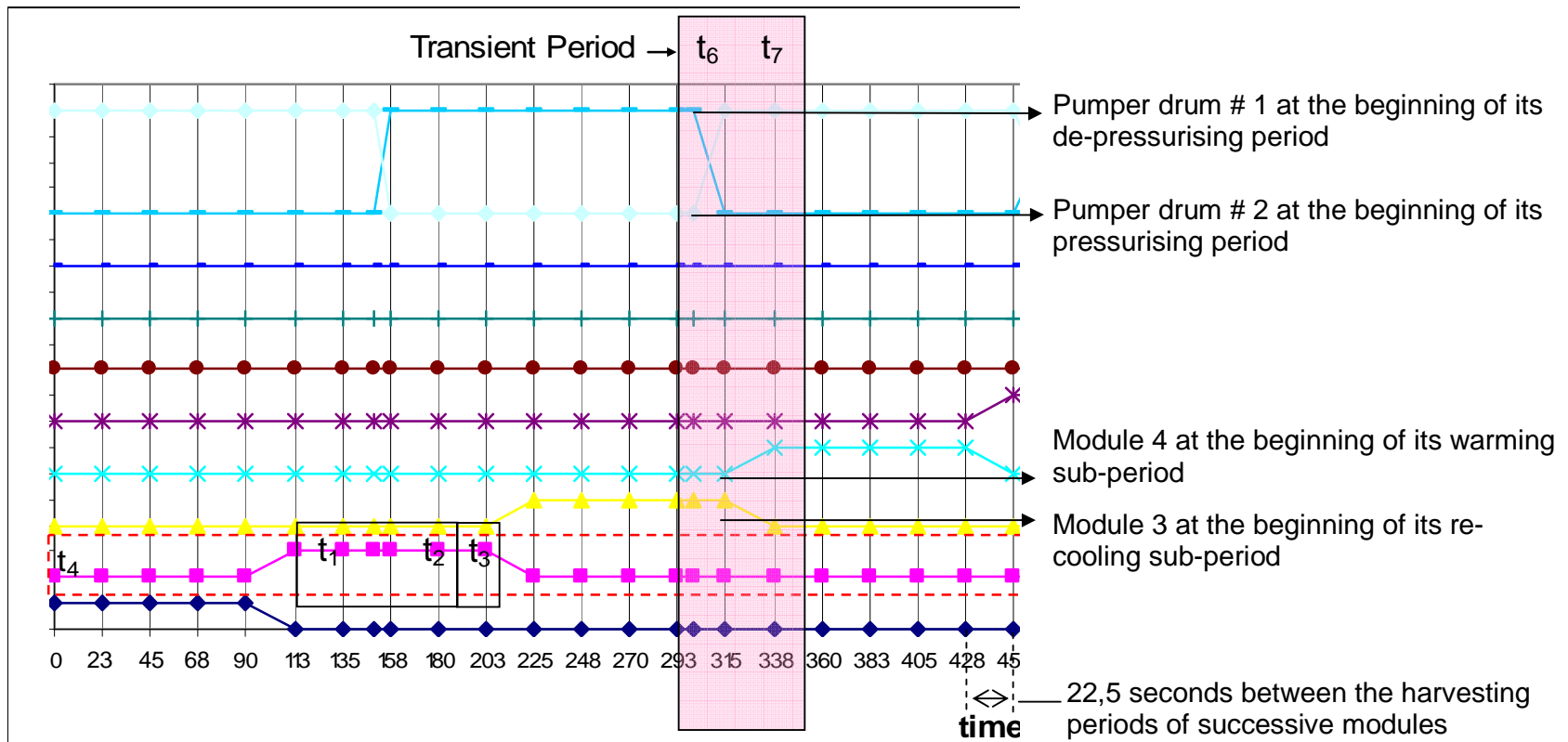


Figure 3.2 Magnified timing diagram for First Half (0 - 450 seconds) of Ice Building and Shedding Cycle

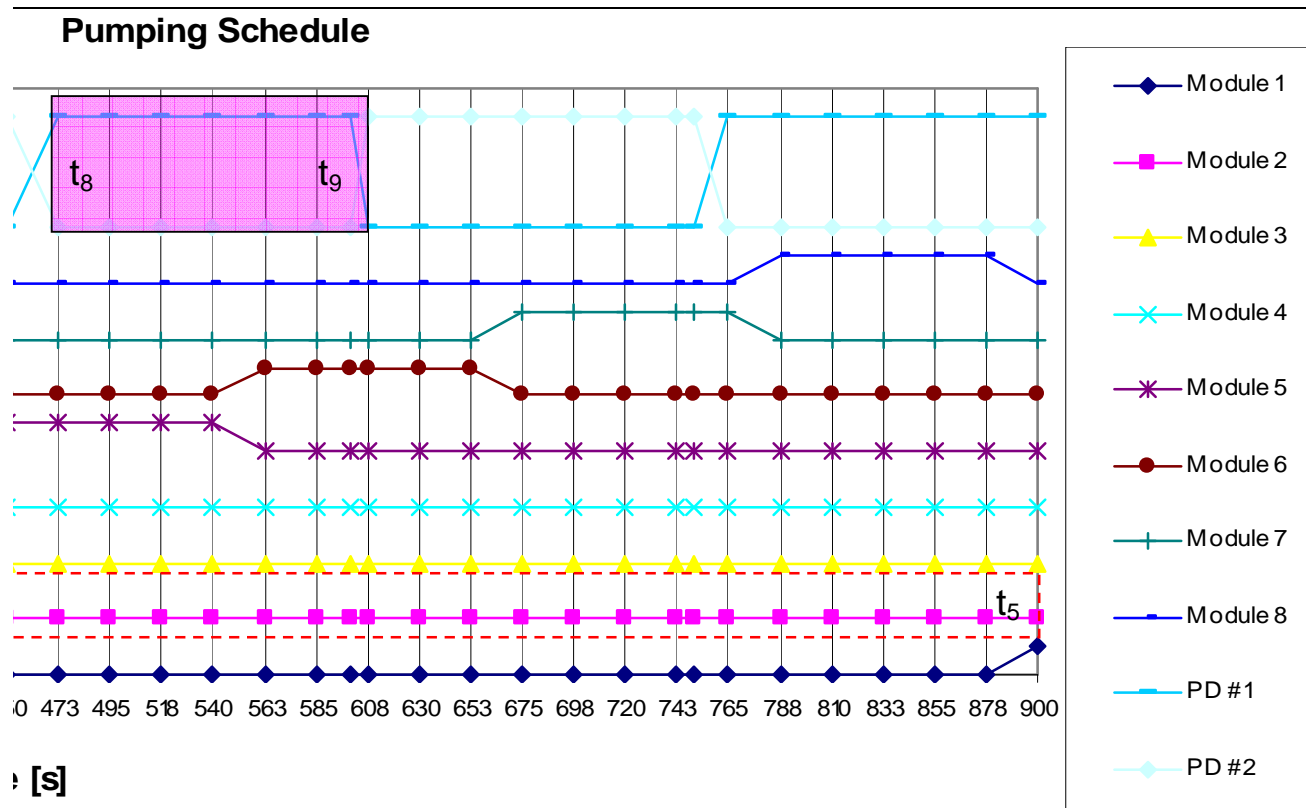


Figure 3.3 Magnified timing diagram for Second Half (450 - 900 seconds) of Ice-Building and Shedding Cycle

Referring to Figure A1.1, Figure 3.1, Figure 3.2 and Figure 3.3, the following is a description of operation of Module 2 of Unit 5.

3.2.1. The Processes at the Pumper Drums

Ice is built on the evaporator plates during the 13,5 minute ice-building period, during which the two pumper drums alternately pump cold liquid ammonia to and through these plates. Whilst one drum pumps, the other fills. Each pumper drum has its own pumping expansion valve, and upper and lower float valves, signalling liquid levels of 80 per cent and 10 per cent of drum height (as shown in Figure 8.9 below). There is an overlapping changeover period, which from Table 3.3 above lasts for 20 seconds, during which throttled flash gas pressurises the pumping pumper drum, and the depressurised pumper drum vents its pressurising gas to the accumulator.

During pumping, the controlled venting valve between the pumper drum and the accumulator is closed. The flash gas arising from this drum's pumping expansion valve throttling the liquid from the condensed liquid receiver down to 2 bar above evaporating pressure, pressurises this drum to circulate its liquid ammonia through the evaporator plates. During this pumping time, which from Table 3.3 above lasts for 130 seconds, the second pumper drum's venting valve is opened to the accumulator. Liquid ammonia from the accumulator enters to fill the pumper drum, whilst venting any displaced vapour to the accumulator. Pumping commences once the upper float valve registers that the liquid in the pumper drum has reached 80 % of drum height, and lasts for approximately 130 seconds. Once the liquid ammonia level in the pumper drum decreases to 10 % of drum height, a signal from the lower float valve stops the pumping, and the filling process recommences.⁽¹⁴⁾

3.2.2. The Process at the Evaporator during Ice Building

During the ice-building period, cold liquid ammonia flows inside channels spaced equally along the length of the plate. Water, falling in thin films down the outer surfaces of the plates, freezes to form thin shells of ice. After 13,5 minutes, ice of 5-6 mm thickness has been built up along the length of the plates.⁽¹³⁾ This ice building period, as well as the harvesting period at the evaporators, is illustrated in Figure 1.1 above.

3.2.3. The Processes at the Accumulator and the Compressor

Refrigerant in a two phase mixture flows from the evaporator exit into the accumulator drum. At the accumulator, the gas in this mixture is drawn into the compressor, whilst the liquid remains in the accumulator. The economizer port of the compressor serves a refrigerating unit used to pre-chill the inlet water from ambient temperature to 12° C. This fresh chilled water enters the water sump below the evaporators (where the temperature of water is close to 0° C as measured at the plant and shown in Table A6.3 of Appendix A6), mixing with the water that has not frozen to ice whilst falling over the evaporator plates. This mixture of unfrozen and fresh chilled water is drawn up to the water distributor, and falls via gravity over the evaporator plates during the ice building period.

It is assumed the mass of water chilled at the pre-chiller, which then further cools down from 12° C to 0° C at the water sump, is equal to the mass of ice delivered to the screw conveyor below the evaporators at the end of the warming sub-period of the harvesting period (defined below). This is illustrated by the control volume of Unit 5 below, where $\dot{m}_{w[PRC]i}$, $\dot{m}_{w[C]i}$ and $\dot{m}_{w[C]o}$ are the mass flow rates of water

at the pre-chiller inlet and condenser in/outlet respectively, and $\dot{m}_{I,req}$ is the mass flow rate of ice required.¹⁴ $\dot{W}_{[CR]mech} + \dot{W}_{[P]mech}$ is the mechanical work input of the compressor and pumps respectively. As $\dot{m}_{w[C]i}$ at the condenser inlet is equal to $\dot{m}_{w[C]o}$ at the outlet, the mass flow rate of ice required is equal to the mass flow rate of water chilled at the pre-chiller. The same is true for the mass flow rate of water chilled at the water sump to 0° C, as it is assumed that the water from the melted ice layer returns to the water sump at the end of the warming sub-period.

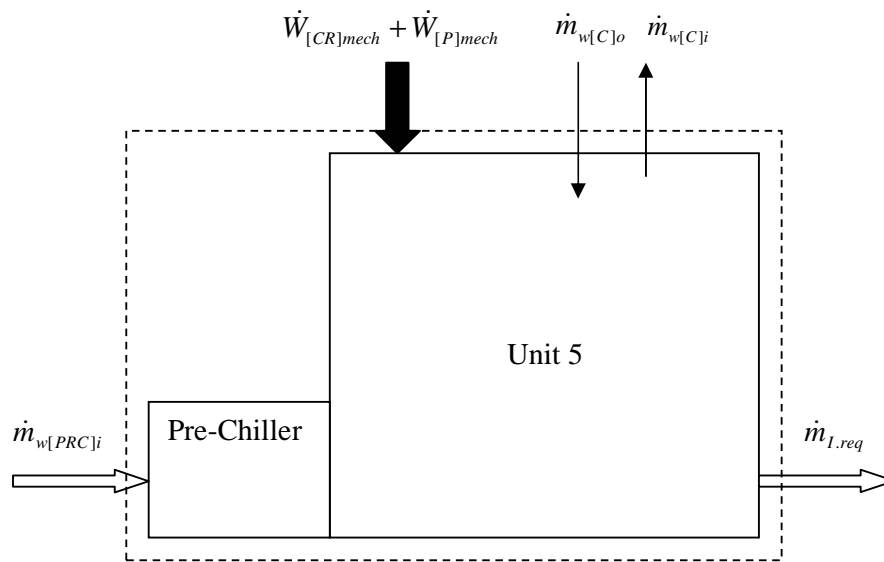


Figure 3.4 Control volume of Unit 5 of the ERPM plant

3.2.4. The Process at the Evaporator during the Warming and Re-Cooling Sub-Period of the Harvesting Period

The warming sub-period is indicated by the hatched portion of Figure 3.2 above, encompassing the time interval $t_1 - t_2$ at Module 2. During the initial part of the 1.5 minute ice-harvesting period, referred to as the warming sub-period, a

¹⁴ $\dot{m}_{I,req}$ is defined in Section 8.1 as the mass of ice that is delivered to the screw conveyor below the evaporator module at the end of the warming sub-period.

controlled valve isolates the evaporator's top refrigerant port from the accumulator. Warm gas from the condensed liquid receiver enters this top port, pressurising the evaporator and so first expelling the cold liquid refrigerant remaining from ice-building to the accumulator, through a float valve at the evaporator's bottom refrigerant port that allows liquid, but not vapour, to pass. Then, as the warm gas condenses to liquid on the cold walls of the plates, these walls are thereby warmed, melting the innermost ice layer holding the ice thereto. (The float valve also allows this condensed liquid to return to the accumulator, whilst trapping uncondensed gas in the plates.) The ice thus falls off the plates and is collected below the module in a screw conveyor. The screw conveyor delivers the ice to feed conveyor belts that transport the ice to the mine shaft.

The re-cooling sub-period is indicated by the dashed portion of Figure 3.2 above, encompassing the time interval $t_2 - t_3$ at Module 2. During the second, final part of the harvesting period, referred to as the re-cooling sub-period, the warm gas supply is shut off. The controlled valve between the evaporator's top port and the accumulator is then opened, so venting the remaining warm gas to the accumulator. Any condensed liquid refrigerant remaining in the evaporator at that point boils at the lower pressure, assisting in cooling down the evaporator. Almost immediately afterward, the controlled valve between the evaporator and the pumper drums opens, so an initial charge of cold liquid refrigerant then enters the evaporator, cooling down the module to ice building temperature before water is fed onto the evaporator and ice building recommences.

4. REASON FOR THE STUDY

From Section 1.2.4, Wright⁽¹⁰⁾ describes the progression of liquid overfeed systems over the past fifty years. For smaller systems, flash gas at intermediate pressure has been used to circulate the liquid refrigerant through the evaporators. The ice making plant at ERPM is based on this principle, possibly due to the fact that mechanically pumped systems were deemed too expensive to implement both in terms of maintenance and overall capital costs.

The URDs due to the harvesting process are unavoidable and common to all pumping arrangements. Therefore, those URDs that are specific to each pumping arrangement arise during the ice building process- from different methods of pumping the liquid refrigerant to and through the evaporators. For a mechanically pumped arrangement, the work input from the pump increases the enthalpy of the liquid refrigerant as it increases its pressure. Thus re-cooling this liquid is a URD specific to mechanically pumped systems.

The interaction of pressurising gas and cold liquid refrigerant in the pumper drums results in URDs specific to gas pumped arrangements. For a cold gas pumped arrangement, “cold” flash gas produced at the outlet of the expansion valve feeding the pumper drum is used to pump the cold liquid refrigerant through the evaporator. However, as described in Section 7.2¹⁵, the unproductive refrigeration demand arising from the interaction of this flash gas and cold liquid refrigerant is both *unavoidable* and *inherent* in any *standard* refrigeration cycle and therefore does not impact negatively on the plant’s efficiency and electrical cost effectiveness. Lorentzen and Baglo⁽⁶⁾ suggest, and Wright⁽¹¹⁾ concludes, that at certain operating conditions, and for smaller operating plants than the ERPM facility, a cold gas pumped arrangement could limit its URDs to the extent that it

¹⁵ And proven in Appendix A13.

is more energy efficient than a mechanically pumped arrangement. However, whether this applies to large batch type ice making systems such as the ERPM plant requires investigation.

A comparison of theoretically predicted total refrigeration demands, and operating costs, for different gas and mechanically pumped arrangements for Unit 5 of the ERPM plant – supported by experimental data obtained from this unit with its actual cold gas pumping arrangement – would predict the most energy efficient and electrical cost effective liquid overfeed pumping arrangement for this large, batch-type refrigerating system. It would provide guidance on those aspects of batch refrigerating processes that are strongly affected by the liquid overfeed pumping arrangement employed, and hence suggest what pumping arrangement(s) might be most effective and efficient for such large systems This would constitute a meaningful illustration and application of engineering knowledge on the subject.

5. OVERVIEW OF METHODOLOGY

The focus of this investigation is to predict, by theoretical performance modelling supported by experimental data (where applicable), the major productive and unproductive refrigeration demands (termed PRDs and URDs respectively) of cold/hot gas and various configurations of mechanically pumped overfeed arrangements at various operating conditions of batch ice making, and hence to predict which system is the most energy efficient and cost effective.

Significant comparisons can be made between the systems in the following areas:

1. The method of pumping liquid refrigerant to and through the evaporators during ice building.
2. The respective URDs of each system.
3. The method of discharging liquid refrigerant from the evaporators prior to ice harvesting, as well as the method of recharging the evaporators with such liquid at the completion of the harvesting period.

4. The yearly electrical power costs of each system.

Theoretical models of the different pumping arrangements are developed in Section 8. and 9. based on thermodynamic principles and supported by experimental data obtained from the ERPM plant.

6. OBJECTIVES OF THE STUDY

The objectives of the study are:

1. For Unit 5 of the ERPM ice-making plant, to develop theoretical models of the performance of (i) the actual cold gas pumped liquid overfeed arrangement, and (ii) alternative hot gas pumped, and two mechanically pumped, overfeed arrangements. These models should predict convincingly the average liquid recirculation ratios, and hence the mass flow rates of the liquid refrigerant through the evaporators for varying evaporating temperatures. The operating parameters required as input to these models are experimental data obtained from the operating Unit 5 of the plant.
2. Based on these predicted mass flow rates and average recirculation ratios at the evaporators, to predict the PRDs and major URDs arising from, and specific to, each modelled pumping arrangement.
3. Based on the total refrigeration demand (the sum of all PRDs and URDs), to predict the annual electrical operating cost for the different pumping arrangements.
4. Hence to suggest which batch-type ice-making overfeed pumping arrangement is the most energy efficient and cost-effective for large batch-type refrigerating systems such as the ERPM plant.

7. THEORETICAL MODELLING OF EXISTING AND ALTERNATIVE BATCH ICE-MAKING ARRANGEMENTS IN ERPM'S PLANT

This Section restates and expands on some vital concepts, such as the liquid recirculation ratio, productive and unproductive refrigeration demands and the ice building and harvesting periods introduced in Sections 1-5. It also defines those unproductive refrigeration demands that are avoidable, and may therefore be specific to the different pumping arrangements, and those that are unavoidable, and therefore common to all arrangements. The Section then concludes by introducing the fundamental basis for, and the purpose of, the theoretical model presented in Section 8 below.

7.1 Key Concepts when Modelling the Different Possible Operating Arrangements of the Plant

7.1.1. Liquid Overfeed Arrangements

As mentioned above in Section 1.1, liquid overfeed systems have an advantage over dry-expansion evaporators in that the greatest wetting of interior tube surfaces, and consequently highest possible heat transfer rate, is obtained. Ice is produced in a batch type process at the ERPM ice making plant. In order for this process to be efficient and to achieve maximum heat transfer between the refrigerant and the water, the evaporator must operate under overfeed conditions. Predicting the recirculation ratio is therefore important, as it affects many of the URDs for all possible pumping arrangements of the operating system.

7.1.2. The Ice Building and Harvesting Periods

The ice building period, as well as the harvesting period, is defined in Section 3.2 above. A brief summary of these periods is presented below.

The harvesting period is divided into two sub-periods; the warming sub-period and the re-cooling sub-period. The warming sub-period is defined as the period in which the evaporator plates are isolated from the cold liquid refrigerant, and warm pressurized refrigerant gas from the condensed liquid receiver is introduced into the plates to melt the innermost ice layer and release the built ice sheet.

The re-cooling sub-period follows the warming sub-period, and occurs when the evaporator plates and the refrigerant remaining inside them, warmed during the warming sub-period, are re-cooled to evaporating temperature prior to the next ice-building period. During this sub-period, and before water from the distributors begins to flow over the plates, an initial charge of liquid refrigerant from the pumper drum enters the evaporator - assisting in re-cooling the module.

The ice building period occurs once the evaporator module has returned to evaporating temperature after the re-cooling sub-period. Water is released into the feed water distributors above the evaporator plates and ice building commences.

7.2 Productive and Unproductive Refrigeration Demands of Thermodynamic Processes in Ice-Making Systems with Different Refrigerant Liquid Overfeed Pumping Arrangements

7.2.1 Productive and Unproductive Refrigeration Demands

Productive Refrigeration Demand, or PRD, is defined as the refrigeration demand to build the particulate ice sheet that is required by, and delivered to the mine for cooling its workings. Ideally, the mass of ice required ($m_{I,req}$) and that built ($m_{I,b}$) over any ice building period should be the same. However, a portion of the mass of ice built must be melted in order to release the ice sheet from the evaporator wall. As the demand of building this subsequently melted ice layer is considered non-productive in that it does not provide any useful cooling capacity to the mine, it is defined as an Unproductive Refrigeration Demand, or URD. Other URDs, both common and specific to the different pumping arrangements, occur at various positions throughout the plant, and during the different operating periods.

As the PRD remains constant, the total URD of each arrangement provides the means of comparison between the different arrangements. Defining the different sub-periods of the batch type ice making cycle allows for the PRDs and URDs associated with each sub-period to be clearly presented and compared for the different arrangements. These demands are presented in detail in Section 8. where the control volume analyses for the different components associated with these periods are performed.

It should be noted that all PRDs and URDs manifest themselves as commensurate quantities of refrigerant vapour arriving at the accumulator, and hence at the compressor inlet to be compressed.

7.2.2 Avoidable and Unavoidable Unproductive Refrigeration Demands

In comparing different pumping arrangements, it is necessary to distinguish between those URDs that are avoidable i.e. URDs that *arise* from particular pumping arrangements, and those URDs that are unavoidable, i.e. those that are *independent of* pumping arrangements. An example of an avoidable URD would be that due to re-cooling of the steel of the pumper drum due to an extra mass inflow of pressurising gas from a hot gas pumped system, expanded on in Section 8.7.2. As hot gas is not the common means used in all pumping arrangements to circulate the liquid refrigerant to and through the evaporators, such re-cooling is considered an avoidable URD. An example of an unavoidable URD is the re-cooling of the evaporator plates and their inlet and outlet manifolds at the end of the re-cooling sub period, expanded on in Section 8.2.2. This URD is *independent of* all pumping arrangements and is unavoidable in that warming of the evaporator plates is necessary to release the ice sheet from the plates.

A further distinction is necessary in the definition of unavoidable URDs. During a *standard* refrigeration cycle, a URD arises that is inherent in this cycle: the flash gas generated in reducing the pressure of condensed liquid to provide cold liquid for the task of refrigerating. Although this flash gas constitutes a URD in that it manifests itself as a commensurate quantity of refrigerant vapour arriving at the accumulator, and hence at the compressor inlet to be compressed, it is both *unavoidable* and *inherent* in any *standard* refrigeration cycle. Such URDs are hereafter termed *inherent* URDs.

7.2.3 Simplified Control-Volume Thermodynamic Analysis of Gas and Mechanically Pumped Arrangements

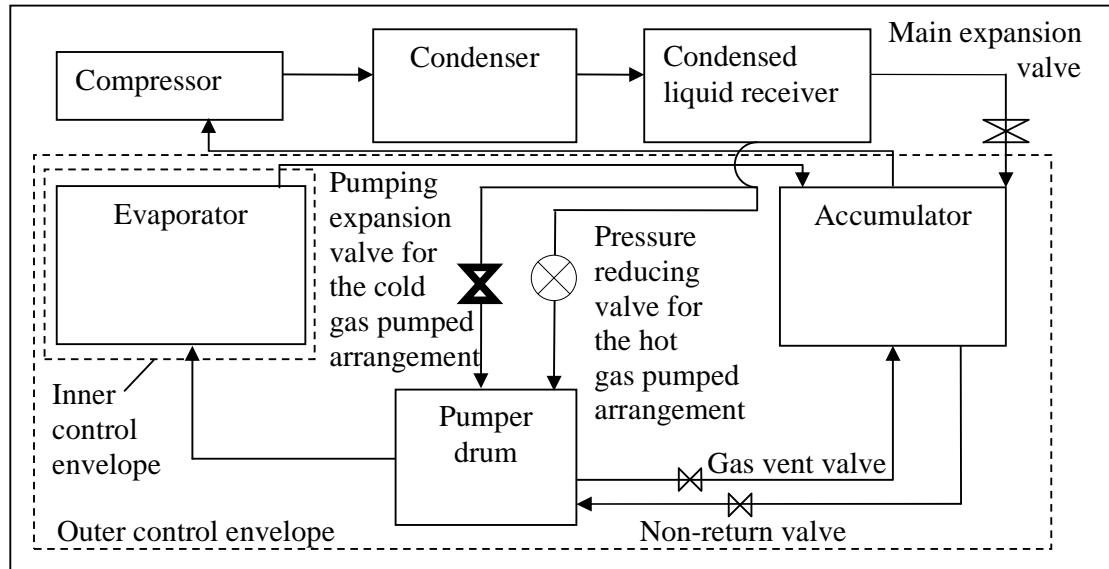


Figure 7.1 Diagram of a simple cold and hot gas pumped liquid overfeed arrangement

To illustrate the difference between avoidable, unavoidable and inherent URDs, a simplified control-volume thermodynamic analysis is presented below for a cold or hot gas pumped arrangement. The diagram above of a simple cold / hot gas pumped arrangement is modified from Figure 1.2 above to include the inner control envelope round the evaporator itself, and the outer control envelope round all components in the refrigerant pumping arrangement. For a Cold Gas Pumped System (CGPS), most of the cold liquid refrigerant needed for ice-building is generated through the main expansion valve into the accumulator. The rest is generated through the *pumping expansion valve* (indicated in bold) into the pumper drum – where the accompanying flash gas generated provides the pressure rise required for pumping.

For a simple Hot Gas Pumped System (HGPS), the pumping expansion valve between the liquid receiver and pumper drum is replaced by a gas pressure reducing valve (PRV) between these two components. For this arrangement, all

the liquid from the high pressure liquid receiver flows through the main expansion valve into the accumulator and all the flash gas generated flows into the accumulator and thence to the compressor. The pressurising gas therefore constitutes an *additional* flow of depressurised gas across the outer control envelope from the liquid receiver to the pumper drum.

The control volume energy analysis of the *evaporator* (the inner control envelope) during the pumping period is not affected by whether the system is cold- or hot-gas pumped. However, for the HGPS during the pumping period, there is an *additional* mass flow into the outer control envelope – this being the depressurised gas into the pumper drum. There is therefore also a corresponding additional mass flow out of the accumulator into the compressor. For both the cold- and hot-gas pumped systems, though, the amount of flash gas generated from expanding warm condensed liquid is identical, because in either system, all such warm liquid is ultimately expanded down to accumulator pressure.

As far as the control volume energy analysis of the *evaporator* is concerned, the evaporator receives the incoming liquid regardless of which pumping system is employed. However, *the effect of gas pumping on the enthalpy of this liquid* is due to very different causes in the two systems. In the CGPS, any rise in this enthalpy above the enthalpy of the original cold liquid generated by expansion, is due to:

- (i) additional, warmer liquid condensed from the warmer, pressurising flash gas that is generated in the pumper drum, and
- (ii) the unflashed liquid (from the pumping expansion valve) accompanying this flash gas.

In passing through the evaporator¹⁶ (and thus reducing in pressure to accumulator pressure), any additional liquid due to (i) re-evaporates. The liquid due to (ii) *that remains liquid* after flashing down to accumulator pressure, *constitutes additional liquid* (in proportion to the flash gas generated) *to do the task of refrigerating*.

¹⁶ And its interconnecting piping from the pumper drum and to the accumulator, of course.

The re-evaporating of (i), and the flash gas generated by (ii) in flashing down to accumulator pressure,¹⁷ make up the balance of the flash gas that is generated by the flow of condensed liquid refrigerant through the pumping expansion valve in ultimately expanding down to accumulator pressure. Ultimately, therefore, *no extra gas arrives at the compressor to be compressed apart from the flash gas that is inherently generated in expanding condensed liquid down to accumulator pressure.* The URD represented by this flash gas is thus an *inherent* URD; *no extra avoidable URD occurs in the CGPS in pumping.* This is elaborated upon in the next section, “Processes during the pumping period at the pumper drum”, below.

A detailed proof by calculation that the URDs generated for the CGPS over a complete pressurising and venting period of one pumper drum amount to (add up to) the *inherent* URD of needing to compress the flash gas generated in expanding liquid down from the condensed liquid receiver to accumulator pressure is given in Appendix A13.

In the HGPS, the rise in enthalpy of the liquid entering the evaporator above that of the original cold liquid generated by expansion is due to the same effect, in principle, as (i) above: additional, warmer liquid condensed from warmer, pressurising gas. *However, because this gas is an **additional** mass flow into the pumper drum, without any corresponding unflashed liquid to provide correspondingly additional refrigerating effect,* it results in a corresponding *additional* mass flow of gas to the compressor which must be considered an *avoidable* URD.

¹⁷ Wherever these processes occur – in the pumper drum, evaporator, interconnecting piping – and in whatever proportions therein.

Processes during the pumping period at the pumper drum

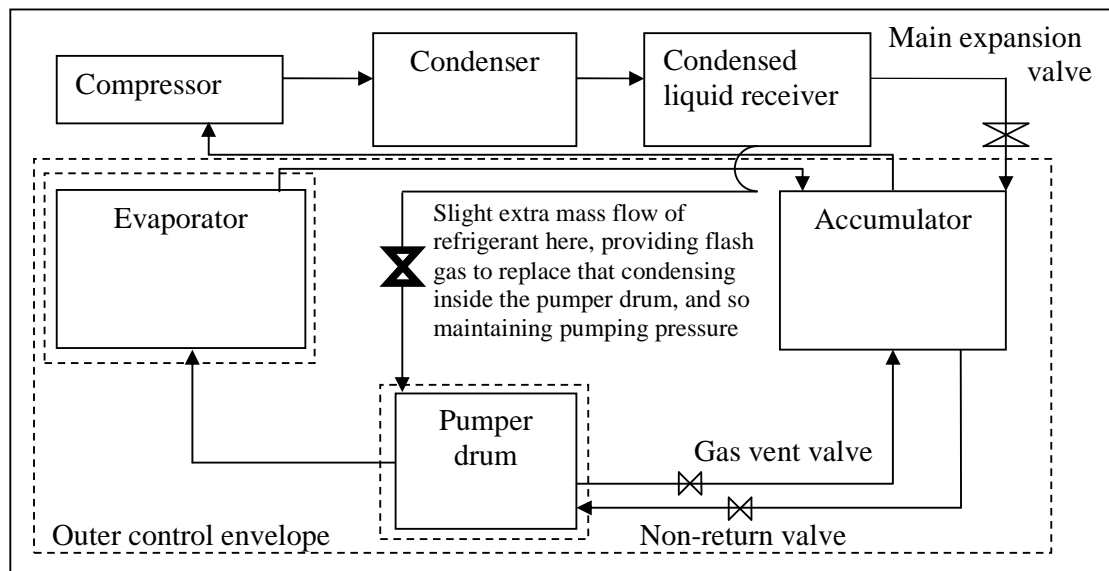


Figure 7.2 Diagram of a simple cold gas pumped system during pumping

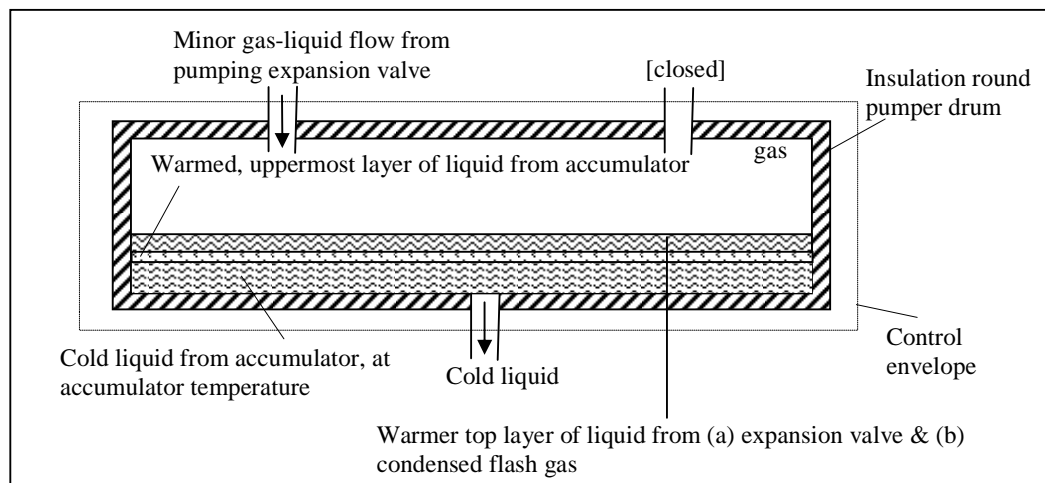


Figure 7.3 Interior of pumper drum during pumping

If the interior of the pumper drum for the CGPS shown in Figure 7.2 above is considered as shown in Figure 7.3, during pumping, the top layer of liquid in the pumper drum – warmer than the cold liquid at the bottom – originates from:

- the unflashed liquid leaving the pumping expansion valve, plus;
- condensation of flash gas:

- (i) on the uppermost layer of cold liquid from the accumulator (this uppermost layer will be warmed by this condensation of flash gas);
- (ii) on the colder steel shell of the pumper drum

Therefore, over the pumping period, the minor refrigerant mass inflow (across the outer control envelope) from the liquid receiver is more than that needed just to pressurise the gas space in the drum. The balance is the extra mass inflow needed to maintain that pressure as some flash gas condenses on top of the cold liquid, and on the pumper drum's shell. If it is assumed here, for convenience, that during this pumping period, no part of the minor refrigerant flow through the pumping expansion valve reaches the evaporator, then the compressor receives only (i) the flash gas from the major refrigerant flow directly to the accumulator; and (ii) the gas due to evaporation in the evaporator. All the mass inflow to the pumper drum from the pumping expansion valve during the pumping period stays in the pumper drum, as a combination of liquid and gas.

Processes during the venting period at the pumper drum

From Figure 7.3, at the end of the pumping period, the pumper drum contains:

- (a) flash gas at pumping pressure;
- (b) a warmer, top layer of liquid, comprising:
 - (i) the unflashed liquid from the expansion valve, plus;
 - (ii) the liquid from flash gas condensing on the surface of the cold liquid from the accumulator, and on the pumper drum walls;
- (c) the uppermost layer of cold liquid from the accumulator – warmed due to condensation of flash gas on top of it;
- (d) underneath, the remaining, unwarmed cold liquid from the accumulator (if any).

When the pumper drum is depressurised to accumulator pressure by venting to the accumulator, any remaining cold liquid (from the accumulator) at the drum's bottom does not flash. However, the warmer, top layer of liquid will partially

flash – until the resulting combination of new, cold liquid and new, cold flash gas is at ‘filling state’ – i.e. at, effectively, accumulator pressure and temperature. This partial flashing is due to:

- (A) cooling-by-evaporation of the unflashed liquid from the expansion valve, and
- (B) cooling-by-evaporation of the *condensed* liquid, due to:
 - (I) re-cooling, down to accumulator temperature, of the uppermost layer of liquid from the accumulator;
 - (II) re-cooling, down to accumulator temperature, of the warmed pumper drum steel;
- (C) cooling of the gas (that remains as gas) in the drum from its saturated state at pumping pressure to saturated state at accumulator pressure.

The amount of new, cold flash gas so produced is that produced by (A) plus (B) plus (C) above, *and equates to the balance of the flash gas that would have been generated had the minor flow of refrigerant expanded, in one step, all the way from condensed liquid pressure to accumulator pressure.* The cold liquid remaining in the pumper drum at the end of this depressurisation is the minor part of the liquid that will be pumped through the evaporator during the next pumping period.¹⁸ Thus both minor and major flows of refrigerant, through their respective expansion valves, supply the corresponding minor and major portions of the cold liquid, at accumulator temperature, which is pumped through the evaporator during the pumping (ice-building) period.

In summary, for the CGPS during pumping, there is a slight extra flow of refrigerant, through the pumping expansion valve, necessary to supply the extra flash gas to keep the system pressurised, because some flash gas will condense on cold liquid and the pumper drum walls. However, this extra flow also supplies correspondingly extra unflashed liquid¹⁹ that is then available as liquid refrigerant

¹⁸ The major part of this liquid being, of course, that obtained from the accumulator during the pumper drum’s filling period.

¹⁹ ALL flow leaving the pumping expansion valve supplies the same proportions of unflashed liquid and flash gas.

for ice-making. During depressurisation by venting, the liquid *condensed from flash gas*, in re-evaporating by the process of (B) above, turns into a (relatively) small extra flow of vapour that reaches the compressor. However, the above correspondingly extra unflashed liquid – once finally flashed down to accumulator pressure – provides correspondingly extra liquid refrigerant for ice-making.²⁰

The vapour flows due to (A), (B) and (C) above are from internal heat exchanges, bringing the residual pumping gas in the drum to its final, saturated state at accumulator pressure. Therefore, they arise from sub-processes in the overall, *inherent* URD of flash gas generated in expanding condensed refrigerant liquid down to accumulator pressure.

For the HGPS, essentially the same pumping process occurs as for the CGPS. However, as the HGPS requires an *additional* mass flow of pressurising hot gas²¹ (that is, additional to the mass flow of condensed liquid) from the liquid receiver to pressurise the pumper drum, the additional vapour flows due to (B) and (C) above that occur during the pumping period for this arrangement constitute *avoidable* URDs²². Similarly for a mechanically pumped system, the work input, in the pump(s), to the liquid refrigerant being pumped constitutes an *avoidable* URD.

The avoidable, unavoidable and relevant inherent URDs that occur during the different sub-periods, and for the different pumping arrangements, are formally defined in Section 8 below. Next, though, it is worthwhile to examine the key aspects of pumping refrigerant in the CGPS in some detail, and this is now done.

²⁰ Hence, during the immediately following filling period, the accumulator needs to supply correspondingly less liquid.

²¹ Which will include extra mass flow to maintain pressure as some hot gas condenses on cold liquid and on the pumper drum's walls (analogous to the CGPS).

²² Because this additional vapour must be recompressed at the compressor.

7.2.4 Refrigerant Pumping by Cold Flash Gas

Figure 7.2 is repeated in Figure 7.4 below. As noted at the beginning of Section 7.2.3 above, most of the cold liquid refrigerant needed for ice-building is generated through the main expansion valve into the accumulator, with the balance being generated through the pumping expansion valve into the pumper drum.

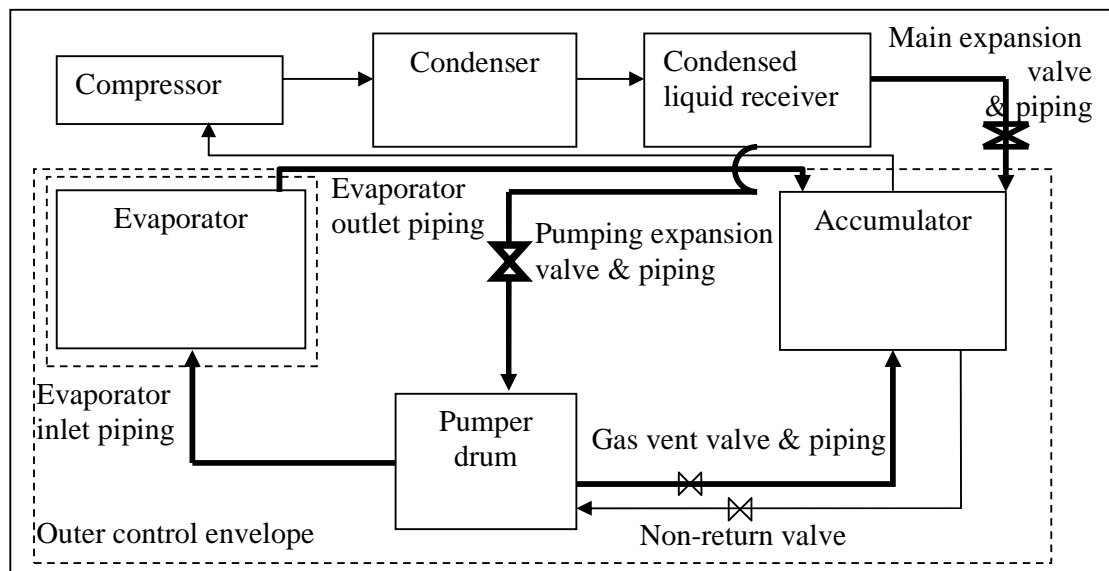


Figure 7.4 (repeated) Diagram of a simple cold gas pumped system during pumping

The split of the flows through these two expansion valves is governed by the following. That through the *pumping* expansion valve needs to supply the volume of flash gas needed to do the pumping (by displacing the liquid in the pumper drum). Obviously, the volume of flash gas generated by *all* the condensed liquid expanding to pumping pressure would be far greater than that needed for such pumping. So the remaining, major flow of condensed liquid that would generate the remaining, unneeded volume of flash gas (unneeded for pumping) comprises the flow through the *main* expansion valve directly into the accumulator.

Considering both the main and the pumping expansion valves – together with their piping - in Figure 7.4, the condensed liquid expansion process thus consists of two semi-parallel flows:

- (1) the major, *main* refrigerant flow through the *main* expansion valve and its piping. This expansion process is from condensed liquid receiver pressure to accumulator pressure - the lowest pressure inside the outer control envelope of Figure 7.4;
- (2) the minor, or auxiliary, *pumping* refrigerant flow through the pumping expansion valve and its piping into the pumper drum (at pumping pressure). Here, the liquid and vapour separate, to ensure that the evaporator is fed with pure liquid. Then;
 - (a) because of the difference in pressure between the pumper drum and the accumulator, most of²³ the *liquid*, pumped by the increasing volume of flash gas in the pumper drum, flows through the evaporator inlet piping into the evaporator itself. Here, a portion of the liquid evaporates to vapour. The resulting liquid-vapour mixture leaves through the evaporator outlet piping and flows to the accumulator;
 - (b) the *vapour (flash gas)* stays in the drum during pumping, but, during subsequent depressurisation, flows through the venting valve and its piping into the accumulator.

The points to note are:

- (A) flow (2) above is exactly the same in principle as flow (1), except that the expansion is from condensed liquid receiver pressure to the intermediate, *pumping* pressure (this being about 2 bar above accumulator pressure). The liquid and vapour separate in the pumper drum, at pumping pressure. Then using the increasing volume of confined flash gas in the pumper drum to displace, and hence to pump, liquid utilises the available difference between pumping and accumulator pressures to pump *pure* liquid

²³ Except that remaining at the end of the pumping period.

refrigerant (as opposed to a mixture of flash gas and unflashed liquid) to the evaporator.

(B) although flow (2) subsequently splits into sub-flows (2)(a) and (2)(b), which occur non-simultaneously, these sub-flows sum up to *the expansion of flow (2) from pumping to accumulator pressure*. Thus flows (2), (2a) and (2b) sum up to *the expansion of the pumping refrigerant flow from condensed liquid pressure to accumulator pressure*. Thus flows (1), (2) (2a) and (2b) sum up to *the expansion of ALL the flow of condensed liquid refrigerant from condensed liquid pressure to accumulator pressure*.

In the CGPS, performing the expansion of condensed refrigerant liquid in this way accomplishes the pumping of liquid refrigerant to and through the evaporator *without any external work input* (unlike hot-gas or mechanically pumped systems)²⁴. The fundamental reason is that, unlike hot-gas and mechanically pumped arrangements, ALL the condensed liquid is not expanded in a single step down to accumulator pressure. In the CGPS, some such liquid – enough to generate the flash gas to displace the required feed rate of liquid to the evaporator – is expanded to intermediate, pumping pressure so that the difference between pumping and accumulator pressures provides the required pressure difference for such pumping.

7.3 Configurations of the Different Operating Arrangements

A thermodynamic analysis of an overfeed refrigeration system with various refrigerant pumping arrangements (hot gas, cold gas or mechanically pumped) provides a fundamental basis for predicting the relative efficiencies of corresponding, differently pumped batch ice-making cycles. For the sake of comparing these differently pumped overfeed systems, it is assumed that all operating parameters such as mass of ice built and required, condensing and

²⁴ This is proven in Appendix A13.

evaporating pressures and temperatures, as well as performance quantities such as refrigerant mass flow rates and average recirculation ratios, remain constant. Based on this assumption, the URDs specific to each overfeed pumping arrangement provide a platform from which a thermodynamic comparison between these arrangements can be performed.

Over one batch ice-making cycle of ice-building followed by ice harvesting, the total refrigeration demand of a cold gas pumped arrangement is:

$$\Sigma\Delta H_{\{CGPS\}} = \Sigma Q_{PRD} + \Sigma\Delta H_{URD\{CGPS\}} \quad (1)$$

Where ΣQ_{PRD} includes the PRD of chilling the incoming feed water at the pre-chiller and at the evaporators, as well as freezing the required ice layer, and is denoted as heat transferred across the evaporator control volume, as shown in Figure 8.1 below. The URDs associated with the system, $\Sigma\Delta H_{URD\{CGPS\}}$, are denoted as changes in enthalpy of the refrigerant liquid and vapour, as described in Section 8 below.²⁵

Similarly for a hot gas pumped arrangement the total refrigeration demand is:

$$\Sigma\Delta H_{\{HGPS\}} = \Sigma Q_{PRD} + \Sigma\Delta H_{URD\{HGPS\}} \quad (2)$$

The URDs of the above two systems differ only in the unavoidable URDs specific to each pumping arrangement.

For a mechanically pumped arrangement as shown in Figure 1.3 above, the unavoidable URDs are primarily confined to those arising from the harvesting process. The avoidable URDs associated with the interactions between

²⁵ The URD of freezing the melted ice layer as well as subcooling the entire built ice layer is strictly also a heat transfer across a control volume and should be denoted Q_{URD} . However, as this is the only URD associated with heat flow across a control volume it is included in the term $\Sigma\Delta H_{URD}$.

pressurising gases and refrigerant liquid are eliminated, but there remain avoidable URDs due to the pumping pressure imparted by the pump to the circulating liquid, as well as friction in the additional piping required. A detailed analysis and comparison of the URDs specific to each arrangement is presented in Section 8 below.

For a mechanically pumped arrangement, the total refrigeration demand is:

$$\Sigma\Delta H_{\{MPS\}} = \Sigma Q_{PRD} + \Sigma\Delta H_{URD\{MPS\}} \quad (3)$$

Finally, assuming that compressor isentropic efficiency changes negligibly for small changes in slide valve position, and that for small changes in URDs the condenser pressure remains constant (this assumption will be validated when the URDs are compared in Section 8. below) the COP of the cold gas pumped arrangement over a complete batch ice making cycle is:

$$COP_{\{CGPS\}} = \frac{\Sigma Q_{PRD}}{\Sigma W_{\{CR\}\{CGPS\}mech}} \quad (4)$$

Where as mentioned above, the sum of PRDs of chilling the incoming feed water and freezing the required ice layer is denoted ΣQ_{PRD} . The denominator of equation (4) is the mechanical work input into the compressor over a complete ice building and harvesting cycle, estimated from electrical power input readings from tests performed at the operating, cold gas pumped Unit 5 of the ERPM plant.

Similarly, for a hot gas pumped arrangement, the COP is:

$$COP_{\{HGPS\}} = \frac{\Sigma Q_{PRD}}{\Sigma W_{\{CR\}\{HGPS\}mech}} \quad (5a)$$

Where

$$\Sigma W_{\{CR\}\{HGPS\}mech} = \Sigma W_{\{CR\}\{CGPS\}mech} \frac{\Sigma\Delta H_{\{HGPS\}}}{\Sigma\Delta H_{\{CGPS\}}} \quad (5b)$$

²⁶In equation (5b), the mechanical work input into the compressor is assumed to be greater than that for the cold gas pumped system by the ratio of the total refrigeration demands $\Sigma\Delta H$ of the two arrangements. This ratio of the total refrigeration demands in the above equation allows for the mechanical and electrical work input into the compressor to be predicted for all arrangements, based on the assumption of negligible changes in compressor isentropic efficiency mentioned above.

For a mechanically pumped arrangement, the COP is:

$$COP_{\{MPS\}} = \frac{\Sigma Q_{PRD}}{\Sigma W_{\{CR\}\{MPS\}mech} + \Sigma W_{\{P\}\{MPS\}mech}} \quad (6a)$$

Where, as for (5b),

$$\Sigma W_{\{CR\}\{MPS\}mech} = \Sigma W_{\{CR\}\{CGPS\}mech} \frac{\Sigma\Delta H_{\{MPS\}}}{\Sigma\Delta H_{\{CGPS\}}} \quad (6b)$$

Therefore, from the equations above, the gas pumped COP does not include a term in the denominator resulting from the additional work input required for the mechanical pump. As mentioned in Section 2.2, Lorentzen and Baglo⁽⁶⁾ predict that an efficient cold gas pumped arrangement would limit the total URD to match that of the mechanically pumped arrangement, resulting in a larger COP for the cold gas pumped system due to the absence of the mechanical power required by the pump in the denominator.

Using data from the tests performed at the operating Unit 5 of the ERPM plant, the electrical operating cost per year for gas and mechanically pumped arrangements can be predicted as follows:

$$\text{Electrical Operating Cost per Year} = (\Sigma \dot{W}_{\{CR\}elec} + \Sigma \dot{W}_{\{P\}elec}) \times \frac{\text{Cents}}{\text{kWh}} \times \frac{\text{hr}}{\text{year}} \quad (7)$$

²⁶ Figure 8.17 below presents the results of the COPs for the different pumping arrangements based on equations (4) – (6). Following the results, the validity and key limitations of the assumptions behind equations (5b) and (6b) are discussed, and again in Section 8.12.

This simplified analysis forms the basis from which the more detailed theoretical models are created below. The purpose of these models²⁷ is to predict whether the cold gas pumped arrangement currently in operation at the ERPM facility is the most energy efficient and electrical cost effective when compared to a hot gas or a mechanically pumped arrangement.

²⁷ Apart from predicting the mass flow rate and average recirculation ratio at the evaporator, as mentioned in the objectives listed in Section 6.

8. MODELLING OF PRODUCTIVE AND UNPRODUCTIVE REFRIGERATION DEMANDS FOR DIFFERENTLY PUMPED LIQUID OVERFEED ARRANGEMENTS

This Section presents the analysis of the URDs and PRDs for four different pumping arrangements²⁸ on the basis of a control volume energy rate balance. These arrangements are, first, the existing cold gas pumped arrangement at Unit 5 of the ERPM ice-making plant. Then, three other possible pumping arrangements for this Unit 5 are considered: hot gas, mechanically pumped and fully mechanically pumped arrangements, in Sections 8.7, 8.8 and 8.9 respectively. This approach pinpoints not only what types of URD occur, but when – i.e. during which period or sub-period – they occur. From the detailed control volume analyses, the URDs seen at the different control volumes can be identified. An annual electrical operating cost comparison for each pumping arrangement is also performed. By comparing the results of these analyses for the different pumping arrangements, for Unit 5 of the ERPM plant, the relative energy efficiency and electrical cost effectiveness of each arrangement can be predicted. The results of this comparative analysis are then compared to the suggestions and conclusions of Lorentzen and Baglo,⁽⁶⁾ ASHRAE⁽⁵⁾ and Wright⁽¹¹⁾ as described in Section 2. above.

As the PRD and URD of building the ice layer are common and unavoidable to all pumping arrangements, they will be presented first.

²⁸ This includes a cold and hot gas as well as two probable mechanically pumped arrangements.

8.1. Productive and Unproductive Refrigeration Demands Directly Related to Ice Building

The investigational method of modelling presented below is based on Bailey-McEwan's⁽¹²⁾ analysis of an earlier batch ice-making plant.

Unit 5 of the ERPM plant consists of one 1700 kW motor (1350 kW shaft power) screw compressor and eight evaporator modules, with 35 plates per module.⁽¹³⁾ As the duration of one complete ice building and harvesting cycle is 15 minutes, each module executes 96 cycles in 24 hours.⁽¹³⁾ The mass of ice required in 24 hours is 1000 tons⁽¹³⁾ (1000 000 kg), therefore the mass of ice required from Unit 5 in one cycle is 10,417 kg. As testing at the plant was performed on one module, an analysis per module is presented below.

Per module, the mass of ice built in one cycle, $m_{I,b}$, consists of the thickness of ice required, $m_{I,req}$, as well as the thickness of the innermost layer of ice that has to be melted to release the ice from the surface of each plate.

$$m_{I,b} = \rho_I n a_{[E]} (2y_{I,req} + 2y_{I,m}) \quad (8)$$

Where n is the number of plates per module, $a_{[E]}$ the surface area of one side of the evaporator plate, and $y_{I,req}$ and $y_{I,m}$ are the thicknesses of the particulate ice delivered to the screw conveyor below the evaporators and of the subsequently melted innermost layer respectively. The factor of two is to account for the fact that ice is built on both sides of the plate.

The ice thickness built on one side of each plate, based on tests performed at the plant as well as Worthington-Smith & Brouwer,⁽¹³⁾ van der Walt & de Kock⁽¹⁸⁾²⁹ and Rankin⁽¹⁴⁾, is approximately 5-6 mm (refer to Appendix A6 for these results). The ice that is delivered to the screw conveyor below the evaporator module is therefore:

²⁹ Who merely *state typical figures* and therefore offer no experimental validation for the thickness of ice built.

$$m_{l,req} = \rho_l n a_{[E]} (2y_{l,req}) \quad (9)$$

Once the evaporator module has returned to evaporating temperature after the re-cooling sub-period of the harvesting period (see Section 8.2.2 below), the control volume of the module appears as follows:

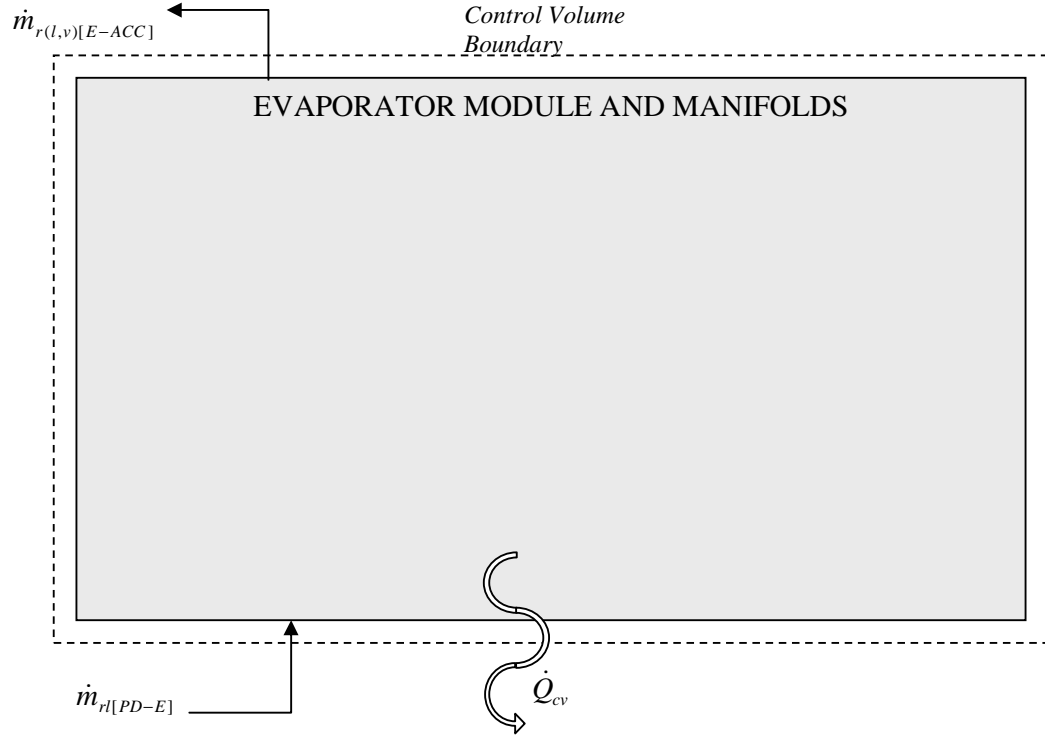


Figure 8.1 Control Volume: Evaporator Plates and Manifolds (Ice Building)

The energy rate balance equation for the control volume of Figure 8.1 is:

$$dE_{cv}/dt = \dot{Q}_{cv} - \dot{W}_{cv} + \sum_i \dot{m}_i (h_i + V_i^2/2 + gz_i) - \sum_o \dot{m}_o (h_o + V_o^2/2 + gz_o) \quad (10)$$

Neglecting changes in kinetic and potential energies, noting that there is no shaft work \dot{W}_{cv} , and naming the individual mass flows,

$$dE_{cv}/dt = \dot{Q}_{cv} + \dot{m}_{r[PD-E]} h_{r_l}(T_{r[E]build}) - \dot{m}_{r(l,v)[E-ACC]} h_{r(l,v)}(T_{r[E]build}, x_{r[E]o}) \quad (11)$$

Where $\dot{m}_{r[PD-E]}$ is the mass flow rate of saturated liquid from the pumper drum to the evaporator inlet; assumed to be saturated liquid at $T_{r[E]build}$; $\dot{m}_{r(l,v)[E-ACC]}$ is the two-phase mass flow rate at the evaporator outlet, and the outlet enthalpy, $h_{r(l,v)}(T_{r[E]build}, x_{r[E]o})$ is a function of the instantaneous recirculation ratio, $x_{r[E]o}$, which is the inverse of the quality of the refrigerant.

Integrating over the time interval $(t_2 - t_1)$ of a complete ice building period, and justifiably assuming inlet enthalpies to be constant, and using an average value of outlet enthalpy:

$$\Delta E_{cv} = \left| Q_{cv} + \Delta m_{r[PD-E]} h_{rl}(T_{r[E]}) - \Delta m_{r(l,v)[E-ACC]} h_{r(l,v)}(T_{r[E]}, \bar{x}_{r[E]o}) \right|_{build} \quad (12)$$

Where the average outlet enthalpy $h_{r(l,v)}(T_{r[E]}, \bar{x}_{r[E]o})_{build}$ is a function of the average recirculation ratio $\bar{x}_{r[E]o}$ (and hence average quality) over the ice-building period.

Since the module is always at evaporating temperature during an ice-building period, there is no change of internal energy in the evaporator walls; however there will be changes in internal energy of the refrigerant content. Thus equation (12) becomes:

$$\Delta E_{cv} - Q_{cv} = \left| \Delta m_{r[PD-E]} h_{rl}(T_{r[E]}) - \Delta m_{r(l,v)[E-ACC]} h_{r(l,v)}(T_{r[E]}, \bar{x}_{r[E]o}) \right|_{build} \quad (13)$$

The change in internal energy of the saturated refrigerant over the ice building period defined as $(t_2 - t_1)$ is denoted as:

$$(m_{r[E](t_2)} - m_{r[E](t_1)}) u_{rl}(T_{r[E]build}) + (m_{rv[E](t_2)} - m_{rv[E](t_1)}) u_{rv}(T_{r[E]build}) \quad (14)$$

Due to the heat absorbed by the refrigerant inside the tubes, a portion of the flowing water changes to ice.

The refrigeration demand during the ice building period arises from two main processes and a third minor process:

Chilling the inlet feed-water from 12° to 0° C;

Freezing this water;

Sub-cooling the ice formed.

With regards to process 3 above, which constitutes an unproductive refrigeration demand (URD), it is assumed, based on Bailey-McEwan⁽¹²⁾ (his page 56) that the relatively small thickness of the ice sheet justifies the use of an arithmetic mean to represent the sub-cooled ice temperature.⁽¹²⁾

Per cycle, the refrigeration demand of chilling the feed water, freezing this water, and sub-cooling the ice layer (assuming that $T_{l.o} = 0^\circ\text{C}$ and that $T_{l.i}$ is at evaporating temperature) is:

$$Q_{cv} = -m_{I,b}(-c_w T_{w[E]i} - h_{sf} + c_I \frac{(T_{r[E]build} + T_{l.o})}{2}) \quad (15)$$

In parenthesis, it is noted that as the sub-cooling effect is assumed to be lost during ice shedding (harvesting), and building the innermost, subsequently melted ice layer is considered a URD in that this layer does not end up as ice delivered by the evaporator, the actual *productive* refrigeration demand is³⁰:

$$Q_{PRD[E]} = m_{I,req}(-c_w T_{w[E]i} - h_{sf}) \quad (16)$$

Substituting equations (14) and (15) into equation (13) above:

³⁰ Note that this PRD, on the refrigerant-circuit side, does not include the *inherent* URD of the flash gas generated in providing the cold liquid refrigerant.

$$\begin{aligned}
& (m_{r[E](t2)} - m_{r[E](t1)})u_{rl}(T_{r[E]build}) + (m_{rv[E](t2)} - m_{rv[E](t1)})u_{rv}(T_{r[E]build}) \\
& - m_{I,b}(-c_w T_{w[E]i} - h_{sf} + c_I \frac{(T_{r[E]build} + T_{I,o})}{2}) \\
& = |\Delta m_{r[PD-E]}h_{rl}(T_{r[E]}) - \Delta m_{r(l,v)[E-ACC]}h_{r(l,v)}(T_{r[E]}, \bar{x}_{r[E]o})_{build}
\end{aligned} \tag{17}$$

8.1.1. URDs and PRDs at the Evaporator during the Ice Building Period

The PRD associated with the evaporator during the ice building period comprises chilling the inlet feed-water from 12° to 0°C and freezing the required ice layer. From Figure 3.4 above, the mass of water initially at around 22,2 °C⁽¹³⁾ that enters Unit 5 equals, during a complete ice-making batch-cycle, the mass of ice delivered by the evaporator. Therefore, per (16) above:

$$Q_{PRD[E]} = m_{I,req}(-c_w T_{w[E]i} - h_{sf}) \tag{18}$$

The unavoidable URDs associated with the evaporator during the ice building period are the freezing of the melted ice layer, as well as the sub-cooling of the entire ice layer.

$$Q_{URD[E]} = m_{I,b}(-c_w T_{w[E]i} - h_{sf} + c_I \frac{(T_{r[E]build} + T_{I,o})}{2}) - Q_{PRD[E]} \tag{19}$$

8.1.2. PRD of Cooling the Incoming Make-Up Feed Water at the Pre-Chiller

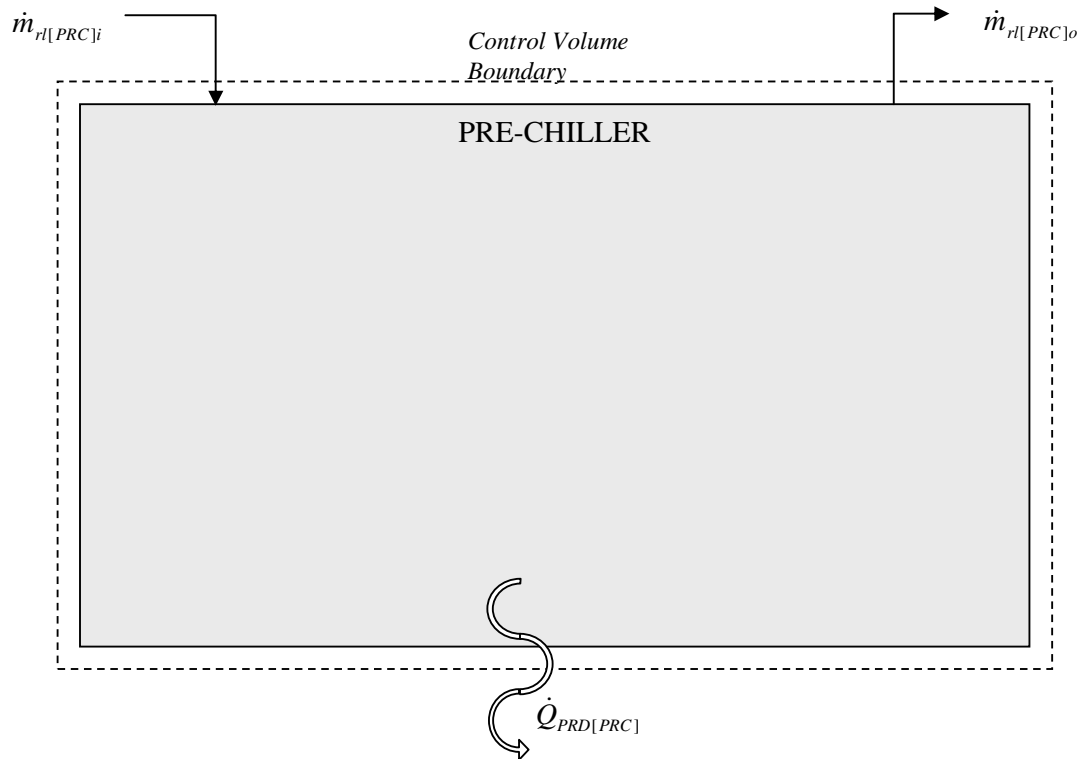


Figure 8.2 Control Volume: Pre-Chiller

The pre-chiller chills the incoming make-up feed water from ambient temperature (22.2°C based on Wothington-Smith & Brouwer⁽¹³⁾ and confirmed by tests performed at the plant (Appendix A6, Table A6.3) to 12°C , from where it enters the feed water basin below the evaporators. This is considered a PRD as it replaces the water that is frozen to ice and delivered to the screw conveyor below the evaporator. The water from the innermost ice layer melted during harvesting returns to the feed water basin once the ice sheet detaches (as illustrated in Figure 1.1 above), and therefore the make-up water replaces only the mass of ice required, $m_{l,req}$. The mass in- and out-flows of Unit 5 of the plant are shown in the control volume of Figure 3.4 above.

As pre-chilling this make-up water is a heat transfer across the control volume as shown in Figure 8.2 above, it is denoted $\dot{Q}_{PRD[PRC]}$.

Per module, the PRD associated with the chilling of make-up water at the pre-chiller is:

$$\dot{Q}_{PRD[PRC]} = m_{l.req} \bar{c}_{w[PRC]} (T_{w[PRC]i} - T_{w[PRC]o}) \quad (20)$$

Where $\bar{c}_{w[PRC]}$ is an averaged specific heat based on the inlet and outlet water temperatures, and the outlet water temperature $T_{w[PRC]o}$ is the same as the inlet temperature at the evaporator $T_{w[E]i}$ of equation (15) above.

8.2. Control Volume Energy Balances to Predict the URDs at the Evaporator during the Harvesting Period

8.2.1 The Warming Sub-Period

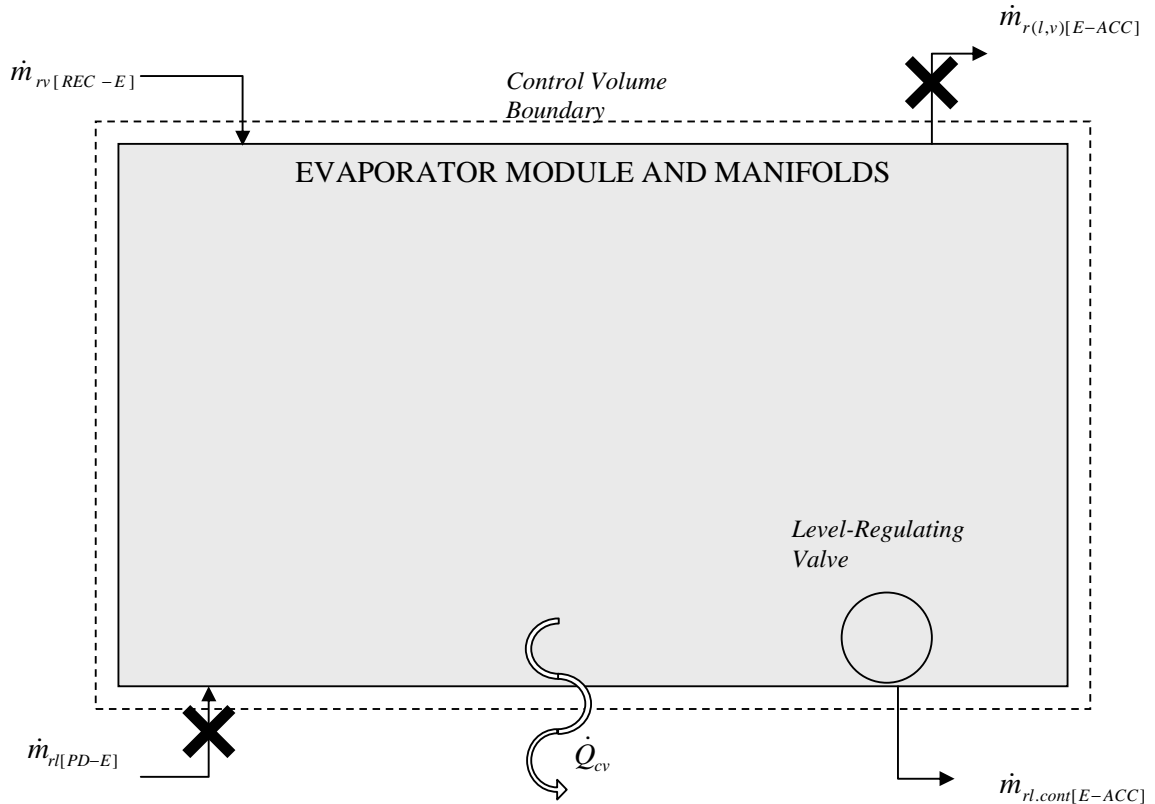


Figure 8.3 Control Volume: Evaporator Plates and Manifolds (Warming Sub-Period)

From the definition in Section 7.1.3 above, the warming sub-period is defined as the period when the evaporator plates are isolated from the cold circulating refrigerant (the crosses through the mass flows from the pumper drum $\dot{m}_{rl[PD-E]}$ and to the accumulator $\dot{m}_{rl[l,v][E-ACC]}$ in Figure 8.3 denote that these flows are zero) and warm pressurized refrigerant gas from the condensed liquid receiver, $\dot{m}_{rv[REC-E]}$ is introduced into the plates to release the built ice sheet. This period is illustrated in the timing diagram of Figure 3.2 by the hatched rectangle across the trace of Module 2, comprising the time period $(t_2 - t_1)$.

Referring to Figure 8.3 above, the energy rate balance equation for the control volume is the same as in equation (10) above.

Neglecting changes in kinetic and potential energies, noting that there is no shaft work \dot{W}_{cv} , and naming the individual mass flows,

$$dE_{cv}/dt = \dot{Q}_{cv} + \dot{m}_{rv[REC-E]}h_{rv}(P_{r[REC]}) - \dot{m}_{rl.cont[E-ACC]}h_{rl}(P_{r[E]har}, T_{r[E-ACC]}) \quad (21)$$

where:

$\dot{m}_{rv[REC-E]}$ is the mass flow rate of incoming harvesting gas from the condensed liquid receiver and $\dot{m}_{rl.cont[E-ACC]}$ is the mass flow rate of liquid that is expelled to the accumulator by contact with this pressurised gas during the warming sub-period.

Integrating over the time interval $(t_2 - t_1)$ of a complete warming sub-period, defined by the abovementioned hatched rectangle in the timing diagram of Figure 3.2, and justifiably assuming enthalpy $h_{rv}(P_{r[REC]})$ to be constant over time,

$$\Delta E_{cv} = Q_{cv} + \Delta m_{rv[REC-E]}h_{rv}(P_{r[REC]}) - \int_{t_1}^{t_2} \dot{m}_{rl.cont[E-ACC]}h_{rl}(P_{r[E]har}, T_{r[E-ACC]}) \cdot dt \quad (22)$$

Assuming that:

- at time t_1 , the start of the warming sub-period, the refrigerant temperature inside the evaporator module and manifolds is $T_{sat}(P_{r[E]build})$, and the steel of the module and manifolds is also at this temperature;
- during the first part of the time interval $(t_2 - t_1)$, the mass $\Delta m_{rl.cont[E-ACC]}$ of cold liquid refrigerant left in the plates at the end of ice-building, at temperature $T_{r[E-ACC]}$,³¹ is expelled to the accumulator by direct contact with the higher-pressure harvesting gas, and then;

³¹ $T_{r[E-ACC]}$ is predicted below and is based on temperatures obtained from tests performed at the plant.

- during the remaining part of this time interval, the mass $m_{rl\{c\}}$ of warm liquid condensing from the incoming harvesting gas, at a mean temperature³² $\bar{T}_{r\{c\}}$, is continually expelled to the accumulator, and
- at time t_2 , the end of the warming sub-period, the refrigerant temperature inside the evaporator module and manifolds is $T_{\text{sat}}(P_{r[E]har})$, and the steel of the module and manifolds is also at this temperature,

and finally, that $P_{r[E]har}$ is constant over $(t_2 - t_1)$,

$$\begin{aligned} \Delta E_{cv} = & Q_{cv} + \Delta m_{rv[REC-E]} h_{rv}(P_{r[E]har}, T_{r[E]har}) - \Delta m_{rl.cont[E-ACC]} h_{rl}(P_{r[E]har}, T_{rl[E-ACC]}) \\ & - m_{rl\{c\}} h_{rl}(P_{r[E]har}, \bar{T}_{r\{c\}}) \end{aligned} \quad (23)$$

Representing ΔE_{cv} in more detail as the sum $\sum(\Delta E)_{cv}$ of the internal energy changes inside the control volume,

$$\sum(\Delta E)_{cv} = \Delta U_{s[E]} + \Delta U_{rl.trap[E]} + \Delta U_{rv.trap[E]} \quad (24)$$

where the internal energy gains are:

$\Delta U_{s[E]}$: of the steel of the evaporator plates and their inlet and outlet manifolds;

$\Delta U_{rl.trap[E]}$: of the refrigerant liquid in the plates and manifolds; and

$\Delta U_{rv.trap[E]}$: of the refrigerant vapour confined in the plates between the beginning and the end of harvesting.

First, $\Delta U_{s[E]}$ is given by

$$\Delta U_{s[E]} = m_{s[E]} c_s (T_{r[E]build}) [T_{\text{sat}}(P_{r[E]har}) - T_{\text{sat}}(P_{r[E]build})] \quad (25)$$

³² Because the warm harvesting gas will initially condense on cold steel surfaces at temperature $T_{\text{sat}}(P_{r[E]build})$, this mean temperature $\bar{T}_{r\{c\}}$ will obviously be between $T_{\text{sat}}(P_{r[E]build})$, and $T_{\text{sat}}(P_{r[E]har})$. However, for the purposes of this investigation the condensed liquid will be assumed to be at $T_{\text{sat}}(P_{r[E]har})$.

Next, unlike the steel, the beginning and ending masses of refrigerant liquid inside the module can be significantly different. The subscripts 1 and 2 refer to the beginning and ending times of the warming sub-period.

$$\Delta U_{rl.trap[E]} = \left(m_{rl.trap[E]}\right)_{(t2)} u_{rl}(P_{r[E]har}) - \left(m_{rl[E]}\right)_{(t1)} u_{rl}(P_{r[E]build}) \quad (26)$$

where $(m_{rl[E]})_{(t1)}$ is the mass of liquid refrigerant in the module at the end of ice-building. This will be much greater than $(m_{rl.trap[E]})_{(t2)}$, the liquid trapped behind the level-regulating valve at the end of the warming sub-period. Also, the beginning and ending masses of refrigerant vapour in the evaporator can be significantly different due to the compressibility of vapour, so

$$\Delta U_{rv.trap[E]} = \left(m_{rv.trap[E]}\right)_{(t2)} u_{rv}(P_{r[E]har}) - \left(m_{rv[E]}\right)_{(t1)} u_{rv}(P_{r[E]build}) \quad (27)$$

where $(m_{rv[E]})_{(t1)}$ and $(m_{rv.trap[E]})_{(t2)}$ are the masses of refrigerant vapour in the module at the beginning and end of the warming sub-period respectively.

The control volume energy balance over the warming sub-period is, finally,

$$\begin{aligned} \Delta U_{s[E]} + \Delta U_{rl.trap[E]} + \Delta U_{rv.trap[E]} = & Q_{cv} + \Delta m_{rv[REC-E]} h_{rv}(P_{r.har}, T_{r.har}) \\ & - \Delta m_{rl.cont[E-ACC]} h_{rl}(P_{r[E]har}, T_{rl[E-ACC]}) \\ & - m_{rl(c)} h_{rl}(P_{r[E]har}, \bar{T}_{r(c)}) \end{aligned} \quad (28)$$

The only significant part of Q_{cv} is the heat transfer to the ice built on the plates in order to melt the innermost ice layer.³³

³³ That is, other heat exchange with the control volume's surroundings is negligible.

Predicting the Mass of Liquid Condensed during the Warming Sub-Period

Harvesting gas condenses to liquid throughout the warming sub-period and is expelled to the accumulator. The re-cooling of this condensed liquid $m_{rl\{c\}}$, which is assumed to be at harvesting temperature for the purpose of this investigation, constitutes an unavoidable URD at the accumulator where it is re-cooled. The value of $m_{rl\{c\}}$ is predicted as follows:

1. Incoming harvesting gas condenses to warm up the steel plates and the manifolds as per equation (25)

$$\Delta H_{r.har.1} = m_{s[E]c_s} (T_{r[E]build}) [T_{sat}(P_{r[E]har}) - T_{sat}(P_{r[E]build})] \quad (29)$$

2. Incoming harvesting gas condenses to reverse the sub-cooling effect in the built up ice layer. As mentioned in Section 8.1, the relatively small thickness of the ice sheet justifies the use of an arithmetic mean to represent the sub-cooled ice temperature.⁽¹²⁾

$$\Delta H_{r.har.2} = -m_{I,b} c_I \left(\frac{T_{r[E]build} + T_{I,o}}{2} \right) \quad (30)$$

3. Incoming harvesting gas condenses to melt the innermost ice layer.

$$\Delta H_{r.har.3} = 2n\rho_I a_{[E]} y_{I,m} h_{sf} \quad (31)$$

URDs 2. and 3. above are heat transfers across the control volume and comprise Q_{cv} in equation (21) above.

Assuming (see footnote 32 above) that the condensed liquid is at temperature $T_{sat}(P_{r[E]har})$, the mass of condensed liquid can be predicted as follows:

$$\begin{aligned} m_{rl\{c\}} [h_{rv}(P_{r[E]har}) - h_{rl}(P_{r[E]har})] &= \Sigma \Delta H_{r.har} = \Delta H_{r.har.1} + \Delta H_{r.har.2} + \Delta H_{r.har.3} \\ \therefore m_{rl\{c\}} &= \frac{\Delta H_{r.har.1} + \Delta H_{r.har.2} + \Delta H_{r.har.3}}{(h_{rv}(P_{r[E]har}) - h_{rl}(P_{r[E]har}))} \end{aligned} \quad (32)$$

Predicting the Mass and Temperature of Liquid Expelled and Warmed by Harvesting Gas at the Beginning of the Warming Sub-Period

Predicting the Mass

Due to the direct contact between the warm harvesting gas and the cold liquid while the former is expelling the latter to the accumulator at the beginning of the warming sub-period, heat is absorbed by this cold liquid.

$\Delta m_{rl,cont[E-ACC]}$ in equation (21) is predicted by estimating the ratio of gas and liquid in the evaporator at the end of the ice building period, and is based on the following assumptions:⁽¹²⁾

1. “The nature of the boiling of two-phase flow is extremely complex”⁽¹²⁾ and can be simplified by assuming that the “temperature of the boiling ammonia is constant along the plate length.”⁽¹²⁾
2. The heat flux is uniform along the entire length of the plate.
3. The ratio of vapour to liquid velocity is constant along the entire length of the plate.

Thus the total internal volume of each plate consists of the volume of gas and the volume of liquid, all at evaporating pressure, and based on the area of the individual channels along the length of the plate. From observations at the plant, there are 30 such channels per plate. Therefore, the internal volume of the plates is:

$$30a_{[E]chl}L_{[E]} = V_{rl[E]} + V_{rv[E]} \quad (33)$$

Where $a_{[E]chl}$ is the internal cross sectional area of the refrigerant channels of one evaporator plate, $L_{[E]}$ is the vertical length of the plate and $V_{rl[E]}$ and $V_{rv[E]}$ are the volumes of the liquid and vapour refrigerant occupying this internal volume at the beginning of the warming sub-period. In modelling, a conservative approach is taken when analysing this transferred mass, and it is predicted, based on the

analysis presented in Appendix A2, that each plate is filled by 30% of its inner volume with liquid ammonia at the beginning of the warming sub-period. Therefore the mass of liquid transferred out of the module³⁴ at the beginning of the warming sub-period, assuming all densities are at evaporating pressure, is

$$\Delta m_{rl.cont[E-ACC]} = 30na_{[E]chl}L_{[E]}(0,3\rho_{rl}(P_{r[E]build}) + 0,7\rho_{rv}(P_{r[E]build})) \quad (34)$$

Predicting the Temperature

Based on tests performed at the plant (Appendix A6 lists all the test results), and referring to Figure A1.1 where a temperature sensor T12 was placed before the level regulating valve, the temperature rise of the expelled liquid above evaporating temperature, $(T_{r[E-ACC]} - T_{r[E]build})$, can be predicted.

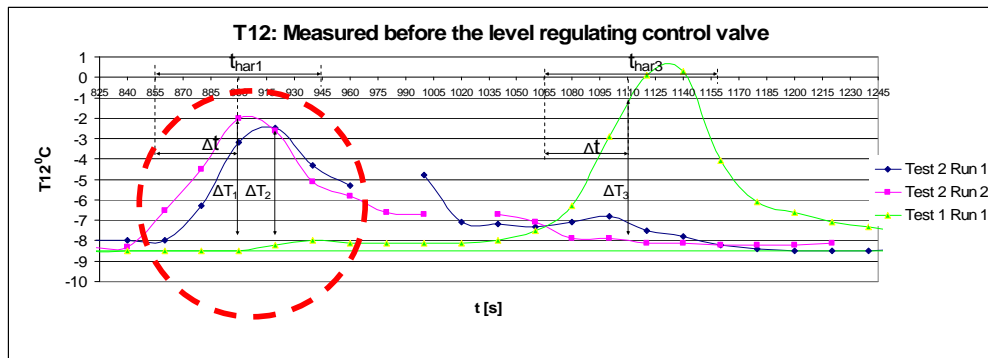


Figure 8.4 Temperature before level regulating valve, T12 versus time for all tests performed at the plant³⁵

³⁴ Recall that $n = 35$ plates per module; each plate has 30 channels.

³⁵ The corresponding plot in Appendix A6 is Figure A6.7, where the change in temperature over the entire testing period of 30 minutes is plotted.

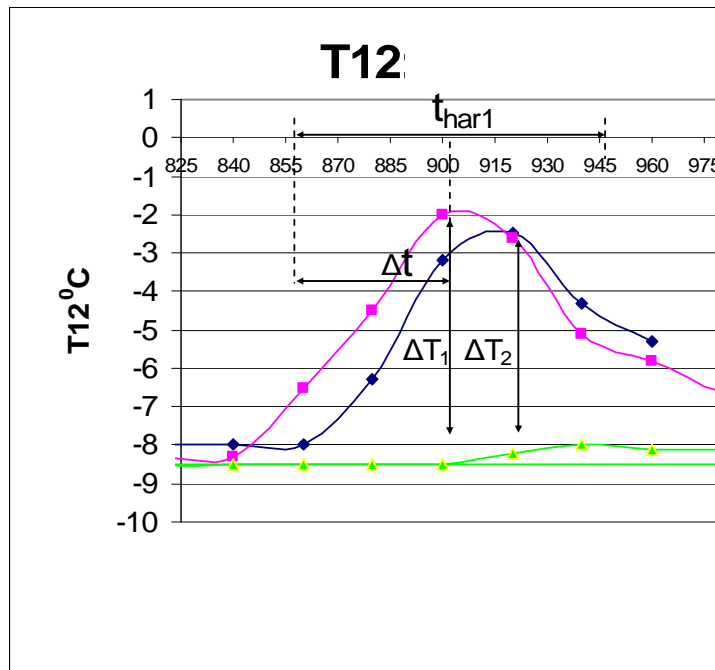


Figure 8.5 Magnified portion of Figure 8.3 to illustrate the method used to obtain the change in temperature of the expelled liquid

From Figure 8.4 and Figure 8.5 above of temperature T12 versus time, the temperature measured before the level regulating valve for all three tests performed shows a peak temperature reached during the warming sub-period. It is conservatively assumed that all the liquid remaining in the module at the end of ice building is expelled to the accumulator within half the harvesting time of 90 seconds.³⁶ The average change in temperature ($T_{r[E-ACC]} - T_{r[E]build}$) of the mass of expelled liquid $\Delta m_{r.cont[E-ACC]}$ for all three tests performed at the plant over the assumed time period is predicted from Figure 8.5 as 2.25 °C.

³⁶ In reality, it would not take the full 45 seconds to expel this liquid, however the total URD for the gas pumped systems are relatively insensitive to this change in temperature, and so a conservative approach is deemed appropriate in this instance. The justifying sensitivity analysis is performed in Appendix A10.1.

8.2.2 The Re-Cooling Sub-Period

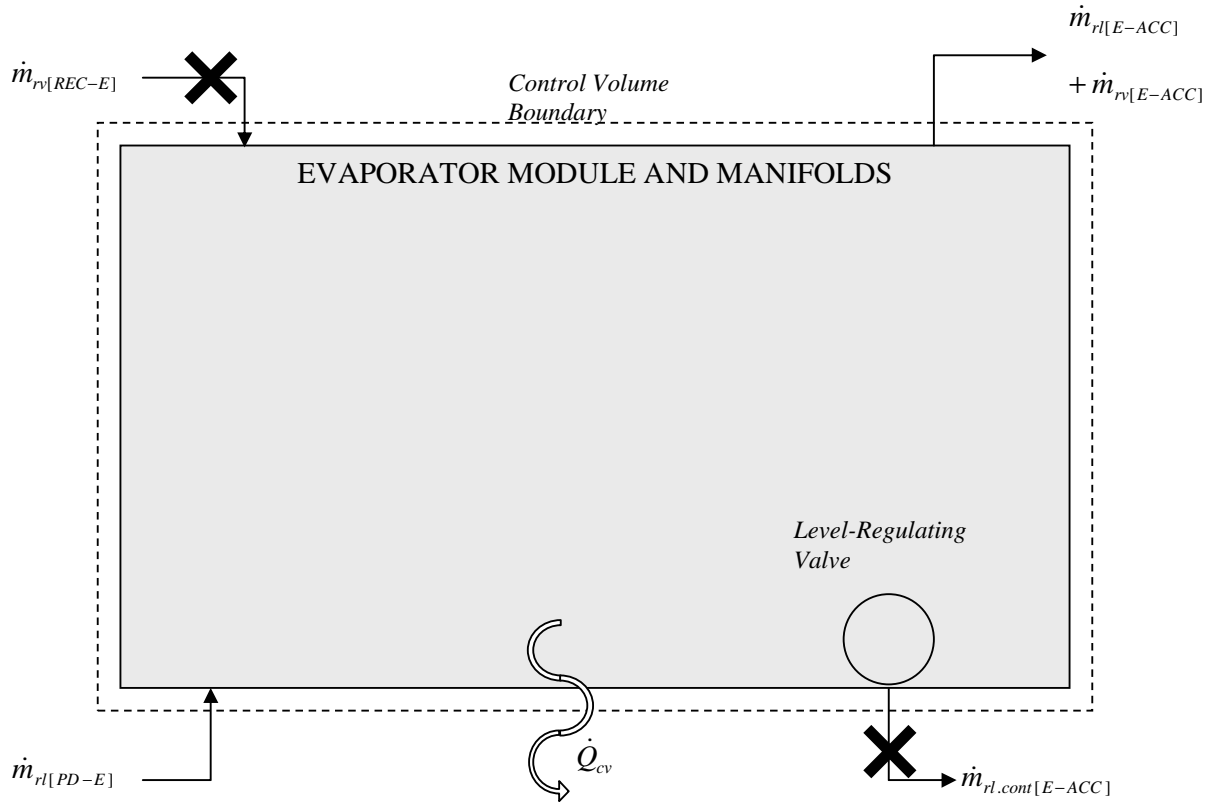


Figure 8.6 Control Volume: Evaporator Plates and Manifolds (Re-Cooling Sub-Period)

At the end of the warming sub-period, the refrigerant content of the module (evaporator plates and manifolds) is the liquid trapped behind the level-regulating valve $m_{rl.trap[E](t_2)}$, and the vapour above it, $m_{rv.trap[E](t_2)}$ as in equations (26) and (27). The re-cooling sub-period now begins. The harvesting gas supply $\dot{m}_{rv[REC-E]}$ ceases; the level regulating valve to the accumulator is closed, so $\dot{m}_{rl[cont][E-ACC]}$ ceases; and the two-phase, liquid-vapour path to the accumulator is opened, so $\dot{m}_{rv[E-ACC]}$ begins. Thus the module first de-pressurises through this liquid-vapour path. Once this de-pressurisation is complete, the feed of cold circulating liquid from the pumper drum $\dot{m}_{rl[PD-E]}$ begins. A resulting liquid outflow $\dot{m}_{rl[E-ACC]}$ also begins after $\dot{m}_{rl[PD-E]}$ starts. The re-cooling sub-period is illustrated in the timing

diagram of Figure 3.2 by the dashed square across the trace of Module 2 extending from $(t_2 - t_3)$ of Module 2.

Referring to Figure 8.6 above, the energy rate balance equation for the control volume is the same as in equation (10) above. Neglecting changes in kinetic and potential energies, noting that there is no shaft work \dot{W}_{cv} , and naming the individual mass flows,

$$\begin{aligned} dE_{cv}/dt = & \dot{Q}_{cv} + \dot{m}_{r[PD-E]}h_{r[PD]} - \dot{m}_{rv[E-ACC]}h_{rv}(P_{r[E]}, T_{r[E-ACC]}) \\ & - \dot{m}_{r[E-ACC]}h_{r}(P_{r[E]}, T_{r[E-ACC]}) \end{aligned} \quad (35)$$

Here, the enthalpy of the incoming liquid refrigerant flow from the pumper drum, $h_{r[PD]}$, is assumed to be that of saturated liquid. The temperature of the two-phase flow at the outlet of the evaporator, due to the initial charge of liquid refrigerant, cannot be assumed to be at saturated evaporating temperature and therefore it is simply denoted as $T_{r[E-CC]}$.³⁷

Integrating over a time interval $(t_3 - t_2)$ for a complete re-cooling of the module to ice-building temperature, and justifiably assuming, over this interval, that the enthalpy at the inlet $h_{r[PD]}$ is constant and that Q_{cv} is negligible,³⁸

$$\begin{aligned} \Delta E_{cv} = & \Delta m_{r[PD-E]}h_{r[PD]} \\ & - \int_{t_2}^{t_3} [\dot{m}_{rv[E-ACC]}h_{rv}(P_{r[E]}, T_{r[E-ACC]}) + \dot{m}_{r[E-ACC]}h_{r}(P_{r[E]}, T_{r[E-ACC]})] \cdot dt \end{aligned} \quad (36)$$

Here, $\dot{m}_{rv[E-ACC]}$ includes the harvesting gas that is vented to the accumulator as well as the vapour component at the outlet of the evaporator resulting from the initial charge of cold liquid refrigerant from the pumper drum $\dot{m}_{r[PD-E]}$. Both these mass flows occur at the beginning of the re-cooling sub-period.

³⁷ $T_{r[E-CC]}$ is distinguished from $T_{r[E-CC]}$ defined in Section 8.2.1 above.

³⁸ That is, heat exchange between the control volume and its surroundings is negligible over this time interval, and no water has begun to flow over the plates.

Considering just the complete re-cooling of the module to ice-building temperature at the end of this re-cooling, assuming that the module has reverted to (ice-building) evaporating temperature $T_{\text{sat}}(P_{r[E]build})$, with a mixture of saturated liquid and vapour inside it, also at $T_{\text{sat}}(P_{r[E]build})$, then the final internal energy of the module is:

$$U_3 = U_{s[E]} [T_{\text{sat}}(P_{r[E]build})] + (m_{rl[E]})_{(t3)} u_{rl}(P_{r[E]build}) + (m_{rv[E]})_{(t3)} u_{rv}(P_{r[E]build}) \quad (37)$$

where $V_{[E]}$, the known internal volume of the module, is occupied according to:

$$V_{[E]} = (m_{rl[E]})_{(t3)} v_{rl}(P_{r[E]build}) + (m_{rv[E]})_{(t3)} v_{rv}(P_{r[E]build}) \quad (38)$$

Now, $\Delta E_{cv} = U_3 - U_2$, and hence from equations (26), (27) and (36), the control volume energy balance over the re-cooling period is:

$$\begin{aligned} & -\Delta U_{s[E]} + (m_{rl[E]})_{(t3)} u_{rl}(P_{r[E]build}) + (m_{rv[E]})_{(t3)} u_{rv}(P_{r[E]build}) \\ & - (m_{rl,trap[E]})_{(t2)} u_{rl}(P_{r[E]har}) - (m_{rv,trap[E]})_{(t2)} u_{rv}(P_{r[E]har}) \\ & = \Delta m_{rl[PD-E]} h_{rl[PD]} \\ & - \int_{t_2}^{t_3} [\dot{m}_{rv[E-ACC]} h_{rv}(P_{r[E]}, T_{r[E-ACC]}) + \dot{m}_{rl[E-ACC]} h_{rl}(P_{r[E]}, T_{r[E-ACC]})] \cdot dt \end{aligned} \quad (39)$$

where $-\Delta U_{s[E]}$ is simply the reverse of $\Delta U_{s[E]}$ in equation (25).

Predicting the Unavoidable URD of Re-cooling the Mass of Liquid Trapped behind the Level Regulating Valve at the Beginning of the Re-Cooling Sub-Period

The level-regulating valve at the bottom of the evaporator allows condensed liquid refrigerant during the warming sub-period to return to the accumulator. However, at the end of the warming sub-period some warm ammonia (refrigerant) liquid will be trapped behind the level-regulating valve and must be re-cooled to ice building temperature $T_{r[E]build}$.

After discussion with Rankin⁽¹⁴⁾, who confirmed that most if not all the liquid is vented to the accumulator prior to harvesting, it is assumed that the trapped liquid occupies approximately 5 percent of the internal volume of the module.³⁹ This assumption is based on the investigation of Bailey-McEwan⁽¹²⁾ (his page 63).

This trapped liquid is denoted as $m_{rl.trap[E](t2)}$ in equation (26) above, and the demand of re-cooling this liquid at the evaporator is:

$$\Delta H_{rl.trap[E]} = -m_{rl.trap[E](t2)} (h_{rl}(T_{r[E]har}) - h_{rl}(T_{r[E]build})) \quad (40)$$

Predicting the URD of Re-cooling the Mass of Vapour Vented to the Accumulator at the Beginning of the Re-Cooling Sub-Period

At the beginning of the re-cooling sub-period, the warm harvesting vapour that is trapped in the evaporator is vented, through the liquid-vapour path, to the accumulator and must be re-cooled to accumulator temperature. This URD is also the final term in Q_{lost} included in the investigation of Lorentzen and Baglo⁽⁶⁾ and is the ‘loss’ of gas due to venting to the accumulator. This vapour is assumed to occupy 95 percent of the internal volume of the evaporator, due to the assumption made above that the liquid trapped behind the level regulating control valve occupies the remaining 5 percent⁴⁰. The mass of vapour remaining inside the plates, $m_{rv.trap[E](t2)}$ (from equation (27)) at the beginning of the re-cooling sub-period is predicted as follows:

$$m_{rv.trap[E](t2)} = \frac{0,95V_{[E]}}{v_{rv}(P_{r.har})} \quad (41)$$

The trapped gas is vented to the accumulator, and therefore the URD associated with re-cooling this warm gas should strictly be seen at the accumulator. However

³⁹ The sensitivity analysis that justifies this assumption is shown in Appendix A10.2, where varying the volume occupied by liquid at the beginning of the re-cooling sub-period from 0-5 % of the internal volume of the module results in a change in total percentage URD of total refrigeration demand for the CGPS of 0,18 %.

⁴⁰ Based on the sensitivity analysis of Appendix A10.2 mentioned in the previous footnote.

$m_{rv.trap[E](t2)}$ returns to the accumulator via the liquid-vapour path and therefore mixes with the return liquid-vapour mixture from the other seven modules that are building ice. In re-cooling this trapped gas, a slight amount of the returning liquid will boil before it enters the accumulator. Nonetheless, the re-cooling of the trapped vapour takes place simultaneously with that of the trapped liquid, so it is convenient to consider them simultaneously. This URD is therefore assumed to be seen where it originates i.e. at the evaporator during the re-cooling sub-period and is predicted as:

$$\Delta H_{rv.trap[E]} = -m_{rv.trap[E](t2)} (h_{rv}(T_{r.har}) - h_{rv}(T_{r[ACC]})) \quad (42)$$

Unavoidable URDs at the Evaporator During the Re-Cooling Sub-Period

The URDs seen by the evaporator during the re-cooling sub-period are:

- (i) The re-cooling of the evaporator plates and their inlet and outlet manifolds:

$$\Delta H_{r.s[E]} = -\Delta U_{s[E]} = -m_{s[E]} c_s (T_{r[E]build} [T_{sat}(P_{r[E]har}) - T_{sat}(P_{r[E]build})]) \quad (43)$$

As mentioned in Section 2.1.3, all URDs manifest themselves as commensurate quantities of refrigerant vapour arriving at the accumulator, and hence at the compressor inlet to be compressed. Therefore, although the URD of re-cooling the evaporator steel (as well as that of the pumper drum and accumulator described in later sections) arises due to a change in internal energy of the steel and not as a result of an enthalpy change of refrigerant, it is eventually re-cooled through a portion of refrigerant boiling to vapour. Therefore all URDs *not* associated with heat exchange across a control volume are denoted as ΔH_r , indicating an enthalpy gain of flowing refrigerant.

- (ii) The re-cooling of the liquid trapped behind the level regulating control valve:

$$\Delta H_{rl.trap[E]} = -m_{rl.trap[E](t2)} (h_{rl}(T_{r[E]har}) - h_{rl}(T_{r[E]build})) \quad (44)$$

- (iii) The re-cooling of the vapour trapped inside the evaporator modules at the beginning of the re-cooling sub-period:

$$\Delta H_{rv.trap[E]} = -m_{rv.trap[E](t2)} (h_{rv}(T_{r[E]har}) - h_{rv}(T_{r[ACC]})) \quad (45)$$

8.3. Control Volume Energy Balances to Predict the URDs at the Accumulator

The control volume below is relevant for the entire ice building and harvesting cycle denoted by the red dashed block in the timing diagram of Figure 3.1, comprising the time $(t_4 - t_5)$ for Module 2.

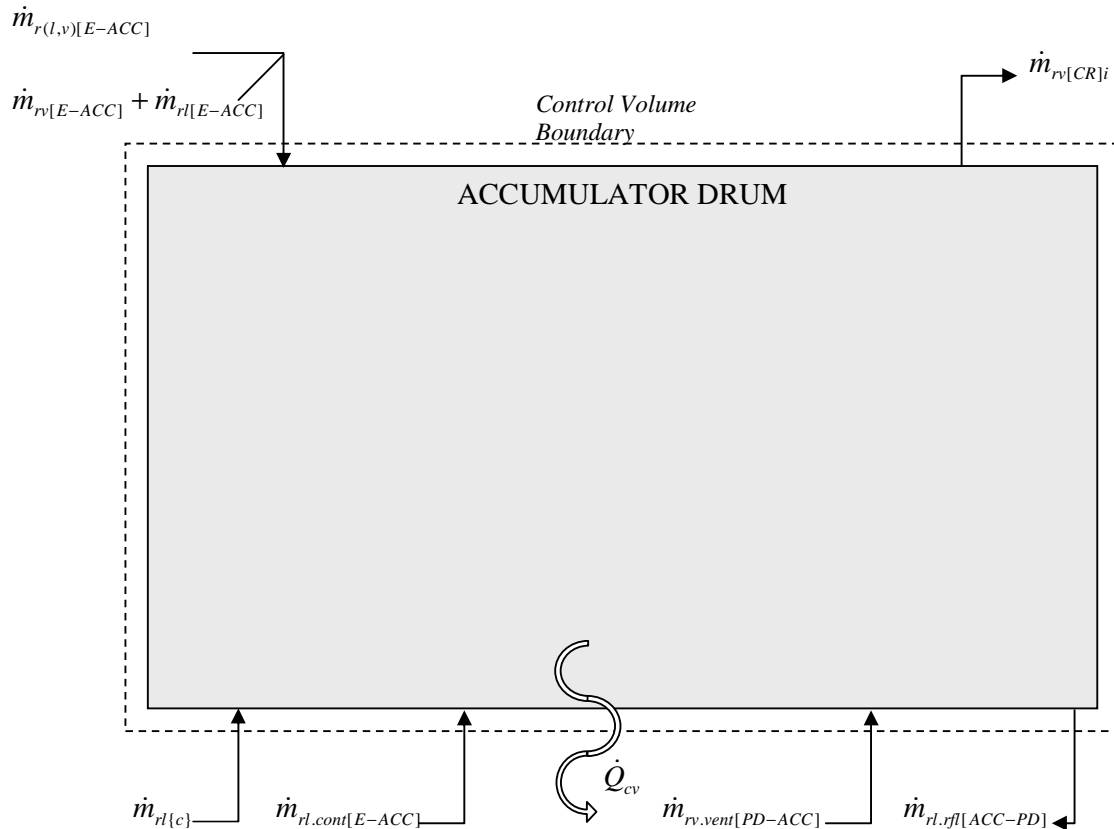


Figure 8.7 Control Volume: Accumulator Drum

The energy rate balance equation for Figure 8.7's control volume is the same as equation (10) above.

Neglecting changes in kinetic and potential energies, noting that there is no shaft work \dot{W}_{cv} , naming the individual mass flows, and justifiably assuming that the liquid refrigerant in the accumulator is saturated,

$$\begin{aligned}
dE_{cv}/dt = & \dot{Q}_{cv} - \dot{m}_{rl,rfl[ACC-PD]} h_{rl}(P_{r[ACC]}) + \dot{m}_{r(l,v)[E-ACC]} h_{r(l,v)}(T_{r[E]build}, x_{r[E]build}) \\
& + \dot{m}_{rl\{c\}} h_{rl}(P_{r[E]har}, T_{rl\{c\}}) + \dot{m}_{rl,cont[E-ACC]} h_{rl}(P_{r[E]har}, T_{rl[E-ACC]}) + \\
& \dot{m}_{rv[E-ACC]} h_{rv}(P_{r[E]}, T_{r[E-ACC]}) + \dot{m}_{rl[E-ACC]} h_{rl}(P_{r[E]}, T_{r[E-ACC]}) \\
& + \dot{m}_{rv,vent[PD-ACC]} h_{rv}(P_{r[PD]}) - \dot{m}_{rv[CR]i} h_{rv}(P_{r[ACC]})
\end{aligned} \tag{46}$$

Where $\dot{m}_{rl,rfl[ACC-PD]}$ is the flow rate of liquid that refills the filling pumper drum, $\dot{m}_{rl\{c\}}$ and $\dot{m}_{rl,cont[E-ACC]}$ are the liquid condensed and expelled respectively from one module during the warming sub-period as defined in Section 8.2.1 above, and $\dot{m}_{rv[CR]i}$ is the mass flow to the inlet of the compressor. The remaining variables are defined below.

Referring to the timing diagram of Figure 3.1, the mass flow $\dot{m}_{rl,cont[E-ACC]}$ of the remaining liquid in the evaporator that is expelled to the accumulator at the beginning of the warming sub-period, and that due to the harvesting gas in another module venting to the accumulator at the beginning of the re-cooling sub-period, $\dot{m}_{rv[E-ACC]}$, do not overlap (from Table 3.1 there is a 22.5 second time lapse between the beginnings of these two⁴¹). However, if the time period evaluated is that of the entire ice building and shedding cycle, then all the mass flows that occur at the accumulator during this cycle can be evaluated.

Integrating over the time interval ($t_5 - t_4$) of a complete ice building and harvesting cycle of one module, and justifiably assuming the enthalpies of (i) the liquid refrigerant leaving the accumulator, and (ii) the liquid refrigerant expelled from each evaporator at the beginning of its warming sub-period, to be constant over the periods where these processes occur,⁴² and that Q_{cv} is negligible,

⁴¹ With the venting occurring first.

⁴² Those enthalpy flows whose properties (pressure, temperature, quality, etc.) are not constant over the periods where they occur within a complete ice-building and harvesting cycle are represented by definite integrals over ($t_5 - t_4$).

$$\begin{aligned}
\Delta E_{cv} = & -\Delta m_{r.l.rf[ACC-PD]} h_{rl}(P_{r[ACC]}) + \int_{t_4}^{t_5} [\dot{m}_{r(l,v)[E-ACC]} h_{r(l,v)}(T_{r[E]build}, X_{r[E]build})] dt \\
& + \left[\int_{t_4}^{t_5} \dot{m}_{rl\{c\}} h_{rl}(P_{r[E]har}, T_{rl\{c\}}) \right] dt + \left[\int_{t_4}^{t_5} \dot{m}_{rl.cont[E-ACC]} h_{rl}(P_{r[E]har}, T_{rl[E-ACC]}) \right] dt + \\
& \int_{t_4}^{t_5} [\dot{m}_{rv[E-ACC]} h_{rv}(P_{r[E]}, T_{r[E-ACC]})] dt + \int_{t_4}^{t_5} [\dot{m}_{rl[E-ACC]} h_{rl}(P_{r[E]}, T_{r[E-ACC]})] dt \\
& + \left[\int_{t_4}^{t_5} \dot{m}_{rv.vent[PD-ACC]} h_{rv}(P_{r[PD]}) \right] dt - \int_{t_4}^{t_5} [\dot{m}_{rv[CR]i} h_{rv}(P_{r[ACC]})] dt
\end{aligned} \tag{47}$$

Where the term

$$\int_{t_4}^{t_5} [\dot{m}_{rv[E-ACC]} h_{rv}(P_{r[E]}, T_{r[E-ACC]})] dt + \int_{t_4}^{t_5} [\dot{m}_{rl[E-ACC]} h_{rl}(P_{r[E]}, T_{r[E-ACC]})] dt$$

is comprised of the following liquid and vapour mass flows from the evaporator:

1. The vapour vented to the accumulator at the beginning of the re-cooling sub-period, when the evaporator de-pressurises.⁴³
2. The two-phase component of incoming refrigerant from the evaporator due to the initial charge from the [pumping] pumper drum that enters evaporator as soon as it has de-pressurised, as defined in Section 8.2.2 above. Some of the liquid, though, evaporates in re-cooling the evaporator and its prior refrigerant content down to ice-building temperature. The liquid component is denoted as: $\int_{t_4}^{t_5} [\dot{m}_{rl[E-ACC]} h_{rl}(P_{r[E]}, T_{r[E-ACC]})] dt$, where, due to the initial temperature of the evaporator module, it cannot be

⁴³ As mentioned above, in reality, the incoming vapour from the evaporator module after harvesting will mix with the incoming two-phase mixture from the other 7 modules that are at ice-building temperature, effectively annulling its heating effect on the accumulator. In re-cooling this trapped gas, a slight amount of the returning liquid will boil before it enters the accumulator. Nonetheless, the URD of re-cooling this vapour is assumed to be seen where it originates i.e. at the evaporator during the re-cooling sub-period

assumed that the enthalpy at the outlet due to this initial charge is at saturated evaporating conditions.⁴⁴

And where the variable

$\int_{t_4}^{t_5} [\dot{m}_{rv,vent[PD-ACC]} h_{rv}(P_{r[PD]})] \cdot dt$ is comprised of the following vapour mass flows

from the pumper drums:

1. The flash gas vapour from the pumping pumper drum that is vented at the end of its pumping period.
2. The vapour from the filling pumper drum that is vented to the accumulator as it is filled with liquid from the accumulator.

And where the variable $\int_{t_4}^{t_5} [\dot{m}_{r(l,v)[E-ACC]} h_{r(l,v)}(T_{r[E]build}, x_{r[E]o})] \cdot dt$ is the two-phase

mixture returning from the 7 evaporator modules that are building ice at any one time.

Representing ΔE_{cv} in more detail as the sum $\sum(\Delta E)_{cv}$ of the internal energy changes inside the control volume,

$$\sum(\Delta E)_{cv} = \Delta U_{s[ACC]} + \Delta U_{rl[ACC]} + \Delta U_{rv[ACC]} \quad (48)$$

Over a complete ice-building and harvesting cycle, $\sum(\Delta E)_{cv} \approx 0$. Therefore, to include the changes in internal energy at the accumulator, it is useful to consider the period during which harvesting gas is vented from one module (at the beginning of its re-cooling sub-period), and 22.5 seconds later when the neighbouring (next) module expels cold liquid refrigerant (at the beginning of its warming sub-period). This period is referred to as the “transient period” and is denoted by the pink rectangle in the timing diagram of Figure 3.2 above, extending from when Module 3 vents its harvesting gas to when Module 4 expels its cold liquid refrigerant. Included in the “transient period” is the changeover

⁴⁴ This incoming two-phase flow is minor and would also be sufficiently cooled to accumulator temperature in the liquid-vapour path before it reaches the accumulator.

period where pumper drum 1 vents its high pressure gas to the accumulator and pumper drum 2 initiates its pressurization. Let the beginning and end of this transient period be denoted by times t_6 ⁴⁵ and t_7 . The internal energy of the accumulator at the end of a transient period is:

$$U_7 = U_{s[ACC]}(T_{heat[ACC]}) + (m_{rl[ACC]})_{(t_7)} u_{rl}(T_{r[ACC]}) + (m_{rv[ACC]})_{(t_7)} u_{rv}(T_{r[ACC]}) \quad (49)$$

$$\text{where } V_{[ACC]} = (m_{rl[ACC]})_{(t_7)} v_{rl}(T_{r[ACC]}) + (m_{rv[ACC]})_{(t_7)} v_{rv}(T_{r[ACC]}) \quad (49b)$$

and $V_{[ACC]}$ is the internal volume of the accumulator. $T_{heat[ACC]}$ is the temperature that the accumulator steel is heated to by the incoming refrigerant vapour vented from the [pumping] pumper drum at the end of its pumping process.⁴⁶

The initial internal energy of the accumulator, at the beginning of the transient period, is:

$$U_6 = U_{s[ACC](t_6)}(T_{r[ACC]}) + (m_{rl[ACC]})_{(t_6)} u_{rl}(T_{r[ACC]}) + (m_{rv[ACC]})_{(t_6)} u_{rv}(T_{r[ACC]}) \quad (50)$$

where it is assumed that at the start of every transient period, the accumulator's refrigerant liquid and vapour are saturated and in equilibrium, and that the accumulator's steel is at the corresponding temperature $(T_{r[ACC]})_{(t_6)}$.

Now, over the transient period, $\Delta E_{cv} = U_7 - U_6$, and hence:

$$\begin{aligned} & U_{s[ACC]}(T_{heat[ACC]}) - U_{s[ACC](t_6)}(T_{r[ACC]}) + (m_{rl[ACC]})_{(t_7)} u_{rl}(T_{r[ACC]}) \\ & - (m_{rl[ACC]})_{(t_6)} u_{rl}(T_{r[ACC]}) + (m_{rv[ACC]})_{(t_7)} u_{rv}(T_{r[ACC]}) - (m_{rv[ACC]})_{(t_6)} u_{rv}(T_{r[ACC]}) \end{aligned}$$

⁴⁵ That is, it is assumed that a "transient period" starts at time t_6 .

⁴⁶ The assumption that $T_{heat[ACC]}$ is due to the vented gas from the [pumping] pumper drum is justified in Section 8.7.1 below.

$$\begin{aligned}
&= -\Delta m_{rl,rfl[ACC-PD]} h_{rl}(P_{r[ACC]}) + \int_{t_6}^{t_7} [\dot{m}_{r(l,v)[E-ACC]} h_{r(l,v)}(T_{r[E]build}, x_{r[E]build})] dt \\
&+ \left[\int_{t_6}^{t_7} \dot{m}_{rl\{c\}} h_{rl}(P_{r[E]har}, T_{rl\{c\}}) \right] dt + \left[\int_{t_6}^{t_7} \dot{m}_{rl,cont[E-ACC]} h_{rl}(P_{r[E]har}, T_{rl[E-ACC]}) \right] dt + \\
&\int_{t_6}^{t_7} [\dot{m}_{rv[E-ACC]} h_{rv}(P_{r[E]}, T_{r[E-ACC]})] dt + \int_{t_6}^{t_7} [\dot{m}_{rl[E-ACC]} h_{rl}(P_{r[E]}, T_{r[E-ACC]})] dt \\
&+ \left[\int_{t_6}^{t_7} \dot{m}_{rv,vent[PD-ACC]} h_{rv}(P_{r[PD]}) \right] dt - \int_{t_6}^{t_7} [\dot{m}_{rv[CR]i} h_{rv}(P_{r[ACC]})] dt
\end{aligned} \tag{51}$$

8.3.1 URDs at the Accumulator during the Transient Period

The URDs specific to the “transient period” are that of re-cooling the steel of the accumulator and the vented pressurising gas after each pumping period at the [pumping] pumper drum. However, as described in Section 7.2.3, both these URDs are *inherent* in that they would have been generated had the minor flow of refrigerant required to pressurise the pumper drum expanded, in one step, all the way from condensed liquid receiver pressure to accumulator pressure. These URDs are nonetheless addressed here, because predicting them using test data from the CGPS allows for the same URDs to be predicted for the HGPS - where they become *avoidable* URDs⁴⁷. Re-cooling the vapour trapped inside the evaporator modules at the beginning of the re-cooling sub-period as well as re-cooling the liquid refrigerant expelled to the accumulator at the beginning of the warming sub-period are not specific to the “transient” period (i.e. they occur continuously throughout the ice making cycle) and are addressed in equations (45) and (54) respectively.

During a complete ice building and shedding period of one module (15 minutes), each pumper drum is pressurised 3 times and therefore vents 3 times, as shown in the pumping schedule of the timing diagram of Figure 3.1.

⁴⁷ Due to the extra mass flow rate of hot gas required to pressurize the pumper drum, as shown in Figure 7.1 above.

The maximum temperature rise of the accumulator steel $T_{heat[ACC]}$ was measured at the ERPM plant (point T3 of Figure A1.1). The temperature change over time was recorded and is presented in Figure 8.8 below, where six temperature peaks occur over the recorded 30 minute time interval.

From Figure 8.8, the first three temperature peaks occur approximately every 150-170 seconds, corresponding to the 130 second pumping period and 20 second changeover period (during which the [pumping] pumper drum vents its gas to the accumulator), defined in Table 3.1 above. The temperature peaks from 500 seconds onward do not however correspond with the [pumping] pumper drum venting periods; for unknown reasons. Therefore, only the first three peaks of Figure 8.8 are regarded as accurately measuring the change in temperature at the accumulator during the venting period of the [pumping] pumper drum. Following the time period of these first three temperature peaks, which as mentioned above, correspond with the venting period of the [pumping] pumper drum, the change in temperature at the pumper drum is conservatively assumed to occur six times per ice building and shedding cycle (15 minutes), corresponding with the three venting periods of each pumper drum in the corresponding time.

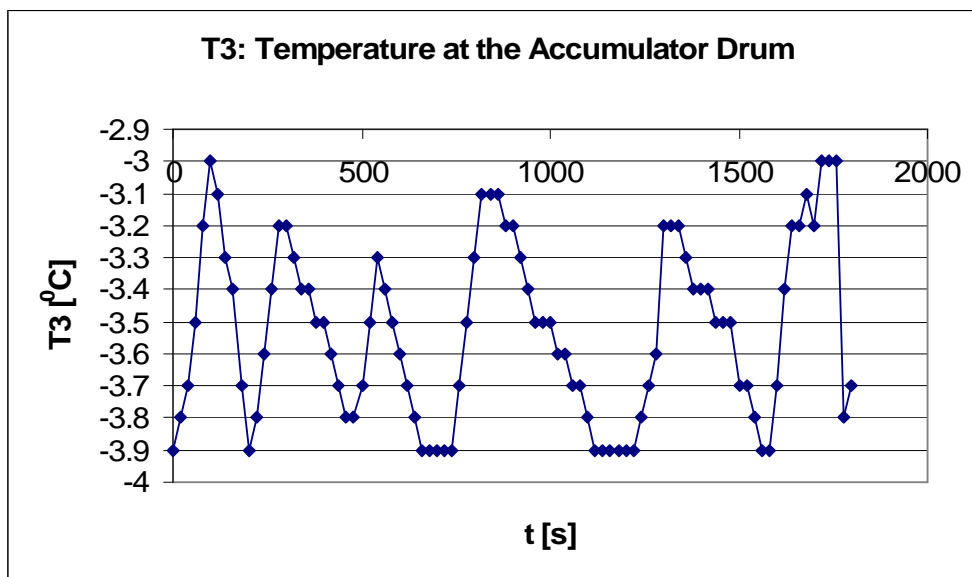


Figure 8.8 Temperature at the accumulator drum for the first test at the ERPM plant

Finally from Figure 8.8 above, the maximum measured temperature change is 0,9 °C. Therefore for the two pumper drums of Unit 5, the *inherent* URD of re-cooling the accumulator per ice building and shedding cycle is:

$$\Delta\hat{H}_{r,s[ACC]} = -m_{s[ACC]}c_s(T_{r[ACC]})(T_{heat[ACC]} - T_{r[ACC]}) \times 3 \times 2 \quad (52)$$

where $T_{heat[ACC]} - T_{r[ACC]}$ is equal to 0,9 °C for the CGPS.

8.3.2 URDs at the Accumulator during the Complete Ice Building and Shedding Cycle of One Module

Unavoidable URDs at the accumulator over the entire ice building and shedding period of one module include⁴⁸:

1. Re-cooling the liquid condensed during the warming sub-period of the module:

$$\Delta H_{rl\{c\}} = -m_{rl\{c\}}(h_{rl}(P_{r[E]har}, \bar{T}_{rl\{c\}}) - h_{rl}(P_{r[ACC]})) \quad (53)$$

As mentioned above, for the purposes of this investigation the mean temperature of the condensed liquid $\bar{T}_{rl\{c\}}$ is assumed to be saturation temperature at harvesting pressure $T_{sat}(P_{r[E]har})$.

2. Re-cooling the liquid refrigerant expelled to the accumulator at the beginning of the warming sub-period of the module:

$$\Delta H_{rl.cont[E-ACC]} = -\Delta m_{rl.cont[E-ACC]}(h_{rl}(P_{r[E]har}, T_{rl[E-ACC]}) - h_{rl}(P_{r[ACC]})) \quad (54)$$

Inherent URDs at the accumulator over the entire ice building and shedding period of one module include

3. Re-cooling the gas vented from the pumping pumper drum. Each pumper drum has level control sensors near its top and bottom as shown in the figure below.

⁴⁸ As these URDs are for one module, over the entire ice building and shedding cycle of one module (15 minutes) the accumulator sees eight times the URDs listed in 1. and 2. below.

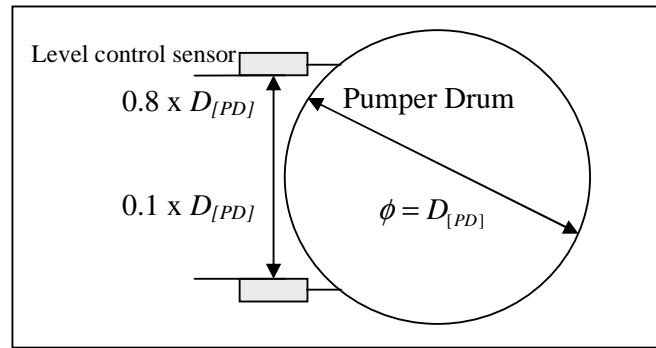


Figure 8.9 Diagram of the pumper drum showing level control sensors

During the filling period, the drum is filled with liquid refrigerant by the accumulator to $0,8 \times D_{[PD]}$, and during the pumping period, pumps its contents out until the liquid level sensor registers a depth of liquid at $0,1 \times D_{[PD]}$. The remainder of the volume of the pumper drum is filled with pressurizing gas, which must be vented to the accumulator at the end of its pumping period. The volume occupied by this gas is predicted in Appendix A8, and the *inherent* URD of re-cooling this volume of gas is:

$$\Delta \widehat{H}_{rv.vent[(PD+)-ACC]} = -m_{rv.vent[(PD+)-ACC]} (h_{rv}(P_{r[PD+]}) - h_{rv}(P_{r[ACC]})) \times 3 \times 2 \quad (55)$$

where the subscript $[PD+]$ denotes pressurised [pumping] pumper drum conditions,⁴⁹ the mass flow of gas is denoted $\dot{m}_{rv.vent[(PD+)-ACC]}$, and it is conservatively assumed that the vapour is at saturated conditions at the pumping pressure⁵⁰ $h_{rv}(P_{r[PD+]})$. From the timing diagram and pumping schedule of Figure 3.1, this URD occurs 3 times per pumper drum over the entire ice building and shedding cycle of one module.

4. Re-cooling the gas vented from the filling pumper drum. During the filling period, vapour is continuously vented from the filling pumper drum to the accumulator. The minor difference in pressure results in the *inherent* URD of re-cooling this vapour to accumulator temperature:

⁴⁹ Conversely, the subscript $[PD-]$ denotes [filling] pumper drum conditions as shown in 4. below.

⁵⁰ Measured at the plant as 200 kPa above filling pumper drum pressure.

$$\Delta \widehat{H}_{rv.vent[(PD-)-ACC]} = -\dot{m}_{rv.vent[(PD-)-ACC]} (h_{rv}(P_{r[PD-]}) - h_{rv}(P_{r[ACC]})) \times 3 \times 2 \quad (56)$$

where the subscript $[PD-]$ denotes [filling] pumper drum conditions, the mass flow of gas is denoted $\dot{m}_{rv.vent[(PD-)-ACC]}$, and it is justifiably assumed that the vapour is at saturated conditions at the filling pressure $h_{rv}(P_{r[PD-]})$. This URD occurs 3 times per pumper drum over the entire ice building and shedding cycle of one module.

8.4. Control Volume Energy Balance to Predict the URDs at the Filling Pumper Drum

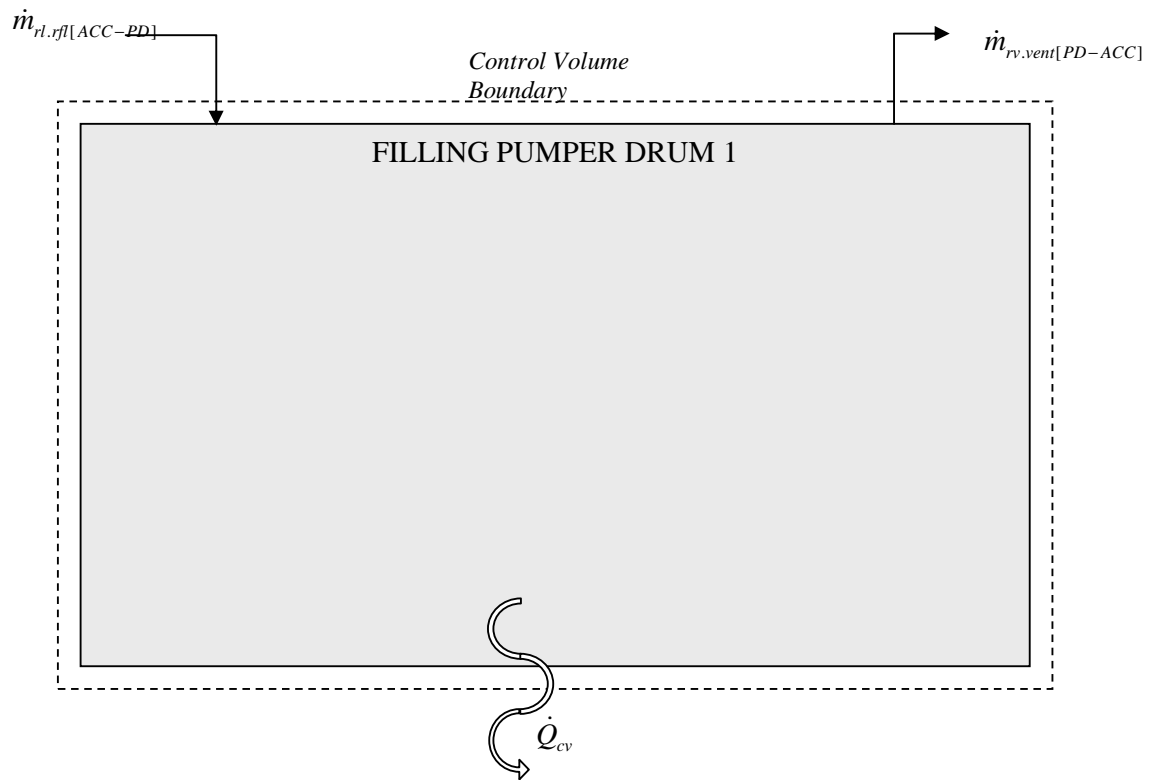


Figure 8.10 Control Volume: Pumper Drum {1} When Filling

At the end of the pumping period, the gas at pressurised pumping temperature and pressure in the pumper drum is vented to the accumulator. This is represented in

the dark pink rectangle of the timing diagram of Figure 3.3, which spans $(t_8 - t_9)$, a complete filling period of pumper drum 1. Assuming that as the vapour is vented, the control valve to refill the pumper drum with liquid is open, then the energy rate balance equation for Figure 8.10's control volume during this transient period is the same as equation (10) above.

Neglecting changes in kinetic and potential energies, noting that there is no shaft work \dot{W}_{cv} , and naming the individual mass flows,

$$dE_{cv}/dt = \dot{Q}_{cv} + \dot{m}_{rl,rf}[ACC-PD]h_{rl}(P_{r[ACC]}) - \dot{m}_{rv,vent}[PD-ACC]h_{rv}(P_{r[PD]}) \quad (57)$$

Integrating over the time interval $(t_8 - t_9)$ of a complete filling period, justifiably assuming the enthalpy $h_{rl}(P_{r[ACC]})$ to be constant over time, and that Q_{cv} is negligible,

$$\Delta E_{cv} = \Delta m_{rl,rf}[PD]h_{rl}(P_{r[ACC]}) - \int_{t_8}^{t_9} [\dot{m}_{rv,vent}[PD-ACC]h_{rv}(P_{r[PD]})]dt \quad (58)$$

Where the variable $\int_{t_8}^{t_9} [\dot{m}_{rv,vent}[PD-ACC]h_{rv}(P_{r[PD]})]dt$ is comprised of the following

vapour mass flows from the pumper drum 1:

1. The pressurising gas that is vented by de-pressurising at the end of its pumping period at t_8 . This mass flow of gas is denoted $\dot{m}_{rv,vent}[(PD+)-ACC]$, and at pumping pressure has an enthalpy of $h_{rv}(P_{r[PD+]})$.
2. Once de-pressurised, the vapour that is vented to the accumulator during the filling period. This mass flow of gas is denoted $\dot{m}_{rv,vent}[(PD-)-ACC]$ and at filling pressure has an enthalpy of $h_{rv}(P_{r[PD-]})$.

Representing ΔE_{cv} in more detail as the sum $\sum(\Delta E)_{cv}$ of the internal energy changes inside the control volume,

$$\sum(\Delta E)_{cv} = \Delta U_{s[PD]} + \Delta U_{rl[PD]} + \Delta U_{rv[PD]} \quad (59)$$

Then the final internal energy of the module is:

$$U_9 = U_{s[PD-](t_9)}(T_{r[PD]}) + (m_{rl[PD-]}(t_9))u_{rl}(T_{r[PD-]}) + (m_{rv[PD-]}(t_9))u_{rv}(T_{r[PD-]}) \quad (60)$$

where $V_{[PD]} = (m_{r[PD-]}(t_9) v_{rl}(T_{r[PD-]})) + (m_{rv[PD]}(t_9) v_{rv}(t_9) (T_{r[PD-]}))$ and $V_{[PD]}$ is the internal volume of the pumper drum. The initial internal energy of the module is:

$$U_8 = U_{s[PD+]}(T_{heat[PD+]}) + (m_{r[PD+]}(t_8) u_{rl}(\bar{T}_{r[PD+]}) + (m_{rv[PD+]}(t_8) u_{rv}(\bar{T}_{r[PD+]}) \quad (61)$$

$T_{heat[PD+]}$ is the temperature that the pumper drum is heated to by the incoming refrigerant liquid and vapour (during pumping). The weighted average temperature of the contents of the pumper drum after the pumping process is denoted by $\bar{T}_{r[PD+]}$ and

Now, $\Delta E_{cv} = U_9 - U_8$. Once the pumper drum has re-cooled to filling temperature $T_{r[PD-]}$, temperatures of the refrigerant in the pumper drum and the pumper drum itself do not change during the filling period.

From equation (58), the rightmost integral, which includes the vented gas from both the filling and the pumping pumper drum, can be split into its two components. Once split, the integral representing these two masses transforms into the last two terms of equation (62) below, where the corresponding enthalpies $h_{rv}(P_{r[PD+]})$ and $h_{rv}(P_{r[PD-]})$ are justifiably assumed to be constant.

From equations (58), (60) and (61):

$$\begin{aligned} & U_{s[PD-](t_9)}(T_{r[PD-]}) - U_{s[PD+]}(T_{heat[PD]}) + (m_{r[PD-]}(t_9) u_{rl}(T_{r[PD-]}) - (m_{r[PD+]}(t_8) u_{rl}(\bar{T}_{r[PD+]}) \\ & + (m_{rv[PD-]}(t_9) u_{rv}(T_{r[PD-]}) - (m_{rv[PD+]}(t_8) u_{rv}(\bar{T}_{r[PD+]}) = \Delta m_{rl,rfl[ACC-PD]} h_{rl}(P_{r[ACC]}) \\ & - m_{rv,vent[(PD+)-ACC]} h_{rv}(P_{r[PD+]}) - m_{rv,vent[(PD-)-ACC]} h_{rv}(P_{r[PD-]}) \end{aligned} \quad (62)$$

8.4.1 URDs at the Filling Pumper Drum

The only URD at the pumper drum seen during the filling process is the re-cooling of the steel of the pumper drum, which is warmed during its pumping period. The rest of the URDs are seen at the accumulator and listed in Section 8.3.2 above. However, as described in Sections 7.2.3 and 8.3.1, for the CGPS, this URD is *inherent* in that it would have been generated had the minor flow of

refrigerant required to pressurise the pumper drum expanded, in one step, all the way from condensed liquid receiver pressure to accumulator pressure. This URD is nonetheless addressed here as it can be predicted using test data from the CGPS, and allows for the same URD to be predicted for the HGPS - where it is an *avoidable* URD⁵¹. The temperature of the pumper drum wall was measured at the ERPM plant (sensor T6 of Figure A1.1) and is plotted in Figure 8.11 below. From the timing diagram of Figure 3.1, pumper drum 1 undergoes 3 pumping periods every 15 minutes, and from Figure 8.11 below, the maximum temperature rise during pumping is 1°C above filling temperature.⁵²

The *inherent* URD of re-cooling the steel of the two pumper drums during the filling period, and for a complete ice making cycle of 15 minutes which comprises three filling periods per pumper drum, is:

$$\Delta\hat{H}_{r,s[PD]} = -m_{s[PD]}c_s(T_{r[PD-]})(T_{heat[PD]} - T_{r[PD-]}) \times 3 \times 2 \quad (63)$$

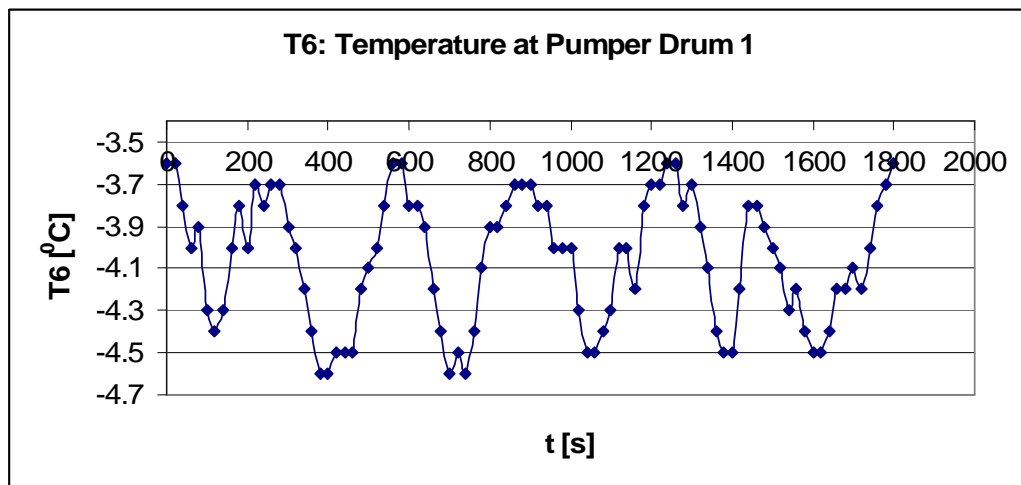


Figure 8.11 Wall temperature of pumper drum 1 for the second test at the ERPM plant

⁵¹ Due to the extra mass flow rate of hot gas required to pressurize the pumper drum, as shown in Figure 7.1 above.

⁵² The plot of Figure 8.11 is repeated in Appendix A6 as Figure A6.11.

8.4.2 URD of Re-Cooling the Upper Portion of Circulating Liquid at the Pumping Pumper Drum

The final *inherent* URD for the CGPS is that of re-cooling the upper portion of warmed liquid in the pumper drum. During the ice making period, cold flash gas throttled down from the expansion valve feeding the pumper drum (as well as a small portion of warm gas from the condensed liquid receiver to boost the pressure in the pumper drum to circulate a sufficient flow of liquid⁵³) is used to pump the liquid ammonia through the evaporator. The interaction of pressurising gas and colder liquid refrigerant in the pumper drum results in a major URD for any *hot* gas pumped system (HGPS), and is the first ‘loss’, or URD in the terminology of this investigation, included in predicting the total ‘refrigeration loss’ of the system by Lorentzen and Baglo⁽⁶⁾.

From Figure 8.9 above, and based on test data collected from the ERPM plant, the pumping pumper drum expels 95% of its volume of liquid to the evaporator in a time of 130 seconds. The upper portion of this liquid is heated by the incoming pressurising gas to $T_{rl.circ[PD-E]}$ (based on temperature measurements at sensing point T7 of Figure A1.1). This URD is not seen at the pumper drum, rather it is seen at the entrance to the evaporator. However, seeing that this URD arises at the pumper drum, it is considered here rather than in Section 8.2 above. Predicting $T_{rl.circ[PD-E]}$ from test data as well as the mass of liquid heated to this temperature $m_{rl.circ[PD-E]}$ is performed in Appendix A8.2.3. The *inherent* URD of re-cooling this portion of liquid is:

$$\Delta\hat{H}_{rl.circ[PD-E]} = -m_{rl.circ[PD-E]}(h_{rl}(T_{rl.circ[PD-E]}) - h_{rl}(T_{r[PD-]})) \quad (64)$$

Where it is assumed that the enthalpy of the upper portion of circulated liquid is initially at [filling] pumper drum temperature.

⁵³ This is necessary if the rate at which cold flash gas generated at the expansion valve is insufficient (which can occur if condensing temperature falls significantly below design value).

8.5. Total PRD and URD for the Cold Gas Pumped Arrangement Per Module

8.5.1. Total PRD Per Module for all Pumping Arrangements

The total PRD per module is identical for all pumping arrangements, and from equations (18) and (20), is:

$$\Sigma Q_{PRD} = Q_{PRD[E]} + Q_{PRD[PRC]} \quad (65)$$

8.5.2. Total URD Per Module for the Cold Gas Pumped Pumping Arrangement

All the URDs for the CGPS are either *unavoidable* and/or *inherent*. Summing the *unavoidable* URDs, the total URD *per module*, from equations (19), (40), (42), (43), (53), (54), and (56) is:

$$\begin{aligned} \Sigma \Delta H_{URD\{CGPS\}} = & Q_{URD[E]} + \Delta H_{r.s[E]} + \Delta H_{rl.trap[E]} + \Delta H_{rv.trap[E]} \\ & + \Delta H_{rl\{c\}} + \Delta H_{rl.cont[E-ACC]} \end{aligned} \quad (66)$$

8.6. Predicting the Average Recirculation Ratio and Compressor Work Input for the Operating Cold Gas Pumped System Per Module

8.6.1 Predicting the Average Recirculation Ratio for the Operating CGPS

From the control volume energy balance at the evaporators during ice building (Section 8.1 above), the enthalpy at the outlet of the evaporator is based on the average recirculation ratio, $\bar{x}_{r[E]o}$, which is the inverse of the quality of refrigerant. From equation (17) above:

$$\begin{aligned}
& \left(m_{r[E](t2)} - m_{r[E](t1)} \right) \mu_{rl} \left(T_{r[E]build} \right) + \left(m_{rv[E](t2)} - m_{rv[E](t1)} \right) \mu_{rv} \left(T_{r[E]build} \right) \\
& - m_{I,b} \left(-c_w T_{w[E]i} - h_{sf} + c_I \frac{(T_{r[E]build} + T_{I,o})}{2} \right) \\
& = \left| \Delta m_{r[PD-E]} h_{rl} \left(T_{r[E]} \right) - \Delta m_{r(l,v)[E-ACC]} h_{r(l,v)} \left(T_{r[E]}, \bar{x}_{r[E]o} \right) \right|_{build} \quad (17)
\end{aligned}$$

The first four terms of equation (17) above comprise the change in internal energy of the refrigerant. As mentioned in Section 8.2.1 above and based on the analysis presented in Appendix A2, it is conservatively assumed that each plate is filled by 30% of its inner volume with liquid ammonia⁵⁴ at the end of ice-building and at the beginning of the warming sub-period. If it is further assumed that the mass of liquid occupying the module at the beginning of the ice building period is negligible, then equation (17) simplifies to:

$$\begin{aligned}
& \left(m_{r[E](t2)} \right) \mu_{rl} \left(T_{r[E]build} \right) + \left(m_{rv[E](t2)} - m_{rv[E](t1)} \right) \mu_{rv} \left(T_{r[E]build} \right) \\
& - m_{I,b} \left(-c_w T_{w[E]i} - h_{sf} + c_I \frac{(T_{r[E]build} + T_{I,o})}{2} \right) \\
& = \left| \Delta m_{r[PD-E]} h_{rl} \left(T_{r[E]} \right) - \Delta m_{r(l,v)[E-ACC]} h_{r(l,v)} \left(T_{r[E]}, \bar{x}_{r[E]o} \right) \right|_{build} \quad (67)
\end{aligned}$$

Substituting into equation (67) the masses of the liquid and vapour in the module at the end of the ice-building period, equation (67) becomes:

$$\begin{aligned}
& 30n a_{[E]chl} L_{[E]} \left(0,3 \rho_{rl} \left(T_{r[E]build} \right) \mu_{rl} \left(T_{r[E]build} \right) + (1-0,7) \rho_{rv} \left(T_{r[E]build} \right) \mu_{rv} \left(T_{r[E]build} \right) \right) \\
& - m_{I,b} \left(-c_w T_{w[E]i} - h_{sf} + c_I \frac{(T_{r[E]build} + T_{I,o})}{2} \right) \\
& = \left| \Delta m_{r[PD-E]} h_{rl} \left(T_{r[E]} \right) - \Delta m_{r(l,v)[E-ACC]} h_{r(l,v)} \left(T_{r[E]}, \bar{x}_{r[E]o} \right) \right|_{build} \quad (68)
\end{aligned}$$

The changes in internal energy, represented by the masses of liquid and vapour in the module at the end of ice building, are accounted for in equation (68). The mass flow rate at the inlet to the evaporator $\dot{m}_{r[PD-E]}$ remains constant throughout the ice building period, and therefore the difference between the inlet and outlet ($\dot{m}_{r(l,v)[E-ACC]}$) mass flow rates is the rate of change of mass in the evaporator. This mass flow rate is predicted from a mass rate balance in Appendix A10.3 to be

⁵⁴ With the remaining volume occupied by refrigerant vapour at ice building temperature.

negligible compared to the inlet mass flow rate⁵⁵. Based on this assumption, and since the evaporating temperature is assumed to remain constant throughout the ice building period⁵⁶, the mass flow of refrigerant at the inlet and outlet of the evaporator are assumed to be identical, and consequently $\Delta m_{r[PD-E]} \approx \Delta m_{r[l,v][E-ACC]}$. Equation (68) thus simplifies to

$$30na_{[E]chl}L_{[E]} \left(0,3\rho_{rl}(T_{r[E]build})\mu_{rl}(T_{r[E]build}) + 0,3\rho_{rv}(T_{r[E]build})\mu_{rv}(T_{r[E]build}) \right) - m_{l,b} \left(-c_w T_{w[E]i} - h_{sf} + c_l \frac{(T_{r[E]build} + T_{l,o})}{2} \right) = \left| \Delta m_{r[PD-E]} \left(h_{rl}(T_{r[E]}) - h_{r(l,v)}(T_{r[E]}, \bar{x}_{r[E]o}) \right) \right|_{build} \quad (69)$$

The thickness of ice sheet delivered, from measurements at the ERPM plant, is approximately 5 mm (from Table A6.3 of Appendix A6). The thickness of ice built however includes a layer of ice that is subsequently melted during the warming sub-period. Both the thickness of the built ice layer and the melted ice layer are predicted from the heat transfer models during ice building and harvesting presented in Section 9. below.⁵⁷ An average built ice layer thickness of 6 mm is input into equation (8) above to obtain the mass of ice built during the ice building period $m_{l,b}$. Thus the only unknowns in equation (69) above are the enthalpy of the two-phase mixture at the outlet of the evaporator, which is based on the average recirculation ratio, and the mass of liquid pumped to and through the evaporator. By varying the average recirculation ratio $\bar{x}_{r[E]o}$ in equation (69) above between realistic limits, the mass flow rate of liquid refrigerant through the evaporators can therefore be predicted.

Based on Figure 8.9 and the analysis performed in Appendix A8, the mass flow rate of liquid pumped through to seven modules (with one module harvesting) can also be predicted from the change in liquid volume of the [pumping] pumper drum over the pumping period. This predicted mass flow rate, and subsequently, the mass pumped to and through the evaporators during ice building, is 0,30 %

⁵⁵ Appendix A10.3 predicts that the rate of change of mass contained within the control volume is 5,90% of the predicted mass flow rate at the inlet of the evaporator.

⁵⁶ i.e. After the re-cooling sub-period the evaporator returns to ice building temperature.

⁵⁷ From Table 9.2, the built ice sheet thickness varies from 5,84 – 6,67 mm based on the *practical* convective boiling heat transfer coefficients. From Table 9.3, the melted ice sheet thickness varies from 0,786 – 1,149 mm based on the *practical* convective condensing heat transfer coefficients.

smaller than $\Delta m_{r\{PD-E\}}$ predicted from equation (69) above- based on an average recirculation ratio $\bar{x}_{r\{E\}o}$ of approximately 5. Therefore, as there is sufficiently accurate agreement between the two methods of predicting the mass flow rate through the evaporator for the cold gas pumped arrangement, the average recirculation ratio is predicted as 5. Hereafter, for simplicity, the average recirculation ratio will be denoted as x_1 .

8.6.2 Predicting the Average Electrical and Mechanical Compressor Work Input for the Operating CGPS

Based on test data obtained from the ERPM plant and from Appendix A6 (Section A6.1), the electrical and mechanical work input into the compressor per module can be predicted:

$$\dot{W}_{[CR]\{CGPS\}elec} = 180,00 \text{ kW/module} \quad (70)$$

Assuming a compressor motor efficiency η_m of 96%, the mechanical power input of the compressor for the CGPS is:

$$\dot{W}_{[CR]\{CGPS\}mech} = \dot{W}_{[CR]\{CGPS\}elec} \eta_m = 172,80 \text{ kW/module} \quad (70b)$$

8.7. Total URD for the Hot Gas Pumped Arrangement Per Module

The more conventional hot gas pumped system uses a mass flow of warm gas from the condensed liquid receiver (at receiver temperature and pressure) to pressurise the pumper drum and circulate the refrigerant through the evaporator. Therefore, although it has the same type of URDs as the cold gas pumped system, the URDs occurring at the pumper drum and accumulator for the hot gas pumped system (HGPS) are larger due to the higher temperature of the pressurising gas in

the [pumping] pumper drum⁵⁸. Based on the simplified control-volume thermodynamic analysis described in Section 7.2.3, these URDs are also *avoidable*, as they arise due to the introduction of an *extra* mass flow of pressurising gas into the pumper drum. The harvesting process is identical for all arrangements, and so the *unavoidable* URDs associated with the warming and re-cooling sub-period at the evaporators remain the same. The *avoidable* URDs are therefore addressed where they occur.

8.7.1 URDs at the Accumulator for the HGPS

As mentioned in Section 8.3.1 above, the URD specific to the “transient period” is that of re-cooling the steel of the accumulator after each venting period at the pumping pumper drum. For the HGPS, this is an *avoidable* URD. During a complete ice building and shedding cycle of one module (15 minutes), each pumper drum is pressurised 3 times and therefore vents 3 times, as shown in the pumping schedule of Figure 3.1. On the basis of the predicted *inherent* URDs at the accumulator for the CGPS, the corresponding *avoidable* ones of the HGPS, and hence the temperature rise at the accumulator for this arrangement, can be predicted. It is recalled from Section 8.3.2 that the URDs seen at the accumulator for the CGPS over the entire ice building and shedding cycle of one module comprise of:

$$\Sigma \Delta H_{URD[ACC]\{CGPS\}} = \Delta H_{rl\{c\}} + \Delta H_{rl.com\{E-ACC\}} + \frac{\Delta \hat{H}_{rv.vent\{(PD+)\}-ACC\}}{8} + \frac{\Delta \hat{H}_{rv.vent\{(PD-)\}-ACC\}}{8} \quad (71)$$

As the comparison is performed per module, the URDs of re-cooling the vented gas from the pumper drum during venting and filling (equations (55) and (56) respectively) are divided by eight (modules). Referring to Figure 1.2, since the pumping pumper drum is filled with gas through the pressure reducing valve from the condensed liquid receiver, the venting gas will be at a higher temperature than

⁵⁸ Assuming that the dimensions of the pumper drums, accumulator and evaporator remain the same and that the only difference in operating pressures is due to the higher pressure of pressurising gas which now comes from the condensed liquid receiver.

that of the CGPS. Assuming that the level control sensors at the pumper drum regulate the mass of liquid pumped in the same manner and within the same time as the CGPS:

$$\Delta H_{rv.vent[(PD+)-ACC]\{HGPS\}} = -m_{rv.vent[(PD+)-ACC]\{HGPS\}}(h_{rv}(P_{r[REC]}) - h_{rv}(P_{r[ACC]})) \times 3 \times 2 \quad (72)$$

where the subscript *[REC]* denotes conditions at the condensed liquid receiver. This URD occurs 3 times per pumper drum over the entire ice building and shedding cycle of one module.

From the control volume at the accumulator drum of Figure 8.7, all the values of mass in-flows and out-flows are identical for the CGPS and HGPS except for that from the [pumping] pumper drum that is vented to the accumulator at the end of its pumping period. From the plotted temperatures at the accumulator for the CGPS of Figure 8.8, temperature peaks were observed to occur six times over the measured period of 1800 seconds. Although as mentioned in Section 8.3.1, the temperature gauge at this position was deemed inaccurate, the gauge was regarded as accurately predicting the *change* in temperature at the accumulator.

From the timing diagram of Figure 3.1, the staggered operation of all 8 modules of Unit 5 allows for maximum smoothing of load on the compressor, as well as evening out re-cooling loads at the accumulator. Of the four URDs seen at the accumulator during the entire ice building period, $\Delta H_{rl\{c\}}$, $\Delta H_{rl.com[E-ACC]}$, $\Delta \hat{H}_{rv.vent[(PD+)-ACC]\{HGPS\}}$, $\Delta \hat{H}_{rv.vent[(PD-)-ACC]}$, $\Delta H_{rl\{c\}}$ and $\Delta H_{rl.com[E-ACC]}$ occur 8 times per ice making cycle of 900 seconds, and so cannot be responsible for the three peaks in temperature observed during this period at the accumulator⁵⁹. $\Delta \hat{H}_{rv.vent[(PD-)-ACC]}$ is justifiably assumed to occur continuously throughout the ice making cycle⁶⁰, and so only $\Delta \hat{H}_{rv.vent[(PD+)-ACC]\{HGPS\}}$, which from Figure 3.1 occurs 6 times per ice making cycle, could possibly be

⁵⁹ From Figure 8.8.

⁶⁰ As filling takes place steadily whilst the other drum is pumping..

responsible for the changes in temperature at the accumulator⁶¹. Thus per module, the change in temperature at the accumulator for the HGPS, $T_{heat[ACC]\{HGPS\}} - T_{r[ACC]}$, is assumed to be predicted by the ratio of the URDs of re-cooling this vented pressurising gas for the HGPS and CGPS, multiplied by the change in temperature measured for the cold gas pumped arrangement, $T_{heat[ACC]} - T_{r[ACC]}$:

$$\left[T_{heat[ACC]\{HGPS\}} - T_{r[ACC]} \right] = \left[T_{heat[ACC]} - T_{r[ACC]} \right] \left[\frac{\Delta H_{rv.vent[(PD+)-ACC]\{HGPS\}}}{\Delta \hat{H}_{rv.vent[(PD+)-ACC]}} \right] \quad (73)$$

Finally, the URD of re-cooling the accumulator for the hot gas pumped arrangement is:

$$\Delta H_{r.s[ACC]\{HGPS\}} = -m_{s[ACC]} c_s (T_{r[ACC]}) (T_{heat[ACC]\{HGPS\}} - T_{r[ACC]}) \times 3 \times 2 \quad (74)$$

8.7.2 URDs at the Filling Pumper Drum for the HGPS

As mentioned in Section 8.4.1 above, the only URD at the pumper drum seen during the filling process is the re-cooling of the steel of this drum at the end of its pumping period.⁶² It is assumed that the URD of re-cooling the residual liquid that is left in the pumper drum at the end of its pumping process is included in the URD of re-cooling the vented pressurising gas to the accumulator (equation (72)), as well as that of re-cooling the steel of the pumper drum.

The URD of re-cooling the steel of the pumper drum during the filling period is:

$$\Delta H_{r.s[PD]\{HGPS\}} = -m_{s[PD]} c_s (T_{r[PD-]}) (T_{heat[PD]\{HGPS\}} - T_{r[PD-]}) \times 3 \times 2 \quad (75)$$

⁶¹ Although as mentioned in Section 8.3.1, the time period between temperature peaks for the last three peaks do not match up with the periods of the venting pumper drum. Thus only the first three peaks of Figure 8.8 are regarded as accurately measuring the change in temperature at the accumulator during the venting period of the [pumping] pumper drum

⁶² From the timing diagram of Figure 3.1, this occurs six times per ice building and shedding cycle of one module (15 minutes).

The pumping period for the HGPS is assumed to be identical to that of the CGPS, except that now gas at pressurized liquid receiver temperature is introduced into the [pumping] pumper drum. It is therefore assumed that the maximum temperature difference reached by the pumper drum $T_{heat[PD]\{HGPS\}} - T_{r[PD-]}$ is predicted by the ratio of pressurising inlet gas temperatures for the HGPS and the CGPS multiplied by the temperature difference measured at pumper drum 1 (Figure 8.11 above) for the cold gas operating plant. As the change in temperature is a measure of the energy gained by the pumper drum by sensible heat, it is justifiably assumed to be proportional to this ratio of pressurising gas temperatures.

$$T_{heat[PD]\{HGPS\}} - T_{r[PD-]} = (T_{heat[PD]} - T_{r[PD-]}) \left[\frac{T_{r[PD+]\{HGPS\}}}{T_{r[PD+]}} \right]^{63} \quad (76)$$

8.7.3 URD of Re-Cooling the Upper Portion of Circulating Liquid at the Pumping Pumper Drum for the HGPS

From Figure 8.9 above, and based on test data collected from the ERPM plant, the pumping pumper drum expels 95% of its volume of liquid to the evaporator in a time of 130 seconds. The upper portion of this liquid is heated by the incoming gas to $T_{rl.circ[PD-E]\{HGPS\}}$ which is predicted based on test data for the circulating temperature of the cold gas pumped arrangement $T_{rl.circ[PD-E]}$. Predicting the increased temperature for the HGPS as well as the mass of liquid heated to this temperature $m_{rl.circ[PD-E]\{HGPS\}}$ is performed in Appendix A8.2.4. The final URD of re-cooling this circulated liquid is:

$$\Delta H_{rl.circ[PD-E]\{HGPS\}} = -m_{rl.circ[PD-E]\{HGPS\}} (h_{rl}(P_{r[PD-]}, T_{rl.circ[PD-E]\{HGPS\}}) - h_{rl}(P_{r[PD-]})) \quad (77)$$

⁶³ $T_{r[PD+]}$ is saturated temperature at 200 kPa above filling pumper drum pressure for the CGPS, and $T_{r[PD+]\{HGPS\}}$ is saturated temperature at condensed liquid receiver pressure.

8.7.4 Total URD for the HGPS

Summing the URDs for the HGPS, and assuming that the URDs of re-cooling the steel of the accumulator and pumper drums, plus all gas vented from both drums to the accumulator, are shared equally amongst the eight modules, the total URD *per module* from equations (19), (40), (42), (43), (53), (54), (56), (72), (74), (75), and (77) is:

$$\begin{aligned}
 \Sigma \Delta H_{URD\{HGPS\}} = & Q_{URD[E]} + \Delta H_{r.s[E]} + \Delta H_{rl.trap[E]} + \Delta H_{rv.trap[E]} + \frac{\Delta H_{r.s[ACC]\{HGPS\}}}{8} \\
 & + \Delta H_{rl\{c\}} + \Delta H_{rl.cont[E-ACC]} + \frac{\Delta H_{rv.vent[(PD+)-ACC]\{HGPS\}}}{8} \quad (78) \\
 & + \frac{\Delta H_{rv.vent[(PD-)-ACC]}}{8} + \frac{\Delta H_{r.s[PD]\{HGPS\}}}{8} + \Delta H_{rl.circ[PD-E]\{HGPS\}}
 \end{aligned}$$

8.8. Total URD for the Mechanically Pumped Arrangement Per Module

For the mechanically pumped arrangement, the URDs due to pressurizing gas circulating the liquid in the pumper drum to the evaporators for the gas pumped arrangements are essentially replaced by the *avoidable* URD of increasing the pressure of the same amount of liquid refrigerant across the mechanical pump. As there is no pressurizing gas vented to the accumulator for this arrangement, it is assumed that the accumulator temperature remains constant throughout the ice building and shedding cycle. Therefore there is no URD of re-cooling the accumulator for this mechanically pumped system (MPS).

8.8.1 URD of Re-Cooling the Circulated Liquid at the Mechanical Pump

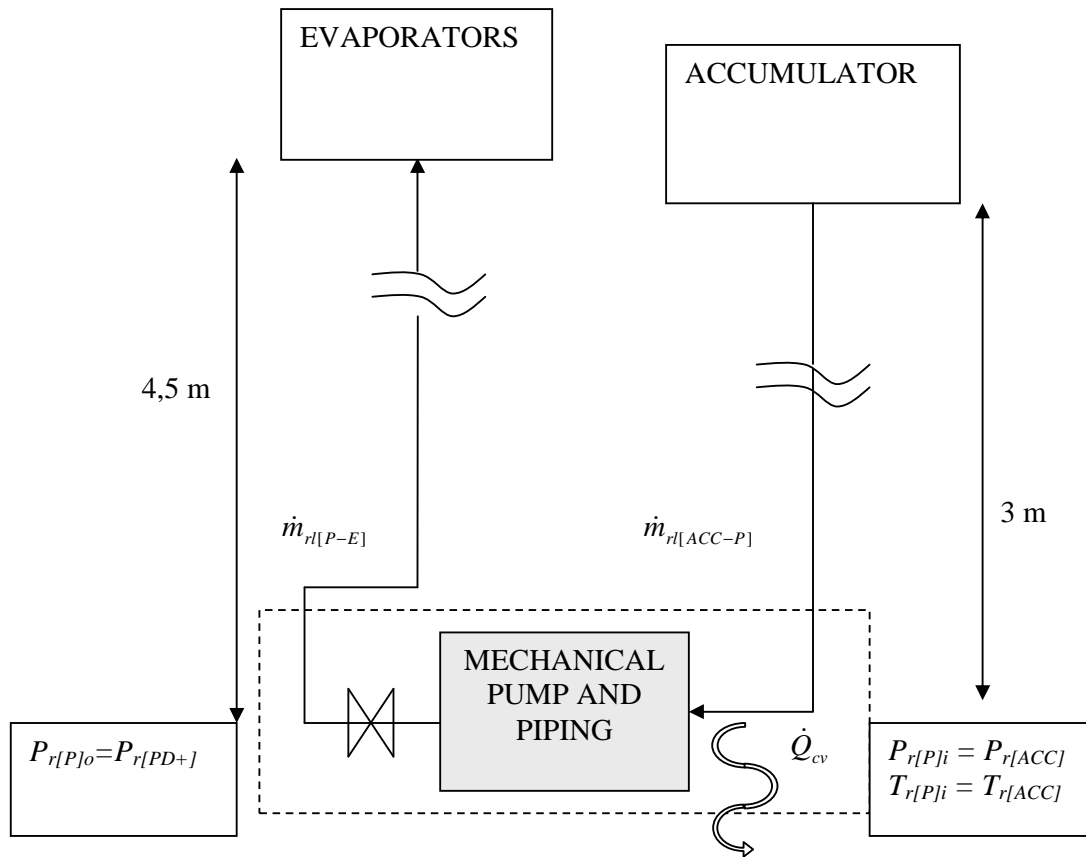


Figure 8.12 Control Volume: Mechanical Pump and Piping

It is normal practice that the mechanical pump is placed directly below the accumulator, and that the pressure rise required to circulate the liquid refrigerant through the evaporator is the same as the pressure increase recorded at the pumper drum of the ERPM plant.

As one mechanical pump would be used to circulate the liquid refrigerant through the 7 ice-building modules of Unit 5, it is inappropriate for sizing purposes to assume that each module possesses its own pump. Rather it will be assumed that one pump circulates the required amount of liquid to all the ice building modules, and the final URD due to the mechanical pump will be split evenly amongst these 7 modules. All variables of friction and inlet and outlet pipe diameters and

lengths are based on the current configuration of the operating plant (summarised in Table A9.1 of Appendix A9).

The energy rate balance equation for Figure 8.12's control volume is the same as equation (10).

Assuming the control volume of Figure 8.12 is at steady state and ignoring heat transfer between the control volume and the surroundings, naming the individual mass flows, and justifiably assuming that the liquid refrigerant at the inlet to the pump is saturated, equation (10) simplifies to:

$$\dot{W}_{cv} = \dot{m}_{r[ACC-P]} (h_{rl}(P_{r[ACC]}) + \frac{V_i^2}{2} + gz_i) - \dot{m}_{r[P-E]} (h_{rl}(P_{r[PD+]}, T_{r[P]o}) + \frac{V_o^2}{2} + gz_o) \quad (79)$$

where naturally $\dot{m}_{r[ACC-P]} = \dot{m}_{r[P-E]}$.

To obtain the mechanical work input of the pump, an energy balance analysis is performed in Appendix A9. The final mechanical work input from the pump is:

$$\dot{W}_{[P]\{MPS\}mech} = \frac{\rho_{rl}(P_{r[PD+]})g\dot{V}_{r[P-E]}H'_{[P]}}{1000\eta_{[P]}} \quad (80)$$

The work input from the pump increases the enthalpy of the liquid refrigerant as it increases its pressure. The URD of re-cooling the warmed liquid refrigerant per module at the evaporator, over a complete ice building period of $(t_2 - t_1)$, is simply the integral of the mechanical work input over this time divided by 7 ice building modules.

$$\Delta H_{r[P]} = -\int_{t_1}^{t_2} \dot{W}_{[P]\{MPS\}mech} dt = \frac{\rho_{rl}(P_{r[PD+]})g\dot{V}_{r[P-E]}H'_{[P]}}{1000\eta_{[P]}}(t_2 - t_1) \quad (81)$$

8.8.2 Total URD for the MPS

From equations (19), (40), (42), (43), (53), (54) and (81) the URDs for the MPS *per module* are:

$$\begin{aligned} \Sigma \Delta H_{URD\{MPS\}} = & Q_{URD[E]} + \Delta H_{r.s[E]} + \Delta H_{rl.trap[E]} + \Delta H_{rv.trap[E]} + \Delta H_{rl\{c\}} \\ & + \Delta H_{rl.cont[E-ACC]} + \Delta H_{rl\{P\}} \end{aligned} \quad (82)$$

8.9. Total URD for a Fully Mechanically Pumped Arrangement Per Module

A theoretical model for a completely mechanically pumped system, based on a proposal by Bailey-McEwan,⁽¹⁶⁾ is developed. The system, utilising two pumps – a pump to circulate the refrigerant through the evaporators and one to discharge/recharge the evaporators with liquid before and after harvesting – would eliminate the URD associated with harvesting gas expelling cold ammonia liquid to the accumulator at the beginning of the warming sub-period, $\Delta H_{rl.cont[E-ACC]}$. It would also eliminate the URD due to the warm ammonia (refrigerant) liquid that is trapped behind the level-regulating valve at the end of the warming sub-period, $\Delta H_{rl.trap[E]}$. The following is a description of this fully mechanically pumped system, denoted FMPS.

The mechanical pump required to circulate the refrigerant through the evaporators for this arrangement is shown in Figure 8.12 above and is identical to that of the mechanically pumped arrangement. Figure 8.13 below shows the added pump and discharge/recharge vessels of the FMPS, which is in addition to the pump of the MPS.

Once the ice building period is completed, a controlled valve below the evaporators opens, allowing the liquid refrigerant therein to flow via gravity to a ‘discharge’ vessel situated below the evaporator module. The contents of the discharge vessel are then pumped using a ‘recharge’ pump (the discharge vessel is

constantly vented to the accumulator) to a ‘recharge’ vessel situated above the evaporator.

Referring to Figure 8.13 below, a float valve on the ‘discharge’ vessel controls operation of the ‘recharge’ pump. During the ice building period⁶⁴, the recharge pump shuts down, and only restarts once harvesting recommences. Alternatively, the cost of the pump can be reduced by allowing it to operate continuously to fill the recharge vessel by 100% of its volume in 13 minutes.⁶⁵ This would reduce the volumetric flow rate required and thus the size of the pump, as well as reduce general wear, as the pump would operate continuously rather than cyclically.

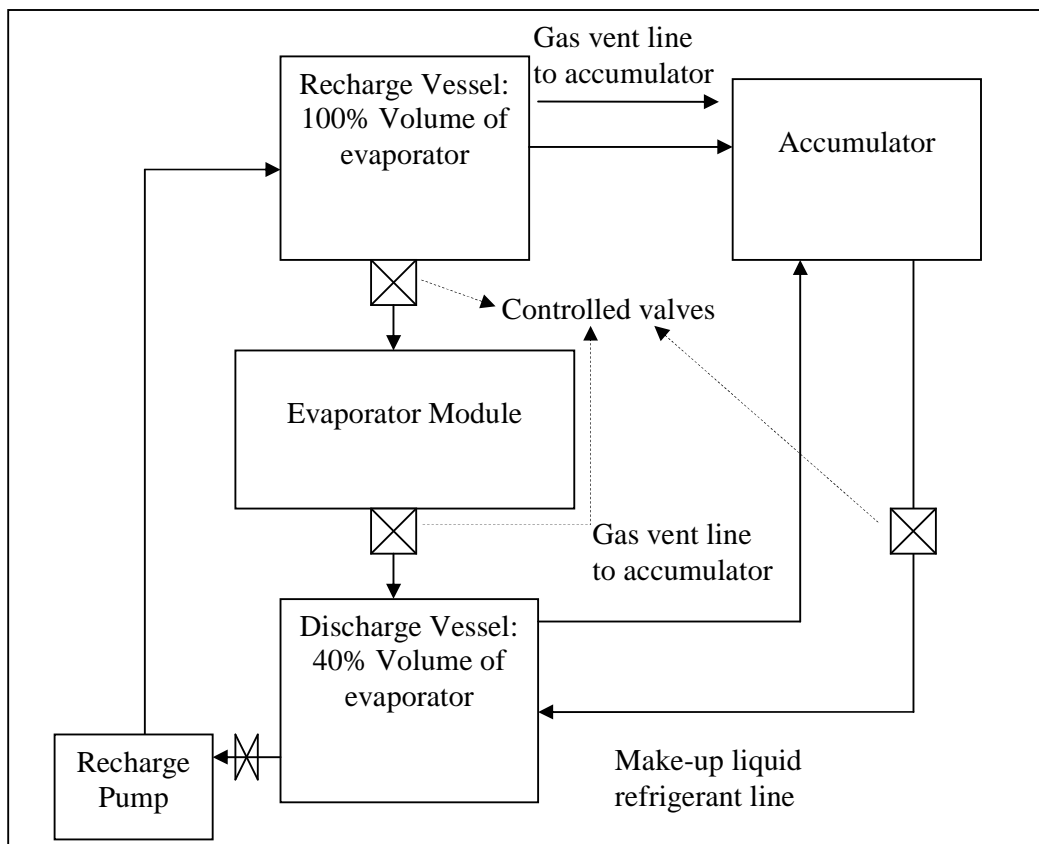


Figure 8.13 Recharge/discharge vessels and pump for the fully mechanically pumped arrangement

⁶⁴ And whilst refrigerant is circulated through the evaporators by the large mechanical pump as shown in Figure 8.12 above.

⁶⁵ A full ice building cycle of one module lasts for 13.5 minutes.

At the end of the warming sub-period, once the controlled valve above the evaporator vents the uncondensed harvesting gas, $m_{rv.trap[E](t_2)}$ to the accumulator, another controlled valve at the bottom of the recharge vessel opens to recharge the evaporator with liquid within 25 seconds. Level control valves at the discharge vessel refill it with liquid from the accumulator if the liquid level is too low. Appendix A4 outlines the analysis to determine the mechanical power required by the recharge pump, as well as the basic design of the vessels and piping.

The final mechanical work input for the recharge pump is:

$$\dot{W}_{[P]\{FMPS\}mech} = \frac{\rho_{rl}(P_{r[ACC]})g\dot{V}_{rl[DV-RV]}H'_{[P]\{FMPS\}}}{1000\eta_{[P]}} \quad (83)$$

The work input from the pump increases the enthalpy of the liquid refrigerant as it increases its pressure. The URD of re-cooling the warmed liquid refrigerant per module at the evaporator, over a complete recharge time of 13 minutes, denoted $(t_2 - t_1)$, is simply the integral of the mechanical work input over this time.

$$\Delta H_{rl[P]\{FMPS\}} = -\int_{t_1}^{t_2} W_{[P]\{FMPS\}mech} dt = \frac{\rho_{rl}(P_{r[ACC]})g\dot{V}_{rl[DV-RV]}H'_{[P]\{FMPS\}}}{1000\eta_{[P]}} (t_2 - t_1) \quad (84)$$

8.9.1 Total URD for the FMPS

From equations (19), (43), (53), (54), (81) and (84) the URDs for the MPS per module are:

$$\Sigma\Delta H_{URD\{FMPS\}} = Q_{URD[E]} + \Delta H_{r.s[E]} + \Delta H_{rl\{c\}} + \Delta H_{rv.trap[E]} + \Delta H_{rl[P]} + \Delta H_{rl[P]\{FMPS\}} \quad (85)$$

8.10. Comparison of Results for the Four Arrangements

Graphs, based on the models described above, comparing the different pumping arrangements at various performance quantities and operating parameters are presented in this section. As discussed in the analysis presented above, the PRDs and *unavoidable* URDs for all arrangements are identical. Therefore the *avoidable* URDs - those specific to each arrangement - are the only means of comparing the energy efficiency of the different systems. By varying performance quantities for all four arrangements, such as the average recirculation ratio, as well as operating parameters such as the evaporating temperature, the relative energy efficiency of each arrangement can be predicted. By comparing the results of the analysis presented above, the most energy efficient and hence, the most cost effective batch-type ice making pumping arrangement can be predicted.

8.10.1 Results for Different Average Recirculation Ratios

The first performance quantity to be compared is the average recirculation ratio. This quantity affects any *avoidable* URDs⁶⁶ of circulating the liquid to and through the evaporators, as cold liquid refrigerant is unavoidably warmed by the pumping mechanisms for all arrangements. Further, as a result of the pressure required at the pumper drum to circulate the liquid to the evaporators, the *avoidable* URDs of re-cooling the refrigerant at, and the steel of, the accumulator and pumper drums for the HGPS, are directly related to the mass flow rate at the evaporator, which in turn is dependent on the average recirculation ratio. Graphs comparing the four arrangements at different average recirculation ratios, x_i , are plotted, and the results are discussed below.

The first graph of Figure 8.14 compares the percentage URD of total refrigeration demand per module over one ice building and shedding cycle of 15 minutes. A magnified scale is shown below in Figure 8.15 to emphasize the slight differences in percentage URD for the different pumping arrangements.

⁶⁶ Specifically, those of the HGPS, MPS and FMPS. There are no avoidable URDs associated with the CGPS as they are all inherent.

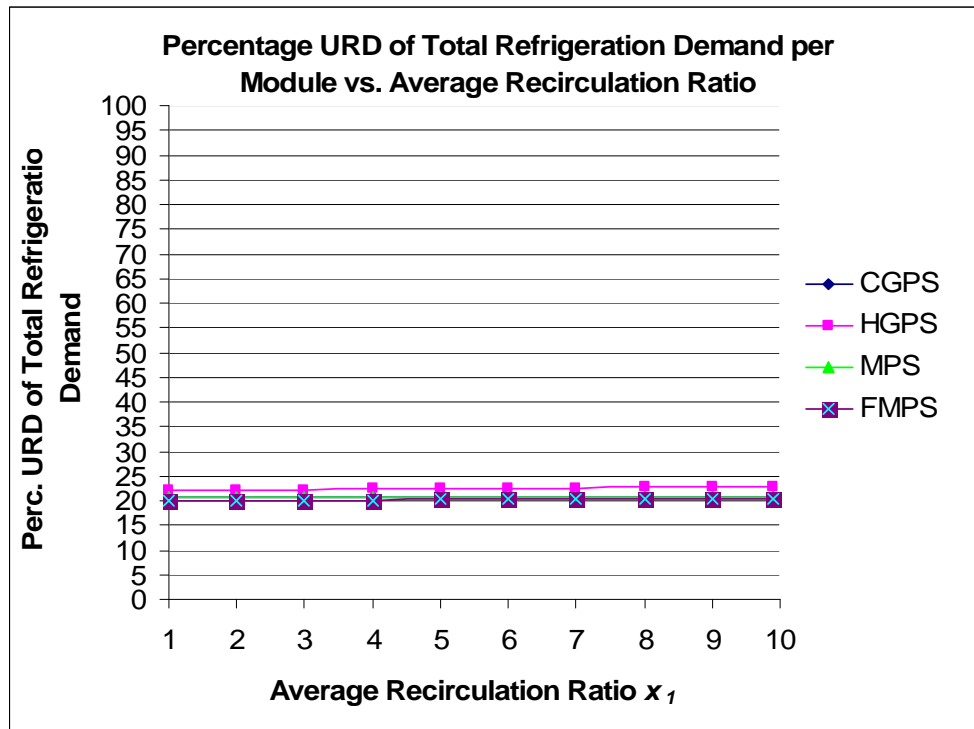


Figure 8.14 Percentage URD of total refrigeration demand per module versus average recirculation ratio for one ice building and shedding cycle of 15 minutes

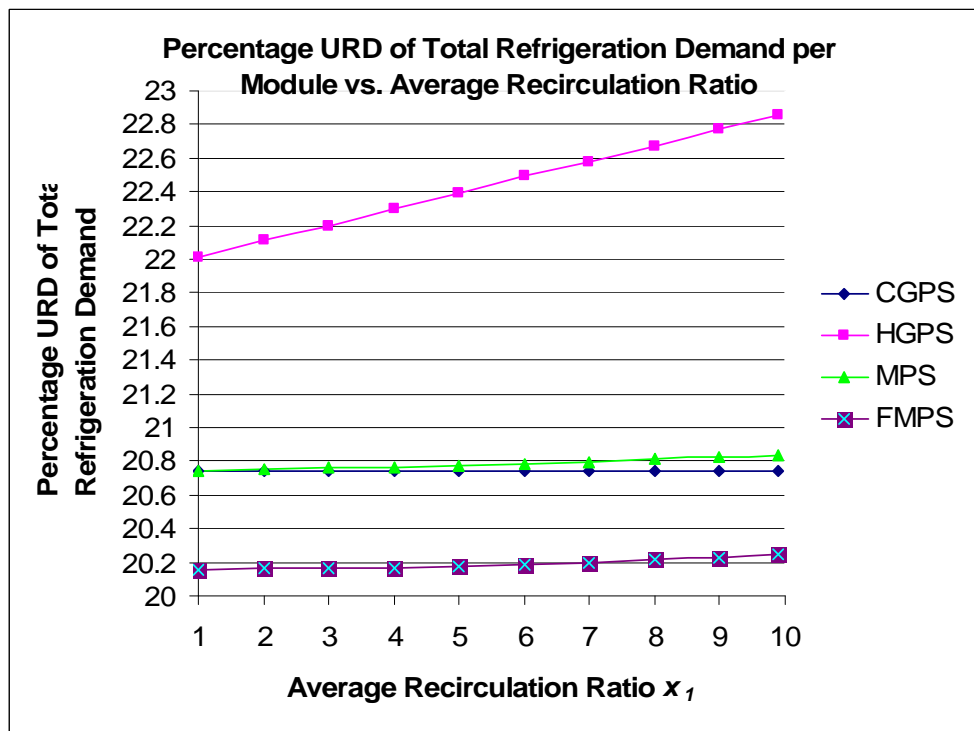


Figure 8.15 Magnified scale of Figure 8.14 above

From Figure 8.14 above, the changes in percentage URD for all arrangements as the average recirculation ratio increases are indiscernible. The magnified portion of the graph as shown in Figure 8.15 reveals that this ratio has a more marked effect on total URD for the HGPS than for the mechanically pumped arrangements. Although the URD due to the work input from the pumps warming the circulating refrigerant is only present in the mechanically pumped arrangements, it is relatively small when compared to the interaction between the warm pressurising gas and the cold circulated liquid refrigerant for the hot gas pumped arrangement. The URD due to this interaction increases as the average recirculation ratio and mass flow rate increase. Unsurprisingly, as the CGPS eliminates all *avoidable* URDs associated with circulating refrigerant to the evaporators, its overall URD is independent of the average recirculation ratio.

Although the percentage URD of total refrigeration demand per module for each arrangement does not differ significantly from the other (the maximum difference between two arrangements is less than 3 %), since the total refrigeration demand of the system is large, small percentage differences are significant when comparing the overall efficiency and cost effectiveness of the different pumping arrangements.

Figure 8.16 below illustrates the increase in total refrigeration demand at increasing average recirculation ratios. It is expected that this graph should follow the same pattern as Figure 8.15 above, however it reveals that the small changes in percentage URD of total demand per module from Figure 8.15 above result in substantial increases in refrigeration demand, especially for the HGPS.

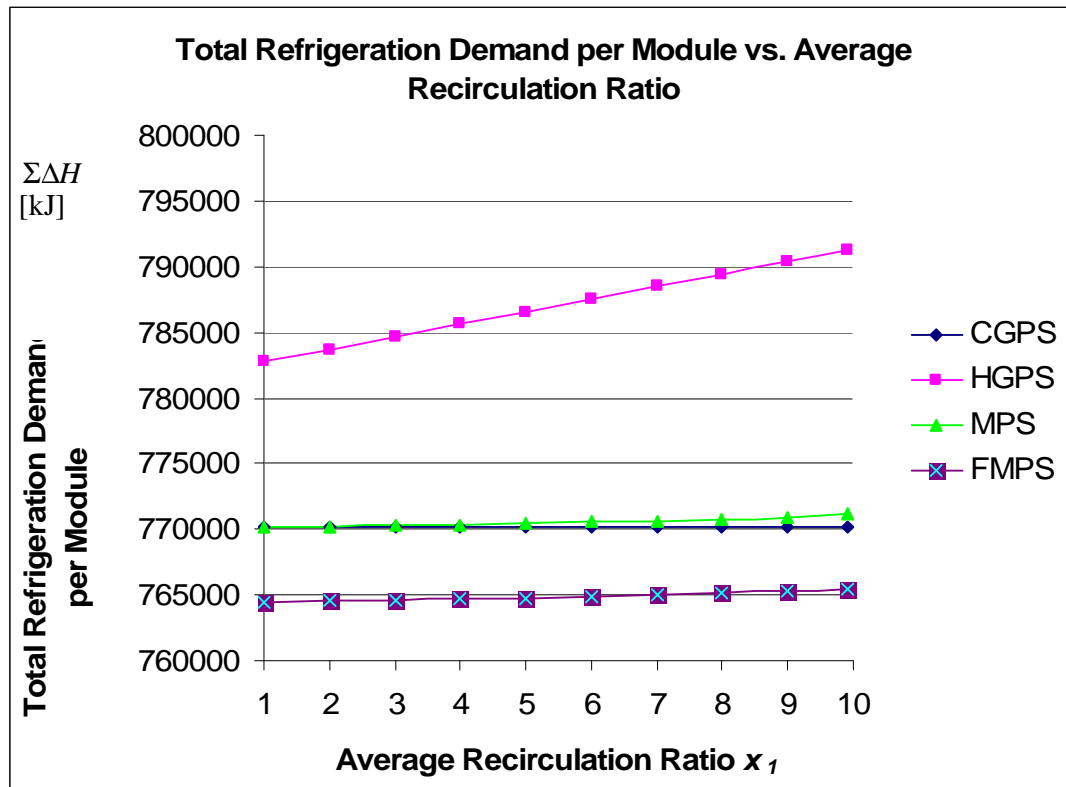


Figure 8.16 Total refrigeration demand per module per 15 minute ice building and shedding cycle versus average recirculation ratio

As in Figure 8.14 above, the total refrigeration demand for the mechanically pumped arrangements are less affected by the increase in average recirculation ratio than the hot gas pumped arrangement. As the average recirculation ratio increases, more liquid must be pumped to and through the evaporators. As a result, a greater volume of liquid comes in contact with the warm pressurising gas, which must be re-cooled. This is because, as the average recirculation increases, the volume of the pumper drums must commensurately increase⁶⁷ to maintain the pumping rate as defined in Table 3.1, which results in a larger URD of re-cooling the warmed steel walls of pumper drum. The increased volume at the pumper drum in turn results in more pressurising gas venting to the accumulator, increasing the URD of re-cooling the walls of the accumulator.

⁶⁷ This increase in volume is achieved by increasing the length of the pumper drum whilst maintaining its cross-sectional area. Appendix A8 Section A8.2.2 describes mathematically how the varying average recirculation ratios affect the volume of the pumper drums.

Therefore, the greater rate of increase in total refrigeration demand for the HGPS is due to the *avoidable* URDs related to the increased volume of warm pressurising gas admitted at the [pumping] pumper drum as the average recirculation ratio increases. The mechanically pumped arrangements are therefore more energy efficient at all probable average recirculation ratios when compared to the HGPS. By eliminating all *avoidable* URDs due to pumping, the CGPS is slightly more energy efficient than the MPS. However the FMPS, by eliminating the URDs associated with harvesting gas expelling cold ammonia liquid to the accumulator at the beginning of the warming sub-period, $\Delta H_{rl,cont[E-ACC]}$, as well as that due to the warm ammonia (refrigerant) liquid that is trapped behind the level-regulating valve at the end of the warming sub-period, $\Delta H_{rl,trap[E]}$, is the most energy efficient pumping arrangement.

Figure 8.17 below is based on equations (4), (5) and (6) and is the final comparison between the pumping arrangements at varying average recirculation ratios. This graph confirms that the HGPS is the least energy efficient of the pumping arrangements. The CGPS is more energy efficient than the MPS, whilst the FMPS is the most energy efficient of the four pumping arrangements at all practical average recirculation ratios⁶⁸.

⁶⁸ Although the COP for the CGPS is larger than the FMPS at average recirculation ratios larger than 9 as shown in Figure 8.17, this is an impractically high ratio and would not be encountered in a working overfeed batch-type ice making plant. This phenomenon is explained in detail below.

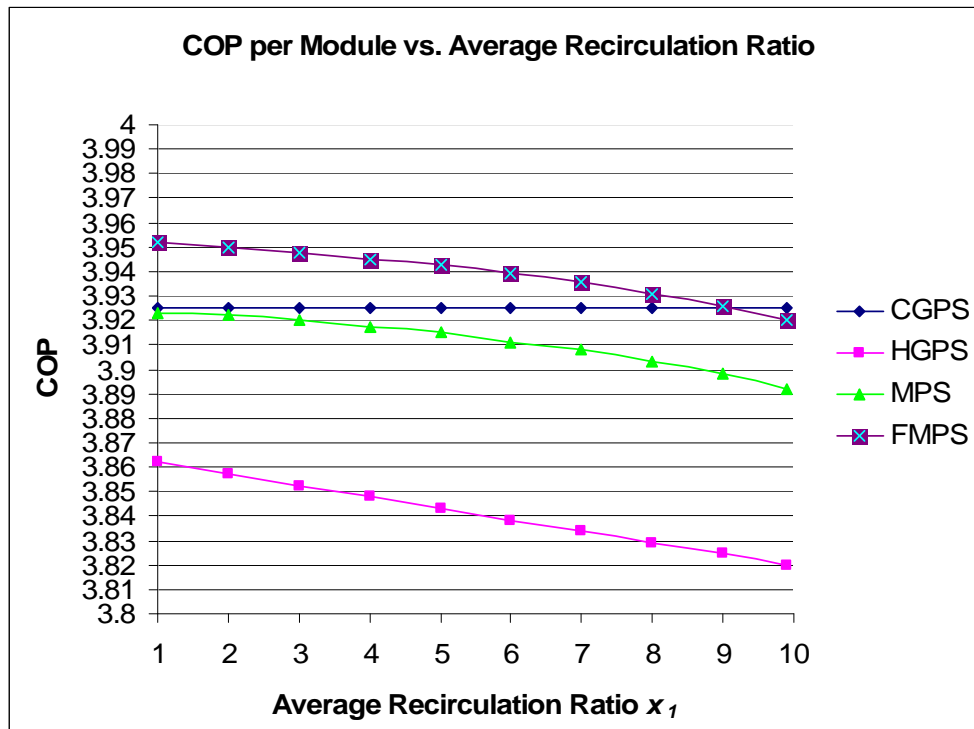


Figure 8.17 COP per module versus average recirculation ratio over a complete 15 minute ice building and shedding cycle

As mentioned above, as the average recirculation ratios increase, URDs associated with pressurising the pumper drum and circulating the liquid refrigerant to the evaporator for the hot gas pumped arrangement increases. From equations (4), (5) and (6), the numerator ΣQ_{PRD} is identical for all pumping arrangements, and the mechanical work input of the compressor in the denominator is dependent on the total refrigeration demand for each system. As in Figure 8.14 above, the COP of the hot gas pumped arrangements is more noticeably affected by the increase in average recirculation ratio and mass flow rate than those of the mechanically pumped arrangements.

Although the COP of the CGPS approaches that of the FMPS, this only occurs at impractically high average recirculation ratios ($> 9,5$). The reason why this ratio is considered impractically high, and why it does not signify that the CGPS is more efficient than the FMPS, is now described.

It is recalled from equation (4) that the COP for the CGPS is

$$COP_{\{CGPS\}} = \frac{\Sigma Q_{PRD}}{\Sigma W_{\{CR\}\{CGPS\}mech}}$$

which only includes, in the denominator, the energy input into the system from the compressor. Equation (6a)⁶⁹, which predicts the COP for the mechanically pumped arrangements, includes the energy input into the system from the compressor and the mechanical pump.

$$COP_{\{MPS\}} = \frac{\Sigma Q_{PRD}}{\Sigma W_{\{CR\}\{MPS\}mech} + \Sigma W_{\{P\}\{MPS\}mech}}$$

Here, the energy input from the compressor for the MPS is

$$\Sigma W_{\{CR\}\{MPS\}mech} = \Sigma W_{\{CR\}\{CGPS\}mech} \frac{\Sigma \Delta H_{\{MPS\}}}{\Sigma \Delta H_{\{CGPS\}}} \quad (6b)$$

In equation (6b), the energy input from the compressor is assumed to be smaller than that for the cold gas pumped system by the ratio of the total refrigeration demands $\Sigma \Delta H$ of the two arrangements.

From the COP equations above, although the total URD, and consequently the compressor energy input, for the CGPS may be larger than that of the FMPS (as shown in Figure 8.16 above), the gas pumped COP does not include a term in the denominator resulting from the additional work input required for the mechanical pump. From Figure 8.16, the small difference in total refrigeration demands between the CGPS and the FMPS results in the ratio of equation (6b) being close to one, even at high average recirculation ratios. At these high ratios (> 9.5), the

⁶⁹ As mentioned above in Section 7.2, the assumption that compressor isentropic efficiency changes negligibly for small changes in slide valve position, and that for small changes in URDs the condenser pressure remains constant, allows for the COP for all arrangements to be predicted from the electrical work input measured at the operating CGPS plant.

sum of the energy inputs from the compressor and mechanical pump for the FMPS is slightly larger than the energy input from the compressor alone for the CGPS. It is recalled from Section 7.2.4 above that although the *pumping* work required to circulate refrigerant through the evaporators is the same (for identical recirculation ratio), the CGPS does not require external work input for this pumping work – it comes internally from the last stage of expansion to evaporating pressure. As the average recirculation ratio increases, more energy input is required from the mechanical pump to handle the higher refrigerant mass flow rate through the evaporators. It is this phenomenon that results in the slightly larger COP for the CGPS at high average recirculation ratios. This is intuitive, as the URDs for the CGPS remain constant as average recirculation ratio increases, whilst those of the mechanically pumped arrangements slowly increase. Eventually, at high average recirculation ratios, the increasing work input from the mechanical pump for the FMPS nullifies any advantage gained by eliminating those URDs during the harvesting process described in Section 8.9. Therefore, the assumption of equation (6b), that the ratio of total demands can predict the compressor energy input for all pumping arrangements appears to be valid *even* at higher average recirculation ratios.

Furthermore, as mentioned in Section 2.2, Lorentzen and Baglo⁽⁶⁾ predict that an efficient cold gas pumped arrangement would limit the total URD to match that of the mechanically pumped arrangement, resulting in less total refrigeration demand and a larger COP - due to the absence of the mechanical power required by the pump. From the predictions of this investigation therefore, as shown in Figure 8.14 above, the total URD for the CGPS is *always* smaller than the MPS. This is therefore in agreement with the suggestion of Lorentzen and Baglo.⁽⁶⁾

Finally, although Lorentzen and Baglo⁽⁶⁾ suggest that the “pumping rate should be made as high as possible”⁽⁶⁾ for an efficient CGPS, the actual rate is never quantified. Both ASHRAE⁽⁵⁾ and Wright⁽¹¹⁾ state that common recirculation ratios for mechanically pumped arrangements are between 4 and 7. Therefore ratios as high as 9,5 would not be encountered in a working liquid refrigerant overfeed

pumping arrangement, and are included in this analysis merely to illustrate the trends at extreme average recirculation ratios.

It can be concluded therefore from the above graphs based on the analysis presented in this Section 8., that there is no average recirculation ratio that favours the HGPS over its mechanically pumped counterparts. Furthermore, there is no average recirculation ratio that favours the MPS over the CGPS.

This is in agreement with the conclusions of Wright⁽¹¹⁾ that a “cold” flash-gas pressurised recirculation arrangement may operate at lower energy cost than a mechanical pump at the same recirculation ratio, “and even lower if the pump is operated at their more common recirculation rates of 4:1 to 6:1.”⁽¹¹⁾ This also agrees with the suggestion of Lorentzen and Baglo’s⁽⁶⁾ that a cold gas pumped arrangement would minimise the URDs to the point that it would be more energy efficient than a conventional mechanically pumped system.

The results also confirm the conclusions of Wright⁽¹¹⁾ and Lorentzen and Baglo’s⁽⁶⁾ that conventional (hot) gas pumped systems yield a considerable loss of refrigeration capacity and power compared to mechanically pumped systems.

8.10.2 Results for Different Evaporator Pressures

A key operating parameter that was measured at the plant is the pressure at the evaporator during the ice building period. The pressures at the accumulator and pumper drum are obviously dependent on this pressure, and from Worthington Smith & Brouwer⁽¹³⁾ the [pumping] pumper drum pressure as well as the harvesting pressure are specified in relation to this pressure⁷⁰. Data obtained from the plant confirmed the pressure differences relative to evaporator pressure as cited in Worthington Smith & Brouwer.⁽¹³⁾ Table 8.1 below summarises some relevant pressures recorded at various locations at the ERPM operating plant as

⁷⁰ For example, the harvesting pressure is referenced as 250 kPa above evaporating pressure, and the [pumping] pumper drum pressure as 220 kPa above evaporating pressure.

shown in Appendix A1 Figure A1.1 and listed in Appendix A7, as well as the difference in pressure relative to evaporator pressure.

Table 8.1 Pressure recorded at the ERPM plant (Absolute, $P_{atm} = 83,5$ kPa)

Position	Pressure [kPa]	Temperature [$^{\circ}$ C]	Difference in Pressure to Evaporating Pressure [Δ kPa]
Evaporator during Ice Building Period (P_{n5} on Figure A1.1)	343,50	-5,83	-
Evaporator during Harvesting Period (P_{n5} on Figure A1.1)	593,50	8,96	+ 250
Condensed Liquid Receiver (P_{n1} on Figure A1.1)	1133,50	29,01	+ 790
Pumper Drum 1 during Filling Period (P_{n2} on Figure A1.1)	357,80	-4,79	+ 14,3
Pumper Drum 1 during Pumping Period (P_{n2} on Figure A1.1)	563,50	7,48	+ 220
Accumulator (P_4 on Figure A1.1)	303,50	-8,94	- 40

Maintaining the pressure differences listed in the table above and assuming that they remain constant, the evaporator pressure, P_{n5} on Figure A-1.1, is varied, and graphs are plotted to compare the four arrangements at different evaporator pressures. The condensed liquid receiver pressure measured at the plant, P_{n1} on Figure A1.1, is however maintained at its constant value (1133,50 kPa absolute). The average recirculation ratio is also maintained constant for all arrangements at the predicted value of 5 for the operating ERPM plant, with the dashed line indicating saturated evaporator temperature measured at the operating ERPM plant. Saturated evaporator temperatures, $T_{R[E]build}$ at the corresponding evaporator pressures are plotted on the x-axis to allow for meaningful comparisons to be made between the different arrangements and to illustrate the differences between the four pumping arrangements at extreme evaporator temperatures.

Figure 8.18 below is a plot of percentage URD of total refrigeration demand for one module over a complete ice building and shedding period at varying saturated evaporator temperatures. This graph indicates the relative energy efficiency of the

four pumping systems at probable and extreme evaporator temperatures and whether there is a point of overlap amongst the different pumping arrangements.

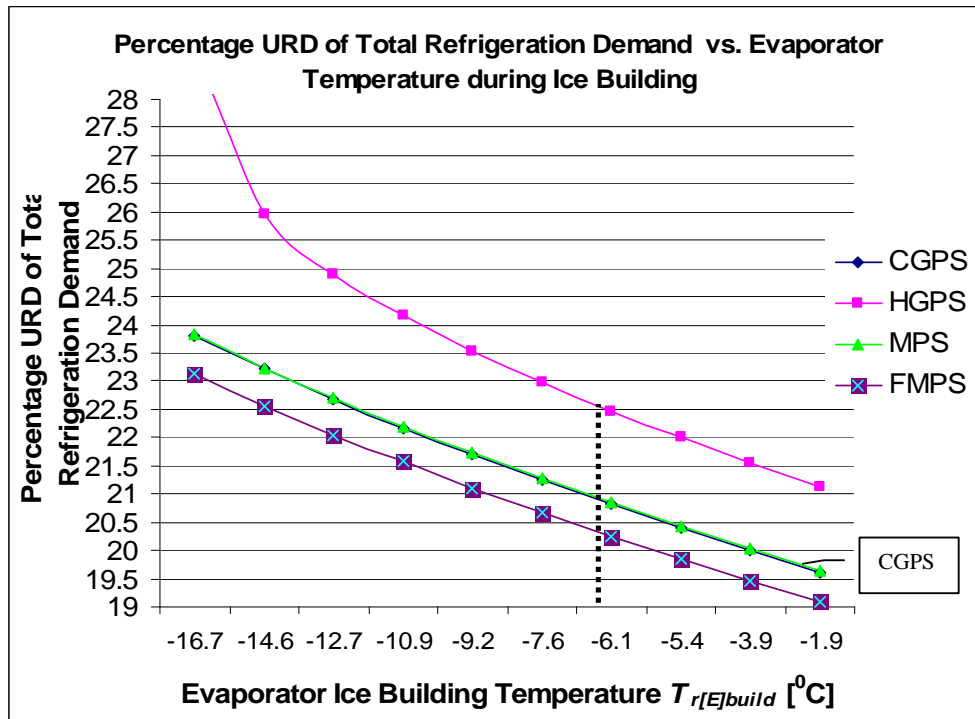


Figure 8.18 Percentage URD of total refrigeration demand per module over one ice building and shedding cycle versus saturated evaporator temperature during ice building. Average recirculation ratio is maintained constant at 5.

From Figure 8.18 above, the percentage URD of total refrigeration demand per module decreases as evaporator temperature $T_{r[E]build}$ increases. This arises directly from the evaporator temperature, since the URDs of re-cooling the trapped refrigerant liquid and vapour in the evaporator, as well as the evaporator steel at the end of the warming sub-period, decrease as evaporator temperature increases. From Table 8.1, as the pressures at the pumper drums, mechanical pumps and accumulator are dependent on evaporator pressure, the change in evaporator temperature affects all the *avoidable* URDs of the four pumping arrangements. Therefore as evaporator temperature decreases, all URDs increase at the same rate.

From Figure 8.18, the URD due to the mechanical pump is responsible for the slight difference in percentage URD between the MPS and CGPS⁷¹ for all probable evaporator temperatures.⁷²

The sharp rise in percentage URD at the lower evaporator temperatures for the HGPS is due to the URD of re-cooling the pumper drum after every pumping period. Recall from equation (75) of Section 8.7.2 that for the HGPS, the maximum temperature difference reached by the pumper drum $T_{heat[PD]\{HGPS\}} - T_{r[PD-]}$ is assumed to be proportional to the ratio of pressurizing gas temperatures multiplied by the temperature difference measured at the cold gas operating plant:

$$T_{heat[PD]\{HGPS\}} - T_{r[PD-]} = (T_{heat[PD]} - T_{r[PD-]}) \left[\frac{T_{r[PD+]\{HGPS\}}}{T_{r[PD+]}} \right].$$

As the condensed liquid receiver pressure is maintained at its constant value as in Table 8.1 above, $T_{r[PD+]\{HGPS\}}$ is constant. However the denominator $T_{r[PD+]}$, which is based on the pressure in the [pumping] pumper drum for the CGPS, approaches zero as evaporator pressure, and consequently, pumping pressure for the CGPS, decreases. Therefore, at lower pumper drum pressurizing temperatures $T_{r[PD+]}$ for the CGPS, the temperature change at the pumper drum for the HGPS, predicted by the equation directly above, drastically increases the URD of re-cooling the pumper drum, and consequently, its percentage URD. The assumption that the change in temperature for the HGPS, which as stated in Section 8.7.2 above is a measure of the energy gained by the pumper drum by sensible heat, is proportional to the ratio of pressurizing temperatures is therefore unreasonable at low evaporator temperatures (lower than -11 °C). For the following graphs, the points where this assumption for the HGPS is no longer valid is indicated by a dashed line.

⁷¹ With the percentage URD of the CGPS slightly less than the MPS.

⁷² Obviously the evaporating temperature of -3.2 and -1.9 °C are impractical as sufficient ice could probably not be built at these temperatures. However they do illustrate extreme ends of the temperature spectrum.

The plot below is of the total refrigeration demand for all four pumping arrangements per module for a complete ice building and shedding cycle, and for an average recirculation ratio of five. This graph reveals that the seemingly small changes in percentage URD at varying evaporator temperatures from Figure 8.18 result in large changes in total refrigeration demand for all four pumping arrangements.

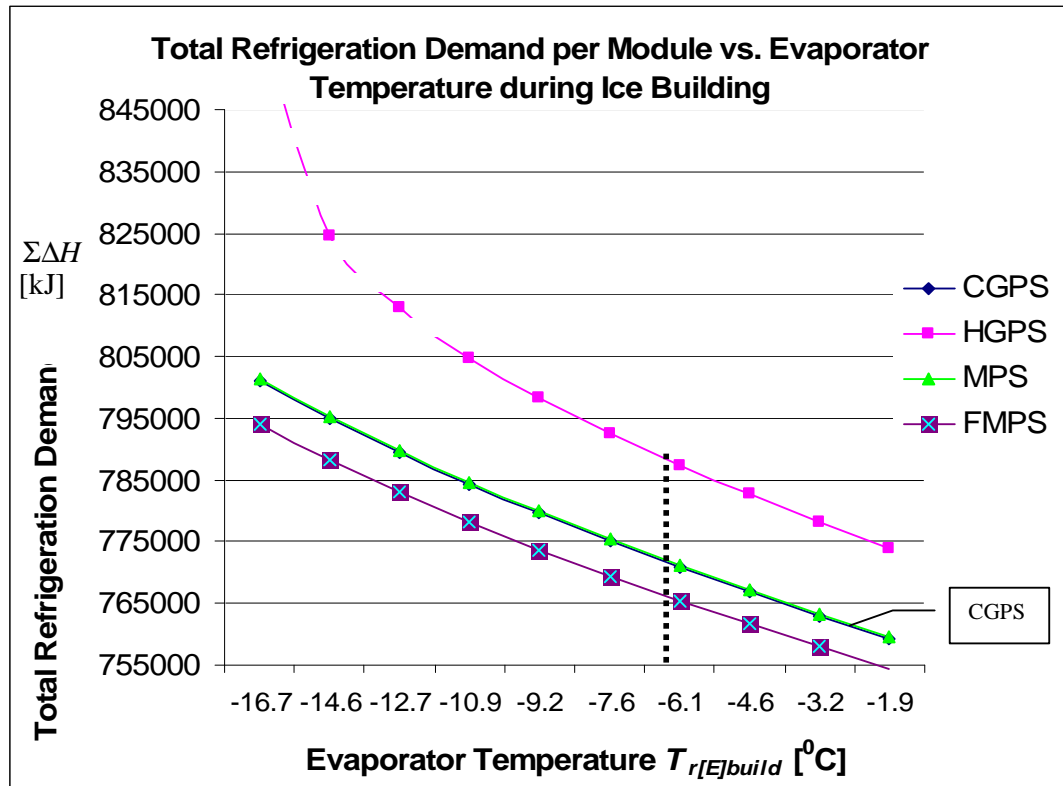


Figure 8.19 Total refrigeration demand per module versus evaporator temperature at an average recirculation ratio of five

As in Figure 8.18 above, the total refrigeration demand for all four arrangements decrease at the same rate with increasing evaporating temperatures, except where low temperatures affect the URD of re-cooling the pumper drum for the HGPS (indicated by dashed lines). For the predicted average recirculation ratio of 5, and assuming the pressure differences listed in Table 8.1 remain constant, there is no evaporating temperature, at identical average recirculation ratios, for which the total refrigeration demand of the MPS is lower than that of the CGPS.

As a final comparison, the COP of the four pumping arrangements is plotted below at varying evaporator temperatures.

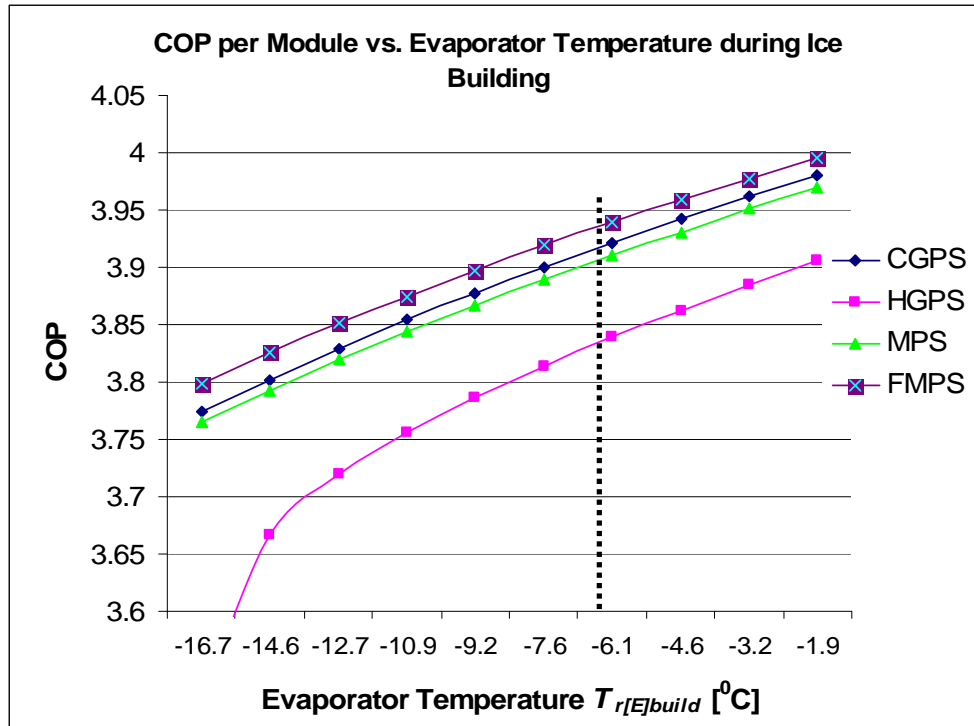


Figure 8.20 COP per module versus evaporator temperature at an average recirculation ratio of five

As expected, with increasing evaporator temperatures and consequently less overall URD, COPs for all arrangements increase. The FMPS has the lowest percentage URD of total refrigeration demand and highest COP of all the pumping arrangements and is therefore the most energy efficient arrangement. Whether it is also the most electrical cost effective is predicted in Section 8.11 below.

8.10.3 Results and Comparison of the Avoidable and Unavoidable URDs for each Arrangement

From the graphs of Sections 8.10.1 and 8.10.2 above, at identical performance quantities and operating conditions, there is no practical point of overlap where

the MPS is more energy efficient than the CGPS⁷³. Therefore an analysis of the individual *avoidable* and *unavoidable* URDs of the various systems, presented below, may identify the URDs that have the largest contribution to the overall URD of each arrangement. The average recirculation ratio is maintained constant for all arrangements at the predicted value of 5 for the operating ERPM plant.

The first graph presented below illustrates the total refrigeration demand per module for all four pumping arrangements over a complete ice building and shedding period. This chart identifies the contributions of the PRDs, and each *avoidable* and *unavoidable* URD, to the total refrigeration demand.

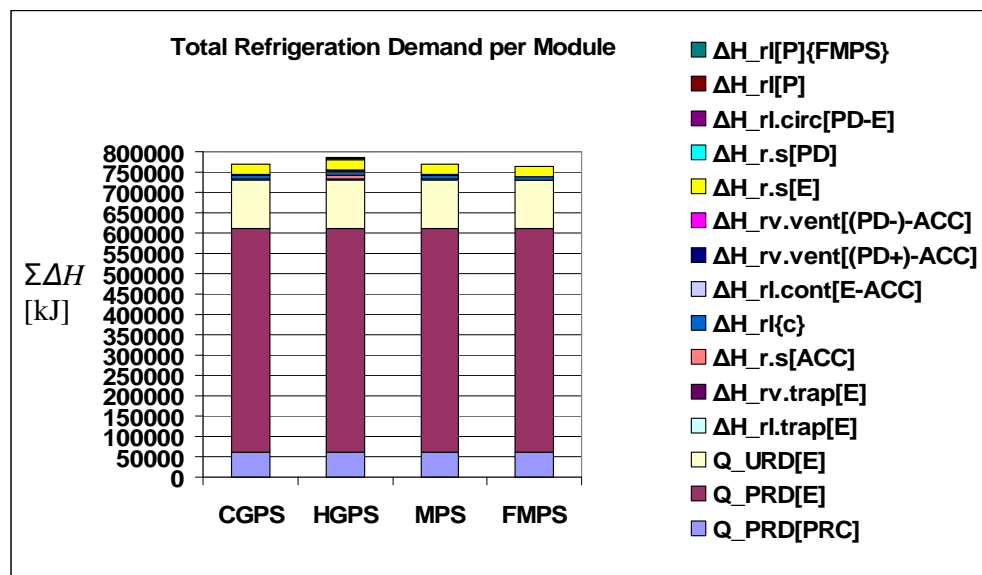


Figure 8.21 Total refrigeration demand per module for the four pumping arrangements over a complete ice building and shedding period

From Figure 8.21 above, the productive ice building load ΣQ_{PRD} which includes the PRD of building the delivered ice layer, as well as that of chilling the incoming feed water at the evaporator constitutes approximately 80% of the total refrigerating demand for all the arrangements, with the PRD at the pre-chiller alone, $Q_{PRD}\{PRC\}$, constituting approximately 7,7 – 8,0 %.

As the PRDs are identical for all pumping arrangements, only their distinctive *avoidable* URDs distinguish the energy efficiency of one arrangement from the

⁷³ Similarly, there is no practical point of overlap where the FMPS is less energy efficient than the CGPS.

other. The next chart illustrates the percentage contribution that these individual URDs make to the overall URD for each arrangement.

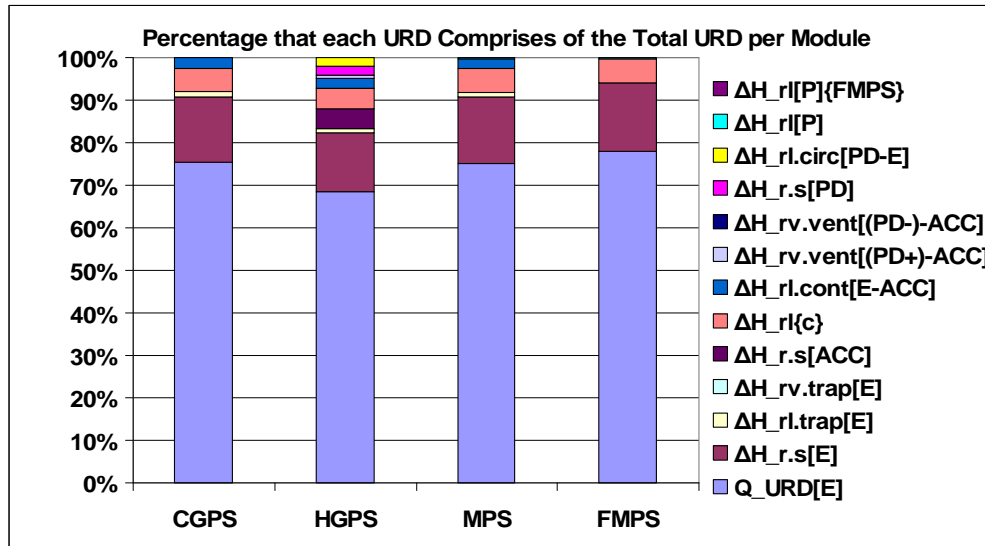


Figure 8.22 Percentage that each individual URD comprises of the total URD per module for the four pumping arrangements

From the Figure above, as the URDs for the HGPS are larger than for the mechanically pumped arrangements, their individual URDs occupy a smaller percentage of total URD. The percentages that the individual URDs comprise of total URD are outlined in Table 8.2 below. The actual values of the individual URDs are shown in Figure 8.23.

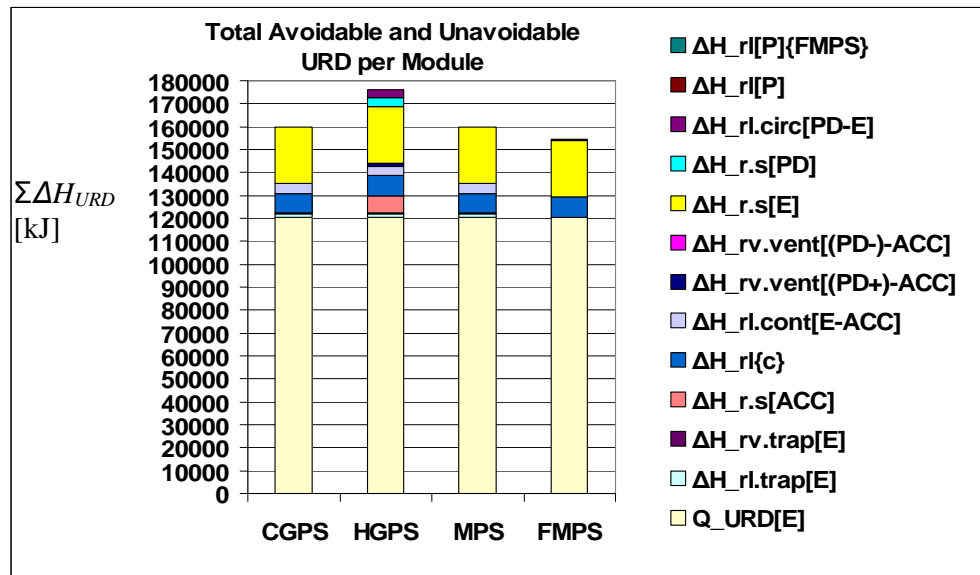


Figure 8.23 Total avoidable and unavoidable URD per module for the four pumping arrangements

Table 8.2 Percentage of total avoidable and unavoidable URDs for the four pumping arrangements over a complete ice building and harvesting period, at ERPM operating conditions and at an average recirculation ratio of 5

URD	CGPS	HGPS	MPS	FMPS
Total URD [kJ]	159715,27	176144,33	160031,97	154339,24
$Q_{URD[E]}$	75,37%	68,34%	75,22%	78,00%
$\Delta H_{r.s[E]}$	15,47%	14,03%	15,44%	16,01%
$\Delta H_{rl.trap[E]}$	1,11%	1,00%	1,10%	-
$\Delta H_{rv.trap[E]}$	0,04%	0,04%	0,04%	0,04%
$\Delta H_{r.s[ACC]}$	-	4,44%	-	-
$\Delta H_{rl\{c\}}$	5,52%	5,01%	5,51%	5,72%
$\Delta H_{rl.cont[E-ACC]}$	2,48%	2,25%	2,48%	-
$\Delta H_{rv.vent[(PD+)-ACC]}$	-	0,74%	-	-
$\Delta H_{rv.vent[(PD-)-ACC]}$	-	0,04%	-	-
$\Delta H_{r.s[PD]}$	-	2,15%	-	-
$\Delta H_{rl.circ[PD-E]}$	-	1,96%	-	-
$\Delta H_{rl[P]}$	-	-	0,20%	0,21%
$\Delta H_{rl[P]\{FMPS\}}$	-	-	-	0,02%

Unavoidable URDs Common to All Pumping Arrangements

Referring to Figure 8.23 and Table 8.2 above, building the subsequently melted ice layer, as well as sub-cooling the entire ice layer $Q_{URD[E]}$, is the largest URD for

all four pumping arrangements, constituting 68 – 78 % of total URD. The second largest URD is that of re-cooling the steel evaporator plates after the warming sub-period, $\Delta H_{r,s[E]}$, which constitutes 14 – 16 %. The third major URD, unavoidable and common to all arrangements, is the re-cooling of the condensed liquid during the warming sub-period at the evaporator, $\Delta H_{rl(c)}$ (5 – 6 % of total URD).

URDs Specific to the Gas Pumped Arrangements

As expected, for both gas pumped arrangements, the URD of re-cooling the trapped liquid in the evaporator at the end of the warming sub-period $\Delta H_{rl.trap[E]}$ is more significant than re-cooling the trapped vapour that is vented to the accumulator during the same period $\Delta H_{rv.trap[E]}$.

For the HGPS, the re-cooling of the vented gas from the pumper drum to the accumulator during the filling and pumping period ($\Delta H_{rv.vent[(PD+)-ACC]}$ and $\Delta H_{rv.vent[(PD-)-ACC]}$ respectively), are relatively minor avoidable URDs (less than 1 %). However, re-cooling the pumper drums $\Delta H_{r,s[PD]}$ and the accumulator $\Delta H_{r,s[ACC]}$, both occurring six times per 15 minute cycle, are large avoidable URDs for the HGPS. Finally, for this system, the avoidable URD of re-cooling the circulated liquid refrigerant that comes in contact with warm pressurising gas at the pumper drums $\Delta H_{rl.circ[PD-E]}$ appears relatively small (less than 2 %). However, when compared with the URD of circulating the same amount of liquid using a mechanical pump $\Delta H_{r[P]}$ (less than 1 %), it becomes apparent why the mechanically pumped arrangements are predicted by this investigation to be more energy efficient than the HGPS.

URDs Specific to the Mechanically Pumped Arrangements

As mentioned above, by eliminating the URDs of re-cooling the accumulator and pumper drums ($\Delta H_{r,s[ACC]}$ and $\Delta H_{r,s[PD]}$ respectively), as well as the interaction

between warm pressurising gas and cold circulating liquid at the pumper drums ($\Delta H_{rl.circ[PD-E]}$), the mechanically pumped arrangements are clearly more energy efficient than the HGPS. However, as the abovementioned URDs are part of the *inherent* ones for the CGPS, its total URD is slightly lower than that of the MPS. The *avoidable* URD of re-cooling any circulated liquid that is warmed due to the pressure increase imparted to it at the mechanical pumps $\Delta H_{rl[P]}$ is greatly offset by the savings in such URD (compared to the HGPS) for these arrangements. The FMPS, the most energy efficient of the four pumping arrangements, eliminates an additional 3.5% URD⁷⁴ (on average) by recharging and discharging the cold liquid refrigerant prior to, and after, the warming sub-period.

By ignoring the common *unavoidable* URDs of building the subsequently melted ice layer $Q_{URD[E]}$, as well as re-cooling the condensed liquid $\Delta H_{rl[c]}$ and evaporator steel $\Delta H_{r.s[E]}$ during, and at the end of the warming sub-period respectively, the “smaller” *avoidable* URDs that distinguish the relative energy efficiency of each arrangement can more clearly be identified.

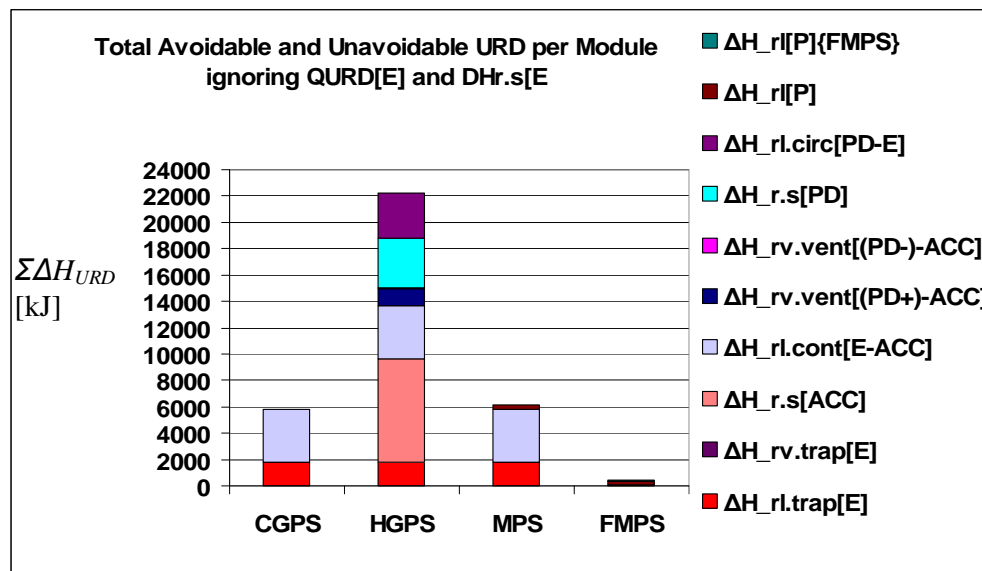


Figure 8.24 Total avoidable URD per module ignoring $Q_{URD[E]}$ and $\Delta H_{r.s[E]}$

⁷⁴ That due to re-cooling the cold liquid that is expelled by harvesting gas to the accumulator at the beginning of the warming sub-period $\Delta H_{rl.cont[E-ACC]}$, as well as re-cooling trapped liquid in the evaporator at the end of the warming sub-period, $\Delta H_{rl.trap[E]}$.

From Figure 8.24 and Table 8.2 above, the total *avoidable* and *unavoidable* URDs of the HGPS are 10,3 % larger than the CGPS. This is due to the URDs resulting from using warm gas at condenser pressure to circulate the refrigerant to and through the evaporators. This warm gas comes in contact with cold liquid refrigerant in the pumper drum, resulting in the warming of a portion of this liquid. The walls of the pumper drum are also warmed by the incoming pressurizing gas. At the accumulator, the vented gas from the [pumping] pumper drum at the end of its pumping period warms the walls of the accumulator. The subsequent URDs of re-cooling the refrigerant and steel walls during and at the end of the pumping period are what cause the HGPS to be the least energy efficient of the four pumping arrangements.

The mechanical pump of the MPS causes its total URD to be 0,2 % larger than for the CGPS. However, this arrangement obviously does not require a pumper drum to circulate the liquid to and through the evaporators. Moreover, as mentioned above, the *avoidable* URD due to the pressure imparted to the liquid at the mechanical pump is minimal when compared to the *avoidable* URD of using “hot” gas as the means of pumping.

Finally, the FMPS, which eliminates the significant URD of re-cooling the cold liquid that is expelled by harvesting gas to the accumulator at the beginning of the warming sub-period $\Delta H_{rl.cont[E-ACC]}$, has 3,4 % less total URD than the CGPS.

As mentioned above, the predictions of this investigation that at similar operating conditions, there is no recirculation ratio or evaporator pressure that favours the MPS over the CGPS agrees with both the conclusions of Wright⁽¹¹⁾ and the suggestion of Lorentzen and Baglo.⁽⁶⁾

The major assumption of the above model is that all the arrangements analysed operate under similar performance quantities (for example average recirculation ratio) and operating parameters (for example evaporator pressure and temperature). Modifying the average recirculation ratio and/or evaporator pressure for each pumping arrangement may yield results that do favour one pumping arrangement over the other. However, predicting these ‘optimal conditions’,

especially for a large plant such as ERPM, is complicated and is beyond the scope of this investigation, which is focused primarily on verifying theoretical models and comparing key aspects of the different arrangements at similar operating conditions.

It should be noted from the results of the data presented above that the total URD and COP for the four arrangements do not differ significantly, as the larger *unavoidable* URDs are common to all pumping arrangements. Therefore, a meaningful comparison between the different pumping arrangements would arise from predicting the annual electrical cost, the relevant capital costs as well as the maintenance costs for each system. The former is predicted below for the operating conditions at the ERPM plant, whilst the latter two are more difficult to predict, and would require further work beyond the scope of this investigation.

8.11. Operating Cost Analysis for the Different Pumping Arrangements

8.11.1 Results for Different Average Recirculation Ratios

From Section 8.6.2 above, the electrical work input into the compressor per module, based on test data from the operating ERPM plant, is predicted as:

$$\dot{W}_{\{CR\}\{CGPS\}elec} = 180 \text{ kW/module} \quad (70)$$

For the mechanically pumped arrangements, and assuming a motor efficiency η_m of 96%, the electrical power input to the pump is:

$$\dot{W}_{\{P\}elec} = \frac{\dot{W}_{\{P\}\{MPS\}mech}}{\eta_m} \quad (70c)$$

where from equation (80) above, $\dot{W}_{\{P\}\{MPS\}mech} = \frac{\rho_{rl} (P_{r\{PD+\}}) g \dot{V}_{r\{P-E\}} H'_{\{P\}}}{1000 \eta_{\{P\}}}$ per module.

Similarly, for the FMPS, the electrical power input for the recharge pump is:

$$\dot{W}_{\{P\}elec} = \frac{\dot{W}_{\{P\}\{FMPS\}mech}}{\eta_m} \quad (70d)$$

where from equation (83) above, $\dot{W}_{\{P\}\{FMPS\}mech} = \frac{\rho_{rl}(T_{r[E]})g\dot{V}_{rl\{P\}\{FMPS\}}H'_{\{P\}\{FMPS\}}}{1000\eta_{\{P\}}}$.

As mentioned in Section 7.2 above, the ratio of the total refrigeration demands in equations (5) and (6) allows for the mechanical and electrical work input into the compressor to be predicted for all arrangements, based on test data obtained for the operating cold gas pumped arrangement, $\Sigma W_{\{CR\}\{CGPS\}mech}$.⁷⁵ Therefore for the HGPS, the mechanical work input of the compressor is:

$$\Sigma W_{\{CR\}\{HGPS\}mech} = \Sigma W_{\{CR\}\{CGPS\}mech} \frac{\Sigma \Delta H_{\{HGPS\}}}{\Sigma \Delta H_{\{CGPS\}}} \quad (5)$$

Similarly for the MPS and FMPS:

$$\Sigma W_{\{CR\}\{MPS\}mech} = \Sigma W_{\{CR\}\{CGPS\}mech} \frac{\Sigma \Delta H_{\{MPS\}}}{\Sigma \Delta H_{\{CGPS\}}} \quad (6b)$$

$$\Sigma W_{\{CR\}\{FMPS\}mech} = \Sigma W_{\{CR\}\{CGPS\}mech} \frac{\Sigma \Delta H_{\{FMPS\}}}{\Sigma \Delta H_{\{CGPS\}}}$$

The annual operating cost for the different pumping arrangements can then be predicted from equation (7) above as follows:

$$\text{Electrical Operating Cost per Year} = (\Sigma \dot{W}_{\{CR\}elec} + \Sigma \dot{W}_{\{P\}elec}) \times \frac{\text{Cents}}{\text{kWh}} \times \frac{\text{hr}}{\text{year}} \quad (7)$$

⁷⁵ As mentioned above in Section 7.2, the assumption that compressor isentropic efficiency changes negligibly for small changes in slide valve position, and that for small changes in URDs the condenser pressure remains constant, allows for the COP for all arrangements to be predicted from the electrical work input measured at the operating CGPS plant.

As opposed to Section 8.10 above, where a comparison of the energy efficiency of the different pumping arrangements is performed per module, for the annual electrical cost analysis presented below, the comparison is performed per unit.⁷⁶

The average industrial rate per kWh is presented in Table A6.2 of Appendix A6. The results of the annual electrical operating cost per arrangement for an average recirculation ratio of 5, and based on operating parameters measured at the ERPM plant, are summarized in the table below.

Table 8.3 Annual electrical power consumption and cost for the different pumping arrangements, at an average recirculation ratio of 5. Annual cost rounded to nearest R1,000.

Pumping Arrangement	$\dot{W}_{[CR]elec}$ [kW]	$\Sigma \dot{W}_{[P]elec}$ [kW]	Electrical Operating Cost / Year	Difference Compared to Operating CGPS of ERPM plant
CGPS	1440,00	-	R4,549,000	-
HGPS	1470,40	-	R4,646,000	+ R97,000
MPS	1440,80	3,26	R4,561,000	+ R12,000
FMPS	1429,60	3,64	R4,528,000	- R21,000

From Table 8.3 above, the annual electrical operating cost of the CGPS is significantly lower than for the HGPS. Considering that the CGPS does not require any more vessels, piping or equipment (except for the additional expansion valves) than the HGPS, it is predicted to be more energy efficient and cost effective than a conventional HGPS. This is in agreement with the both Lorentzen and Baglo⁽⁶⁾ and Wright⁽¹¹⁾ who both concluded that hot gas pumped systems are the least energy efficient (and subsequently the least cost effective) of all probable overfeed pumping arrangements.

The MPS, which appears to be less cost effective than the CGPS, does not require pumper drums; however, the capital cost of the mechanical pump as well as annual maintenance costs should be investigated and compared with that of the pumper drums before it can be concluded whether this arrangement is indeed less cost effective than the CGPS.

The FMPS would require an additional recharge pump and a recharge/discharge vessel per module. As for the MPS, the capital and maintenance costs of this

⁷⁶ Each unit consists of eight modules.

additional equipment require further investigation before concluding whether this arrangement is more cost effective than the CGPS, despite its substantial annual electrical cost saving over the cold gas pumped arrangement.

By varying the average recirculation ratio as shown in Figure 8.25 below, whilst maintaining the evaporator pressure measured at the ERPM plant as constant, the annual electrical operating costs for the four pumping arrangements at the different ratios can be compared.

From Table 8.3 and Figure 8.25, when comparing the annual electrical operating costs, there is no practical average recirculation ratio⁷⁷ for which the CGPS is less cost effective than the MPS. This is in agreement with Lorentzen and Baglo⁽⁶⁾ who suggested that at high recirculation ratios, power consumption for a cold gas pumped system would be lower than a mechanically pumped system. It is also in agreement with Wright⁽¹¹⁾ who concluded that at low recirculation ratios (2:1), a gas pressure recirculation system (CGPS) “may operate at lower energy cost than a mechanical pump at the same recirculation rate.”⁽¹¹⁾ Furthermore, the cost analysis presented above agrees in principle with the following statement in ASHRAE⁽⁵⁾ : “Moreover gas pumped systems offer no advantage over their mechanically pumped counterparts when the overall capital and operational costs of both systems are compared.”⁽⁵⁾

Although as mentioned above, this investigation does not predict the capital and maintenance costs for the different pumping arrangements, based solely on the annual electrical operating costs, the MPS is less cost effective than the CGPS. This analysis should therefore be expanded to include the capital and maintenance costs of each pumping system to predict conclusively which pumping arrangement is the most cost effective. A rigorous way of so including the capital and maintenance costs would be through a Net Present Value (NPV) analysis.

⁷⁷ As mentioned in Section 8.10.1, although the annual operating cost for the CGPS is less than the FMPS at average recirculation ratios larger than 9,5, this is an impractically high ratio and would not be encountered in a working liquid refrigerant overfeed plant. It is therefore only included in the plot to illustrate the trends at extreme average recirculation ratios.

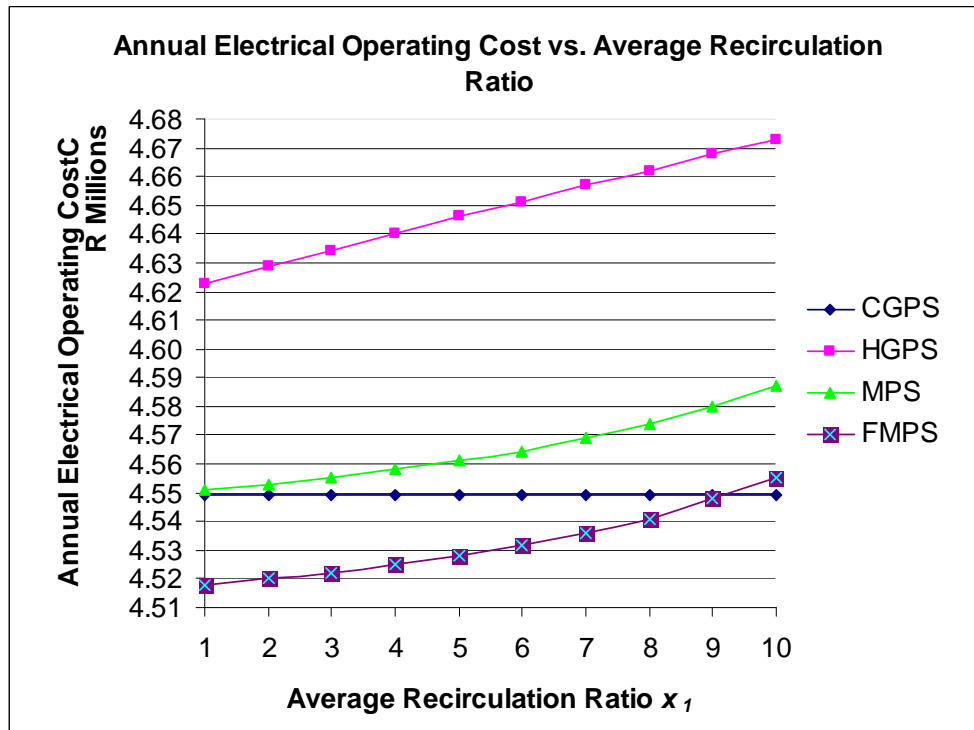


Figure 8.25 Annual electrical operating cost for the four pumping arrangements versus average recirculation ratio

8.12 Remark: Accuracy of Predicted URDs and COPs

The model presented in this section predicts and compares the URDs, COPs and energy consumption of four different pumping arrangements. For the CGPS, these predictions are based on operating parameters measured at the ice-making plant. Based on these measured operating parameters, some major assumptions are made to predict those same parameters for the other three theoretical pumping arrangements. These major assumptions as well as the key limitations on their accuracy are discussed below.

Referring to equations (5b) and (6b) of Section 7.2, to predict the COP for *all* pumping arrangements, it is assumed that compressor isentropic efficiency changes negligibly for small changes in slide valve position, and that for small

changes in URDs the condenser pressure remains constant. This assumption is reasonable for the results of the model presented above, as shown in Figure 8.14 through Figure 8.16, where the maximum variation in percentage URDs and total refrigeration demand between the pumping arrangements is approximately 3 %.

From Figure 8.17, at higher average recirculation ($> 9,5$), the COP for the FMPS is slightly larger than that of the CGPS. As discussed in detail in Section 8.10.1, this is intuitive, because the increasing total refrigeration demand⁷⁸ for the FMPS as the average recirculation ratio increases should *eventually* match and then surpass the *constant* demand of the CGPS. Therefore, the assumption of equation (6b) (and hence that of equation (5b)), that the ratio of total demands can predict the compressor energy input for all pumping arrangements appears to be valid *even* at higher average recirculation ratios.

Referring to Section 8.7, three assumptions are made to predict three critical URDs for the HGPS.

Firstly, in equation (73) of Section 8.7.1, the change in temperature and subsequent re-cooling of the accumulator for the HGPS is assumed to be proportional to that of the CGPS. Secondly, in equation (77) of Section 8.7.3, at the pumper drum of the HGPS, the upper portion of liquid that is heated by the incoming hot gas is predicted through rigorous mathematical modelling in Appendix A8.2.4, based on test data from the CGPS for the same performance quantity.

From the results of the model presented in Figure 8.15 and Figure 8.18, the URDs for the HGPS increase proportionally to those of the CGPS with increasing average recirculation ratios and evaporator pressures respectively. Therefore both assumptions appear to remain reasonably valid for the range of recirculation ratios considered above.

However, the third assumption of predicting the URD of re-cooling the steel of the pumper drum during the filling period (in equation (76) of Section 8.7.2) based on data from the CGPS does have limitations. As discussed in Section

⁷⁸ Due to the increasing work input required from the mechanical pump to circulate the larger volume of liquid.

8.10.2, the denominator in equation (75) ($T_{r[PD+]}$), which is based on the pressure in the [pumping] pumper drum for the CGPS, approaches zero as evaporator pressure, and consequently pumping pressure for the CGPS, decreases. Therefore, at these lower pumper drum pressurizing temperatures ($T_{r[PD+]}$) the change in temperature at the pumper drum for the HGPS, predicted by equation (75), unrealistically increases the URD of re-cooling the pumper drum for this arrangement, and consequently, its percentage URD. Therefore, evaporator temperatures where equation (76) of Section 8.7.2 is unacceptably invalid for the HGPS are indicated by a dashed line in Figure 8.18 and Figure 8.19 (at evaporator temperatures lower than -11°C).

As a result of the limitation of validity of this last key assumption, major comparisons between the four pumping arrangements must be confined to where *all* assumptions are valid. As all assumptions are deemed valid at (and close to) the performance quantities⁷⁹ predicted for, and operating parameters⁸⁰ measured at the ERPM plant, comparisons between the pumping arrangements are performed in this region.

Brief Review of Section 8.

This Section identified the major URDs and PRDs for four different pumping arrangements, based on operating parameters at the ERPM ice-making plant. By predicting the refrigeration demands for each pumping arrangement, their relative energy efficiency and electrical cost effectiveness could be compared. It was predicted from the model that the HGPS is the least, and the FMPS is the most, energy-efficient and electrical cost effective pumping arrangement at all probable performance quantities and operating parameters. This observation is in agreement with the conclusions of both Lorentzen and Baglo⁽⁶⁾ and Wright⁽¹¹⁾

⁷⁹ Such as average recirculation ratios and mass flow rates through the evaporator.

⁸⁰ Such as evaporator, accumulator and pumper drum temperatures and pressures.

regarding the inefficiency of hot gas pumped arrangements when compared to their mechanically pumped counterparts.

The CGPS is predicted to be more energy efficient and cost effective than the MPS, an observation which is in agreement with the suggestion of Lorentzen and Baglo⁽⁶⁾ and the conclusions of Wright⁽¹¹⁾ for cold gas pumped systems. Further work is required to predict whether this investigation agrees with the conclusions of ASHRAE⁽⁵⁾ regarding the relative cost effectiveness of gas and mechanically pumped arrangements. Finally, the major assumptions as well as the key limitations of the theoretical models presented in this Section are discussed.

9. HEAT TRANSFER MODEL TO CORROBORATE THE AVERAGE RECIRCULATION RATIO AND MASS FLOW RATE PREDICTED BY THE MODEL OF SECTION 8

This Section presents two heat transfer models that have been developed to predict the thickness of ice built and shed during the ice building and harvesting cycle of one module. The inputs to the models are the operating parameters measured at the ERPM plant, as well as the mass flow rate and average recirculation ratio predicted in Section 8. above. As mentioned in Section 2.4, knowledge of performance quantities such as the mass flow rate of refrigerant through the evaporators and average recirculation ratio are vital when modelling any overfeed refrigeration system. The mass flow rate through the evaporators in particular affects all the URDs associated with ice building for the four pumping arrangements modelled in Section 8.

Since the operating ERPM plant did not have flow meters, and installing any invasive equipment to predict the mass flow rate at the evaporators was prohibited for safety reasons, the only means of predicting this performance quantity is by theoretical modelling of the ice making cycle based on operating conditions and parameters that were available to be measured at the plant (evaporator pressure and temperature, dimensions of the pumper drum etc.).

As the mass flow rate through the evaporators is such an important input variable to the model of Section 8. above, and despite the fact that two independent methods of predicting this variable are presented in Section 8.6.1, a third independent theoretical model to predict this mass flow rate is developed and presented in Section 9.1 below. In addition, a theoretical model to predict the thickness of ice that is subsequently melted during the warming sub-period is developed in Section 9.2 to further substantiate the predicted thickness of ice built from Section 9.1. The thickness of the ice layer that is subsequently melted is also

an important performance quantity in the model of Section 8. when predicting the URD of building this layer. Therefore any means of corroborating performance quantities such as the mass flow rate, average recirculation ratio and thickness of ice layers built and melted would lend further validation to the results of the model developed in Section 8.

9.1. Heat Transfer Model during the Ice Building Period

To corroborate the average recirculation ratio predicted in Section 8. above for the operating ERPM plant, a heat balance model at the evaporator plates during the ice building period and the warming sub-period of the harvesting period is developed. The mass flow rate of refrigerant circulating through the channels in the plates, as well as the average recirculation ratio predicted in Section 8. above, are inputs to the model, and the thicknesses of ice built and shed in the requisite time are the outputs. These thicknesses can then be corroborated with measured data from the operating plant, as well as from Worthington-Smith & Brouwer,⁽¹³⁾ van der Walt & de Kock⁽¹⁸⁾⁸¹ and Rankin.⁽¹⁴⁾ Corroboration of the thickness of ice built and shed would therefore also corroborate the mass flow rate and hence the average recirculation ratio predicted in Section 8. above.

As Senatore⁽⁴⁾ summarises, “The aim of the heat balance method is to provide an approximate solution to non-linear, transient heat conduction problems.” Linearising the transient heat conduction equation, by assuming thermal properties to be independent of temperature and that the subcooling of the ice is negligible compared with the latent heat of fusion of ice formation, leads to a simplification of the numerical solution. This assumption⁸² is justified when it is considered that the variation in ice thermal conductivity between 0° C and -20° C is only 1.1%. (Senatore’s Appendix A pp. 69-73⁽⁴⁾)

⁸¹ Who, as mentioned above, merely *state typical figures* and therefore offer no experimental validation for the thickness of ice built.

⁸² The specific heat of ice at 0° C, from EES⁽⁴⁰⁾ is 2,041 kJ/kg.C. Even if it is conservatively assumed that the entire ice layer is subcooled to evaporator temperature (-5,833° C), this would result in 11,91 kJ/kg of subcooling, which, when compared to the latent heat of ice formation of 335 kJ/kg, is negligible.

A heat balance across the phase change interface yields:

$$k_2 \frac{\partial T_2}{\partial x} - k_1 \frac{\partial T_1}{\partial x} = \pm \rho_2 L \frac{\partial x}{\partial t}$$

+ :Freezing -:Melting

Subscript 1 liquid Subscript 2 solid”

Here, L is the latent heat of ice formation, k_1 and k_2 are the thermal conductivity of water and ice respectively, ρ_2 is the density of ice, T is temperature and x is the thickness of ice built⁸³. Thus the difference between the heat flux entering and that leaving the interface where a change of phase occurs is equal to the latent heat absorbed or released.

The thermal resistance of an ice layer varies depending on its layer thickness: “...this results in the heat flow to the colder medium (refrigerant) being in excess of that required to maintain freezing, by the amount of thermal energy abstraction required to subcool the ice.”⁽⁴⁾ A linearised temperature profile within the ice layer being built, based on the assumptions mentioned above is illustrated in Figure 9.1 below.

⁸³ This nomenclature is that of Senatore⁽⁴⁾ and is different from this investigation’s nomenclature.

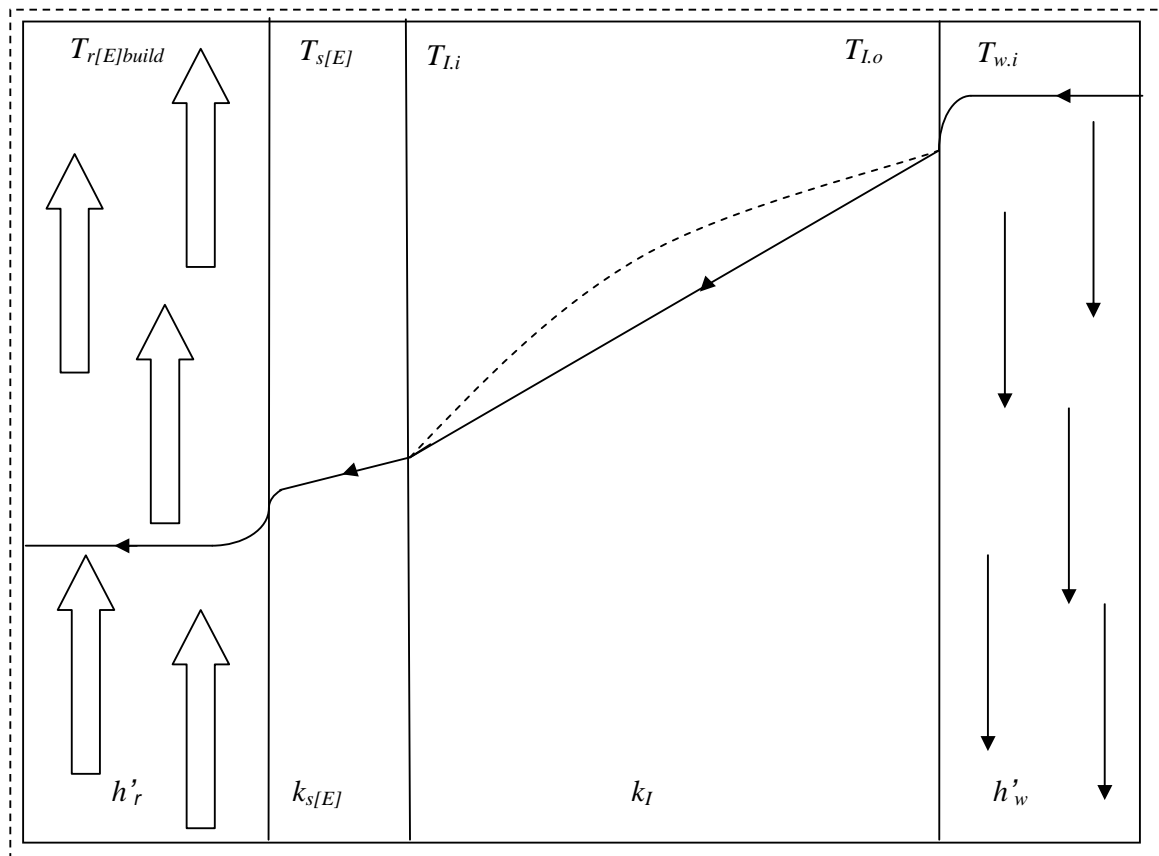


Figure 9.1 Linearised temperature profile for ice being built on one side of an evaporator plate. The actual temperature profile within the ice layer is shown in dashed lines, and the entire system is treated as a control volume. Adapted from Senatore's Fig. 4.3, p. 28⁽⁴⁾

The freezing process consists of the solidification of water, flowing downwards, on the outside of a steel plate. Two-phase ammonia, liquid and vapour, flows upwards in channels inside the plate. It is assumed, based on observations at the plant, that along the length of the plate there are 30 channels within which the refrigerant flows, and that each channel acts independently i.e. the refrigerant flows through each separate channel and does not mix with the fluid in other channels of the plate. A detailed diagram of one plate and its channels is shown in Figure 9.2 below. As each channel of the evaporator appears to be semi-elliptical as shown in Figure 9.2, it is approximated as a circular tube, with a diameter based on the channel's cross sectional area.

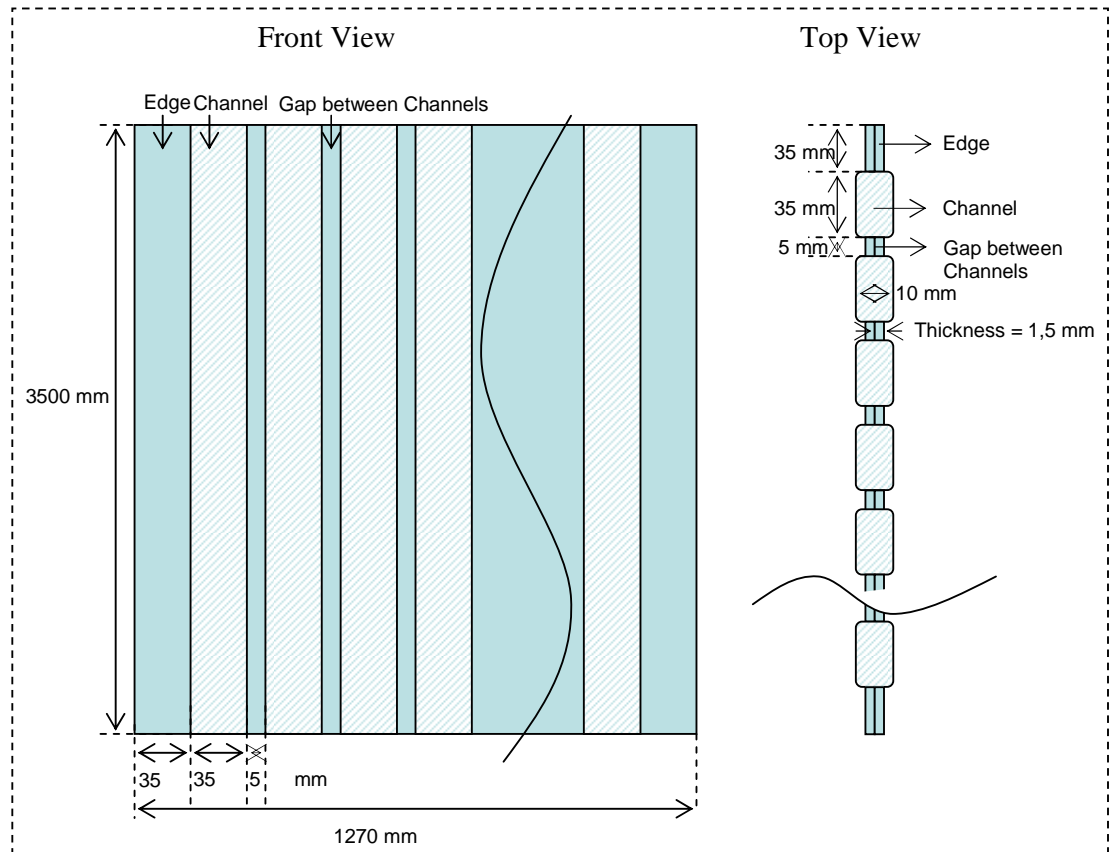


Figure 9.2 Front and top view of evaporator plates with dimensions and details of the channels within which the refrigerant flows.

The water-ice interface moves outwards over time due to the increasing thickness of ice forming on the plate. Thus it can be approximated as a “Stefan problem” whose definition is “heat transfer problems with phase-changes such as from the liquid to the solid.”⁽³⁰⁾ Heat is transferred from the falling water at a temperature of $T_{w,i}$ by convection, through the ice outer layer (at $T_{l,o}$) to the plate wall (at $T_{s[E].o}$) by conduction, and by convective boiling heat transfer to the refrigerant at saturated evaporating temperature, $T_{r[E]build}$. At the plate wall/ice interface, the ice is sub-cooled, and at the water/ice interface ice is at freezing temperature (0°C). As mentioned above, in order to model the temperature profile within the ice layer, it is assumed that the heat extracted due to sub-cooling is negligible when compared to the latent heat of fusion extracted from the water. Applying the principle of energy conservation to the control volume of Figure 9.1 above, and assuming that all thermophysical properties are independent of temperature, the heat flux from the water/ice interface to the refrigerant is

$$\dot{q}_1 = \frac{T_{I.o} - T_{r[E]build}}{\frac{1}{h'_{r[E]}} + \frac{y_{s[E]}}{k_{s[E]}(T_{r[E]build})} + \frac{y_I}{k_I(T_{r[E]build})}} \quad (86)$$

And the heat flux at the ice/water interface, based on the average external convection heat transfer coefficient for free-falling water \bar{h}'_w is

$$\dot{q}_2 = \frac{T_{w.i} - T_{I.o}}{\frac{1}{\bar{h}'_w}} \quad (87)$$

The difference between \dot{q}_1 and \dot{q}_2 is equal to the rate at which latent heat is removed from the water per unit area, and is predicted as

$$\rho_I h_{sf} \frac{\partial y_I}{\partial t} = \dot{q}_1 - \dot{q}_2 \quad (88)$$

To predict the average external heat transfer coefficient of water flowing over the plate, the External_Flow_Plate procedure of the EES external library is used.⁽³¹⁾ Inputs to the procedure include the free stream fluid temperature (determined from tests performed at the ERPM ice plant and shown in Appendix A6 Table A6.3), the outer ice surface temperature and pressure, as well as the free stream velocity, which is predicted to be 0,274 m/s based on tests performed at the plant (refer to Appendix A3 for this calculation). A brief description of the EES procedure is presented below:

“This procedure determines the property data of the fluid specified and calculating the Reynolds and Prandtl number. The Prandtl, Reynolds and Nusselt number are based on film temperature, which is the average of the free stream and the surface temperature. This procedure then passes the Reynolds and Prandtl number to the non-dimensional procedure External_Flow_Plate_ND. The non-dimensional procedure then returns the values for friction coefficient and Nusselt number. From the friction coefficient and the Nusselt number, External_Flow_Plate calculates the average shear stress and the heat transfer coefficient for convection.”⁽³¹⁾

9.1.1. Brief Overview of the Heat Transfer Correlations used to Predict the Refrigerant Side Convective Boiling Heat Transfer Coefficient

Although “ammonia has been used for more than a century as a refrigerant”⁽³²⁾, “no formal database is currently available on ammonia heat transfer.”⁽³²⁾ Thus, the “great majority of the known correlations for heat transfer in forced convection boiling have not been experimentally validated for the case of ammonia flow boiling in vertical tubes.”⁽³²⁾ However, due to the global trend of environmental and energy awareness, “the industry is now seriously reviewing options for expansion of ammonia into areas other than industrial refrigeration, where it has been successfully used for decades.”⁽³³⁾ Ohadi et al.⁽³³⁾ have performed “a critical review of the available correlations in the open literature for prediction of ammonia two-phase heat transfer.”⁽³³⁾

Zamfirescu and Chiriac⁽³²⁾ have developed a data bank to check the applicability of the available correlations to the heat transfer in subcooled and saturated flow boiling of ammonia in two 0,032m diameter vertical tubes, based on correlations for ammonia found in the literature.⁸⁴ The mass flow rate of the gravitational ammonia flow⁸⁵ was obtained using an ultrasonic flowmeter, with 10 thermocouples placed along the length of the tube to predict the heat transfer coefficient. Results showed that “for a $\pm 20\%$ bandwidth the Shah⁽²⁶⁾ correlation predicted 52% of the (experimental) data (collected) ... (compared to) the Gungor-Winterton⁽²⁸⁾ correlation (which predicted) 85%.”⁽³²⁾ Thus it appears that the Gungor-Winterton correlation predicts experimental data more accurately than that of Shah. An important conclusion from the abovementioned results is that the accuracy of predictions decrease the more general the correlation used. For specific operating parameters (hydraulic diameter, refrigerant, orientation of tubes etc.), the only means of accurately predicting the heat transfer coefficient is by performing tests on the working plant. However, as illustrated in Figure 9.6

⁸⁴ The equivalent hydraulic diameter of one channel of the ERPM plant is 0,012 m.

⁸⁵ Pressurised gas pumps the cold liquid refrigerant through the diameter channels of the evaporator plates at the ERPM plant. Nonetheless, it is assumed that the Shah⁽²⁶⁾ and Gungor-Winterton⁽²⁸⁾ correlations are applicable to this arrangement.

below, accurate predictions of the heat transfer coefficient may not lead to commensurately more accurate results.

An interesting point from the conclusions of Zamfirescu and Chiriac⁽³²⁾ is that “the influence of thermodynamic quality, heat flux and mass velocity on heat transfer is qualitatively the same for ammonia boiling and other refrigerants (i.e. freons, hydrocarbons, water).”⁽³²⁾

Both the Shah⁽²⁶⁾ and Gungor-Winterton⁽²⁸⁾ heat transfer correlations are used to model the refrigerant side convective boiling heat transfer coefficient during ice building. These correlations are outlined below.

The Shah Correlation

Shah⁽²⁶⁾ estimated “the heat transfer coefficient during saturated boiling at subcritical heat flux in tubes and annuli.”⁽²⁶⁾ Shah⁽²⁶⁾ developed his correlations “using data that included eight fluids and a wide range of parameters”⁽²⁶⁾, including horizontal and vertical orientations, varying diameters of tubes and mass flow rates, as well as ammonia boiling experimental data. “Starting with research on heat transfer and pressure drop characteristics of ammonia evaporators, Shah developed a Chart correlation for generalized applications in flow boiling in pipes. Later Shah proposed equations expressing his widely referred Chart correlation.”⁽³³⁾

Shah⁽²⁶⁾ predicts that using the average mean quality across the tube, and by applying four dimensionless parameters, the boiling heat transfer coefficient can be predicted for a wide range of hydraulic diameters and mass flow rates within 14% accuracy. These equations agree with the Chart correlations within 6% over most regions.⁽³³⁾ The following is a brief summary of the methodology used to predict the Shah coefficient.⁽²⁶⁾

The Shah coefficient employs four dimensionless coefficients. The ratio of the heat transfer coefficients of the two-phase flow $h'_{2ph[Sh]}$ and the superficial liquid flow h'_l is denoted as:

$$\psi = h'_{2ph[Sh]} / h'_l \quad (89)$$

Where the superficial heat transfer coefficient of the liquid phase h'_l is calculated by the Dittus-Boelter equation as:

$$h'_l = 0,023 \left(\frac{G(1-x')D}{\mu_{rl}(T_{r[E]build})} \right)^{0,8} Pr_{rl}^{0,4} (T_{r[E]build}) \frac{k_{rl}(T_{r[E]build})}{D} \quad (90)$$

Where G is the mean mass flux on the cross-section of the tube, D is the internal diameter of the tube, μ_{rl} is the dynamic viscosity of liquid ammonia at $T_{r[E]build}$, x' is the vapour quality, k_{rl} is the thermal conductivity of the liquid, and Pr_{rl} is the Prandtl number, both at $T_{r[E]build}$. The ratio ψ is dependent on the convection number Co , and the boiling number Bo :

$$Co = \left(\frac{1}{x'} - 1 \right)^{0,8} \left(\frac{\rho_{rv}(T_{r[E]build})}{\rho_{rl}(T_{r[E]build})} \right)^{0,5} \quad (91)$$

$$Bo = \frac{\dot{q}_1}{Gh_{fg}(T_{r[E]build})}$$

Finally, the value of ψ in the bubble suppression regime based on, and at various values of Co is:

$$\psi_{bs} = 15,43Bo^{0,5} \exp(2,47Co^{-0,15}) \quad (92)$$

And in the convective boiling regime:

$$\psi_{cb} = \frac{1,8}{Co^{0,8}} \quad (92b)$$

The larger of ψ_{bs} or ψ_{cb} is substituted into equation (89) to obtain $h'_{2ph\{Sh\}}$.

Shah's data was compared with "a large amount of data for boiling in tubes"⁽²⁶⁾ and correlation with all experimentation results of between 23 % - 30 % was achieved. Owing to the fact that the model was verified with some 3000 data points, and for various fluids (including ammonia) in tubes of various diameters, "one can feel considerable confidence in its reliability and general applicability."⁽²⁶⁾ As mentioned above, although the shape of the channels of the plate through which refrigerant flows is elliptical, they are modelled as a vertical tube with the same cross sectional area, and serving both sides of the plate.

This model is compared to the flow boiling in a vertical tube procedure in EES⁽³⁴⁾, which is based on the Shah⁽²⁶⁾ correlation and considers both nucleate and convective boiling conditions. The governing equations of the EES⁽³⁴⁾ procedure are not provided: however, this procedure is used as a comparison to the Shah correlation as well as to the Gungor-Winterton correlation now described.

The Gungor-Winterton Correlation

A third model used to predict the refrigerant side convective boiling heat transfer coefficient is that of Gungor & Winterton,⁽²⁸⁾ who calculated the boiling heat transfer coefficient for various fluids at saturated and subcooled boiling conditions. This correlation aims to be as general as possible whilst attempting to be a close fit to the data accumulated. The correlation covers a large range of fluids in horizontal and vertical orientations and tube diameters ranging from 3 – 32 mm. This correlation is therefore similar to that of Shah in that it provides a general procedure for predicting the convective boiling heat transfer coefficient for many fluids (including ammonia) in vertical tubes of various diameters.

Gungor & Winterton⁽²⁸⁾ divided the heat transfer into two parts, a microconvective (nucleate boiling) contribution based on pool boiling, and a macroconvective contribution (non-boiling forced convection), based on the famous Dittus-Boelter

equation (equation (90) above). The following is the form of the correlation to predict the convective boiling heat transfer coefficient of ammonia and other refrigerants in vertical tubes:

$$h'_{2ph[G]} = Eh'_l + Sh'_p \quad (93)$$

where

$$h'_l = 0,023 \left(\frac{G(1-x')D}{\mu_{rl}(T_{r[E]build})} \right)^{0.8} Pr_{rl}^{0.4} (T_{r[E]build}) \frac{k_{rl}(T_{r[E]build})}{D}$$

$$h'_p = 55 Pr_{rl}^{0.12} (T_{r[E]build}) \left[\log_{10} Pr_{rl} (T_{r[E]build}) \right]^{-0.55} m_m^{-0.5} \dot{q}_1^{0.67} \quad (94)$$

Here, m_m is the molecular weight of the fluid, which in the case of ammonia, is 17.03.⁽³⁾ In equation (93) above, the enhancement factor, E , takes into account the two-phase nature of the refrigerant. The final values for E and S (suppression factor) make use of the boiling number, Bo from Shah⁽²⁶⁾ and the Lockhart-Martinelli parameter X_{tt} in equation (95b) below:

$$E = 1 + 24000 \cdot Bo^{1.16} + 1,37 * (1 / X_{tt})^{0.86}$$

$$S = \frac{1}{1 + 1,15 * 10^{-6} E^2 \left(\frac{G(1-x')D}{\mu_{rl}(P_{r[E]build})} \right)^{1.17}} \quad (95)$$

$$X_{tt} = \left| \left(\frac{\rho_{rv}}{\rho_{rl}} \right)^{0.5} \left(\frac{\mu_{rl}}{\mu_{rv}} \right)^{0.1} \left(\frac{1-x'}{x'} \right)^{0.9} \right|_{T_{r[E]build}} \quad (95b)$$

Gungor & Winterton state, “Only the equations developed in the present paper Gungor et. al⁽²⁸⁾ and those of Shah give reasonable agreement with all of the saturated boiling data. If a more detailed comparison is made with data of individual authors the disagreement (on mean deviation) does not exceed 58% (present study) or 65% (Shah).”⁽²⁸⁾ Thus it appears that the Shah and Gungor-Winterton correlations are the most general of all the ammonia convective boiling

heat transfer coefficients. The three correlations described above⁸⁶ are used to predict the refrigerant side convective boiling heat transfer coefficient h_r' . Due to the generality of these correlations, based on large data banks for various fluids⁸⁷ (including ammonia), pipe diameters and orientations, they are considered suitably accurate to predict operating conditions at the ERPM plant. Since the Gungor-Winterton correlation is shown from the study of Zamfirescu and Chiriac,⁽³²⁾ outlined in Section 9.1.1 above, to predict experimental data within greater accuracy than that of Shah (85 % as compared to 52 % for Shah), this correlation will be used as the basis for comparing the other two correlations (Shah and EES) described above.

9.1.2. Predicting the Layer of Ice Built during the Ice Building Period

Predicting the Time Required for the Steel Wall to reach Ice Building Temperature during the Re-Cooling Sub-Period⁸⁸

Before the heat transfer model during ice building can be presented, the time required to re-cool the outer wall of the evaporator plate to evaporating temperature, which occurs at the beginning of the re-cooling sub-period of the harvesting period - before feed water is introduced and ice starts to build - is predicted. Three predictions of the convective boiling heat transfer coefficient are used, based on Shah (equation (89)), Gungor & Winterton (equation (91)) and EES.⁽³⁴⁾ It is assumed (and validated below from predictions of the model during the warming sub-period of the harvesting period) that at the end of the warming sub-period, the inner steel wall reaches saturated harvesting temperature $T_{r.har}$.

Using the one-term approximation of the Fourier series for transient heat conduction⁽²⁴⁾, and verifying the results with the corresponding one-term procedure in EES⁽⁴⁰⁾, the transient response of a semi-infinite plate with the inner wall exposed to convection and the outer wall adiabatic is predicted. Assuming all steel properties (density, specific heat etc) are uniform and constant at evaporating

⁸⁶ That of Shah, EES and Gungor & Winterton.

⁸⁷ As mentioned above, the EES correlation is based on the Shah⁽²⁶⁾ correlation

⁸⁸ This period is defined in Section 8.2.2 and by the dashed rectangle between $(t_3 - t_2)$ in the timing diagram of Figure 3.2

temperature, the mid-point temperature of the evaporator's steel wall is predicted based on the Fourier and Biot numbers as follows:

$$\begin{aligned}
 B_i &= \frac{h'_r L_{c.s[E]}}{k_{s[E]} (T_{r[E]build})} \\
 \alpha_{s[E]} &= \left[\frac{k_{s[E]}}{\rho_{s[E]} c_{s[E]}} \right]_{(T_{r[E]build})} \\
 F_o &= \frac{\alpha_{s[E]} t_{l,b}}{L_{c.s[E]}} \\
 \frac{(T_{s[E]} - T_{r[E]build})}{(T_{r[E]har} - T_{r[E]build})} &= C e^{-\xi^2 F_o}
 \end{aligned} \tag{96}$$

Where for a plane wall, the values of C and ξ are functions of Biot number only:

$$\begin{aligned}
 (\xi) \tan(\xi) &= B_i \\
 C &= \frac{4 \sin(\xi)}{2(\xi) + \sin(2(\xi))}
 \end{aligned} \tag{97}$$

Inputting the known variables into equations (96) and (97) above and solving for the mid-point steel wall temperature $T_{s[E]}$, the change in temperature over time at the mid-point of the steel wall can be predicted. As mentioned above, the one-term procedure in EES⁽⁴⁰⁾ for transient conduction in a plane wall is used to obtain the change in temperature over time for the steel wall. The inputs to the procedure are the distance from the adiabatic surface (for the mid point of the evaporator's steel wall $0,5L_{c.s[E]}$), the Biot and the Fourier number.

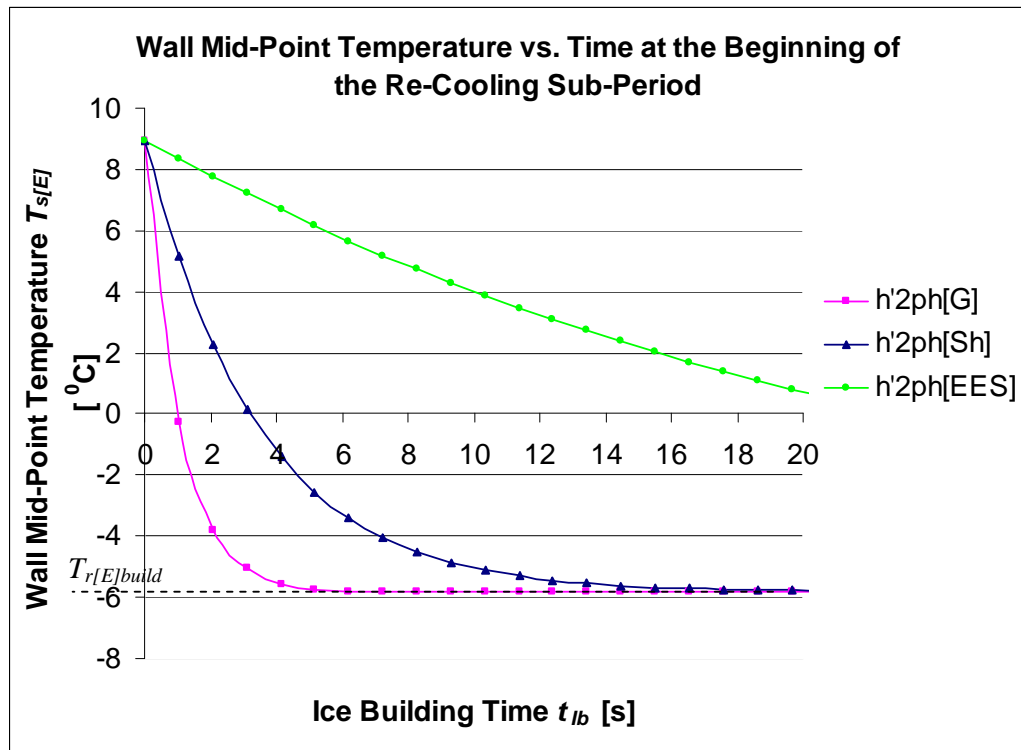


Figure 9.3 Wall mid-point temperature versus time at the beginning of the re-cooling sub-period.

Referring to the figure above, both the Shah and Gungor-Winterton correlations predict that the mid-point of the steel wall reaches evaporating temperature within 20 seconds from the beginning of the re-cooling sub-period. The EES correlation predicts that the mid-point of the wall approaches $T_{r[E]build}$ only after 150 seconds. From Section 8.2.2, because there is liquid at harvesting temperature trapped behind the level regulating valve at the beginning of the re-cooling sub-period, when the evaporator module is depressurised, this trapped liquid flash boils to accumulator pressure. The cooling effect of this boiling liquid materially assists in lowering the temperature of the steel module, and therefore the module will re-cool in an even faster time than predicted by Figure 9.3 above.

Predicting the Layer of Ice Built from the Different Convective Heat Transfer Coefficients

An ice building period of one module lasts for 13,5 minutes. The mass flow rate of liquid through the evaporator is predicted from equation (69) of Section 8.6.1 above and is based on an assumed thickness of 5 mm for the particulate ice delivered, and 1 mm for the innermost subsequently melted ice layer.

As mentioned in Section 8.6.1, the mass flow rate predicted in Appendix A8, based on the dimensions of the pumper drum and the mass circulated to the evaporator in the measured pumping time, is 0,3 % smaller than that predicted from equation (69) for an input average recirculation ratio of 5. Therefore, as there is sufficiently accurate agreement between the two methods of predicting the mass flow rate through the evaporator for the cold gas pumped arrangement, the mass flow rate through the channels based on equation (69) is an input into the heat transfer model developed in the equations above.

Based on this input mass flow rate of refrigerant through the channels of the evaporator, and varying the average recirculation ratio (denoted as x_1), the three coefficients of the convective boiling heat transfer model during ice building are plotted and shown in the graph below. It is recalled that there are 35 plates per module and 30 channels per plate. If it is assumed that the refrigerant flows uniformly through each channel, each channel is in effect two sub channels - serving opposite sides of the plate. Thus the refrigerant mass flow can be considered as being split among sixty channels. This assumption facilitates the analysis presented in equations (86), (87), (88) and (96) where it is assumed in these equations that ice is built on one side of the plate.

The results presented below therefore apply for one sub-channel feeding one side of the plate.

Figure 9.4 below shows the two convective boiling heat transfer coefficients developed above of Shah (equation (89)) and Gungor & Winterton (equation (91)), and including the coefficient predicted by EES⁽³⁴⁾ for comparison purposes, at varying average recirculation ratios. As the mass flow rate to build the required

ice layer increases as the average recirculation ratio increases, this graph illustrates the effect that increasing the average recirculation ratio has on the three heat transfer coefficients.

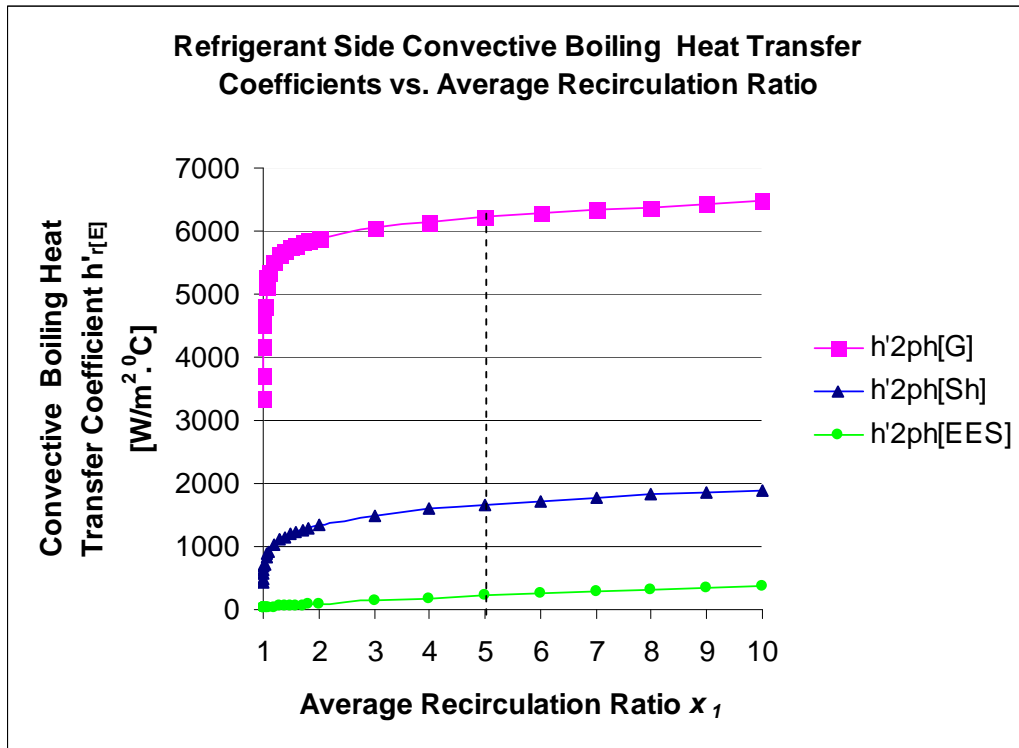


Figure 9.4 Refrigerant side convective boiling heat transfer coefficients versus inverse of quality (average recirculation ratio x_1). The average recirculation ratio of 5 predicted for the operating ERPM plant is shown as a dashed line

From the figure above, the convective boiling heat transfer coefficient based on Shah⁽²⁶⁾ and that of the EES procedure show a wide divergence as average quality of refrigerant decreases (average recirculation ratio increases). Although both $h'_{2ph[Sh]}$ and $h'_{2ph[EES]}$ are based on the correlations of Shah⁽²⁶⁾, for recirculation ratios close to one, the EES model returns the heat transfer coefficient for a single phase vapour at the given mass velocity and diameter.⁽³⁴⁾ Thus the discrepancy at lower recirculation ratios between the two coefficients is due to the fact that the EES procedure does not assume that all the refrigerant flow is changed to vapour at lower recirculation ratios (approaching one). In this limit, not only does the vapour not wet the interior surface of the tube sufficiently to maintain good thermal contact, but the heat transfer along the tube is due to sensible heat only.

Both these factors effectively lower the convective boiling heat transfer coefficient predicted by the EES procedure at lower average recirculation ratios (<5). At higher average recirculation ratios, the low ratio of the mass flow rate to the cross-sectional area of the tube (mass velocity) is responsible for the low heat transfer coefficient. As mentioned above, the governing equations for the EES procedure could not be investigated and it is therefore included for comparison purposes only.

From Figure 9.4 above, the Shah ($h'_{2,ph[Sh]}$) and Gungor-Winterton ($h'_{2,ph[G]}$) correlations predict that as the average recirculation ratio approaches one, the heat transfer coefficient approaches a lower limit⁸⁹, however, they both increase rapidly as the ratio increases. However, there also appears to be a wide divergence between these two correlations. From Section 8.6.1, the average recirculation ratio at the operating ERPM plant, based on test data, is predicted as 5. At this ratio, the convective boiling heat transfer coefficients for the three correlations and the percentage difference as compared to $h'_{2,ph[G]}$ are shown in the table below.

Table 9.1 Refrigerant side convective boiling heat transfer coefficients at an average recirculation ratio of 5

$h'_{2,ph[G]}$ [W/m ² .C]	$h'_{2,ph[Sh]}$ [W/m ² .C]	$h'_{2,ph[EES]}$ [W/m ² .C]
6219	1666	221
0 %	73,21 %	96,45 %

From Table 9.1 above, the three heat transfer coefficients, at an average recirculation ratio of 5, differ significantly, with the Gungor-Winterton model predicting the largest coefficient. Whether this large divergence between the three correlations results in the Gungor-Winterton correlation predicting a commensurately larger thickness of ice built is determined by substituting the coefficients from

⁸⁹ As can be seen in the compressed scale of Figure 9.4 above, between average recirculation ratios of 1 and 2.

Table 9.1 above into $h'_{r[E]}$ of equation (86) above. The final thickness of ice built over the ice building period of 13,5 minutes⁹⁰, from the numerical solution to equation (88), is predicted and shown in the graph below:

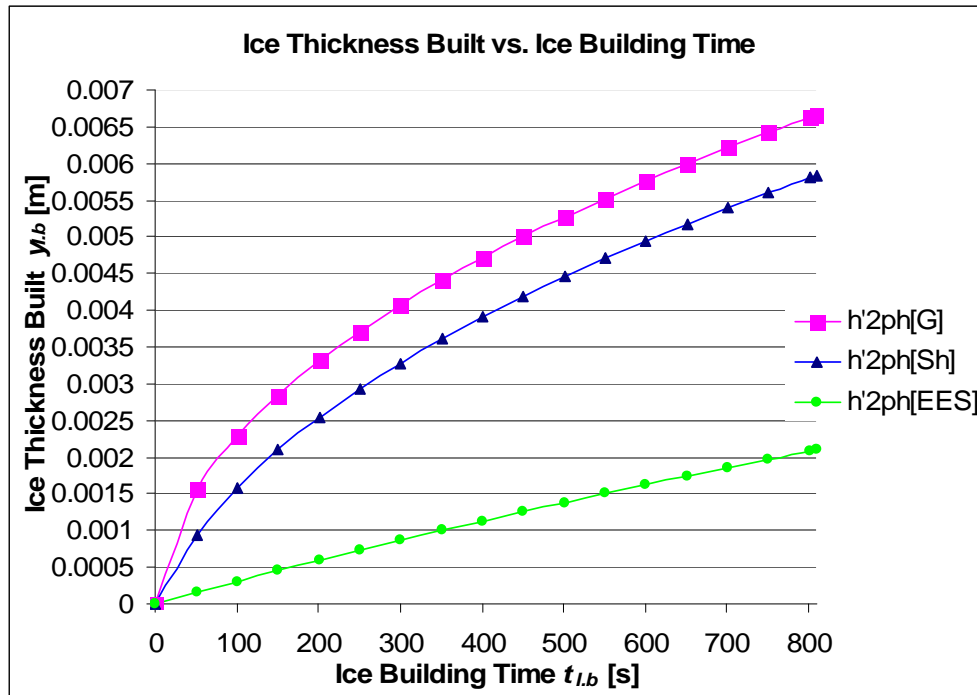


Figure 9.5 Thickness of ice built versus time at an average recirculation ratio of five

From the above graph, for the predicted mass flow rate at the operating ERPM plant yielding an average recirculation ratio of 5, the thickness of ice built does not vary significantly for the correlations of Gungor-Winterton and Shah, but does differ considerably if the EES correlation is used. The ice thickness built on one side of each plate, based on tests performed at the plant and from Worthington Smith & Brouwer⁽¹³⁾ and Rankin⁽¹⁴⁾ is approximately 5-6 mm (refer to Appendix A6 for these results). Therefore, considering that some ice is melted during the harvesting process (Section 9.2 below predicts this melted layer to be approximately 1 mm thick), the correlations of Gungor-Winterton and Shah slightly over-predict and under-predict respectively the thickness of ice built on

⁹⁰ From Figure 9.3 it is justifiably assumed for all correlations except that of EES that the mid-point of the evaporator wall reaches ice building temperature relatively quickly, and therefore it can further be assumed that ice is built over the full 13,5 minutes.

one side of the plate during one ice building period. The thicknesses of ice built using the correlation of Gungor & Winterton and for the input mass flow rate and average recirculation ratio based on the model of Section 8. above, agree to within 11,0 % with the same thickness input into equation (69) of Section 8.⁹¹ If the Shah correlation is used, the percentage difference is 2,7 %. Therefore, the model presented in this section is a further substantiation of the average recirculation ratio and mass flow rate predicted in the model of Section 8. above.

The EES correlation considerably under-predicts the ice built layer and as mentioned above, is therefore only included in the model for the purpose of comparison.

Referring to Figure 9.5 and Table 9.1 above, the large difference in the values of the convective boiling heat transfer coefficients of Gungor & Winterton and Shah does not result in a commensurately large difference in thickness of ice built (12,37 % difference in Table 9.2 below). In fact, from Figure 9.6 below, the variation in the thickness of ice built for convective boiling heat transfer coefficients ranging from 1600 – 11500 W/m².C is only 14,66 %.

The values of the convective boiling heat transfer coefficient, together with the thickness of ice built that is predicted from equation (88) by inputting these coefficients into equation (86) above, is shown in the table below.

Table 9.2 Parameters predicted from the heat transfer model during ice building at an average recirculation ratio of 5

h'_r [W/m ² .C]	$h'_{2ph[G]}$ [W/m ² .C]	$h'_{2ph[Sh]}$ [W/m ² .C]	$h'_{2ph[EES]}$ [W/m ² .C]
Final values	6219	1666	221
Final predicted thickness of ice built $y_{l,b}$	6,67 mm	5,84 mm	2,11 mm
% Difference: $y_{l,b}$	0%	12,37 %	68,37 %

⁹¹ 6 mm is used in equation (69) as the upper limit based on Worthington Smith & Brouwer⁽¹³⁾ and Rankin⁽¹⁴⁾

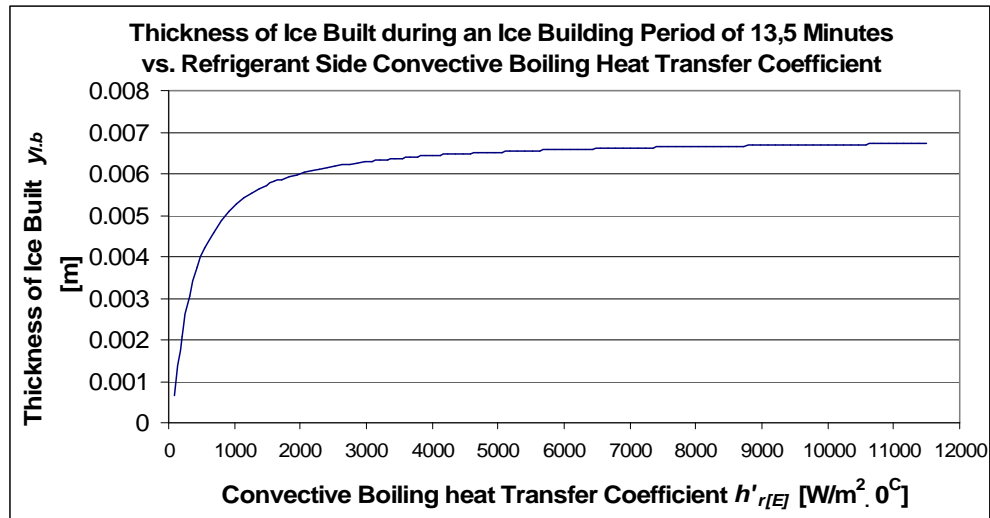


Figure 9.6 Ice thickness built during an ice building period of 13,5 minutes versus refrigerant side convective boiling heat transfer coefficient

From Figure 9.7 below, the thickness of ice built during an ice building cycle is dependent on the refrigerant mass flow rate, which in turn is dependent on the average recirculation ratio. For an average recirculation ratio above 2, sufficient wetting of the inner tube surface allows for the ice thickness built, based on the heat transfer coefficients of Gungor-Winterton and Shah, to approach convergence - irrespective of increasing ratios. From Section 8.6.1 above, the predicted average recirculation ratio at the operating ERPM plant is 5. From Figure 9.7 below, the ice layer built is approximately at its maximum value for the Gungor-Winterton and Shah convective boiling heat transfer coefficients at a recirculation ratio of 5.

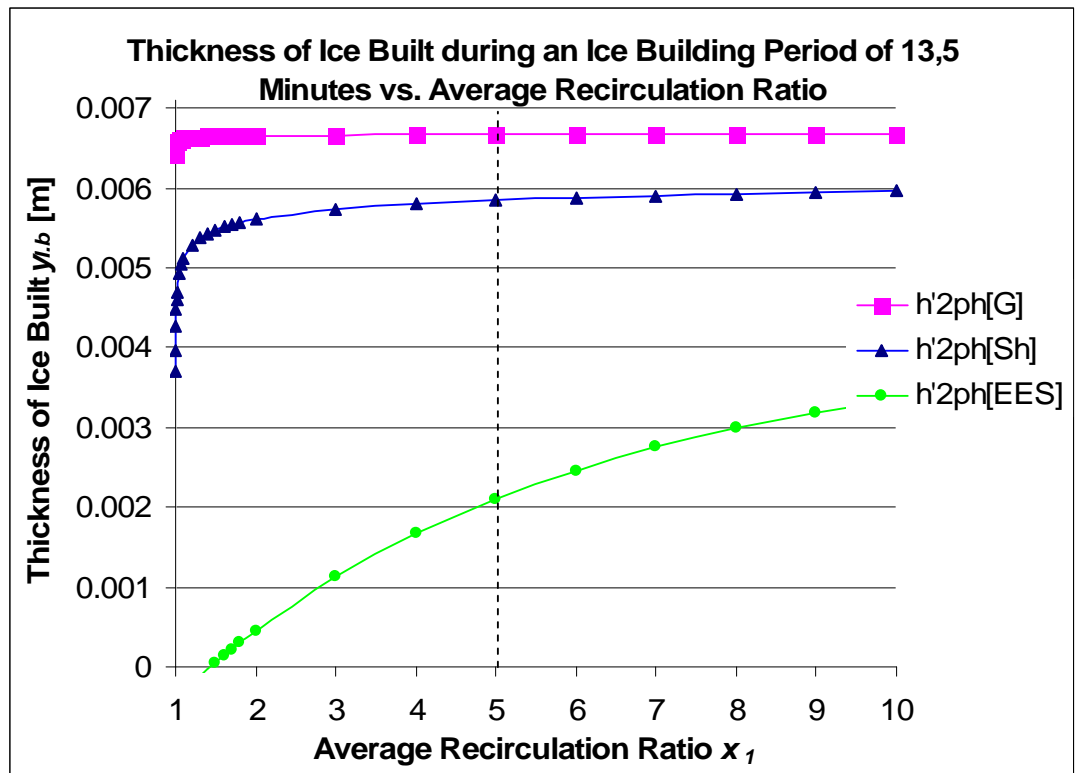


Figure 9.7 Thickness of ice built during the ice building period of 13,5 minutes versus average recirculation ratio for the different heat transfer coefficients. The average recirculation ratio of 5 predicted for the operating ERPM plant is shown as a dashed line.

As the model presented above only predicts the ice layer that is built during the 13,5 minute ice building period, it cannot predict what percentage of this layer is subsequently melted during the warming sub-period. Therefore to accurately predict the URD of building this subsequently melted ice layer, which from Table 8.2 of Section 8.10.3, constitutes 68 - 78 % of the total URD for all pumping arrangements, a heat transfer model during the warming sub-period is developed below.

9.2. Heat Transfer Model during the Warming Sub-Period of the Harvesting Period

As with the ice building period, predicting the refrigerant side convective condensing heat transfer coefficient during the warming sub-period of the harvesting period⁹² is complex. The transient nature of the warming sub-period makes it difficult to model accurately, as well as to corroborate with experimental data. Nonetheless, the following model attempts to predict the thickness of ice melted $y_{l,m}$ over the warming sub-period based on fundamental heat transfer analysis, assuming that the ice sheet falls off the plate only at the end of this period.

“Harvesting” or ice shedding is achieved by passing hot refrigerant gas at harvesting pressure $P_{r,har}$ through the channels in the plate. As the ice layer is sub-cooled, the following assumptions are made in order to develop the fundamental equations:

1. At the beginning of the warming sub-period there is a linear temperature distribution within the ice layer.
2. The warming sub-period lasts for 90 seconds, and the ice sheet falls off the evaporator plates only at the end of this period.
3. The inner ice layer is at saturated evaporating temperature of the liquid refrigerant, $T_{r[E]build}$ and the temperature of the outer ice layer $T_{l,o}$ is at zero degrees as shown in Figure 9.8 below.

⁹² This period is defined in Section 8.2.1 and by the hatched rectangle between $(t_2 - t_1)$ in the timing diagram of Figure 3.2 above.

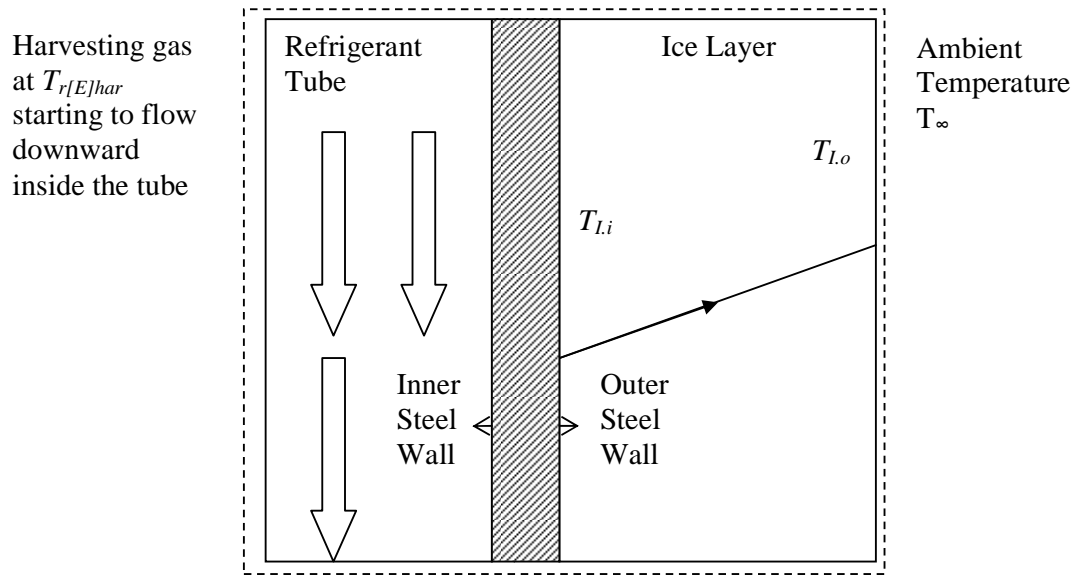


Figure 9.8 Linear temperature distribution in the built up ice layer at the beginning of the warming sub-period

Theoretically, when the melted ice layer reaches zero degrees, the ice sheet should slide off the wall. However, the ice layer would tend to “stick” to the plate wall due to surface roughness and shear forces within the melted ice layer, and it would be necessary to melt a portion of this ice layer. Senatore⁽⁴⁾ investigated this “stiction” time, and predicted the “stiction” parameter based on observations of the ice sticking to the outside of tube evaporators at the end of the warming sub-period of a harvesting period.

Modelling the shear force in the melted ice layer using viscous flow models may suggest that although the requisite ice is melted in a shorter time period than predicted by Worthington Smith & Brouwer⁽¹³⁾ of 90 seconds, this period may include some time to allow for the ice sheet to overcome its “stiction”. Although predicting the “stiction” parameter for the operating plant is beyond the scope of this investigation, it is nonetheless assumed for the model presented below, that due to “stiction” the melted ice layer is warmed up to an intermediate temperature whilst it remains in contact with both the plate and the ice sheet.

9.2.1 Predicting the Evaporator Steel Temperature Distribution during the Warming Sub-Period

It was first assumed that before the inner ice layer can begin melting, the entire ice layer must first lose all of its sub-cooling and reach zero degrees. Under this assumption, the time required for this process to be completed before any ice is melted is approximately the same time required for the outer steel wall to reach 0°C. Assuming that the steel wall can be modelled as a semi-infinite plate, is insulated adiabatically on one side (outer wall) by the ice layer, and is exposed to the refrigerant at harvesting pressure and temperature on the inside, the one-term approximation of the Fourier series for transient heat conduction⁽²⁴⁾ can be used to predict the time required for the outer wall to reach 0°C. All steel properties (density, specific heat etc) are assumed uniform and constant at harvesting temperature $T_{r[E]har}$. As for the transient conduction model during ice building of Section 9.1 above, results are compared to and verified with the one-term procedure in EES.⁽⁴⁰⁾ The Biot and Fourier numbers during harvesting are predicted as:

$$\begin{aligned}
 B_i &= \frac{h'_{r.har} L_{c.s[E]}}{k_{s[E]} (T_{r[E]har})} \\
 \alpha_{s[E]} &= \left[\frac{k_{s[E]}}{\rho_{s[E]} C_{s[E]}} \right]_{(T_{r[E]har})} \\
 F_o &= \frac{\alpha_{s[E]} t_{har}}{L_{c.s[E]}^2} \\
 \frac{(T_{s[E]har} - T_{r[E]har})}{(T_{r[E]build} - T_{r[E]har})} &= C e^{-\xi^2 F_o}
 \end{aligned} \tag{98}$$

Where for a plane wall, the values of C and ξ are functions of Biot number only:

$$\begin{aligned}
 (\xi) \tan(\xi) &= B_i \\
 C &= \frac{4 \sin(\xi)}{2(\xi) + \sin(2(\xi))}
 \end{aligned} \tag{99}$$

The refrigerant side convection condensing heat transfer coefficient $h'_{r.har}$ is derived below. Inputting the known variables into equations (98) and (99) above

and solving for the steel wall temperature $T_{s[E]har}$, the change in temperature over time at the inner and outer steel wall can be predicted and is shown in the figure below.

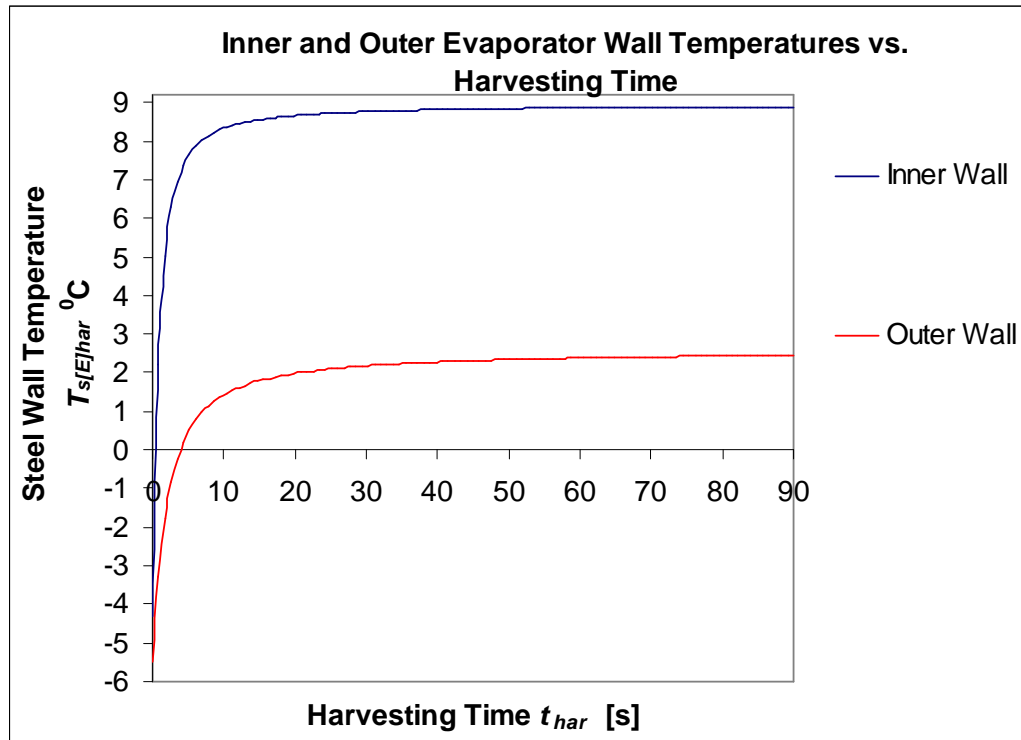


Figure 9.9 Temperatures of the inner and outer evaporator steel wall versus time during harvesting, assuming that the outside of the plate is insulated adiabatically by the ice layer.

Referring to the above graph, the harvesting gas heats up the outer steel wall to 0° C (and thus ice melting can begin) in a relatively short period of time (within 4 seconds). The final outer plate wall temperature at the end of the warming sub-period from the one-term approximation is 2,45 °C.

9.2.2 Predicting the Temperature reached by the Melted Ice Layer at the end of the Warming Sub-Period

Now, based on a suggestion of Bailey-McEwan⁽³⁵⁾, the above assumption is disregarded⁹³, and it is assumed that only the melted ice layer loses its sub-cooling

⁹³ That the inner ice layer only begins melting once the entire ice sheet has lost its sub-cooling.

prior to melting, whilst the remaining ice layer retains all of its sub-cooling. This melted ice layer which has turned to water (reaching temperatures of $T_{I.m.har}$ (initially at zero degrees) at the end of the warming sub-period), would now act as an additional conductive resistance to heat flow, absorbing heat from the wall at one end, whilst being cooled by the remaining ice layer at the other, as illustrated in Figure 9.10 below. Thus it must be assumed that even though a layer of water is stationary between the remaining ice layer and the wall, only at the end of the warming sub-period does the ice sheet detach itself from the wall. As mentioned above, this assumption is based on Senatore⁽⁴⁾ who predicted that the ice sheet would remain in position due to “stiction” between the sheet and the steel evaporator wall.

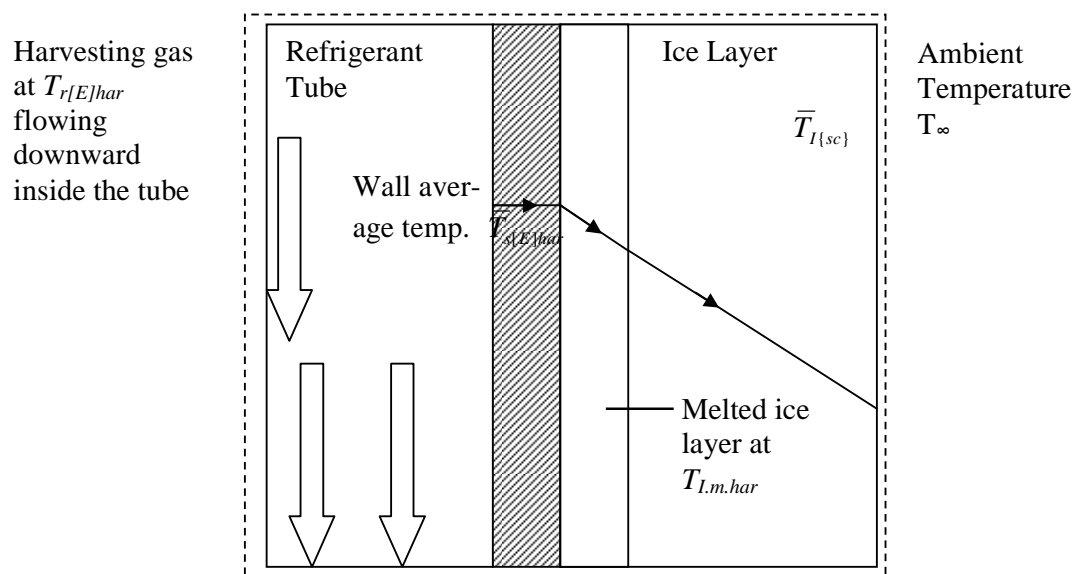


Figure 9.10 Temperature distribution of the control volume at the evaporator during the warming sub-period, including the melted ice layer at temperature $T_{I.m.har}$ (ignoring the natural convection effect of the ambient air at T_{∞}).

Modifying the heat balance equation of the control volume shown in Figure 9.10 to include conduction from the plate wall through the melted ice layer to the remaining ice sheet, the temperature change of the melted ice layer ($T_{I.m.har}$) at the end of the warming sub-period can be predicted by solving the following equation:

$$-\left[\rho_w c_w\right]_{T_{I,o}} y_{I,m} \frac{\partial T_{I,m,har}}{\partial t} = -k_s (T_{r[E]har}) (\bar{T}_{s[E]har} - T_{I,m,har}) + k_l (\bar{T}_{I\{sc\}}) (T_{I,m,har} - \bar{T}_{I\{sc\}}) \quad (100)$$

Where $\bar{T}_{I\{sc\}}$ is the average temperature of the linearly sub-cooled ice layer, and the wall temperature during harvesting $\bar{T}_{s[E]har}$ is assumed to be the average of the inner and outer wall temperatures as shown in Figure 9.9 above.

As the melted ice layer's thickness $y_{I,m}(t)$ is a function of time, the equation above is solved simultaneously with equations (98), (104) and (105). The solution of equation (100) over the entire warming sub-period of 90 seconds, is shown in the figure below.

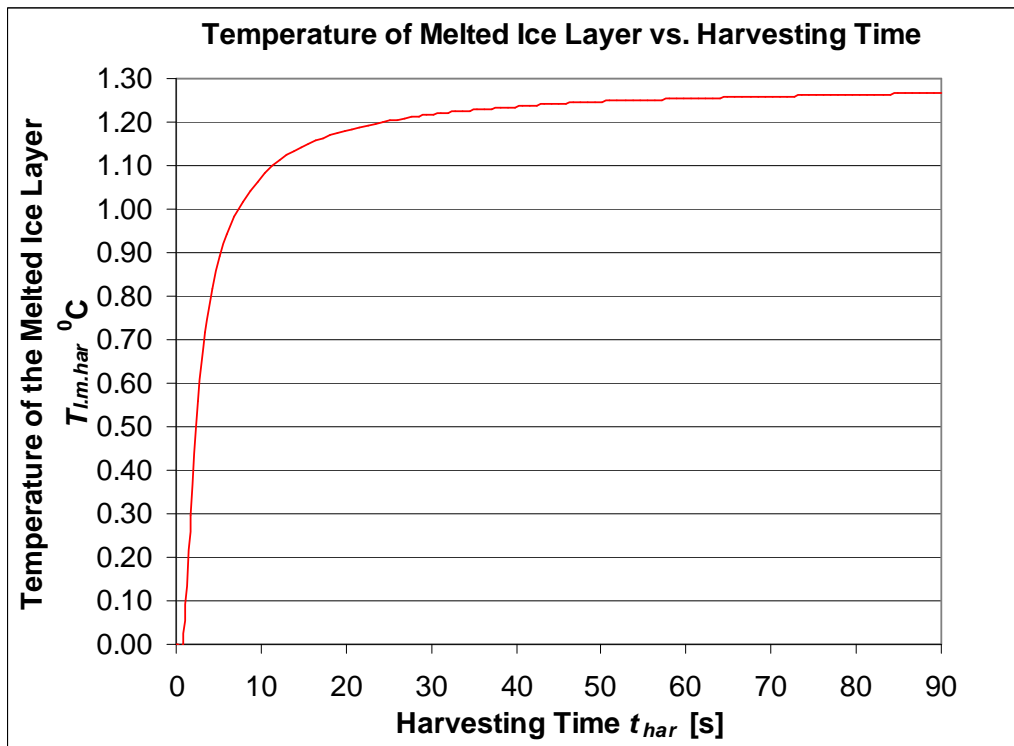


Figure 9.11 Temperature of the melted ice layer during the warming sub-period

Referring to Figure 9.11 above, the melted ice layer reaches $1,27^{\circ}\text{C}$ at the end of the warming sub-period. Since the inner ice layer can only begin melting once the outer plate wall temperature reaches 0°C as shown in Figure 9.9 above, the

melted ice layer does not vary significantly from zero degrees throughout the warming sub-period.

9.2.3 Predicting the Melted Ice Layer Thickness

Applying the principle of energy conservation to the control volume of Figure 9.10 above, and assuming that all thermophysical properties are independent of temperature, the heat flux from the refrigerant to the melted ice layer is

$$\dot{q}_1 = \frac{(T_{r[E]har} - T_{I.m.har})}{\frac{1}{h'_{r.har}} + \frac{y_{s[E]}}{k_{s[E]}(T_{r[E]har})} + \frac{y_{I.m}}{k_w(T_{I.m.har})}} \quad (101)$$

And the heat flux at the melted / remaining ice layer interface, based on the average sub-cooled temperature of the remaining layer is

$$\dot{q}_2 = \frac{(T_{I.m.har} - \bar{T}_{I\{sc\}})}{\frac{y_{I.b} - y_{I.m}}{k_I(\bar{T}_{I\{sc\}})}} \quad (102)$$

The difference between \dot{q}_1 and \dot{q}_2 is equal to the rate at which ice is melted and warmed per unit area, and is predicted as

$$\rho_I h_{sf} \frac{\partial y_{I.m}}{\partial t} = \dot{q}_1 - \dot{q}_2 \quad (103)$$

The final heat transfer equation during the warming sub-period of the harvesting process, including the melted ice layer at $T_{I.m.har}$, and the ice layer at $\bar{T}_{I\{sc\}}$ is:

$$\rho_I h_{sf} \frac{\partial y_{I.m}}{\partial t} = \frac{(T_{r[E]har} - T_{I.m.har})}{\frac{1}{h'_{r.har}} + \frac{y_{s[E]}}{k_{s[E]}(T_{r[E]har})} + \frac{y_{I.m}}{k_w(T_{I.m.har})}} - \frac{(T_{I.m.har} - \bar{T}_{I\{sc\}})}{\frac{y_{I.b} - y_{I.m}}{k_I(\bar{T}_{I\{sc\}})}} \quad (104)$$

Where $y_{l,b}$ is the thickness of the ice sheet that is built during the ice building period and is predicted in Table 9.2 above to be 6,31 mm (which is the average thickness of ice built from the Gungor-Winterton and Shah correlations). Equation (104) is integrated over the 90 second harvesting period and solved numerically in EES, simultaneously with equations (98), (100) and (105). The various convective condensation vertical-tube heat transfer coefficients predicted in the models of Section 9.2.5 below are substituted into $h'_{r,har}$ of equation (104) above, and the results are shown in Figure 9.13 below.

9.2.4 Predicting the Mass Flow Rate of Harvesting Gas during the Warming Sub-Period

To predict the convective condensing heat transfer coefficients described below, it is first necessary to predict the mass flow rate of harvesting gas during the warming sub-period. Recall from equation (28) of Section 8.2.1 above that the final energy rate balance equation for the control volume of Figure 8.3 is:

$$\begin{aligned} \Delta U_{s[E]} + \Delta U_{rl.trap[E]} + \Delta U_{rv.trap[E]} = & Q_{cv} + \Delta m_{rv[REC-E]} h_{rv}(P_{r,har}, T_{r,har}) \\ & - \Delta m_{rl.comt[E-ACC]} h_{rl}(P_{r[E]har}, T_{r[E-ACC]}) \\ & - m_{rl\{c\}} h_{rl}(P_{r[E]har}, \bar{T}_{r\{c\}}) \end{aligned} \quad (28)$$

where the internal energy gains on the left-hand side of the equation are:

$\Delta U_{s[E]}$: of the steel of the evaporator plates and their inlet and outlet manifolds;

$\Delta U_{rl.trap[E]}$: of the refrigerant liquid in the plates and manifolds; and

$\Delta U_{rv.trap[E]}$: of the refrigerant vapour confined in the plates between the beginning and the end of harvesting.

The heat transfer across the control volume Q_{cv} is that required to melt the innermost layer of ice and to release its sub-cooling. As the additional heat transfer required to warm this melted ice layer to $T_{l,m,har}$ is an assumption and could not be verified by testing at the operating plant, it is not considered in Q_{cv} . Furthermore,

the specific heat of water is considered negligible when compared to the latent heat of fusion of ice formation (4,186 kJ/kg.C and 335,0 kJ/kg respectively). Therefore, to retain consistency between the models of Section 8. and Section 9.1, and *only* for the purpose of predicting the mass flow rate of harvesting gas, it is assumed that the ice detaches from the steel wall once it reaches 0 °C as opposed to $T_{L.m.har}$.

The remaining variables are defined in Section 8.2.1 above, however, equation (28) is based on the following assumptions that have been outlined in Section 8.2.1, and are summarised briefly here for the purpose of clarity:

1. At the beginning of the warming sub-period, denoted (t_1) in equations (26) and (27) above, the internal refrigerant volume of the plates is comprised of 30 % liquid and 70 % vapour at saturated ice building temperature $T_{r[E]build}$.
2. At the end of the warming sub-period, denoted (t_2) in equations (26) and (27) above, the internal volume of the plates is comprised of 5 % trapped liquid and 95 % trapped vapour at saturated harvesting temperature $T_{r[E]har}$.
3. The mass of liquid condensed $m_{r\{c\}}$, at saturated harvesting temperature $T_{r[E]har}$ is predicted in equation (32) above.
4. The mass of liquid transferred out of the module $\Delta m_{r\{cont\}[E-ACC]}$ at the beginning of the warming sub-period, assuming all densities are at evaporating pressure, is predicted in equation (34) above.
5. The incoming harvesting gas condenses to warm up the steel plates and the manifolds as per equation (25) above.

Therefore, the final form of equation (28) over the warming sub-period of 90 seconds is:

$$\begin{aligned}
& m_{s[E]} c_s (T_{r[E]build}) \left[T_{sat}(P_{r[E]har}) - T_{sat}(P_{r[E]build}) \right] \\
& + (0,05V_{[E]} \rho_{rl}(P_{r[E]har}))_{(t2)} u_{rl}(P_{r[E]har}) - (0,30V_{[E]} \rho_{rl}(P_{r[E]build}))_{(t1)} u_{rl}(P_{r[E]build}) \\
& + (0,95V_{[E]} \rho_{rv}(P_{r[E]har}))_{(t2)} u_{rv}(P_{r[E]har}) - (0,70V_{[E]} \rho_{rv}(P_{r[E]build}))_{(t1)} u_{rv}(P_{r[E]build}) \quad (105) \\
& = -2n \rho_I a_{[E]} y_{I,m} (h_{sf} - c_I \left(\frac{T_{r[E]build} + T_{I,o}}{2} \right) + \Delta m_{rv[REC-E]} h_{rv}(P_{r.har}, T_{r.har}) \\
& - \Delta m_{rl.cont[E-ACC]} h_{rl}(P_{r[E]har}, T_{rl[E-ACC]}) - m_{rl\{c\}} h_{rl}(P_{r[E]har}, \bar{T}_{r\{c\}})
\end{aligned}$$

where the number of plates per module, denoted by n is 35. As the melted ice layer $y_{I,m}(t)$ is a function of time, the equation above is solved simultaneously with equations (98), (100) and (104) above.

Solving the above equation yields the mass of gas $\Delta m_{rv[REC-E]}$ from the condensed liquid receiver introduced at the inlet of the evaporator during the warming sub-period. The mass flow rate of the harvesting gas per module is therefore:

$$\dot{m}_{rv[REC-E]} = \frac{\Delta m_{rv[REC-E]}}{t_{har}} \quad (106)$$

And per channel (there are 30 channels per plate) feeding one side of the plate, the mass flow rate is:

$$\dot{m}_{rv[REC-E]chl} = \frac{\Delta m_{rv[REC-E]}}{t_{har} \times n \times 30 \times 2} \quad (107)$$

9.2.5 Predicting the Refrigerant Side Convective Condensing Heat Transfer Coefficient

Three correlations are presented below for predicting the refrigerant side convective condensing heat transfer coefficient in vertical tubes during the warming sub-period.

A comparison to other correlations found in the literature is presented in Appendix A5 for flow in horizontal tubes as a comparison, to investigate the dependence of the convective condensing heat transfer coefficient on tube orientation.

The Shah Correlation for Film Condensation inside Vertical Pipes

Shah⁽²⁹⁾ modified his two phase convective boiling heat transfer coefficient⁽²⁶⁾ model developed in Section 9.1 above to apply to film condensation inside vertical pipes. Shah⁽²⁹⁾ noted “the similarity between the mechanisms of heat transfer during film condensation and boiling without nucleation.”⁽²⁹⁾ Just as for the convective boiling heat transfer coefficient, the convective condensation correlation has been verified over a large range of conditions (pipe diameters between 7-40 mm, horizontal/vertical orientations, mass flow rates from laminar to turbulent, velocities from 3 to 300 m/s etc.) for a variety of refrigerants (including ammonia), and is supported by independent studies “with a mean deviation of about 15% (from tested data).”⁽²⁹⁾ Based on the test data and “as long as the entire pipe surface remains wetted by the liquid, the following equation applied to all flow orientations:”⁽²⁹⁾

$$\psi_{har} = \frac{h'_{2ph[Sh]\{c\}}}{h'_1} \quad (108)$$

Here, $h'_{2ph[Sh]\{c\}}$ is the Shah⁽²⁹⁾ two phase convective condensing heat transfer coefficient, and the superficial heat transfer coefficient of the liquid phase only h'_1 is calculated by the Dittus-Boelter equation to predict the heat transfer coefficient - assuming all the mass flowing as a liquid.

$$h'_{l\{c\}} = 0,023 \left(\frac{GD}{\mu_{rl}(T_{r[E]har})} \right)^{0.8} Pr_{rl}^{0.4} (T_{r[E]har}) \frac{k_{rl}(T_{r[E]har})}{D} \quad (109)$$

and h'_1 is given by

$$h'_1 = h'_{l\{c\}}(1 - x'_{har})^{0.8} \quad (110)$$

where x'_{har} is the thermodynamic vapour quality of the harvesting gas. The ratio ψ_{har} is dependent on the condensing convection number Co_{har} :

$$Co_{har} = \left(\frac{1}{x'_{har}} - 1 \right)^{0.8} \left| \frac{\rho_{rv}}{\rho_{rl}} \right|_{T_{r,har}}^{0.5} \quad (111)$$

$$\psi_{har} = \frac{1,8}{Co_{har}^{0.8}} \quad (112)$$

$h'_{2ph[Sh]\{c\}}$ is predicted by substituting equation (108) into equation (112).

Shah further states that “in the process of condensation, liquid will be formed whenever vapour contacts the pipe surface and thus the pipe circumference will always be wetted at all flow rates and in all flow orientations. Hence (the above) equation may be expected to apply to condensation in all flow orientations with minimum modification.”⁽²⁹⁾ A major assumption of this model is that vapour quality variation is linear with channel length, $L_{[E]chl}$. Shah⁽²⁹⁾ simplifies equation (108) where saturated vapour enters the tube and saturated liquid exits the tube to one term, if the arithmetic mean quality, x'_{har} of 0,5 is used.

$$\bar{h}'_{2ph[Sh]\{c\}} = h'_{l\{c\}} \left(0.55 + \frac{2.09}{Pr_{rl}^{0.38} (T_{r[E]har})} \right) \quad (113)$$

The Nusselt Equation for Flow in Vertical Tubes

A theoretical correlation for flow in vertical tubes, based on Nusselt's equation for film condensation⁽²⁷⁾ is developed as a comparison to both Shah⁽²⁹⁾ correlations presented above. This correlation can be used for film condensation at the inner or outer walls of vertical tubes if the tube diameter is large compared to the film thickness (which in this case is true). The average steel wall temperature $\bar{T}_{s[E]har}$, predicted from equation (98) above, is used in this correlation.

$$h'_{2ph[Nu]\{c\}} = 0,943 \left[\frac{h_{fg} g(\rho_{rl} - \rho_{rv}) k_{rl}^3}{L_{[E]chl} (T_{r[E]har} - \bar{T}_{s[E]har}) \frac{\mu_{rl}}{\rho_{rl}}} \right]^{\frac{1}{4}}_{T_{r[E]har}} \quad (114)$$

The three convective condensing heat transfer coefficients are plotted below over the 90 second harvesting period.

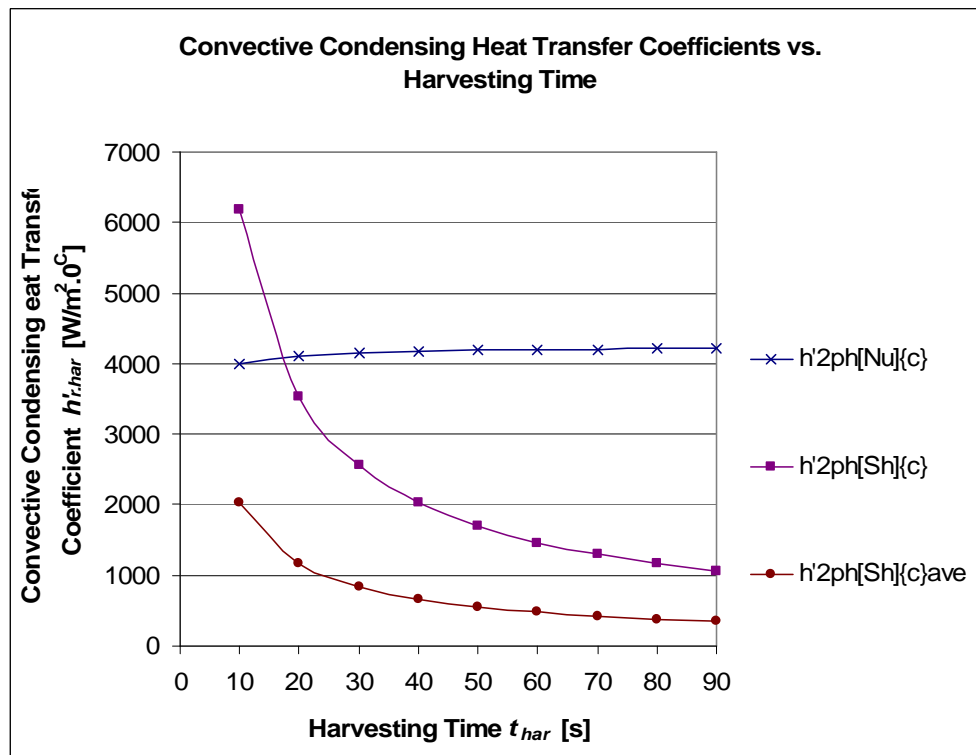


Figure 9.12 Convective condensing heat transfer coefficients versus harvesting time

From Figure 9.12 above and at t_{har} of 90 seconds, all three vertical tube coefficients predicted in the model lie within the band of 182 – 4211 W/m².°C which demonstrates the variation of predictions based on the different heat transfer models. As both Shah⁽²⁹⁾ correlations are strongly dependent on mass flow rate of harvesting gas, and since the mass flow rate per channel is typically quite low, there is a concern that they may under-predict the heat transfer coefficient. Although both the Shah correlations are corroborated with data, the lower limit of tube velocity for these models is 3 m/s, which is three orders of

magnitude larger than the velocity predicted from the mass flow rate of equation (107). Therefore, as the Nusselt correlation is based on average evaporator wall temperature, and as such has no lower limit, it will be the primary coefficient used as the convective condensing heat transfer coefficient for the model further developed below. This coefficient is also used to predict the parameters $T_{s[E]har}$ and $T_{I.m.har}$ in equations (98) and (100) above, respectively.

The melted ice layer over time is plotted below by inputting the three vertical tube convective condensing heat transfer coefficients into equation (104) above.

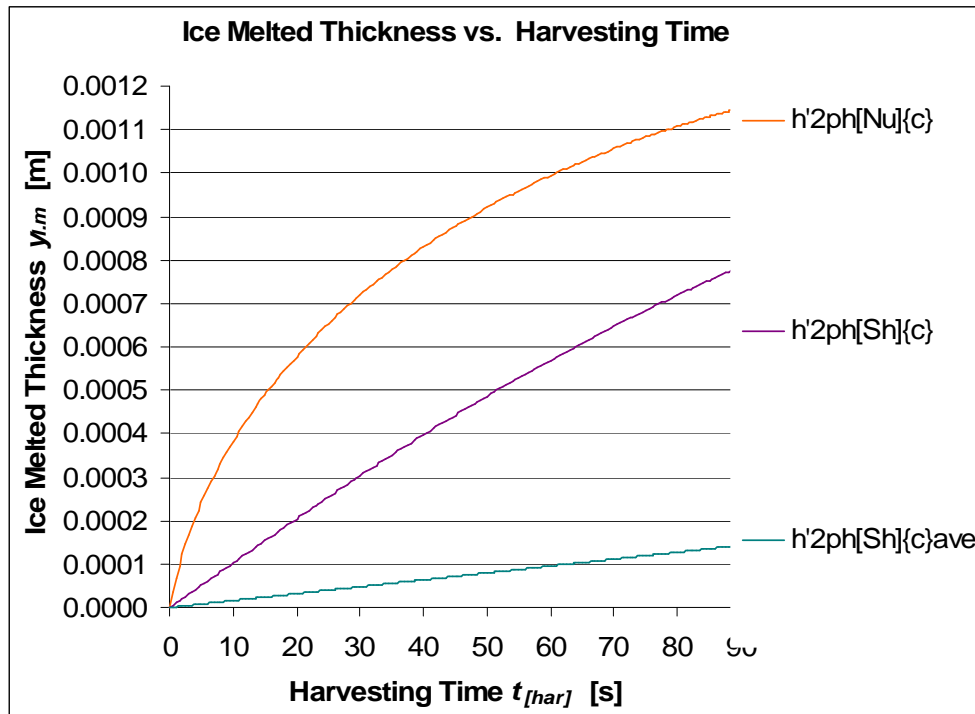


Figure 9.13 Ice melted thickness versus harvesting time for the predicted vertical-tube film condensation heat transfer coefficients.

Table 9.3 Convective condensing heat transfer coefficients and corresponding thickness of melted ice layer

$h'_{r.har}$ [W/m ² .C]	$h'_{2ph[Nu]\{c\}}$ [W/m ² .C]	$h'_{2ph[Sh]\{c\}}$ [W/m ² .C]	$\bar{h}'_{2ph[Sh]\{c\}}$ [W/m ² .C]
Final values	4211	893	182
Final predicted thickness of melted ice layer $y_{L,m}$ [mm]	1,149	0,786	0,143
% Difference: $y_{L,m}$	0 %	31,63 %	87,54 %

As mentioned above from Shah,⁽²⁹⁾ assuming a linear quality distribution along the length of the tube, the modified correlation $\bar{h}'_{2ph[Sh]\{c\}}$ predicts the mean heat transfer coefficient more accurately than $h'_{2ph[Sh]\{c\}}$. However, as mentioned above, both these correlations apply for mass flow rates much larger than that predicted by equation (107) above. From the heat transfer model during ice building (Table 9.2 above), the predicted thickness of the ice built varies from 5,84 – 6,67 mm depending on the *applicable* convective boiling heat transfer coefficient used in the model. Thus a melted ice layer thickness of around 1.1 mm, based on the Nusselt correlation $h'_{2ph[Nu]\{c\}}$ is acceptable; as final ice sheet thickness was observed during testing to be approximately 5-6 mm (see Appendix A6 for the test data). As mentioned above, Worthington Smith & Brouwer,⁽¹³⁾ and Rankin⁽¹⁴⁾ also confirm that ice built on each side of the plate should be 5 – 6 mm.

Figure 9.13 above is based on the assumption that the ice melts for the entire harvesting period of 90 seconds. The time required for the harvesting gas to expel the cold liquid to the accumulator prior to the warming sub-period could not be predicted from testing at the plant. From Figure 9.9 above, assuming that the ice layer acts as an adiabatic boundary, the time required for the outer steel wall to reach 0 °C (and begin to melt the inner ice layer) is approximately 4 seconds. Therefore, if it is assumed conservatively⁹⁴, based on observations of the harvesting process at the plant, that the valve change-over time, plus the time

⁹⁴ This assumption should be considered a lower limit of the thickness of ice melted, with the predictions shown in Figure 9.13 above considered as an upper limit.

required to expel the liquid to the accumulator and the time required to heat up the steel wall to zero degrees at its outer surface takes up half of the warming sub-period of 90 seconds, the final melted ice thickness on one side of the plate is shown in the figure below.

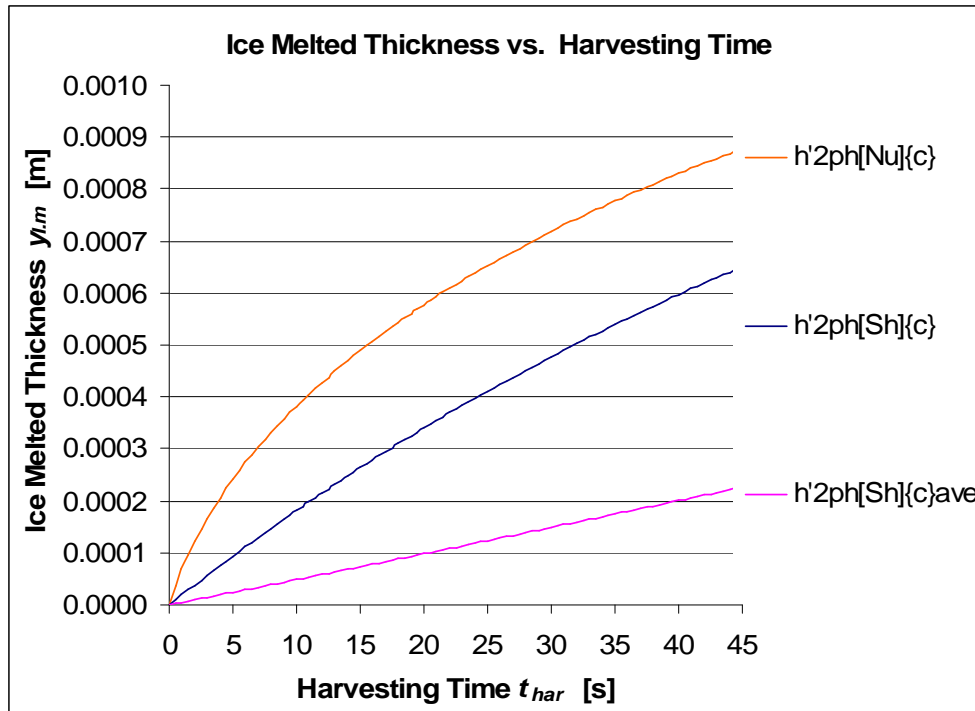


Figure 9. 14 Ice melted thickness versus harvesting time assuming that ice is melted for only half of the total harvesting time of 90 seconds

Table 9.4 Convective condensing heat transfer coefficients thickness of melted ice for a harvesting time of 45 seconds

$h'_{r.har}$ [W/m ² .C]	$h'_{2ph[Nu]\{c\}}$ [W/m ² .C]	$h'_{2ph[Sh]\{c\}}$ [W/m ² .C]	$\bar{h}'_{2ph[Sh]\{c\}}$ [W/m ² .C]
Final values	4179	1435	343
Final predicted thickness of melted ice layer $y_{L,m}$ [mm]	0,877	0,651	0,226
% Difference: $y_{L,m}$	0 %	25,82%	74,20 %

From Table 9.3 and Table 9.4 above, if the harvesting time is halved, the thickness of ice melted decreases by only 17 % for $h'_{2ph[Sh]\{c\}}$, and increases by

58 % for $\bar{h}'_{2ph[Sh]\{c\}}$. Although this seems counter-intuitive, as mentioned above, the Shah⁽²⁹⁾ correlations are dependent on the mass flow rate of harvesting gas, which increases as harvesting time decreases. Therefore the decreased harvesting period that the warm gas is in contact with the steel evaporator wall is offset by the increased convective condensing heat transfer coefficients for these correlations. The Nusselt correlation $h'_{2ph[Nu]\{c\}}$ however is not as dependent on mass flow rate, although it is solved simultaneously with the mass flow rate during the warming sub-period of equation (105). Based on this correlation, the upper and lower limit of thickness of ice melted is 1,149 and 0,877 mm respectively, which constitutes a 24 % difference. For the model developed in Section 8. above, a mean value for the thickness of ice melted of 1,00 mm is assumed when predicting the URD associated with the building of the subsequently melted ice layer. Thus this assumption of melted ice layer thickness is substantiated and is further corroboration of the mass flow rate and average recirculation ratio required to build the entire ice layer that is predicted in Sections 8. and 9.1.

Brief Summary of Section 9

Section 9.1 above presents a third independent method of predicting the mass flow rate and average recirculation ratio. The heat transfer model is developed based on convective boiling heat transfer coefficients that are both general in terms of their applicability to varying tube diameters, mass flow rates etc. and also specific to ammonia as the circulating refrigerant. From Table 9.2, by inputting the mass flow rate and average recirculation ratio during ice building predicted in Section 8.6.1 into the model of Section 9.1, the thickness of the built ice layer, depending on the *applicable* coefficients used, varies from 5,84 – 6,67 mm. These values agree to within 11,0 % with the same thickness input into equation (69) of Section 8. (6 mm), which is based on Worthington Smith & Brouwer,⁽¹³⁾ and Rankin.⁽¹⁴⁾ This in turn further corroborates the abovementioned predicted performance quantities from Section 8.

A heat transfer model during the warming sub-period is developed in Section 9.2. to substantiate the predicted thickness of ice built of Section 9.1, as well as to corroborate the URD of building this layer predicted in the model of Section 8. Based on the only *applicable* coefficient used (that of Nusselt⁽²⁷⁾ $h'_{2ph[Nu]\{c\}}$), this layer varies from 0,877 – 1,149 mm. Therefore, the thickness of ice delivered to the screw conveyor at the end of the warming sub-period, predicted from both heat transfer models presented above, is approximately 5 mm. This agrees with tests performed at the operating plant, where from Table A6.3 of Appendix A6, ice of 5 - 6 mm was measured at the screw conveyor.

The predictions of both heat transfer models agree with tests performed at the operating plant and further corroborate the performance quantities of mass flow rate and average recirculation ratio predicted by the model developed in Section 8.

One important observation from the models of this section is that in the absence of test data to confirm heat transfer coefficients, caution should be employed when using the general theoretical and empirical models that are available. There is such a large variation in values between these correlations that it is only through knowledge of the system that the coefficients that most closely resemble the operating plant are selected.

10. CONCLUSIONS

Theoretical modelling of the existing and alternative liquid overfeed pumping arrangements at Unit 5 of the ERPM ice making plant, and providing some validation of these models' performance quantities, are the main objectives of this investigation.

For the same operating parameters measured at Unit 5 with its actual cold gas pumping arrangement, other possible liquid overfeed pumping arrangements are modelled. It is with these models that meaningful comparisons can be made between the different possible pumping arrangements. The models also predict performance quantities that could not be measured at the plant, such as the average liquid recirculation ratio and the refrigerant mass flow rate through the evaporators during ice building. As mentioned in Section 2.4, it is only by reliably predicting these quantities that the comparisons between the different pumping arrangements in Section 8. achieve some level of validity.

By inputting variables predicted from the refrigeration demand model of Section 8. into the heat transfer model of Section 9., and corroborating the resultant predictions from these models with operating data (where available), both models achieve a level of substantiation. One example, shown in the table below, is that of the mass flow rate of refrigerant through the evaporators during the ice building period, which is dependent on the average recirculation ratio x_l . By inputting the mass flow rate predicted by the refrigeration demand model of Section 8. into the heat balance model during ice building of Section 9., the predicted thickness of the built ice layer matches values measured at the plant, as well as from

Worthington-Smith & Brouwer,⁽¹³⁾ and Rankin.⁽¹⁴⁾⁹⁵ This in turn corroborates the mass flow rate and subsequently the average recirculation ratio predicted from the model of Section 8.

The table below summarises the key performance quantities predicted by both models, and where applicable, the corresponding values obtained from testing at the ERPM plant.

Table 10.1 Key performance quantities predicted by the different models.

Performance Quantity	Predicted from	Used as input to	Predicted Value	Test data or reference source
Refrigerant mass flow rate per module ⁹⁶ : $\dot{m}_{r[PD-E]} / \dot{m}_{r(l,v)[E-ACC]}$	Refrigeration demand model of Section 8. and Appendix A8.2.2	Heat transfer model during ice building of Section 9.	3,354-3,363 [kg/s]	N/A = None Available
Average Refrigerant Recirculation ratio: x_I	Refrigeration demand model of Section 8.	Heat transfer model during ice building of Section 9.	5	N/A
Thickness of Ice layer built $y_{l,b}$	Heat transfer model during ice building of Section 9.	The referenced value of 6 mm is input into the model of Section 8. and confirmed with that predicted by Section 9.	5,84 – 6,67 [mm]	5-6 mm of ice measured at the screw conveyor below evaporators and confirmed by Worthington-Smith & Brouwer, ⁽¹³⁾ and Rankin. ⁽¹⁴⁾

⁹⁵ As mentioned in Section 8.1, all three sources mentioned above state that ice thickness built on one side of each plate is approximately 5 – 6 mm. From Table A6.3, the thickness of ice delivered was measured at the screw conveyor beneath the module to be 5 – 6 mm.

Table 10.2 (continued) Key performance quantities predicted by the different models.

Performance Quantity	Predicted from	Used as input to	Predicted Value	Test data or reference source
Thickness of Ice layer melted $y_{l,m}$ [mm]	Heat transfer model during ice shedding of Section 9. Based on a warming sub-period of 90 seconds ⁹⁷	Mean value of 1 mm input into the refrigeration demand model of Section 8.	0,786– 1,149 [mm]	N/A
Convective boiling heat transfer coefficient in vertical tubes h'_r	Heat transfer model during ice building of Section 9.	N/A	1666 – 6219 [W/m ² .C]	N/A
Convective condensation heat transfer coefficient in vertical tubes $h'_{r,har}$	Heat transfer model during ice shedding of Section 9.	N/A	893– 4211 [W/m ² .C]	N/A

Modelling the channels of the evaporator plate within which refrigerant flows as circular tubes, the heat transfer model of Section 9. predicts the temperature changes of the steel evaporator walls during the ice building and harvesting periods, as well as the convective boiling and condensing heat transfer coefficients during both these periods.

Referring to Table 10.1 above, although the convective boiling heat transfer coefficients predicted by the different correlations during ice building vary considerably from each other, the percentage difference of predicted thickness of ice built, from Table 9.2, reveals that (except for the EES⁽³⁴⁾ correlation) their relative effect is minimal. Similarly during the harvesting period, the variation in the different convective condensation heat transfer coefficients, used in the heat

⁹⁶ Based on the assumption mentioned in Section 8.6.1 above.

⁹⁷ If the warming sub-period is halved as shown in Table 9.4 above, the melted ice thickness varies from 0,651-0,877 mm.

transfer model, does not yield a commensurate change in melted ice thickness (except for the modified Shah⁽²⁹⁾ correlation), as shown in Table 9.3.

By predicting the mass flow rate and average recirculation ratio through the evaporators, the theoretical model of Section 8. also predicts the various URDs associated with each pumping arrangement. The productive and unproductive refrigeration demands predicted from these theoretical models are then used to compare the energy efficiency and cost effectiveness of each pumping system.

The refrigeration demand model of Section 8. includes all major productive and unproductive refrigeration demands that are incorporated in the models of Lorentzen and Baglo⁽⁶⁾, Wright⁽¹¹⁾, and Bailey-McEwan⁽¹²⁾, as well as some other URDs that are not included in any of these analyses. It is therefore a comprehensive model of the PRDs and URDs associated with the current cold gas pumping arrangement. This model is adapted to include the URDs associated with other possible pumping arrangements under, as far as possible, the same operating conditions,⁹⁸ which allows for valid comparisons to be made between the different pumping arrangements.

A fully mechanically pumped system (FMPS), suggested by Bailey-McEwan⁽¹⁶⁾ is presented in Section 8.9. This arrangement would minimise the interaction between the warm harvesting gas and the expelled cold liquid in the evaporator at the beginning of the warming sub-period, as well as eliminate any trapped liquid behind the level regulating valve at the end of this period, and would rapidly

⁹⁸ Such as pressures in the evaporator during ice building and harvesting as well as their associated time periods, pumper drum pressures and filling/pumping periods for the gas pumped arrangements, condenser and accumulator pressures, mass flow rates, average recirculation ratios etc.

recharge the evaporator plates with refrigerant prior to ice building.⁹⁹ Although the time required to expel the liquid to the accumulator at the beginning of the warming sub-period could not be measured at the plant, it will certainly minimise this expelling time, which is unknown.

The results of the refrigeration demand model of Section 8. predict that, for similar evaporating temperatures and similar *practical* average recirculation ratios, the CGPS is always more energy efficient than the MPS, but less energy efficient than the FMPS. As mentioned in Section 8.10.1, based on the plot of COP at varying average recirculation ratios illustrated in Figure 8.17, the intersection of the COP for the CGPS and FMPS at high recirculation ratios (>9,5) is intuitive. The increasing total refrigeration demand¹⁰⁰ for the FMPS as the average recirculation ratio increases should *eventually* match and then surpass the *constant* demand of the CGPS. Therefore, the assumption of equation (6b) (and hence that of equation (5b)), that the ratio of total demands can predict the compressor energy input for all pumping arrangements appears to be valid even at higher average recirculation ratios. Nonetheless, ratios as high as 9,5 would not be encountered in a working liquid refrigerant overfeed pumping arrangement.¹⁰¹

The results of the model of Section 8. agree with the suggestion of Lorentzen and Baglo⁽⁶⁾¹⁰² and the conclusion of Wright⁽¹¹⁾ that a cold gas pumped system, (at

⁹⁹ Within 25 seconds from Section 8.9 based on the analysis performed in Appendix A4. The predicted liquid transfer period remains the same for all arrangements at 10 seconds from Table 3.1 above.

¹⁰⁰ Due to the increasing work input required from the mechanical pump to circulate the larger volume of liquid.

¹⁰¹ ASHRAE⁽⁵⁾ and Wright⁽¹¹⁾ both state that common recirculation ratios for mechanically pumped arrangements are between 4 and 7.

¹⁰² Lorentzen and Baglo⁽¹³⁾ make conclusions based on tests of hot gas and mechanically pumped arrangements, and suggest that an efficient cold gas pumped system would be more energy efficient than a mechanically pumped system.

high recirculation ratios according to Lorentzen and Baglo⁽⁶⁾) would be more energy efficient than a mechanically pumped system. It should be noted however that the operating systems of both Lorentzen and Baglo⁽⁶⁾ and Wright⁽¹¹⁾ are conventional continuous refrigeration processes, and do not include many of the inherent inefficiencies of batch type processes. More significantly, those URDs associated with the harvesting process are obviously absent in both models.

Wright⁽¹¹⁾, based on tests for a 422 kW¹⁰³ refrigerating system, also predicts that a cold gas pumped liquid overfeed arrangement would be more energy efficient than a conventionally mechanically pumped one. However, as opposed to Lorentzen and Baglo⁽⁶⁾, he predicts that at lower recirculation ratios (2:1), and at evaporating temperatures of -29° C (-20° F) or lower, the cold gas pumped system is more energy efficient than the mechanically pumped system. He further asserts that if the latter system is operated at its customary recirculation ratio of 4 to 6, the benefit of the cold gas pumped system operated at a recirculation ratio of 2 is even more marked. In the investigation of this report, though, the refrigeration demand models of the different pumping arrangements described in Section 8. predict that evaporating temperatures have little effect on the relative energy efficiencies of both arrangements (based on Figure 8.18 above and for an average recirculation ratio of 5) whilst the CGPS becomes *more* energy efficient than the MPS as the average recirculation ratio for both arrangements increases (based on Figure 8.15 and above and for an evaporating temperature of -5,83° C).

Both Lorentzen and Baglo⁽⁶⁾ and Wright⁽¹¹⁾ reach their conclusions¹⁰⁴ for a cold gas pumped arrangement based on observations of smaller systems than the ERPM plant (total refrigeration demand of 11,6 kW and 422 kW respectively, compared to 6850 kW), and at a lower evaporator temperature (-30° C compared

¹⁰³ The total refrigeration demand of Unit 5 (8 modules) of the operating ERPM plant, based on Figure 8.21 for one module, and for the 15 minute ice making cycle, is approximately 6850 kW.

¹⁰⁴ In the case of Lorentzen and Baglo⁽⁶⁾ it is a suggestion and not based on test data.

to -5.83°C). Nonetheless, based on the predictions of this investigation, the suggestion of Lorentzen and Baglo⁽⁶⁾ and the conclusion of Wright⁽¹¹⁾, that a cold gas pumped system, operating at similar evaporating temperatures (but not similar recirculation ratios) will be more energy efficient than a mechanically pumped arrangement, holds true for large batch-type overfeed systems such as that of the ERPM plant.

Lorentzen and Baglo⁽⁶⁾, Wright⁽¹¹⁾ and ASHRAE⁽⁵⁾ also conclude that a hot gas pumped system is the least energy efficient of all pumping arrangements, which agrees with the conclusions of this investigation.

An annual electrical cost analysis is performed in Section 8. to compare the cost effectiveness of the different pumping arrangements. Referring to Table 8.3, the cold gas pumped arrangement is predicted to be more electrical cost effective, by R97,000 per year, than the hot gas pumped arrangement. As mentioned in Section 8.11.1, the capital cost of both gas pumped systems should be almost identical, and therefore there is no advantage of the HGPS over the CGPS.

The annual electrical cost of operating the CGPS is lower than for the MPS for all similar *practical* recirculation ratios, but it is not as electrically cost effective as the FMPS.¹⁰⁵ As mentioned in Section 2.1 and based on ASHRAE⁽⁵⁾, the capital and maintenance costs of the additional pumps for a mechanically pumped system¹⁰⁶ may offset any achievable increase in efficiency. This aspect would require further investigation before concluding whether the FMPS is indeed the most cost effective pumping arrangement. The lower URD, and subsequently the lower annual electrical cost of the FMPS should also be offset against the capital cost of the additional recharge pumps and recharge/discharge vessels.

¹⁰⁵ From Figure 8.25.

¹⁰⁶ Such as the MPS and the FMPS

On the basis of predicting the annual electrical cost as well as the total refrigeration demand for each pumping arrangement, it can be concluded that the MPS is less energy efficient and electrically cost effective than the CGPS. As mentioned above, this agrees with the suggestion of Lorentzen and Baglo⁽⁶⁾ and the conclusion of Wright.⁽¹¹⁾ It can also be concluded that the FMPS is the most energy efficient and electrically cost effective of the four pumping arrangements investigated.

ASHRAE⁽⁵⁾ states that the gas pumped arrangements offer no advantage over their mechanically pumped counterparts “when the overall capital and operational costs of both systems are compared.”⁽⁵⁾ It would therefore appear from ASHRAE⁽⁵⁾ that the capital and operational costs unique to the gas pumped arrangements, which include two pumper drums, are similar to, or greater than, those of using a mechanical pump - irrespective of the efficiency of either system. Further investigation is therefore required relating to the capital costs of both arrangements, as the electrical operating cost of the CGPS is predicted by this investigation to be lower than the MPS.

ASHRAE⁽⁵⁾ also states that “for each evaporator, there is an ideal circulating rate for every loading condition that will result in the minimum temperature difference and the best evaporator efficiency.”⁽⁵⁾ Predicting the optimal average recirculation ratios of each arrangement is beyond the scope of this investigation, however it is recommended for further work and would be a progressive step in determining which pumping arrangement is more energy efficient and cost effective.

11. SUGGESTIONS FOR FURTHER WORK

1. Varying key operating parameters, such as evaporator pressure, as well as performance quantities such as the average recirculation ratio, affecting the refrigeration demand model of Section 8. may result in conditions which would favour the MPS over the CGPS-operating under different conditions.
2. Accurately predicting the compressor energy input for all pumping arrangements, especially at high average recirculation ratios, would support any comparisons of energy efficiency and electrical cost effectiveness for the different systems. This would then replace the assumptions made in equations (5b) and (6b) of Section 7.2 above.
3. Verifying the key performance quantities predicted by the different theoretical models in Table 10.1 above with test data would validate the models further, and would allow for more credible conclusions to be made regarding the efficiency and effectiveness of the different pumping arrangements. This would however require invasive equipment (flow meters, accurate temperature sensors etc.) to be fitted to the plant.
4. Modelling the “transient period” during the harvesting period¹⁰⁷ more effectively by including the valve change-over times, as well as predicting and experimentally verifying the exact time required for the harvesting gas to expel the liquid to the accumulator at the beginning of the warming sub-period, would allow for more credible suggestions to be made regarding minimising unproductive refrigeration demand of the operating plant. This would also predict whether the discharge process of the FMPS would result in a shorter warming sub-period; a further advantage of the FMPS.
5. Predicting more accurately the ice-steel ‘stiction’ defined in Section 9. would provide more accuracy when modelling the convective boiling heat transfer coefficient during the warming sub-period. An optimal warming sub-period could subsequently be predicted.

¹⁰⁷ Based on the timing diagram of Figure 3.2, where the venting period of one module is followed 22,5 seconds later by the expulsion of cold liquid refrigerant from its neighbour

6. The capital and operating costs of the pumper drum system for the gas pumped arrangements could be compared to those of any mechanical pumps or vessels required by the mechanically pumped arrangements. A rigorous way of so including the capital and maintenance costs would be through a Net Present Value (NPV) analysis. This would credibly refine the conclusions of the electrical operating cost analysis of Section 8.11, and predict more conclusively which pumping arrangement is the most cost effective.

12. REFERENCES

1. Dossat, R. J. *Principles of Refrigeration*, John Wiley & Sons, Inc., Second Edition, SI Version, 1981.
2. Bailey-McEwan, M. *Chapter 23 Refrigeration Theory and Equipment*. Submitted for publication as Chapter 23 in “*Occupational environmental engineering handbook*”, to be published in 2008 by the Mine Ventilation Society of South Africa.
3. Moran, M. J., Shapiro, H. N. *Fundamentals of Engineering Thermodynamics*, John Wiley & Sons, Inc., Third Edition, SI Version, 1998.
4. Senatore, P. *Theoretical Analysis Of The Freezing And Harvesting Cycles In A Conventional Ice Making Process*, Thesis (MSc.) University of the Witwatersrand, 1989.
5. ASHRAE Handbook (Refrigeration), *Chapter 1 Liquid Overfeed Systems*, American Society of Heating, Refrigeration and Air-Conditioning Engineers (ASHRAE) Inc., Atlanta, Georgia, USA, 2006.
6. Lorentzen, G., Baglo, O.A. *An Investigation of a Gas Pump Recirculation System*, Proceedings of the Xth International Congress of Refrigeration, pp. 215-224. Date unknown.
7. Du Preez, B.A. *Gas Pumped Liquid Overfeed Systems: A Modern Day Study*, Investigational Project Report submitted to School of Mechanical, Industrial & Aeronautical Engineering, University of the Witwatersrand, 04 September 2000.
8. Sinnott, R.K., *Chemical Engineering Design*, Elsevier Butterworth-Heinemann, Fourth Edition, 2005, pp. 204.
9. Klostermann, K. *Largest ice plant in the world*, The South African Mechanical Engineer, Vol 38, June 1988, pp.307-313.
10. Wright, J.D., *The Development of gas pressure recirculation systems-an American phenomenon*. IIAR Annual Meeting, Memphis, Tennessee, 1990. Obtained from Mr. Mike Fischer. mfisher@coldsystemsllc.com 20 July 2007.

11. Wright, J.D., *Gas powered liquid recirculation compared to mechanical pumps*. IIAR Annual Meeting, Memphis, Tennessee, 1990. Obtained from Mr. Mike Fischer. mfisher@coldsystemsllc.com 20 July 2007.
12. Bailey- McEwan, M. *Investigations carried out at ice-making installation, Merriespruit No. 1 Shaft, Harmony Gold Mining Co. Ltd.* Internal report no. 499/99, Chamber of Mines of S.A. Research Organisation, August 1988.
13. Internal document of Worthington-Smith and Brouwer, consulting engineers and designers of ERPM ice making plant, Reference J911, 24 July 1992.
14. Direct communications from Mr. C. Rankin, refrigeration consultant at ERPM, July through December 2007.
15. Barber, A., *Pneumatic Handbook*, Elsevier Science Ltd., Eighth Edition, 1997, pp. 140.
16. Direct communication from Dr. M. Bailey-McEwan, July 5th 2007.
17. Direct communication with Eskom service call centre, July 2007.
18. van der Walt, J., de Kock, E.M. *Developments in the engineering of refrigeration installations for cooling mines*, International Journal of Refrigeration, Vol. 7 No. 1, pp. 27-40, January (1984).
19. Sheer, T.J., del Castillo, D., Csatory, C., *Unconventional systems for removing heat from deep mines*, The South African Mechanical Engineer, Vol. 36, pp 207-217, June (1986) citing Sheer, T.J., Cilliers, P., Chaplain, E. and Correia, R., Some recent developments in the use of ice for cooling mines, Journal of the Mine Ventilation Society of South Africa, Vol 38 (1985).
20. Khan, J.R., Zubair, S.M., *Design and performance of reciprocating refrigeration systems*, International Journal of refrigeration, Vol. 22 pp. 235-243, (1999).
21. Browne, M.W., Bansal, P.K., *Transient simulation of vapour –compression liquid chillers*, International Journal of Refrigeration, Vol. 25 pp. 597-610 (2002).
22. Koury, R.N.N., Machado, L., Ismail, K.A.R., *Numerical simulation of a variable speed refrigeration system*, International Journal of Refrigeration, Vol. 24 pp. 192-200 (2001).

23. Mocoenyane, K. Fourth year research project in the school of mechanical engineering, 2007.
24. Cengel, Y.A., Ghajar, A.J., *Heat and Mass Transfer, Fundamentals and Applications*, McGraw-Hill, 2010 pp. 217-284.
25. www.eskom.co.za WEPS Tariff rates 2010-2011. Cited 14 February 2011
26. Shah, M. M. *Chart Correlation for Saturated Boiling Heat transfer: Equations and further study*, Ashrae Transactions, No. 88 , pp. 185-196 (1982).
27. Johnson, R.W., *The handbook of fluid dynamics*, CRC Press LLC, 1998, pp. 17-91
28. Gungor, K.E., Winterton, R.H.S., *A general correlation for flow boiling in tubes and annuli*, International Journal of Heat and Mass transfer, Vol. 29, No. 3 pp. 351-358, (1986).
29. Shah, M.M., *A general correlation for heat transfer during film condensation inside pipes*, International Journal of Heat and Mass Transfer, Vol. 22, pp. 547-556, (1979).
30. Gupta, S.C., *The Classical Stefan Problem, Basic concepts, modelling and analysis*, North Holland Series in Applied Mathematics and Mechanics, Elsevier Science B.V., 2003, Preface.
31. EES-Engineering Equation Solver, Academic Commercial V7.966 (08/26/07), 1992-2007, Help for External Libraries; Internal_flow, External_flow, 10 December 2007.
32. Zamfirescu, C., Chiriac, F., *Heat transfer measurements on ammonia forced convection boiling in vertical tubes*, Journal of Experimental Thermal and Fluid Science Vol. 25, pp. 529-534 (2002)
33. Ohadi, M.M., Li, S.S., Radermacher, R., Dessiatoun, S., *Critical review of available correlations for two-phase heat transfer of ammonia*, International Journal of Refrigeration, Vol. 19 No. 4 pp. 272-284, (1996)
34. EES-Engineering Equation Solver, Academic Commercial V7.966 (08/26/07), 1992-2007, Help for External Libraries; Boiling, 10 December 2007.
35. Direct personal communication from Dr. M. Bailey-McEwan, Tuesday 10 January 2008.

36. Dobson, M. K., and Chato, J. C., *Condensation in Smooth Horizontal Tubes*, ASME Journal of Heat Transfer, Vol. 120, pp. 193-213. (1998).
37. EES-Engineering Equation Solver, Academic Commercial V7.966 (08/26/07), 1992-2007, Help for External Libraries; Condensation, 10 December 2007
38. Chisholm, D. *Two-phase flow in pipelines and heat exchangers*, Longman Inc., New York, 1983.
39. http://www.engineeringtoolbox.com/moody-diagram-d_618.html Cited 14 February 2011
40. EES-Engineering Equation Solver, Academic Commercial V7.966 (08/26/07), 1992-2007, Help for External Libraries; Transient Conduction, 10 December 2007.
41. Online Oxford English Dictionary, www.oed.com
42. Hemp, R., *A 29 MW Ice System for Mine Cooling*", 4th International Mine Ventilation Congress, Brisbane, Australia, 3-6 July 1988; A.D.S. Gillies (ed.), Australasian Institute of Mining & Metallurgy, Melbourne, 1988, pp. 415-423.
43. Direct communications from Bailey-McEwan, Dr. M., September through December 2010.
44. www.engineeringtoolbox.com/minor-loss-coefficients-pipes-d_626.html Cited 16 February 2011
45. http://members.multimania.co.uk/maxboost/htms/Moronic27_files/image018.jpg Cited 30 January 2011
46. Zhou, W.W., Gambaryan-Roisman, T., Stephan, P., *Measurement of water falling film thickness to flat plate using confocal chromatic sensing technique*, Journal of Experimental Thermal and Fluid Science, Volume 33, 2009, pp. 273-283
47. Eschenburg, H.M.V., Middleton, J.V.G., Hemp, R., *1000 ton per day ice plant for underground cooling at Harmony Gold Mine*, International Journal of Refrigeration, Volume 9, November 1986, pp.357-361

APPENDICES

APPENDIX A1

P&I and P-h Diagrams of the Cold Gas and Mechanically Pumped Arrangements of Unit 5 of the ERPM Plant

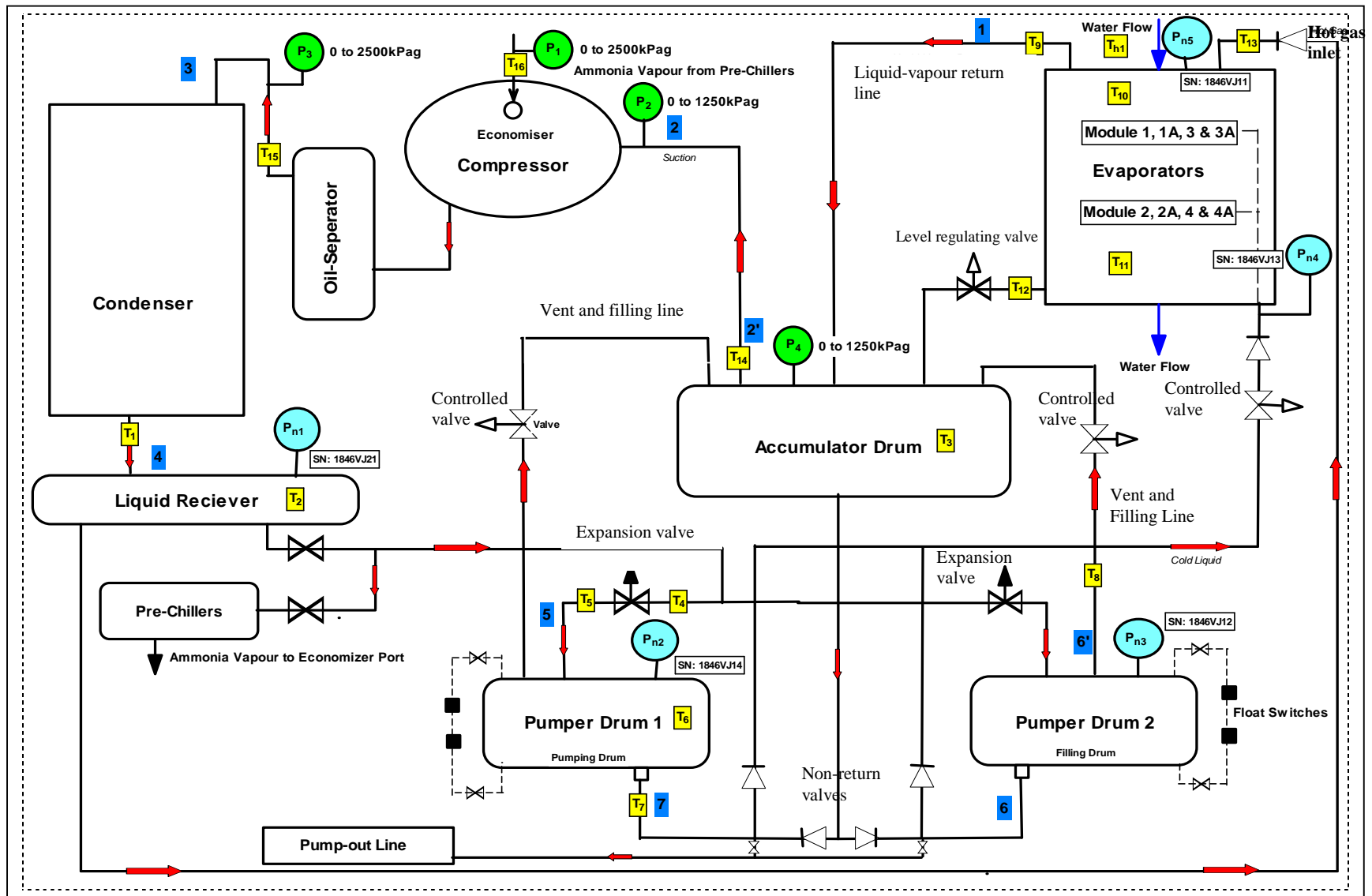


Figure A1.1 Detailed P & I diagram of Unit 5 of ERPM Plant, showing placement of pressure gauges and temperature sensors [23]

A1.1 The Cold Gas Pumped Arrangement

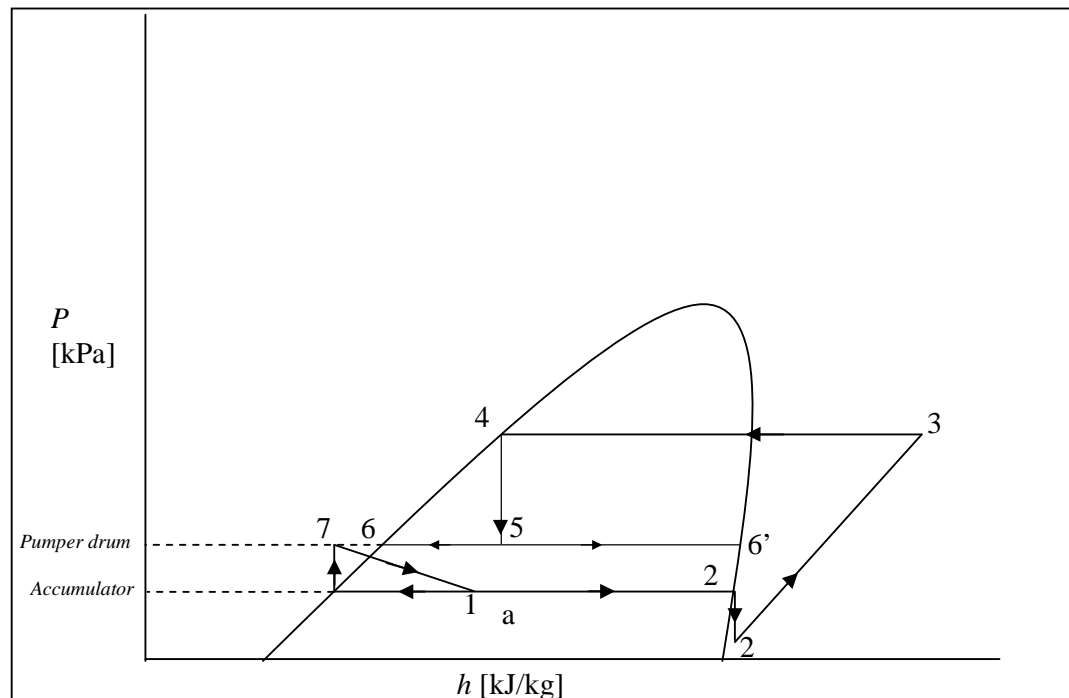


Figure A1.2 P-h diagram of refrigerating cycle in Unit 5 with its cold gas pumping arrangement (based on Figure 7.2).

Referring to Figure 7.2, and from the P-h diagram above, saturated vapour at state 2' at the accumulator is drawn to the compressor inlet at state 2, dropping in pressure and so becoming slightly superheated. This vapour is then compressed to condensing pressure, at state 3. Saturated liquid at state 4 in the condensed liquid receiver expands across the pumping expansion valve to pumping pressure at state 5 in the pumping pumper drum. Slightly sub-cooled (compressed) liquid at state 7 is then circulated through to the evaporators. The two-phase mixture at the exit of the evaporators, at state 1, then passes into the accumulator, where it is separated into saturated liquid and vapour. The residual liquid layer in the pumper drum is at state 6, whilst the flash gas remaining in the pumper drum is vented to the accumulator, at state 6'.

A1.2 Mechanically Pumped Arrangement

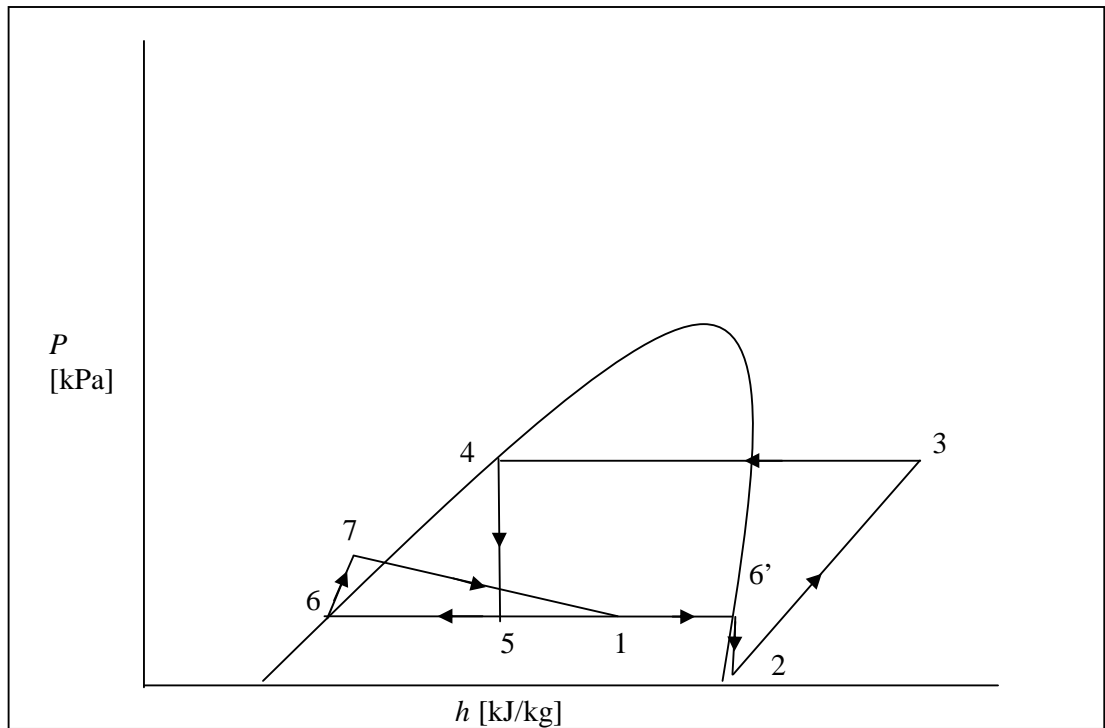


Figure A1.3 P-h diagram of refrigerating cycle in the mechanically pumped system of Unit 5, based on Figure 1.3 above

Referring to Figure 1.3, as in the cold gas pumped system, slightly superheated gas enters the compressor suction at state 2 and is compressed to condensing pressure at state 3. Saturated liquid from the high pressure receiver (state 4) expands across the hand expansion valve to accumulator pressure. The pump raises the liquid pressure at its inlet (point 6) to point 7, where the subcooled liquid is circulated to the evaporator, partly evaporating to state 1, the quality of which depends on the recirculation ratio.

APPENDIX A2

Model Developed to Predict the Amount of Liquid Ammonia Remaining in an Evaporator Module at the End of the Ice Building Period

A theoretical model was developed to predict the amount of liquid ammonia remaining in the evaporator plates of a module at the end of the ice building process and before harvesting begins. Modelling the channels along the length of the plate where refrigerant flows as a circular tube, saturated liquid ammonia enters at the bottom of the channel, and a two-phase mixture exits at the top of the channel. This model is based on Bailey-McEwan⁽¹²⁾, where an investigation of an ice making plant similar to that at ERPM was undertaken.

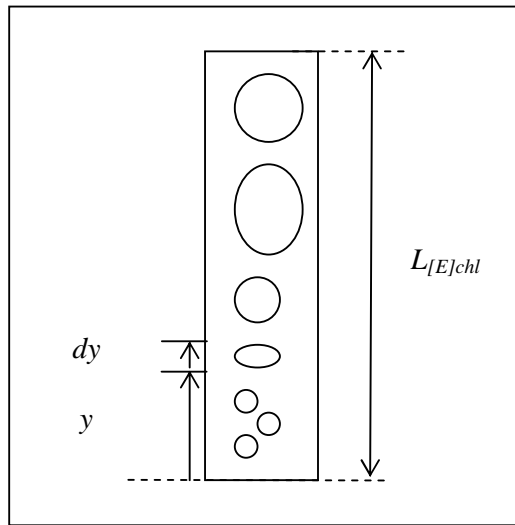


Figure A2.1 Flow of ammonia within a channel of the evaporator plate

The mass flow rate of the ammonia within the channel consists of the mass flow rate of each phase at any point along the length of the channel (y)¹⁰⁸, and is denoted by

$$\dot{m}_{r[E]} = \dot{m}_{r[E]}(y) + \dot{m}_{rv[E]}(y) \quad (1)$$

¹⁰⁸ Note that the definition of y here without any subscripts is the distance traveled along the length of the tube, and not thickness as defined in the nomenclature.

At any point along the length of the channel, (y), the cross-sectional area $a_{[E]chl}$ of a channel is the sum of the sub-areas occupied by each phase:

$$a_{[E]chl} = a_{r[E]chl}(y) + a_{rv[E]chl}(y) \quad (2)$$

The average velocities of each phase over their cross-sectional sub-areas are

$$\bar{v}_{rl}(y) = \frac{\dot{m}_{r[E]}(y) \nu_{rl}(P_{r[E]build})}{a_{r[E]}(y)} \quad (3)$$

$$\bar{v}_{rv}(y) = \frac{\dot{m}_{rv[E]}(y) \nu_{rv}(P_{r[E]build})}{a_{rv[E]}(y)}$$

$$\theta = \frac{\bar{v}_{rv}}{\bar{v}_{rl}} \quad (4)$$

Where θ is the velocity ratio of liquid to vapour.

The nature of the two phase flow depends on the “volume ratio of vapour to liquid, the average velocity of flow, and the heat flux through the [evaporator] wall, among other things,”⁽¹²⁾ and is complex to model theoretically. Thus, simplifying assumptions must be made in order to approximate the liquid content of the tubes prior to harvesting:⁽¹²⁾

1. The temperature of the ammonia is constant along the length of the channel.
2. The heat flux is uniform along the length of the channel.
3. The velocity ratio of liquid to vapour, θ , is constant along the length of the channel.

At the top of the channel, where length y equals evaporator channel length $L_{[E]chl}$, the mass flow rate of ammonia vapour leaving the channel at evaporating pressure $P_{r[E]build}$ is

$$\dot{m}_{rv[E]}(L_{[E]chl}) = \frac{\dot{q}_{[E]chl}}{h_{fg}(P_{r[E]build})} \quad (5)$$

where the heat flux $\dot{q}_{[E]chl}$ is given by Equation (6):

$$\dot{q}_{[E]chl} = \frac{T_{I.o} - T_{r[E]build}}{\frac{1}{h'_{r[E]}} + \frac{y_{s[E]}}{k_{s[E]}(T_{r[E]build})} + \frac{y_I}{k_l(T_{r[E]build})}} \quad (6)$$

-the solution of which has been predicted in equation (86) of the heat transfer model developed in Section 9.1 above using the Gungor-Winterton convective boiling heat transfer coefficient $h'_{2ph[G]}$.

The definition of the time averaged recirculation ratio over the ice building period, x_1 , at evaporator inlet temperature and pressure, is

$$\begin{aligned} x_1 &= \frac{\dot{m}_{r[E]i}}{\dot{m}_{rv}(L_{[E]chl})} \\ x_1 &= \frac{\dot{m}_{r[E]i} h_{fg}(P_{r[E]build})}{\dot{q}_{[E]chl}} \end{aligned} \quad (7)$$

And in terms of the average recirculation ratio, the vapour mass flow rate at length y can be represented as

$$\dot{m}_{rv}(y) = \frac{\dot{m}_{r[E]i}}{x_1} \frac{y}{L_{[E]chl}} \quad (8)$$

Manipulating equations (4), (5), (6), (7) and (8) to obtain the cross-sectional area $a_{r[E]chl}$ occupied by liquid at any point, y , along the length of the channel (all specific volumes are at $T_{r[E]build}$):

$$a_{r[E]chl}(y) = \frac{a_{[E]chl} \theta v_{rl} (x_1 L_{[E]chl} - y)}{y(v_{rv} - \theta v_{rl}) + \theta v_{rl} L_{[E]chl} x_1} \quad (9)$$

The liquid content of the tube is:

$$V_{r[E]chl} = \int_0^{L_{[E]chl}} a_{r[E]chl}(y) dy \quad (10)$$

and noting that the volume of the channel is

$$V_{[E]chl} = a_{[E]chl} L_{[E]chl} \quad (11)$$

Finally, integrating equation (10), the fractional liquid content of the channel is:

$$F_{rl[E]chl} = \frac{V_{rl[E]chl}}{V_{[E]chl}} \quad (12)$$

$$F_{rl[E]chl} = \left[\frac{\theta v_{rl}}{v_{rv} - \theta v_{rl}} \cdot \left[\frac{x_1 v_{rv}}{v_{rv} - \theta v_{rv}} \ln \left(\frac{v_{rv} - \theta v_{rv}}{\theta \cdot x_1 v_{rl}} + 1 \right) - 1 \right] \right]_{T_{sat(E)build}}$$

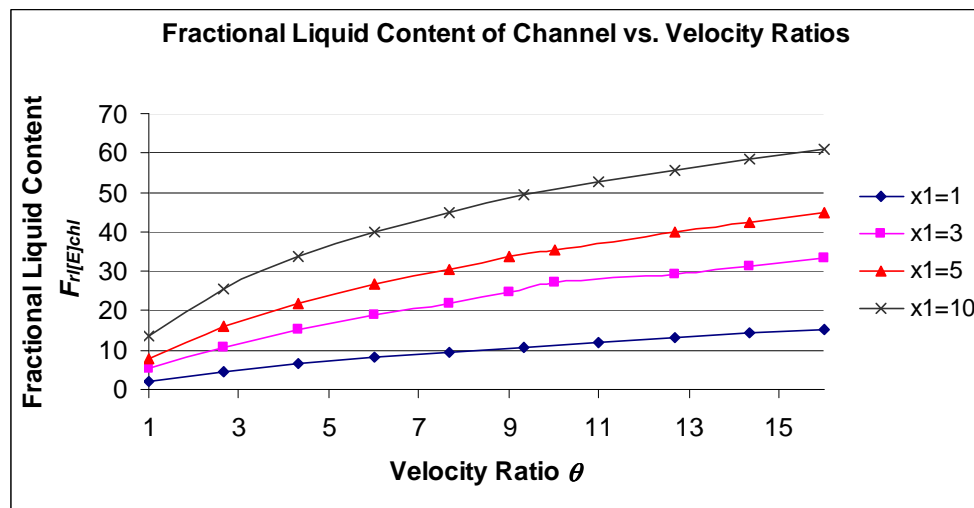


Figure A2.2 Fractional liquid content of evaporator channels versus velocity ratio at various average recirculation ratios

From Figure A2.2 above, the volume fraction of liquid varies according to the velocity ratio and the average recirculation ratio. As it is impossible to accurately predict the actual flow rate within the channels at the ERPM plant, the velocity ratio is varied at intervals of possible recirculation ratios. From the theoretical model of Section 8., it is predicted that the average recirculation ratio is five, and assuming a velocity ratio of 7,5 at the end of the ice-building process, the fractional liquid content of the tubes at the end of ice making and prior to harvesting is approximately 30 %. This value is used in the model of Section 8. to predict how much liquid refrigerant must be transported out of the plate and expelled to the accumulator prior to the warming sub-period.

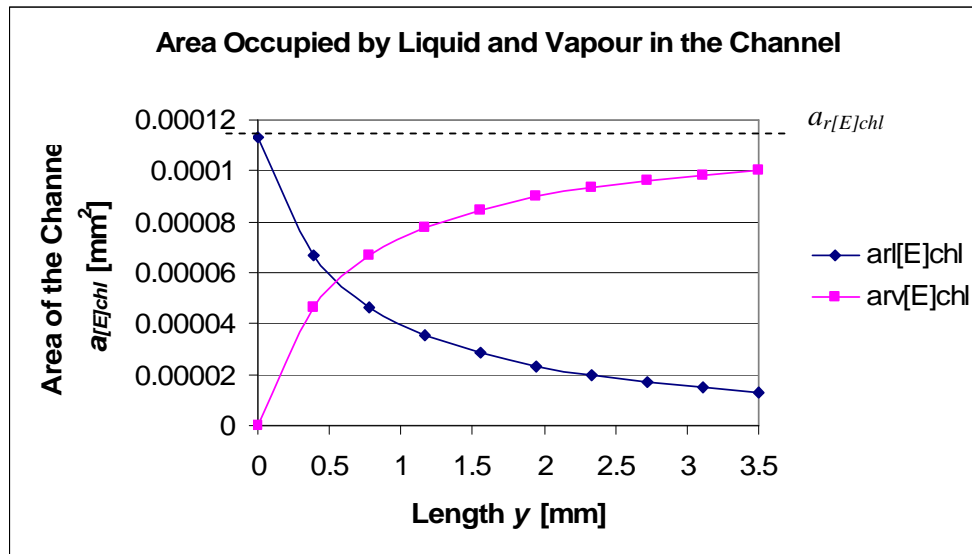


Figure A2.3 Areas occupied by liquid and vapour, predicted by equation (12), throughout the length of the evaporator channels. The actual channel cross sectional area is shown dashed

From Figure A2.3. above, the area occupied by saturated liquid ammonia at the cross section of the channel varies from channel inlet to outlet. At the top of the channel (evaporator outlet), the area of the channel is almost completely occupied by saturated vapour.

It would be desirable, of course, to model the flow within the channel using two-phase flow approximations. Whether any benefit can be achieved in developing an adequate two-phase flow model remains unclear. Based on the fact that the URD and heat transfer models of Sections 8. and 9. respectively predict the mass flow rate and recirculation ratio satisfactorily (i.e. there is correlation between these two models), modeling the mass flow rate using two-phase techniques is not sufficiently justified in this investigation. A two-phase flow analysis is however suggested for further work in Section 11, as it would more accurately predict the mass flow rate and average recirculation ratios at the evaporator.

APPENDIX A3

Calculations for Predicting the Free Stream Film Velocity of the Falling Water over the Evaporator Plates during the Ice Building Period

The water distributors at the top of an evaporator module each feed five plates (there are 35 plates per module, requiring 7 water distributors per module).

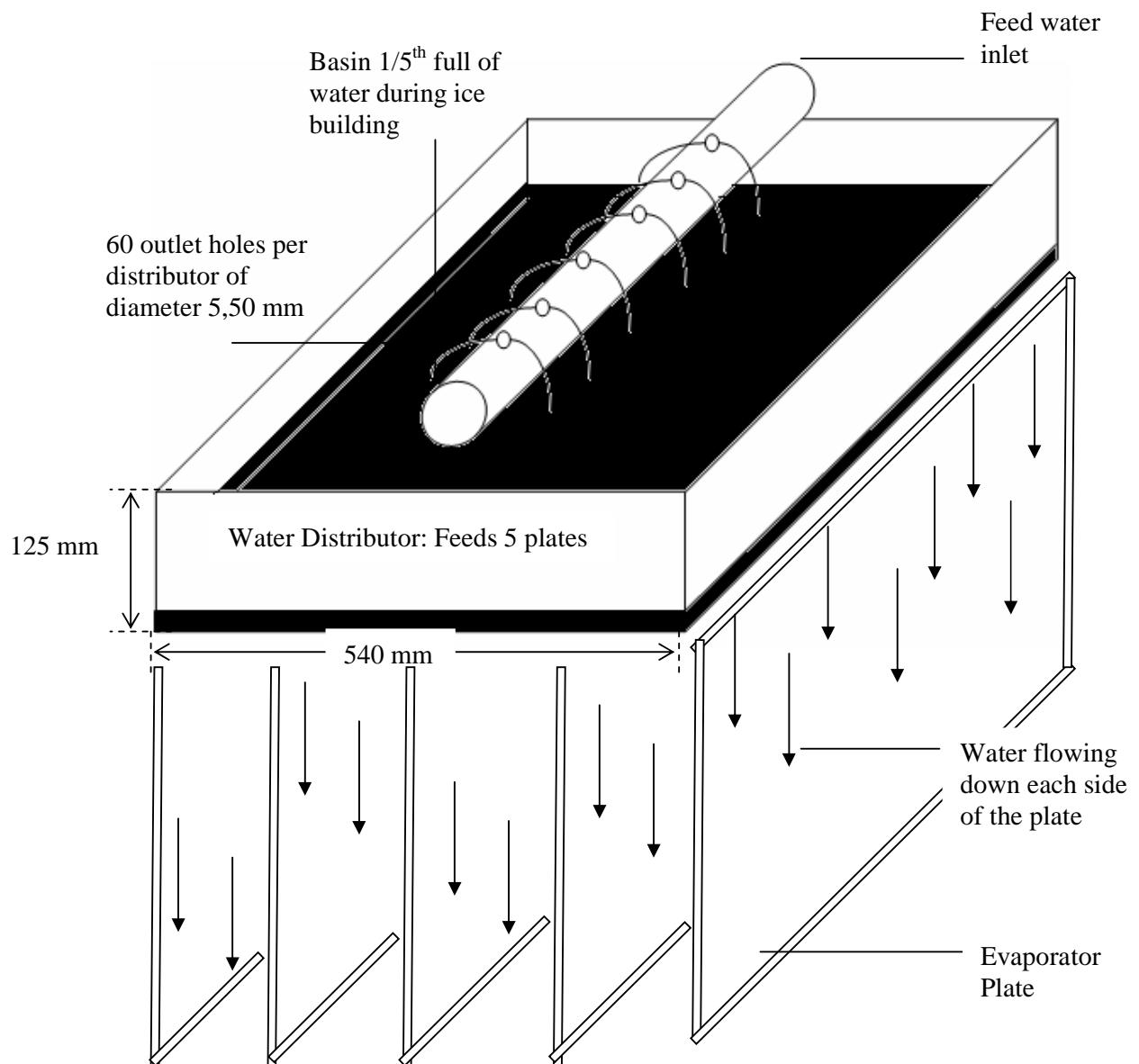


Figure A3.1 Diagram of one water distributor above the evaporator

Based on Worthington-Smith & Brouwer,⁽¹³⁾ the amount of water circulated at the feed water distributors is 12 times the mass of ice built. Therefore, knowing the mass of ice built from equation (8) of Section 8.1, the mass of water circulated per module over one ice building period is:

$$\dot{m}_{w[E]i} = 12\dot{m}_{i,b}$$

$$\dot{m}_{w[E]i} = 12 \frac{(1712)}{13,5 \times 60} = 25,36 \text{ kg/s (per module)}$$

And per water distributor:

$$\dot{m}_{w[E]i} = \frac{25,36}{7} = 3,62 \text{ kg/s (per water distributor)}$$

Finally, as each water distributor feeds five plates, and ice is built on each side of the plate, per side the mass flow rate of incoming feed water is:

$$\dot{m}_{w[E]i} = \frac{3,62}{5 \times 2} = 0,362 \text{ kg/s (per side of one plate)}$$

Which can be expressed in terms of the velocity of the falling water as:

$$\dot{m}_{w[E]i} = \rho_w (w_{[E]} \delta_w) \dot{v}_\infty$$

Where ρ_w is the density of the incoming water at approximately 0 °C, $w_{[E]}$ is the plate width, and δ_w and \dot{v}_∞ are the film layer thickness and velocity respectively of the falling water.

Now, from the Nusselt equation for water flowing via gravity over a plate⁽⁴⁶⁾, the film thickness of the water layer can be predicted:

$$\delta_w = \left(\frac{3\nu_w \Gamma_n}{\rho_w g \sin(\beta)} \right)_{T_{w[E]}}^{1/3}$$

Where ν_w is the kinematic viscosity, Γ_n is the liquid feed rate per unit width and β is the plate inclination angle (90°). All variables are at feed water temperature, $T_{w[E]}$ which based on tests performed at the operating plant is $1,5^\circ\text{C}$.

Substituting values into the above equation:

$$\delta_w = \left(\frac{3(1,7066 \times 10^{-6}) \frac{0,362}{3,5}}{1000(9,81) \sin(90)} \right)^{1/3} = 0,000377927 \text{ m}$$

Finally, the velocity of the falling water \dot{v}_∞ can be predicted:

$$\begin{aligned} \dot{m}_{w[E]i} &= \rho_w (w_{[E]} \delta_w) \dot{v}_\infty \\ 0,362 &= 1000(3,5 \times 0,000377927) \dot{v}_\infty \\ \dot{v}_\infty &= 0,274 \text{ m/s} \end{aligned}$$

This value of \dot{v}_∞ is used when predicting the heat transfer coefficient of the falling water in Section 9.1.

APPENDIX A4

Model to Predict the Time Required by the Fully Mechanically Pumped Arrangement to Recharge the Evaporator Plates after Harvesting

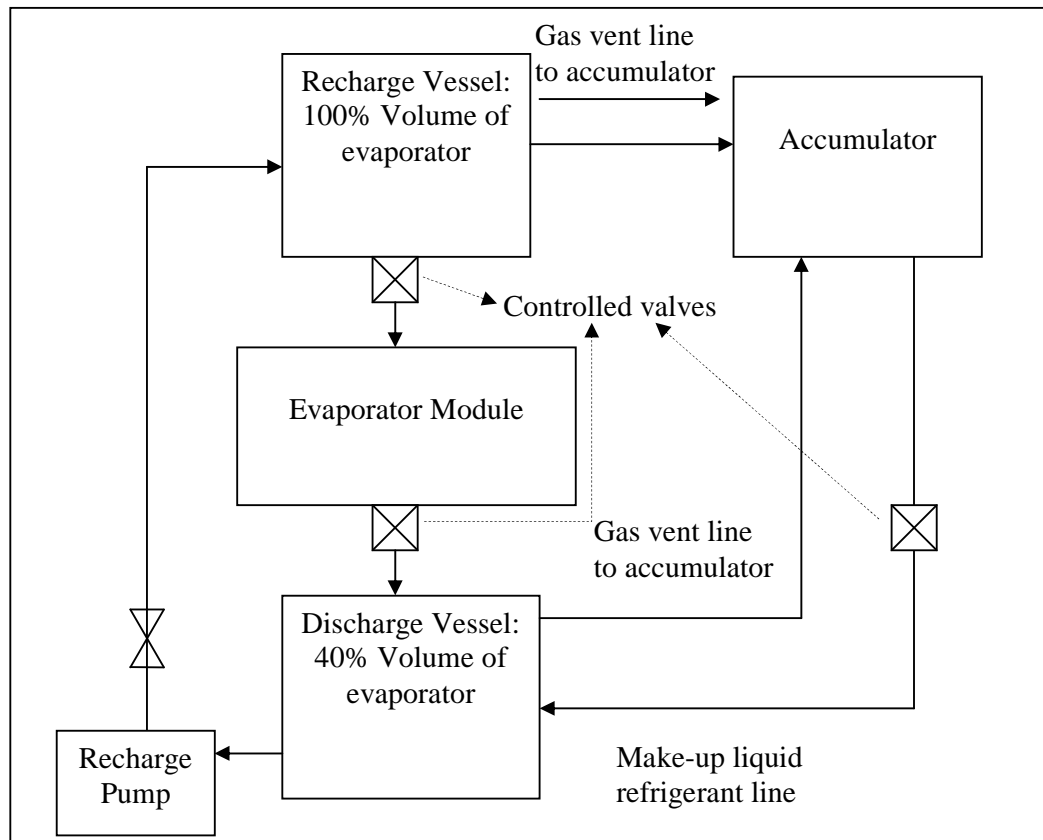


Figure A4.1 Recharge/discharge vessels and pump for the fully mechanically pumped arrangement

A fully mechanically pumped arrangement to empty the liquid refrigerant remaining in a module prior to the warming sub-period, and to refill the module at the beginning of the re-cooling sub-period, is developed in Section 8.9. This arrangement is described in more detail below.

A4.1 Required Recharge Pump Mechanical Input Power

The dimensions of one evaporator plate are shown in Figure 9.2 above. The steel wall thickness of the evaporator plate is 1,5 mm, and therefore the cross sectional area per channel is:

$$a_{[E]chl} = (0,035 - 2(0,0015))(0,01 - 2(0,0015)) = 0,000224 \text{ m}^2$$

The internal volume of the evaporator plates of one module, consisting of 30 channels per plate and 35 plates per modules is

$$V_{[E]} = 30 \times 35 \times a_{[E]chl} \times L_{[E]} = 0,823 \text{ m}^3$$

Therefore based on the dimensions of the recharge/discharge vessels defined in Figure A4.1 above, the volumes of these vessels are:

$$V_{[RV]} = V_{[E]} = 30 \times 35 \times a_{r[E]chl} \times L_{[E]} = 0,823 \text{ m}^3$$

$$V_{[DV]} = 0,4V_{[E]} = 0,329 \text{ m}^3$$

It is assumed that the module discharges its contents prior to harvesting in a maximum time of 10 seconds, and after harvesting, is recharged – with a volume of liquid refrigerant equal to its internal volume – from the recharge vessel in a maximum time of 25 seconds.⁽¹⁶⁾ It is recalled from Section 8.2.1 that at the beginning of the warming sub-period each plate is assumed to be filled by 30% of its inner volume with liquid ammonia. Therefore, the volumetric flow-rate at the inlet to the discharge vessel at the beginning of the warming sub-period is:

$$\dot{V}_{[DV]i} = \frac{0,3V_{[E]}}{10} = 0,025 \text{ m}^3/\text{s}$$

The volumetric flowrate at the outlet of the recharge vessel at the beginning of the re-cooling sub-period is:

$$\dot{V}_{[RV]o} = \frac{V_{[E]}}{25} = 0.033 \text{ m}^3/\text{s}$$

The energy equation between the discharge and the recharge vessels, assuming that changes in velocity and pressure¹⁰⁹ of the refrigerant liquid from one vessel to the other can be neglected is:

$$z_{[E-DV]} + H'_{[P]\{FMPS\}} = z_{[DV-RV]} + \left(f_{[PI]\{FMPS\}} \frac{l_{[PI]\{FMPS\}}}{d_{[PI]o\{FMPS\}}} + \Sigma K_{[PI]\{FMPS\}} \right) \frac{\dot{V}_{r[Dv-RV]}^2}{2g}$$

Where $l_{[PI]\{FMPS\}}$ is the total length of piping, $f_{[PI]\{FMPS\}}$ is the constant friction factor of the pipe and $\Sigma K_{[PI]\{FMPS\}}$ is the sum of the minor loss coefficients, predicted from Sinnott⁽⁸⁾. The Reynolds number is determined and the Moody diagram⁽³⁹⁾ is used to obtain the constant frictional factor $f_{[PI]\{FMPS\}}$ for the pipe.

The diameter of the inlet and outlet piping is assumed to be 0,05 m. The volumetric and mass flow rate required of the recharge pump, assuming it fills the recharge vessel by the internal volume of the module in 13 minutes, is¹¹⁰

$$\dot{V}_{r[Dv-RV]} = \frac{V_{[E]}}{13 \times 60} = 0,0011 \text{ m}^3/\text{s}$$

$$\dot{V}_{r[Dv-RV]} = \frac{\dot{V}_{r[Dv-RV]}}{\frac{\pi d_{[PI]o\{FMPS\}}^2}{4}} = 0,538 \text{ m/s}$$

The Reynold number is therefore:

¹⁰⁹ Both vessels are at accumulator pressure.

¹¹⁰ This is within the 13,5 minute ice building period.

$$Re_{\{FMPS\}} = \dot{v}_{r\{DV-RV\}} d_{\{PI\}\{FMPS\}} \frac{\rho_{r\{P_{r\{ACC\}}\}}}{\mu_{r\{P_{r\{ACC\}}\}}} = 93013$$

From the Moody Diagram of Figure A9.3 below, and assuming a relative roughness for refrigeration-grade steel piping from Barber⁽¹⁵⁾ of $e/d = 0,003$, $f_{\{PI\}\{FMPS\}} = 0,029$. Assuming minor loss coefficients for the exit, a valve and two elbows, from Sinnott⁽⁸⁾:

$$\Sigma K_{\{PI\}\{FMPS\}} = (K_{\text{Valve}} + 2K_{\text{Elbow}} + K_{\text{Exit}}) = (5 + 2(1,5) + 1) = 9$$

Based on measurements taken at Unit 5 of the ERPM plant, the recharge pump would be situated 3 metres below the discharge vessel, and be required to pump 8,5 metres vertically upward to the recharge vessel inlet.

From the energy conservation equation above:

$$3 + H'_{\{P\}\{FMPS\}} = 8,5 + \left(0,029 \frac{8,5}{0,05} + 9 \right) \frac{0,538^2}{2(9,81)}$$

Whence:

$$H'_{\{P\}\{FMPS\}} = 5,71 \text{ m}$$

The shaft power needed to drive the pump, assuming a mechanical pump efficiency of 85 % is:

$$\dot{W}_{\{P\}\{FMPS\}mech} = \frac{\rho_{r\{P_{r\{ACC\}}\}} g \dot{V}_{r\{DV-RV\}} H'_{\{P\}\{FMPS\}}}{1000 \eta_{\{P\}}} = \frac{650,70 \cdot 9,81 \cdot 0,0011 \cdot 5,71}{1000 \cdot 0,85} = 0,045 \text{ kW}$$

The work input from the pump increases the enthalpy of the liquid refrigerant as it increases its pressure. The URD of re-cooling the warmed liquid refrigerant per module at the evaporator, over a complete recharge time of 13 minutes, is obtained by inputting the mechanical input power predicted in this section into equation (84) of Section 8.9 above.

A4.2 Vessel and Piping Design Parameters for the FMPS

Referring to Figure A4.3 below, liquid refrigerant flows from the recharge vessel, initially filled to a height of $H'_{[RV]}$, into the evaporator plates via gravity within 25 seconds. Each plate has a recharge and discharge pipe (assume a constant diameter of $d_{[PI]rech}$) to allow liquid to enter/exit via gravity. Based on the dimensions of the plates, and noting that the recharge vessel is at accumulator conditions, the diameter of the recharge pipe can be predicted.

Applying conservation of energy equations at the control volume shown in Figure A4.3 below, as the recharge vessel empties, refrigerant liquid exits through the recharge pipe (The subscript $[PI]rech$ refers to the recharge pipe):

$$\frac{\dot{V}_{[PI]rech}^2 - \dot{V}_{[RV]}^2}{2g} = H'_{[RV]} \quad [A]$$

Manipulating the above equation to reflect the volumetric flow rate of the emptying recharge vessel:

$$\frac{\dot{V}_{[RV]}^2}{2g} \left(\frac{1}{a_{[PI]rech}^2} - \frac{1}{a_{[RV]}^2} \right) = H'_{[RV]} \quad [B]$$

Where the area $a_{[PI]rech}$ is of one recharge pipe for one plate of one module, and $n_{[PI]rech}$ is the number of recharge pipes required per module.

$$a_{[PI]rech} = n_{[PI]rech} \times \frac{\pi d_{[PI]rech}^2}{4} \quad [C]$$

$$a_{[RV]} = \frac{V_{[RV]}}{H'_{[RV]}}$$

The volumetric flow rate, from equation [B] above, is

$$\dot{V}_{[RV]} = \sqrt{\frac{2gH'_{[RV]}}{\left(\frac{1}{a_{[PI]rech}^2} - \frac{1}{a_{[RV]}^2}\right)}} \quad [D]$$

And by definition,

$$\dot{V}_{[RV]} = -a_{[RV]} \frac{\partial H'_{[RV]}}{\partial t} \quad [E]$$

Where the negative sign denotes emptying of the recharge vessel.

Referring to Figure A4.1 above, the internal volume of the recharge vessel is equal to the internal volume of all the plates in one module. Therefore, the amount of recharge pipes required to recharge the evaporator by its internal volume can be predicted by substituting equation [D] into equation [E] and integrating:

$$t_{[RV]rech} = \int_{1.2 \times L_{[RV]}}^{0.1 \times L_{[RV]}} \frac{-a_{[RV]} \sqrt{\left(\frac{1}{a_{[PI]rech}^2} - \frac{1}{a_{[RV]}^2}\right)}}{\sqrt{2gH'_{[RV]}}} dH'_{[RV]} \quad [F]$$

By varying the time to recharge the module $t_{[RV]rech}$, the number of recharge pipes required per module can be predicted.

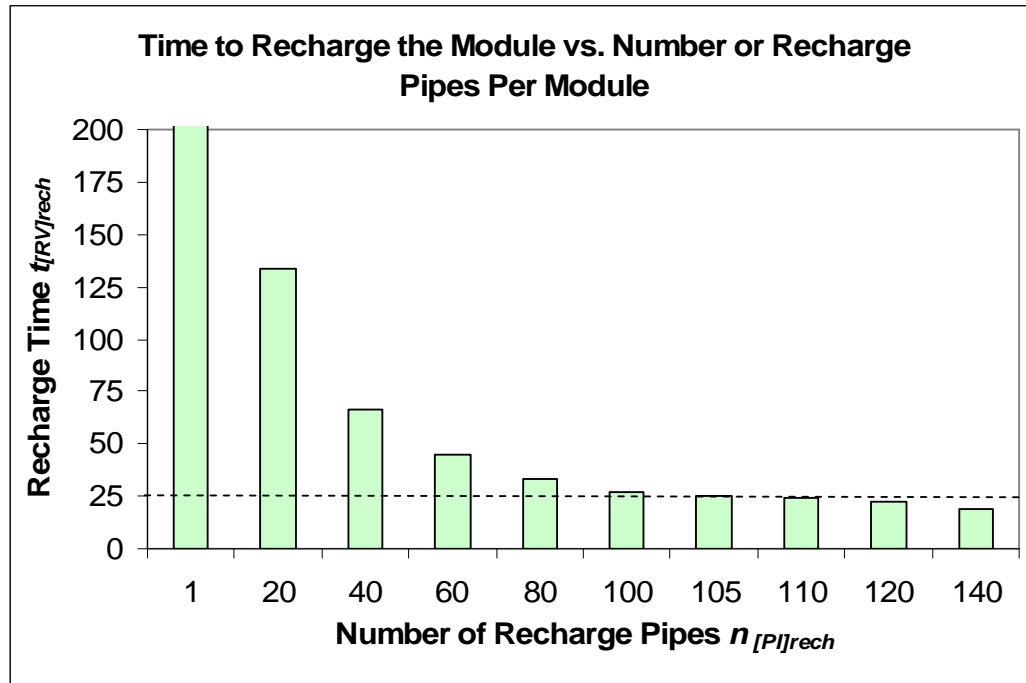


Figure A4.2 Time required to recharge the evaporator plates vs. number of pipes of equal diameter connected to the evaporator module

From Figure A4.2 above, assuming a pipe diameter $d_{PI/RV}$ of 15 mm which is smaller than the equivalent diameter based on the channel's cross-sectional area (from Section 9. this equivalent diameter is 17 mm) the number of recharge pipes of equal diameter required to recharge the evaporator in 25 seconds is 110. It is possible therefore to recharge the thirty channels of each plate within 25 seconds with 4 recharge pipes per plate. This diameter would also be adequate for the outlet piping from the bottom of each plate to the discharge vessel, as the volume of liquid ammonia discharged at the end of ice building (30%) is less than that required for recharging the plates. The methods of connecting the channels within the plate to the recharge pipe to allow them to be recharged within the requisite time require further investigation. Basic dimensions of the recharge and discharge vessels are however shown in Figure A4.3 above.

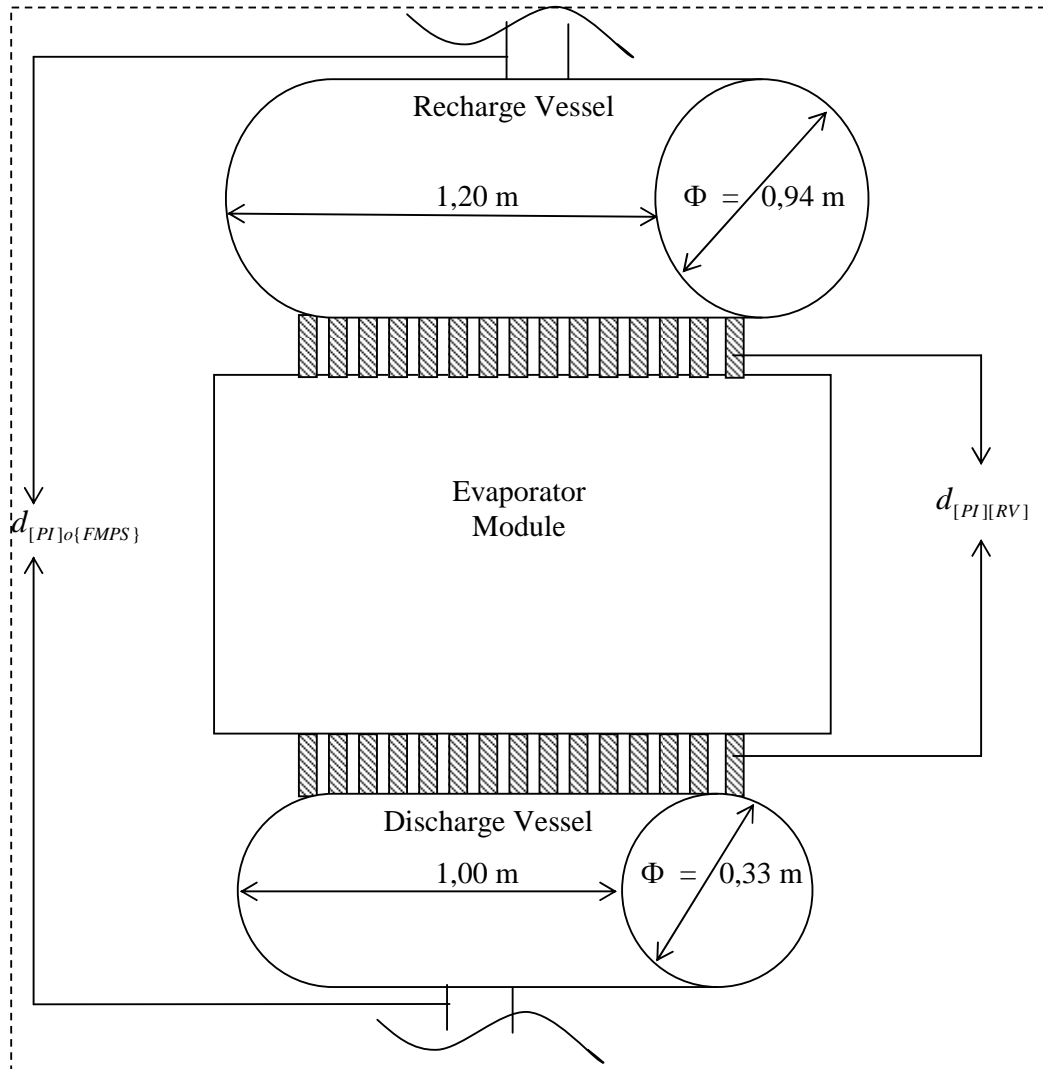


Figure A4 3 Control Volume for Fully Mechanically Pumped System: The recharge / discharge vessels and basic positions and dimensions

APPENDIX A5

A Brief Investigation, for Purpose of Comparison to the Shah and Nusselt Correlations, of Convective Condensing Heat Transfer Correlations for Flow in Horizontal Tubes

Three correlations are presented in Section 9.2 above for predicting the refrigerant side convective condensing heat transfer coefficient in vertical tubes during the warming sub-period. A comparison to other correlations found in the literature is presented here for flow in horizontal tubes as a comparison, and to investigate the dependence of the convective condensing heat transfer coefficient on tube orientation.

A5.1 The Dobson and Chato⁽³⁶⁾ Correlation

Dobson and Chato⁽³⁶⁾ predicted that in horizontal tubes and for forced condensation at high Reynolds number, the film condensation heat transfer coefficient in a horizontal tube is “independent of temperature difference (with the wall) but very dependent on mass flux and quality.”⁽³⁶⁾ This analysis would be appropriate for the operating ERPM plant were the tube orientation horizontal, as the plate wall temperature during harvesting is not constant over time and length. The formula to determine the heat transfer coefficient is found to be “a better predictor of the experimental data than any of the correlations from the literature.”⁽³⁶⁾ Although as mentioned above this correlation only applies to horizontal tubes, it is nonetheless included as a comparison to the correlations developed for vertical tubes.

$$h'_{2ph[D\&C]\{c\}} = 0,023 \left| Re_{rl}^{0.8} Pr_{rl}^{0.4} \left(1 + \frac{2.22}{X_{tt.har}^{0.89}} \right) \frac{k_{rl}}{D} \right|_{T_{r\{E\}har}} \quad (1)$$

Where the turbulent-turbulent Lockhart Martinelli parameter $X_{tt.har}$ during the warming sub-period is:

$$X_{tt.har} = \left| \left(\frac{\rho_{rv}}{\rho_{rl}} \right)^{0.5} \left(\frac{\mu_{rl}}{\mu_{rv}} \right)^{0.1} \left(\frac{1 - x'_{har}}{x'_{har}} \right)^{0.9} \right|_{T_{r[E]har}} \quad (2)$$

A5.2 The Jaster and Krosky⁽³⁷⁾ Correlation

Dobson and Chato⁽³⁶⁾ compared their data to the gravity-driven film condensation heat transfer coefficient in horizontal tubes of Jaster and Krosky⁽³⁷⁾, but stated that this model over predicted the earlier model of Dobson and Chato⁽³⁶⁾ for laminar flow. The Jaster and Krosky⁽³⁷⁾ model is included here as an upper limit when determining the convective condensation heat transfer coefficient in horizontal tubes. The wall temperature $\bar{T}_{s[E]har}$ is an average of the inner and outer wall temperatures predicted as shown in Figure 9.9 of Section 9.2 above.

$$h'_{2ph[J\&K]\{c\}} = 0,728 \left| \left(1 + \left(\frac{\rho_{rv}}{\rho_{rl}} \right)^{\left(\frac{2}{3}\right)} \right)^{-1} \right)^{\left(\frac{3}{4}\right)} \left(\frac{\rho_{rl} (\rho_{rl} - \rho_{rv}) h_{fg} g k_{rl}^3}{D \mu_{rl} (T_{r[E]har} - \bar{T}_{s[E]har})} \right)^{\left(\frac{1}{4}\right)} \right|_{T_{r[E]har}} \quad (3)$$

A5.3 The EES⁽³⁷⁾ Correlation

EES⁽³⁷⁾, based on Dobson and Chato's⁽³⁶⁾ correlations in different flow regimes, predicts the average film condensation heat transfer coefficient for condensation of saturated vapour to saturated liquid in a horizontal tube. The procedure then predicts whether the flow is laminar and dependent on temperature, or turbulent, and dependent on mass flux and quality. This coefficient is denoted $h'_{2ph[EES]\{c\}}$.

The convective condensing heat transfer coefficients based on the models presented above are plotted over the harvesting time of 90 seconds in Figure A5.1 below, starting at 10 seconds. From Figure A5.1, the coefficients vary significantly (from 182-12000 W/m².°C). Except for the correlation of Dobson & Chato $h'_{2ph[D\&C]\{c\}}$, the convective condensation heat transfer coefficients are

much larger for the horizontal tube orientation models ($h'_{2ph[J\&K]\{c\}}$ and $h'_{2ph[EES]\{c\}}$) than for the vertical ($\bar{h}'_{2ph[Sh]\{c\}}$, $h'_{2ph[Sh]\{c\}}$ and $h'_{2ph[Nu]\{c\}}$), and are clearly distinguishable in the graph below. The correlations that are strongly dependent on mass flow ($\bar{h}'_{2ph[Sh]\{c\}}$, $h'_{2ph[Sh]\{c\}}$, $h'_{2ph[D\&C]\{c\}}$ and $h'_{2ph[EES]\{c\}}$), decrease rapidly (except for $h'_{2ph[EES]\{c\}}$) as condensed fluid velocity decreases. Those correlations that are dependent on average evaporator wall temperature ($h'_{2ph[Nu]\{c\}}$ and $h'_{2ph[J\&K]\{c\}}$) increase as average wall temperature increases. This illustrates the uncertainty when predicting the coefficient accurately, even for those of similar tube orientation, and it is clear that not all the models above may apply to the specific working conditions of the evaporator at the ERPM plant.

Values of correlations for flow in horizontal tubes, based on an average recirculation ratio of 5, are listed in the table below, and in Figure A5.1 for different harvesting periods.

Table A5.1 Convective condensing heat transfer coefficients for flow in horizontal tubes, based on an average recirculation ratio of 5

Horizontal Tube Correlation	Convective Heat Transfer Coefficient [W/m ² .C]
$h'_{2ph[D\&C]\{c\}}$	13060,00
$h'_{2ph[J\&K]\{c\}}$	2380,00
$h'_{2ph[EES]\{c\}}$	8751,00

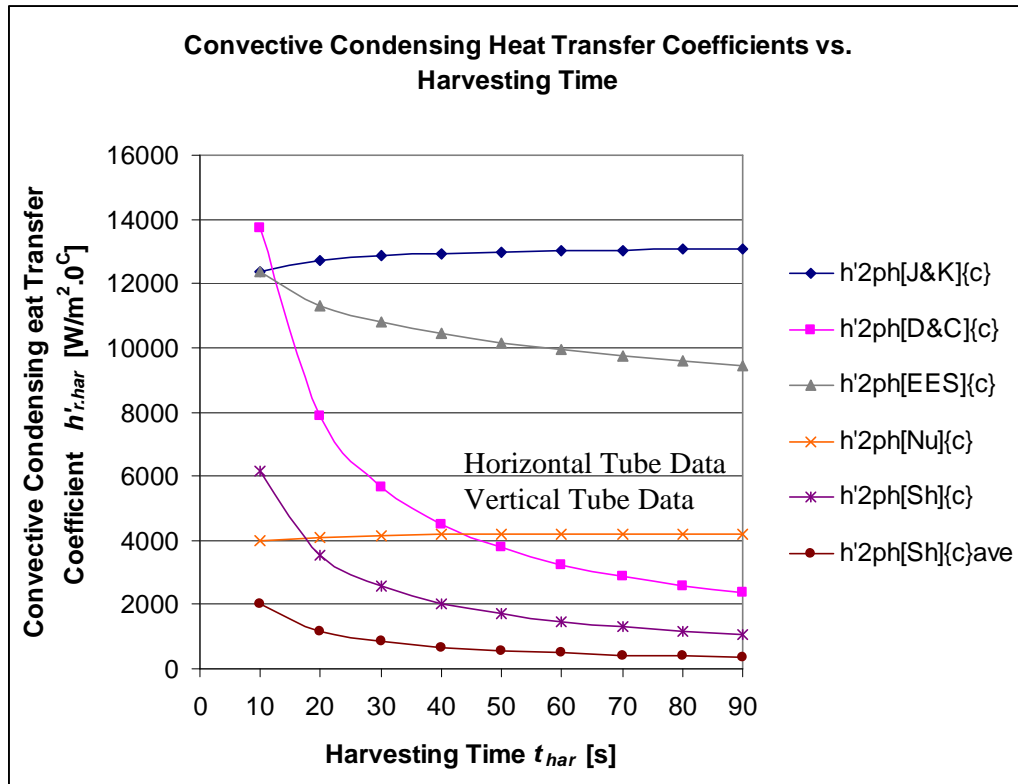


Figure A5.1 Convective condensing heat transfer coefficients versus harvesting time for horizontal and vertical tubes

APPENDIX A6

Presentation of Test Data Obtained from Testing at the ERPM Ice Making Plant

Data was obtained from one module of Unit 5 of the ERPM ice making plant on four occasions. The first test was performed to calibrate the pressure and temperature sensors and the data is therefore not included here. On the 22nd of October 2007 the first set of useable data was obtained, with volunteers standing at various points in the plant recording data at set time intervals. On the 12th of November 2007 the second set of test data was recorded, which included two runs lasting 30 minutes each. As the temperature in the ice room is below freezing point, no more than two runs of thirty minutes each were performed at each test. The measuring stations are shown in Figure A1.1, and a samples of the recorded variables and data sheets are provided in Appendix A7. The plant was visited on the 9th of March 2008, primarily to record some outstanding data.

Pressure sensors of varying accuracy (Table A7.1 of Appendix A7 lists the accuracies of the various installed pressure sensors) were installed throughout the plant to measure pressures, as per Figure A1.1. Most of the pressure sensors that were already installed at the plant were removed and fitted with more accurate gauges. All refrigerant temperature sensors were mounted non-invasively on metal surfaces. To ensure good thermal contact, copper compound was placed between the sensor and the metal surface, and the sensor's exterior was insulated from the surroundings with cork-based insulating tape.

As testing conditions at the plant during the two test days were not identical, and where the actual test data is not identical for the two tests, the 2nd test data is used, unless there is a reason to rely on the 1st test's data. The 2nd test data is deemed more reliable as experience gained from the first test allowed for better positioning of the data capturers throughout the plant. Some of the less critical data points, for example at the economizer port and compressor, were not recorded for the second test. This allowed for data capturers to be positioned at

the more critical locations (evaporators and pumper drums) and allowed them to focus on one sensor/gauge reading, as opposed to two or three for the first test.

The data is presented below in the form of graphs. Actual tabulated data is provided in the data disk accompanying this report. Observations and anomalies observed during testing are noted below each graph. “Test 1 / 2” refers to test day 1 and 2 respectively. “Run 1/2” refers to the 2 runs performed at each test. As mentioned above, each run lasted 15 minutes, corresponding to one full ice building (13,5 minutes) and shedding (1,5 minutes) cycle of one module.

As mentioned in Section 1.2.3, underground operations at the mine were suspended on 31 October 2008, however, testing at the cooling plant took place whilst the mine was still fully operational.

A6.1 Electrical Meter Readings for the Compressor and the Rate per kWh

For the second test, the following readings were recorded at the ERPM plant’s electrical power usage meters. It is assumed that the 7 minutes of measuring kWh at the electrical power usage meter, which is just under half a complete cycle time of 15 minutes, is deemed sufficiently representative of the average power consumption.

Table A6 1 Recorded data for the 2nd test at the electrical power usage meters

Time	Power Usage Meter Reading [kW]	Product of Voltage and Current Transformer Ratio
13:19	7696,815	2400
13:26	7696,885	2400

Over the time recorded, the kWh consumed are:

$$(7696,815 - 7696,885)2400 = 168,00 \text{ kWh}$$

The electrical power consumed over the recorded time is therefore:

$$\dot{W}_{[CR][CGPS]elec} = 168 \frac{60 \text{ minutes/hour}}{7 \text{ minutes}} = 1440,00 = 180,00 \text{ kW/module}$$

Assuming a compressor motor efficiency η_m of 96%, the mechanical power input of the compressor for the CGPS is:

$$\dot{W}_{[CR][CGPS]mech} = \dot{W}_{[CR][CGPS]elec} \eta_m = 172,80 \text{ kW/module}$$

Table A6 2 Industrial kWh tariffs (>132 kV) from Eskom⁽²⁵⁾ for the period 2010-2011

Period	Rate Definition	Cents / kWh High Demand Season [June-August]	Cents / kWh Low Demand Season [September-May]
07:00 – 10:00	Peak	150,,58	41,82
10:00 – 18:00	Standard	38,93	25,51
18:00 – 20:00	Peak	150,58	41,82
20:00 – 22:00	Standard	38,93	25,51
22:00 – 07:00	Off-Peak	20,66	17,76

Assuming that due to maintenance and shutdown periods, the unit operates 11 months of the year (shutdown for one month during High Demand Season), the compressor and pumps, where relevant, would operate for 8030 operating hours per year. Per 24 hour period, the average rate per kWh is 55,34 cents and 26,00 cents for the High Demand and Low Demand Season respectively. For six months, the unit operates at the Low Demand Season rate (as during the Winter months the mine's demand for cooling is less), and for 5 months at the High Demand Season rate. Therefore, the average annual rate per kWh is:

$$365 \times 24 \times \left(\frac{6}{12} \times 26,00 + \frac{5}{12} \times 55,34 \right) = 315871 \text{ Cents/kW/year}$$

A6.2 Water and Ice Quantities Measured at the Plant

Table A6 3 Water and ice quantities measured at the plant

Measured Quantity	Measuring Point	Typical Value
Thickness of Harvested Ice	At conveyor belt adjacent to evaporator module	5 - 6 mm
Temperature of water in the water distributor	At the water distributor	1 – 2 °C
Ambient feed water temperature	Inlet to Pre-Chiller	22,2 °C
Atmospheric pressure P_{atm}	Pressure gauge at condenser	83,5 kPa

Data at various points throughout the plant is presented below. Comments on the graphs follow each plot. All pressures are gauge pressures.

A6.3 Data at the Evaporators

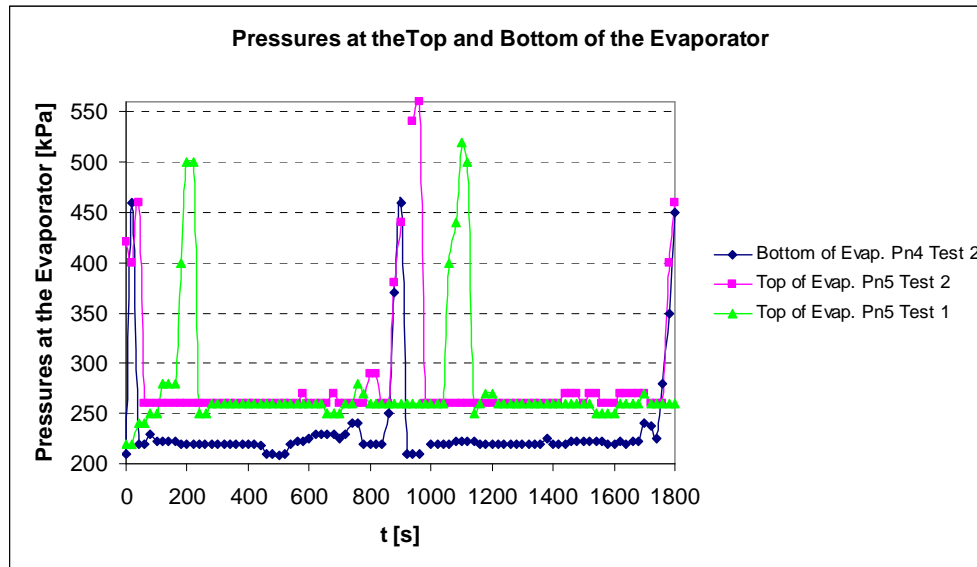


Figure A6.1 Refrigerant Pressure at Top and Bottom of Evaporator Plates

Comment: The 'spike' in the figure above is due to increasing pressurization during the warming sub-period, with the rapid fall signifying the onset of the re-cooling sub-period. The ice building period is approximately 810 seconds, with shedding lasting for approximately 90 seconds. Peak harvesting pressures recorded for the 2nd test are lower than expected at the beginning and end of recorded data, perhaps due to the fact that the beginning and end of the test seemed to coincide with a harvesting period.

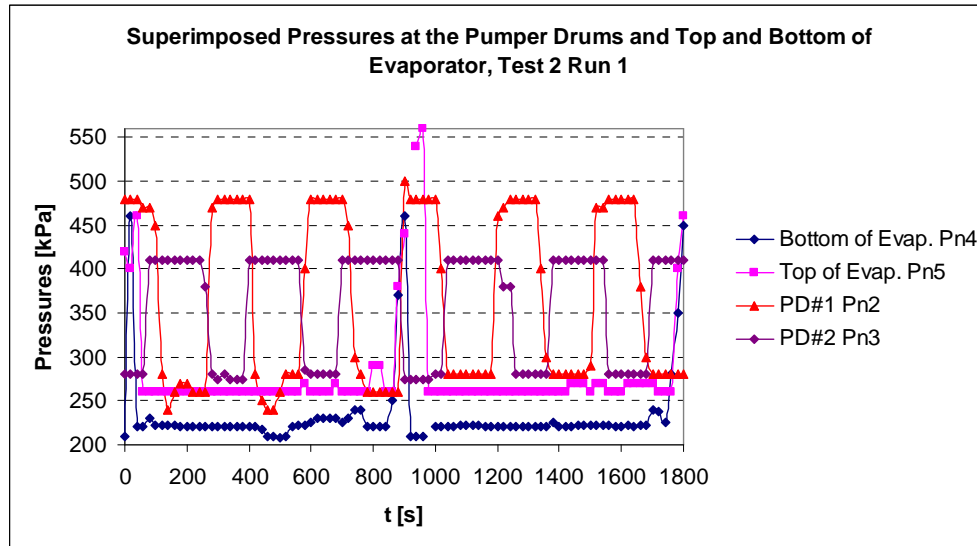


Figure A6.2 Refrigerant Pressures at Evaporator and Pumper Drums, Test 2 Run 1

Comment: The pressures at the evaporator are the same as in Figure A6.1 above. Pumper drum #2 has a smaller pressure differential than pumper drum #1 and therefore its pumping period is slightly longer. This is discussed in more detail in Section A6.3 below.

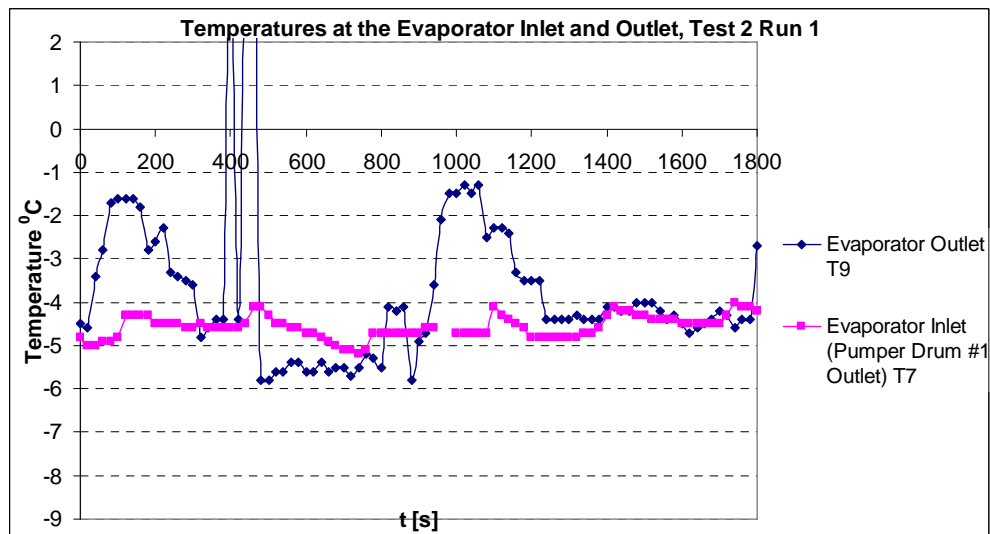


Figure A6.3 Surface Temperatures at Evaporator Bottom Ports: Liquid Inlet and Liquid Outlet

Comment: Although from Figure A1.1, the temperature T7 is measured at the outlet of pumper drum #1, nevertheless, this temperature is close to evaporator temperature (once the pressure drop across the evaporator is included). The reason for the temperature ‘spike’ for T9 at 400 seconds is unclear.

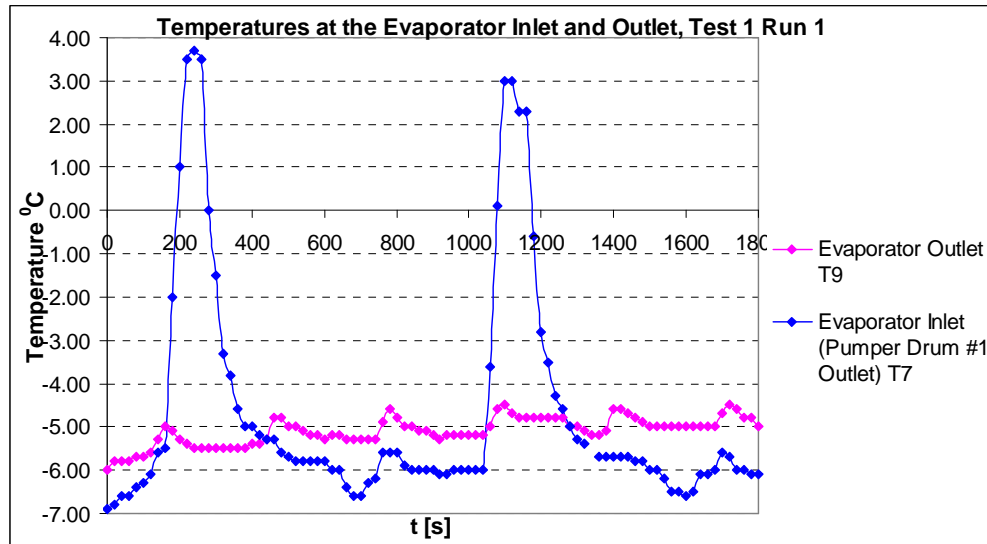


Figure A6.4 Surface Temperatures at Evaporator Bottom Ports: Liquid Inlet and Liquid Outlet, Test 1 Run 1

Comment: Temperature ‘peaks’ at the evaporator outlet correspond with the harvesting period. The peak temperatures reached at the outlet do not match for the 2 tests (as shown in Figure A6.5 below), with substantially higher, and more probable temperatures recorded for the 1st test. Test data for the first test seem more probable; perhaps the temperature sensors did not record accurately for the 2nd test.

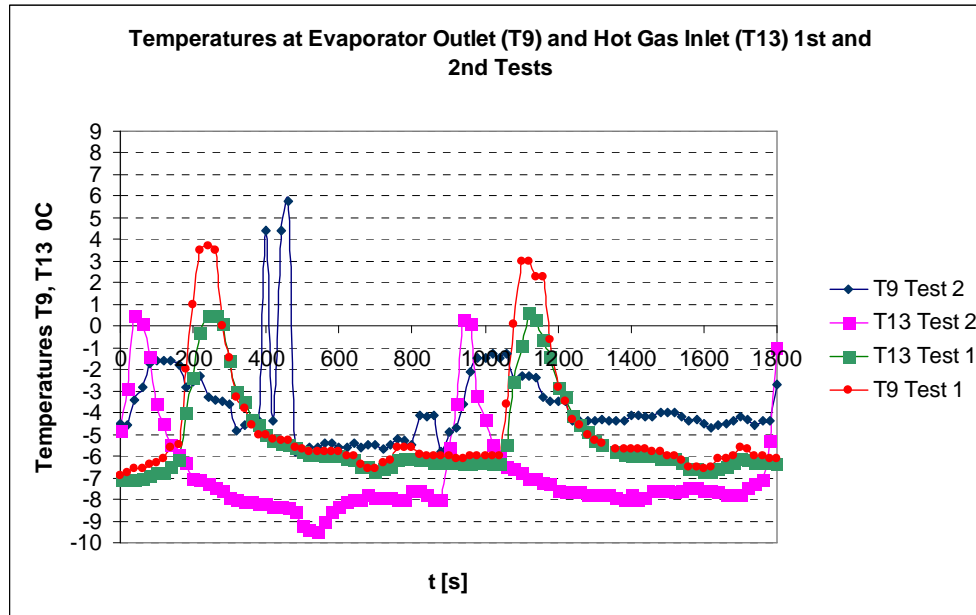


Figure A6.5 Surface Temperatures at Evaporator Top Ports: Warm Gas Inlet and Liquid-Vapour Outlet

Comment: T13 measures the warm gas that flows into the evaporator inlet during the warming sub-period. Data at the hot gas inlet (T13) over the two tests are inconsistent (the behaviour was not identical). The temperatures recorded for the 2nd test are lower than saturated evaporator outlet temperature (at Pn5); therefore this temperature sensor must have been faulty. The 1st test data is a more probable recording of the temperature at the hot gas inlet to the evaporator, as the temperatures measured at T13 during ice building match up well with that of the evaporator outlet (T9).

In conclusion, comparing data at the evaporator outlet for tests 1 and 2, the temperatures measured at T9 differed. Again, the 1st test's data is more reliable as temperatures correspond better with saturated evaporator pressure (Pn5).

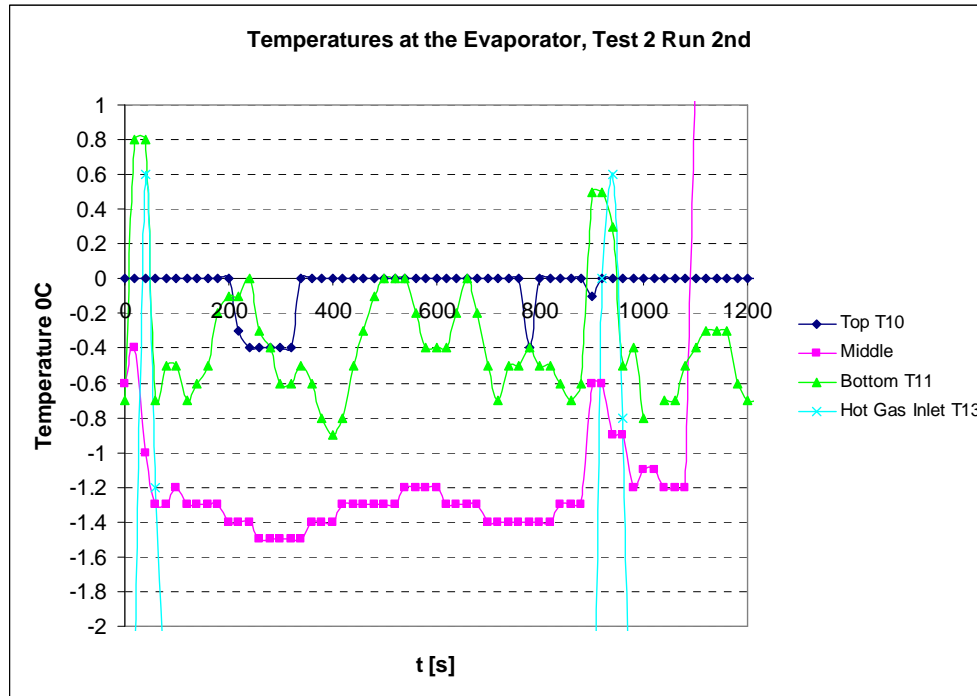


Figure A6.6 Surface Temperatures at Top, Middle and Bottom of Evaporator Plate

During the 2nd run of test 2, an extra temperature sensor was placed at the middle of one evaporator plate. This run did not extend for the full 1800 seconds as for the previous runs. The changes in temperature correspond well with that of the inlet of the hot gas (T13). However, these temperatures were inaccurate as the middle temperatures should be lower than that of the top. This graph is therefore merely a representation of the changes in temperature at the evaporator.

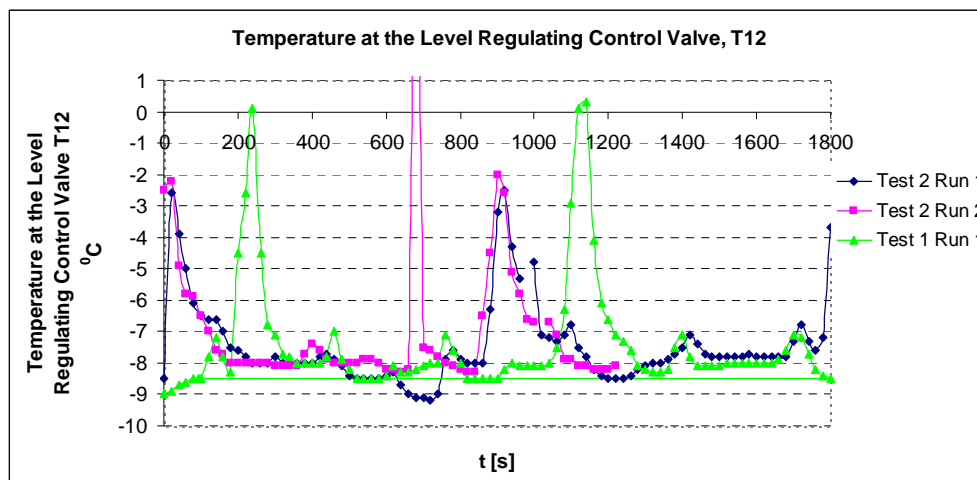


Figure A6.7 Temperature at the Level Regulating Control Valve of the Evaporator

Comment: From Section 8.2.1, due to the direct contact between the warm harvesting gas and the cold liquid while the former is expelling the latter to the accumulator at the beginning of the warming sub-period, heat is absorbed by this liquid in the evaporators. The temperature of the expelled liquid above evaporating temperature, $(T_{r[E-ACC]} - T_{r[E]build})$, is predicted from the above graph, where a temperature sensor T12 was placed before the level regulating valve. The URD of re-cooling this warmed liquid is predicted in Section 8.3.2.

A6.4 Data at the Pumper Drums

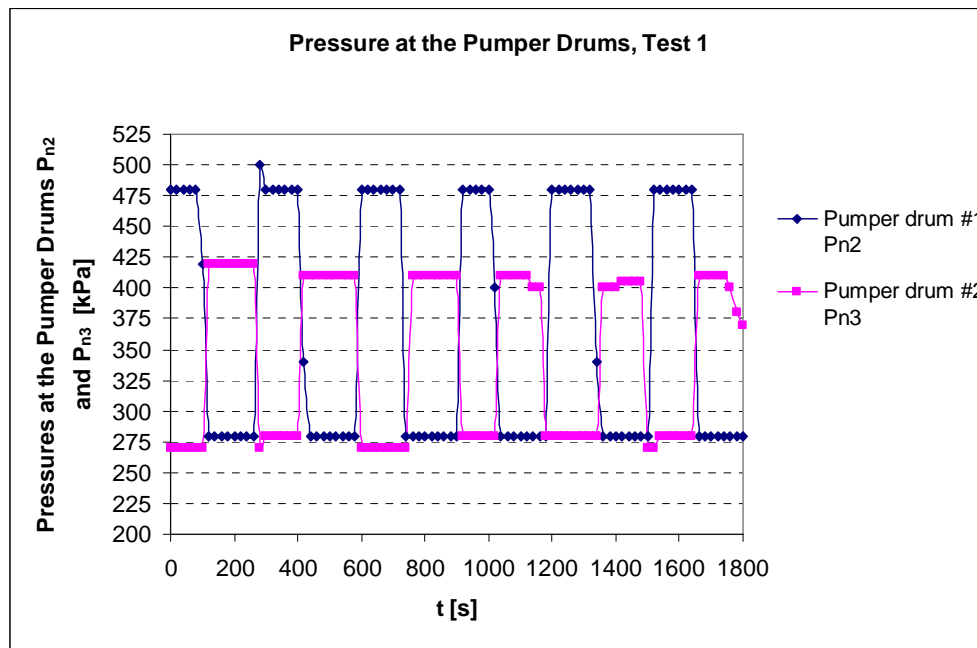


Figure A6.8 Pumper Drum Pressures (Test 1)

Comment: For Pumper drum #1, pumping times are somewhat shorter than filling times – the reverse is true for Drum 2. This stands to reason; within a *set* pumping & filling cycle, the shorter the pumping time (due to a higher pressure), the longer the filling time, and vice versa.

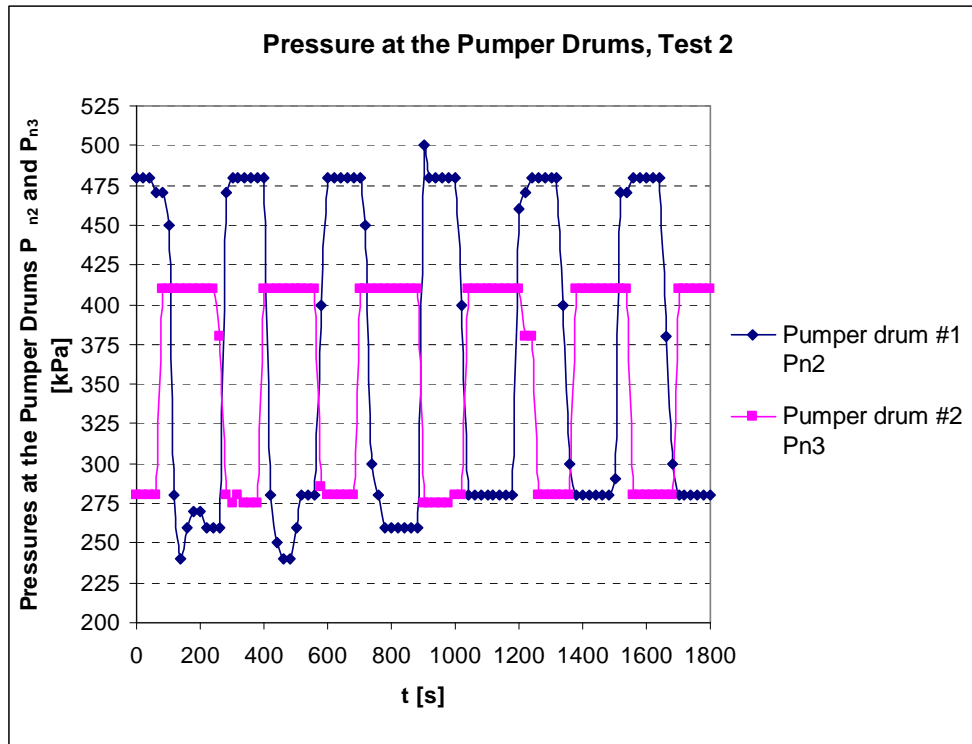


Figure A6.9 Pumper Drum Pressures (Test 2)

Comment: The lower pressure and longer pumping period at pumper drum #2 is evident for both tests.

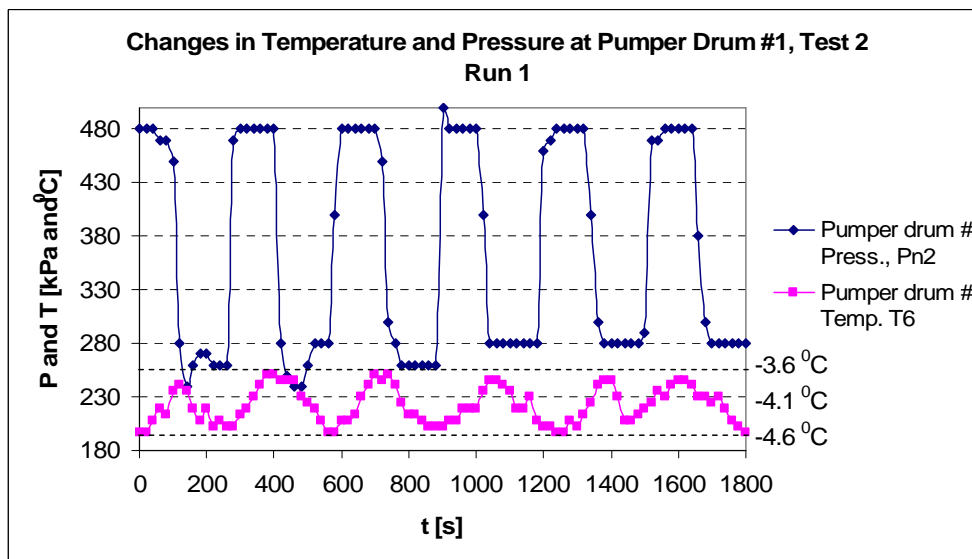


Figure A6.10 Pressures and Surface Temperatures (magnified to show effect) at Pumper Drum 1 (Test 2, Run 1)

Comment: The above graph illustrates that at the conclusion of every pumping period, corresponding to the venting of the pressurizing pumping gas to the accumulator, the pumper drum is re-cooled to filling temperature.

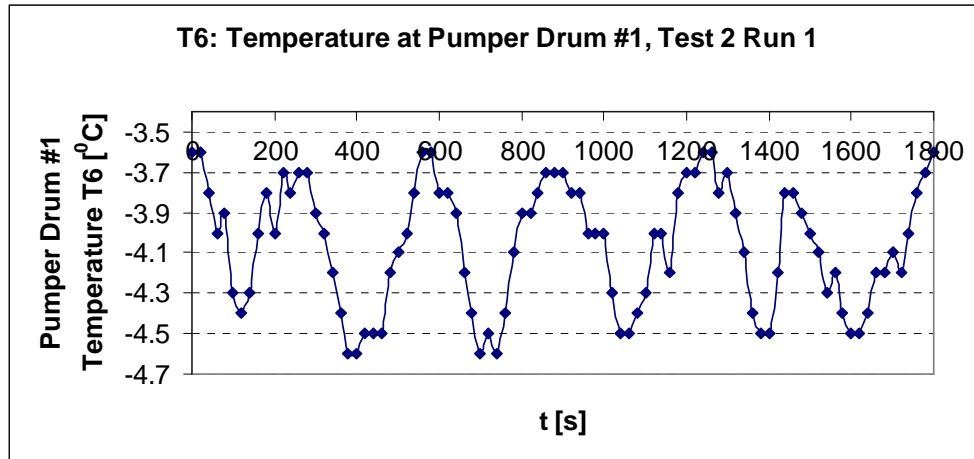


Figure A6.11 Surface Temperatures at Pumper Drum 1 (Test 2, Run 1)

Comment: From Section 8.4.1, the only URD at the pumper drum seen during the filling process is the re-cooling of the steel of the pumper drum, which is warmed during its pumping period. The rest of the URDs are seen at the accumulator and listed in Section 8.3.2 above. The temperature at the pumper drum wall was measured (sensor T6 of Figure A1.1) and is plotted in the figure above. From the timing diagram of Figure 3.1, pumper drum 1 undergoes 3 pumping periods every 15 minutes, with the maximum temperature rise during pumping recorded as 1°C above filling temperature.

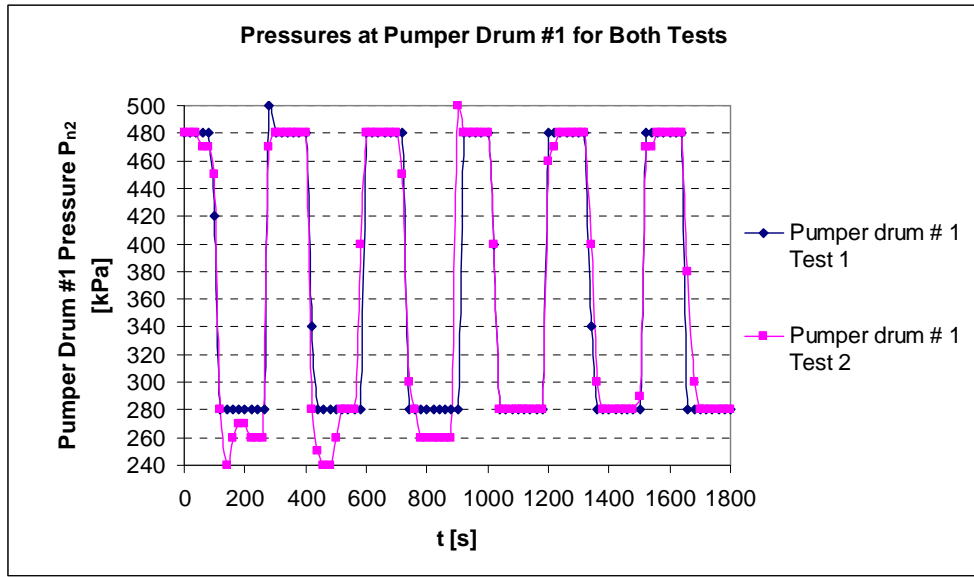


Figure A6.12 Pressures at Pumper Drum 1 (Tests 1 and 2)

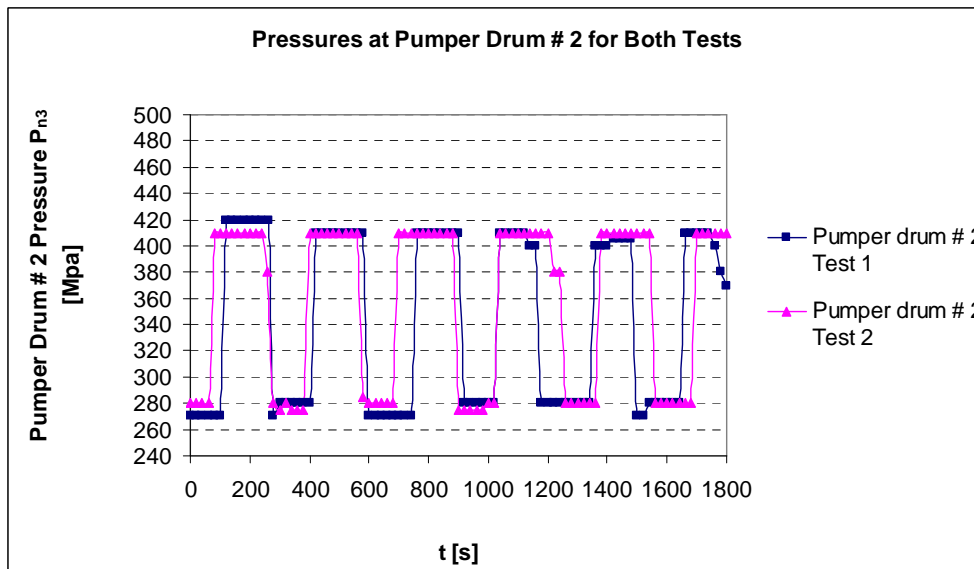


Figure A6.13 Pressures at Pumper Drum 2 (Tests 1 and 2)

Comment: As mentioned above, for both tests, pumper drum #2 is at a lower pumping pressure and has a longer pumping period than Pumper drum #1. This stands to reason; a lower pumping pressure means a longer time to pump out the same volume of liquid. The difference in pumping pressures is most likely due to slightly different downstream pressure settings on the expansion valves.

The pumping and filling periods for pumper drum #1 are approximately 130 seconds, with a changeover time of 20 seconds. This is as expected, as from the timing diagram of Figure 3.1 of Section 3.2 above, there are three pumping periods per pumper drum per ice making cycle of one module, which lasts for 15 minutes. The pumping period of pumper drum #2 is slightly longer, (160 seconds) and therefore its filling period is shortened to approximately 100 seconds.

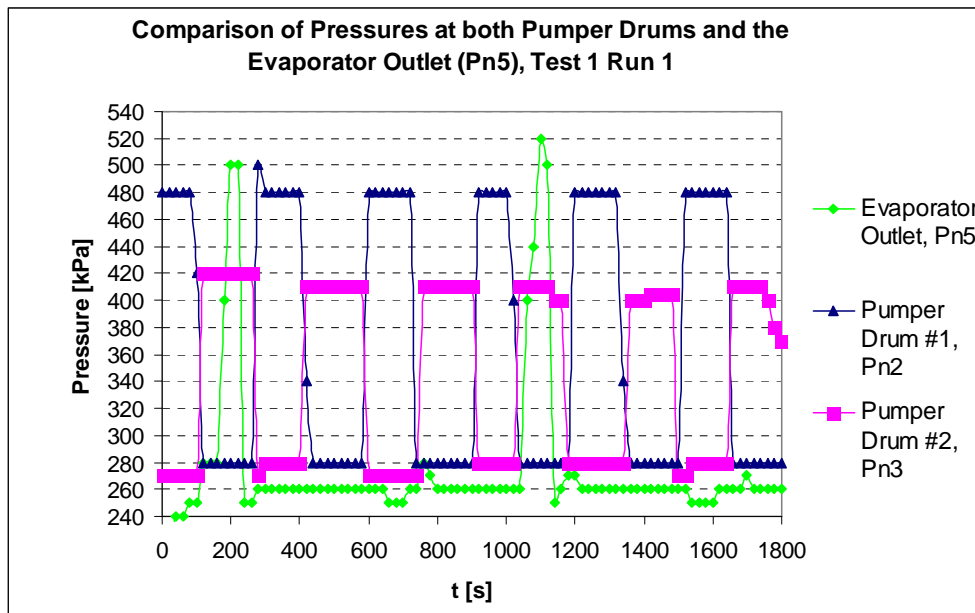


Figure A6.14 Pumper Drum and Evaporator Pressures

Comment: The above graph compares the pumper drum pressures with those at the evaporator outlet. From this it appears that the difference in pressure between the filling pumper drums and the evaporator during ice building is approximately 14,30 kPa. This pressure difference is significant for the model of Section 8., as in Section 8.10.2 the operating pressures for the four pumping arrangements are varied according to their pressure difference relative to the evaporator.

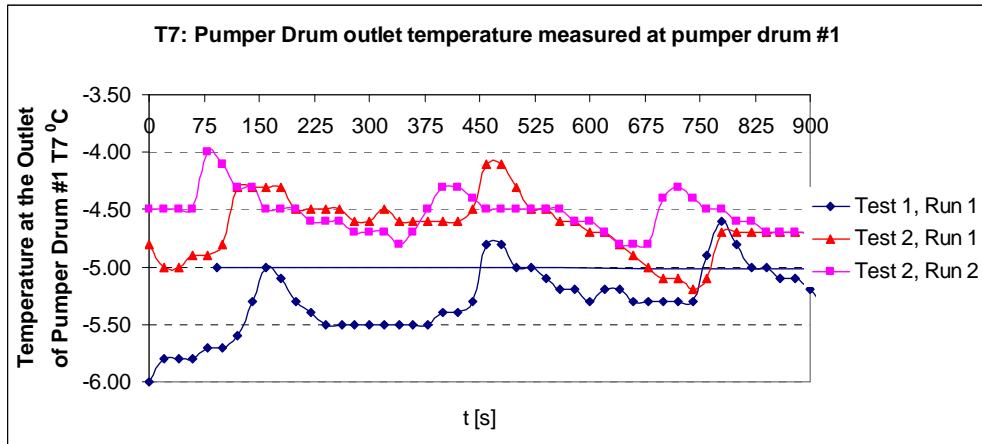


Figure A6.15 Surface Temperatures of Liquid Outlet of Pumper Drum 1

Comment: From Appendix A8, during the pumping period at the pumper drum, an upper portion of pumped liquid is warmed due to its interaction with the warmer pressurising gas. As it was prohibited to install temperature sensors inside the pumper drum, the change in temperature of this upper portion of pumped liquid was predicted by placing a temperature sensor at the outlet of pumper drum 1 (T7 on Figure A1.1). The temperature peaks of the figure above correspond to the temperature rise of the liquid refrigerant, which occurs during the last stage of pumping. This graph is therefore used to predict the change in temperature of the upper pumped layer of liquid during the pumping period.

A6.5 Data at the Accumulator

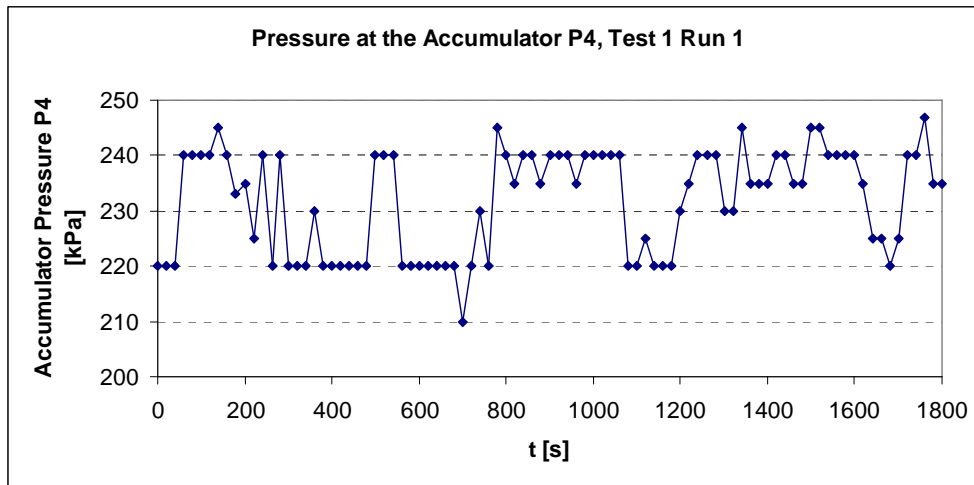


Figure A6.16 Accumulator Pressure for the 1st Test

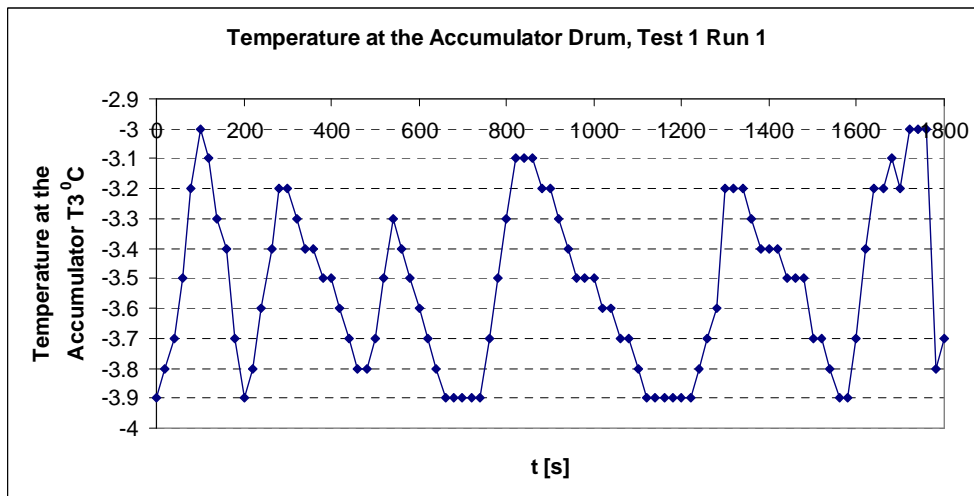


Figure A6.17 Accumulator Temperatures for the 1st Test

Comment: From Section 8.3.1, the maximum temperature rise at the accumulator $T_{heat[ACC]}$ was measured (T3 of Figure A1.1). The temperature change over time was recorded and is presented in the figure above, where six temperature peaks occur over the recorded 30 minute time interval. The temperature sensor at this position was deemed inaccurate and disregarded for the second set of tests performed at the plant.

From the figure above, the first three temperature peaks occur approximately every 150-170 seconds, corresponding to the 130 second pumping period and 20 second changeover period (during which the [pumping] pumper drum vents its gas to the accumulator), defined in Table 3.1 above. The temperature peaks from 500 seconds onward do not however correspond with the [pumping] pumper drum venting periods; the reason for this is unknown. Therefore, only the first three peaks of the figure above are regarded as accurately measuring the change in temperature at the accumulator during the venting period of the [pumping] pumper drum. Following the time period of these first three temperature peaks, which as mentioned above, correspond with the venting period of the [pumping] pumper drum, the change in temperature at the pumper drum is conservatively assumed to occur six times per ice building and shedding cycle (15 minutes), corresponding with the three venting periods of each pumper drum in the corresponding time.

A6.6 Data at the Condensed Liquid Receiver

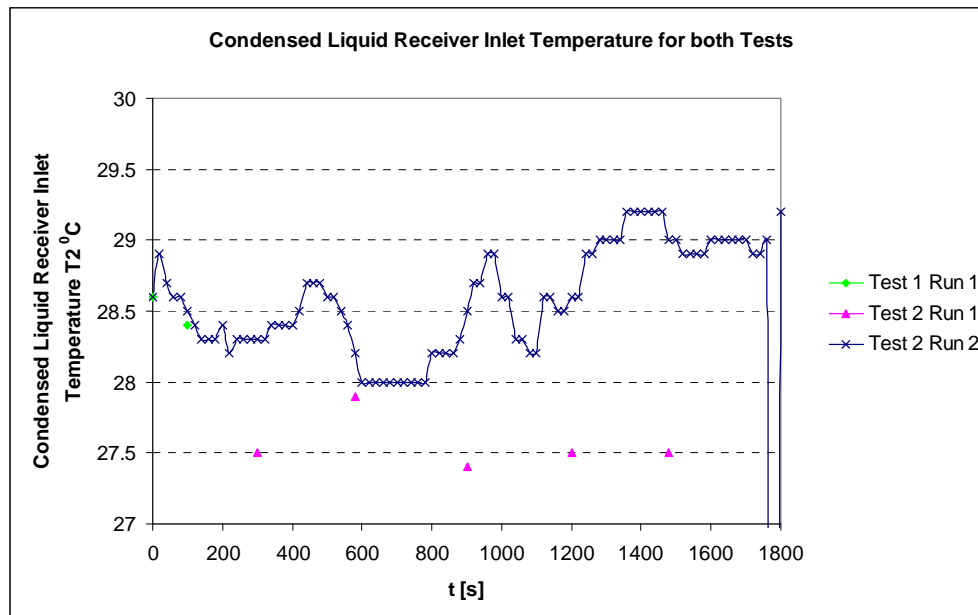


Figure A6.18 Condensed Liquid Receiver Temperatures for both Tests

Comment: As the condensed liquid receiver is outside the plant building, this temperature sensor was also outside and was exposed to the elements. This may

be the reason that temperatures were slightly lower than expected (saturated condensed liquid receiver refrigerant temperature is 29,01 °C). Only two data points were captured for the 1st test (as shown in green in the figure above) and 5 for the 1st run of the 2nd test. Therefore the data for the 2nd run of the 2nd test should be regarded as the primary measurement of temperature at the receiver. The ‘dip’ in temperature for the 2nd run of the 2nd test may be due to inaccurate gauge reading by the data recorder, as the remaining temperatures are relatively consistent over the measured period.

A6.7 Data at the Compressor

All data below is from the 1st run of the 1st test. As data collected for this test showed little variation, there was no need to repeat these data recordings for the 2nd test.

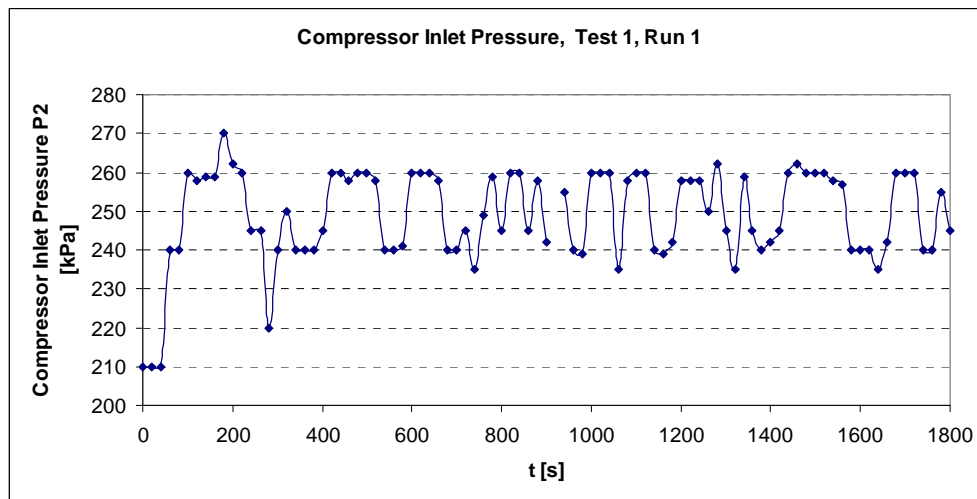


Figure A6.19 Compressor Inlet Pressure

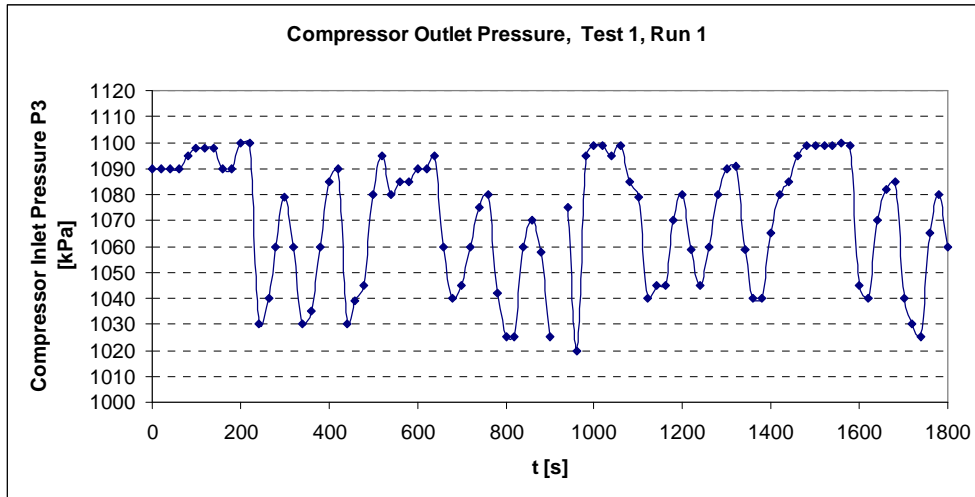


Figure A6.20 Compressor Outlet Pressure

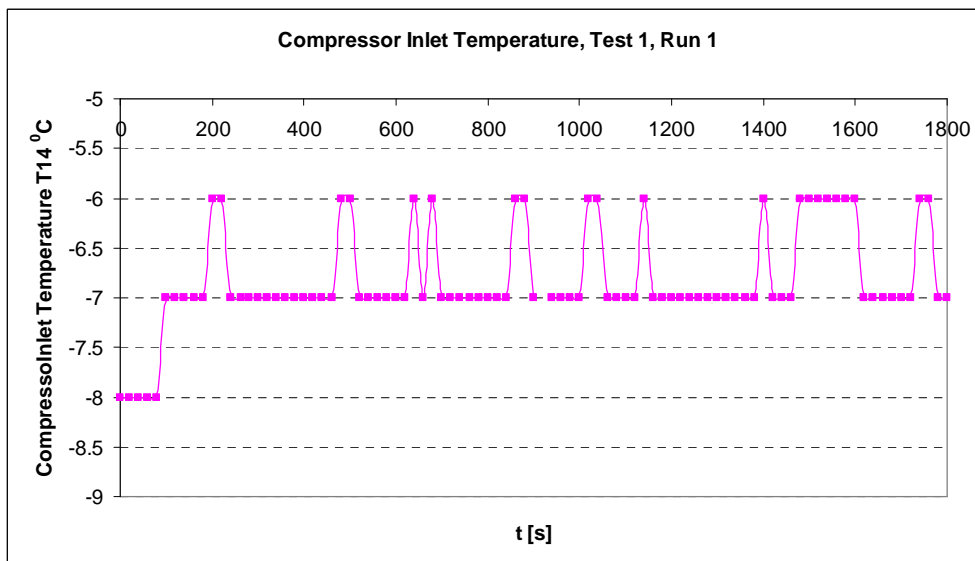


Figure A6.21 Compressor Inlet Temperature

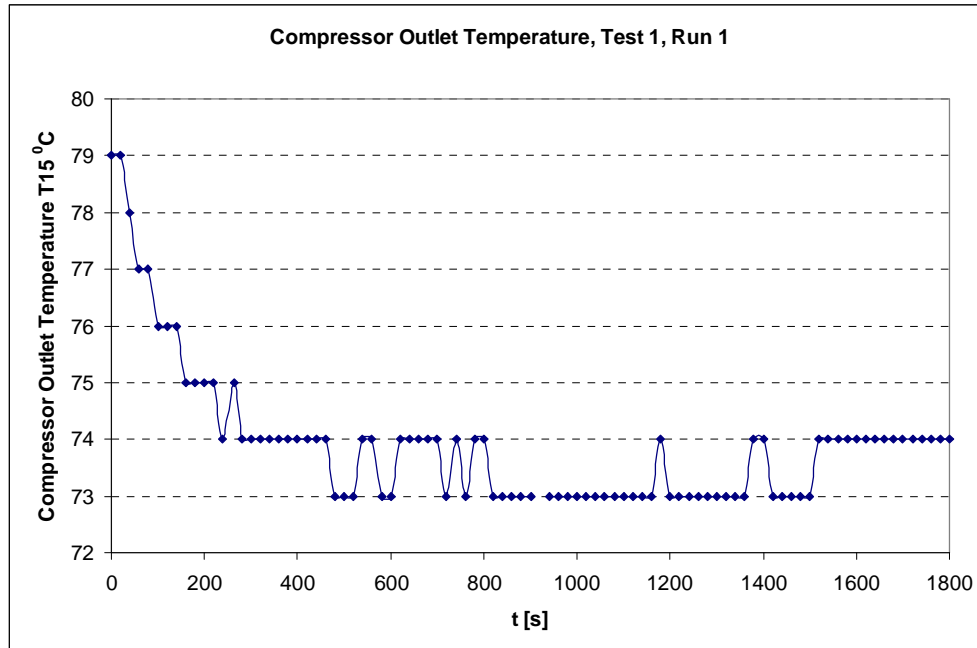


Figure A6.22 Compressor Outlet Temperature

Comment: Although data at the compressor is not used in developing the models of this investigation, as stated in Section 7.1.2 above, all PRDs and URDs manifest themselves as commensurate quantities of refrigerant vapour arriving at the accumulator, and hence at the compressor inlet to be compressed. The staggered operation of all 8 modules of Unit 5, as shown in the timing diagram of Figure 3.1, can predict when the different processes commence and conclude and allows for maximum smoothing of load on the compressor. As shown above, the inlet and outlet pressures at the compressor remained relatively constant throughout the testing period, which indicates that the staggering of the different processes effectively evens out the load on the compressor.

A6.8 Comparison of the Theoretical and Actual Timing Diagram / Pumping Schedule

The theoretical timing diagram / pumping schedule of Figure 3.1 for the operating plant, modified to correspond with test data, is superimposed on actual test data in Figure A6.23 below. As the pumping schedule for both tests are similar, data from

the 1st test is used. TH. denotes the theoretical pumping schedule and timing diagram (illustrated in dashed lines) and ACT. denotes actual test data (illustrated with various markers).

From the figure below, pumper drum # 1 matches the theoretical pumping schedule quite accurately. Pressures of pumper drum #2 however, with its shorter filling period and longer pumping period (less evident in the figure below than in Figure 6.13 above) to compensate for its smaller pressure differential, do not match the theoretical schedule as accurately.

The actual harvesting period appears shorter than the theoretical period; however the 22,5 seconds between the start of the warming sub-period of one module and the re-cooling sub-period of the next module, as shown in Table 3-3 above, is not accounted for in the actual test data readings. Therefore, the period that the theoretical module is at peak harvesting pressure should be compared to the beginning of the warming sub-period of the actual test module. As it takes some time for the module to pressurize to harvesting pressure, the actual module spends a shorter period at harvesting pressure than shown in the theoretical module. The harvesting pressure of the theoretical module is also 10 kPa above that of the actual module. Nonetheless, from the superimposed pumping schedule / timing diagram it can be concluded that test data corroborates the theoretical timing diagram and pumping schedule developed in Section 3.2 above.

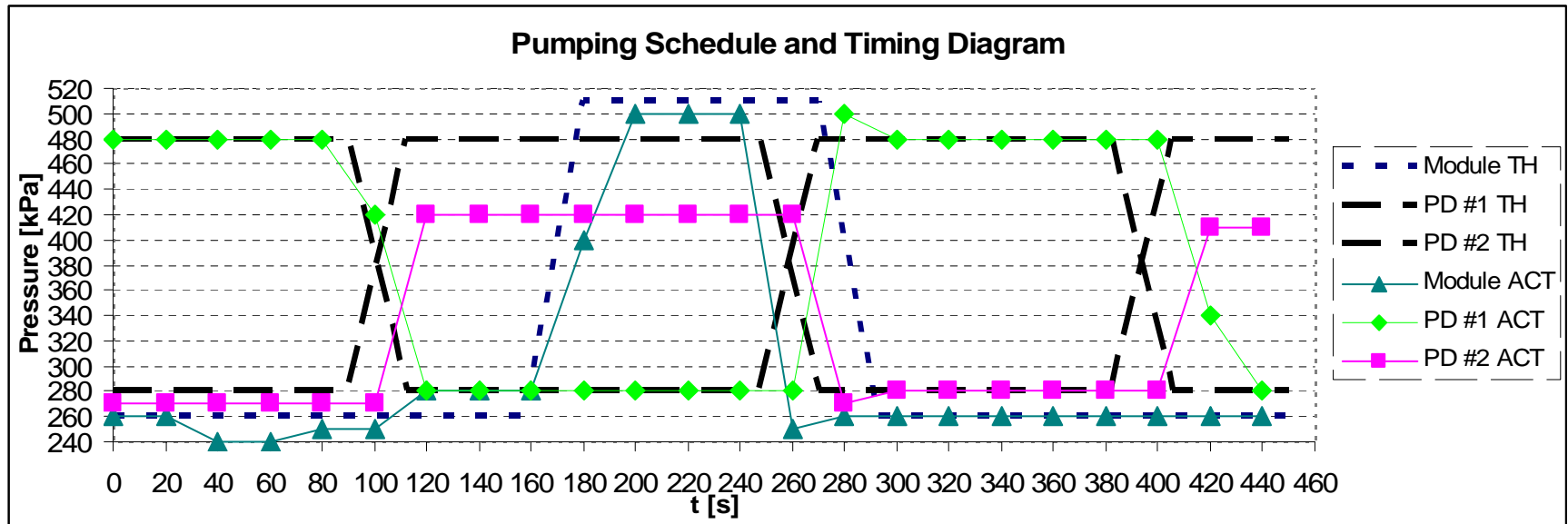


Figure A6.23 Overlay Plot of Theoretically Predicted (denoted TH) and Actually Measured (denoted ACT) Pumper Drum and Evaporator Pressures during a Harvesting Period of One Module

APPENDIX A7

Measured Operating Parameters and List of Facilities and Testing Equipment for the Test Days at the ERPM Ice Making Plant

A7.1 Component List

Component: Liquid Condenser unit

Pressure Readings: P_{n1}
 Temperature Readings: T_1, T_2
 Number of People: 1

Component: Pumper Drum 1

Pressure Readings: P_{n2}
 Temperature Readings: T_4, T_5, T_6, T_{exp}
 Number of People: 2

Component: Pumper Drum 2

Pressure Readings: P_{n3}
 Temperature Readings: T_7, T_8
 Number of People: 1

Component: Accumulator Drum

Pressure Readings: P_{n5}
 Temperature Readings: T_3
 Number of People: 1

Component: Evaporator Plates (Modules)

Pressure Readings: P_{n4}, P_{n5}
 Temperature Readings: $T_9, T_{9a}, T_{h1}, T_{10}, T_{11}, T_{12}, T_{13}$,
 Number of People: 3

Component: Compressor

Pressure Readings: P_{n3}, P_{n4}
 Temperature Readings: T_{14}, T_{15}, T_{16}
 Position of Slide Valve:
 Number of People: 2

Total number of observers: 10.

A7.2 Schedule of Gauges

P_{n1} - Accurate Gauge on condenser liquid receiver (replace existing gauge) 0-2500 kPa

P_{n2} - Accurate Gauge on pumper drum #1 (replace existing gauge) 0-1600 kPa

P_{n3} - Accurate Gauge at inlet to evaporators (replaces current gauge) 0-1600 kPa

P_{n4} - Accurate Gauge at outlet of evaporators (place available for gauge) 0-1600 kPa

P_{n5} - Accurate Gauge on pumper drum #2 (replace existing gauge) 0-1600 kPa

P₁ - Non-accurate Gauge to replace available Gauge at economizer port 0-2500 kPa

P₂ - Non-accurate gauge to replace available Gauge at compressor inlet 0-1250 kPa

P₃ - Non-accurate Gauge to replace available Gauge at pumper drum #2 0-1250 kPa

P₄ - Non-accurate Gauge to replace available Gauge at outlet of compressor. 0-2500 kPa

T₁ - Gauge on condenser liquid receiver

T₂ - Gauge on liquid line from condenser to receiver

T₃ - Gauge on accumulator drum

T₄ - Gauge at inlet piping to pumper drum from throttled gas line before expansion valve

T₅ - Gauge on pumping pumper drum from throttled gas line after expansion valve

T₆ - Gauge on piping from drum to evaporator inlet

T₇ - Gauge on filling pumper drum

T₈ - Gauge on piping from drum to accumulator during venting

T_{exp} - Gauge on piping before the expansion valve.

T_{h1} - Thermometer at water inlet

T₉ - Gauge at cold liquid outlet to accumulator

T_{9a} - Gauge at cold liquid inlet to evaporator

T₁₀ & T₁₁ - Gauge on evaporator plates

T₁₂ - Gauge at hot gas outlet to accumulator

T₁₃ - Gauge at hot gas inlet to evaporator

T₁₄ - Available temperature sensor at inlet to compressor (perhaps replace)

T₁₅ - Available temperature sensor at outlet of compressor (perhaps replace)

T₁₆ - Gauge at inlet to economizer port

Pressure sensors of varying accuracy (Table A7.1 of Appendix A7 lists the accuracies of the various installed pressure sensors) were installed throughout the

plant to measure pressures, as per Figure A1.1. Most of the pressure sensors that were already installed at Unit 5 were removed and fitted with more accurate gauges. All refrigerant temperature sensors were mounted non-invasively on metal surfaces. To ensure good thermal contact, copper compound was placed between the sensor and the metal surface, and the sensor's exterior was insulated from the surroundings with cork-based insulating tape.

Table A7.1 List of testing apparatus and positions for tests performed at the ERPM plant

Apparatus	Position	Method of positioning	Description	Initial Calibration
Temperature sensor	Various positions as outlined in the diagram of Figure A1.1 and labelled T ₁ , T ₂ , etc. Total: 16 sensors.	Sensors were attached to pipe and vessel walls using insulation tape, and where fast response was required for accurate readings, copper grease was also applied to ensure good thermal contact between the probe and the metal surfaces.	REFCO DIG Thermowell. Range of -50 ⁰ to +99 ⁰ C. Purchased from KOVCO (PTY) Ltd.	The sensors were calibrated in ice water to read 0 ⁰ C before they were installed
“Accurate” pressure gauge – 5 kPa Divisions	Various positions as outlined in the diagram of Figure A1.1 and labelled P _{n1} , P _{n2} etc. Total: 5 gauges	Mounted at pressure tappings where existing pressure gauges were currently fitted, except for P _{n5} where only a tapping existed.	Blanes pressure gauges, Range 0-1600 kPa, Accuracy 1%, 5kPa divisions, max. error of 16 kPa.	Calibrated by the importer of the pressure gauge prior to purchase.
“Non-accurate” pressure gauges – 20 kPa divisions	Various positions as outlined in the diagram of Figure A1.1 and labelled P ₁ , P ₂ etc. Total: 4 gauges	Mounted at pressure tappings where existing pressure gauges were currently fitted.	Wika pressure gauge, 3 X 0-1250 kPa and 2 X 0-2500 kPa, 1% accuracy, 20 kPa divisions.	These were not calibrated, but as they were new, they were assumed to meet their maker’s specified accuracy limits.

Testing Schedule at the Compressor: 1 Person

Time (s)	P ₂ : Inlet Pressure		P ₃ : Outlet Pressure		T ₁₅ : Outlet Temp.	
	Run 1	Run 2	Run 1	Run 2	Run 1	Run 2
0:00						
15:00						

Testing Schedule at the Economizer Port: 1 Person

Time (s)	P ₁ : Economizer Press.		T ₁₆ : Economizer Temp.		Slide Valve Position %
	Run 1	Run 2	Run 1	Run 2	
0:00					
15:00					

Testing schedule at Pumper Drum # 1: 1 Person

Time (s)	P _{n2} : Drum Pressure		T ₆ : Drum Temperature	
	Run 1	Run 2	Run 1	Run 2
0:00				
15:00				

Testing schedule at Pumper Drum # 1 Outlet: 1 Person

Time (s)	T ₄ :Temp. b/f exp. vlv		T ₅ : Temp a/f exp. vlv		T ₇ : Evap inlet Temp.	
	Run 1	Run 2	Run 1	Run 2	Run 1	Run 2
0:00						
15:00						

Testing Schedule at Pumper Drum # 2: 1 Person

Time (s)	P _{n3} : Drum Pressure		T ₈ : Venting to Acc. Temp.	
	Run 1	Run 2	Run 1	Run 2
0:00				
15:00				

Testing Schedule at Top of Evaporators: 1 Person

Time (s)	P _{n5} : Evap. Liquid Outlet Press.	
	Run 1	Run 2
0:00		
15:00		

Testing Schedule at Top of Evaporators: 1 Person

Time (s)	T ₉ :Temp at Outlet to Acc.		T ₁₀ : Temp on Evap plates		T ₁₃ : Hot gas inlet Tp.	
	Run 1	Run 2	Run 1	Run 2	Run 1	Run 2
0:00						
15:00						

Testing Schedule at bottom of Evaporators: 1 Person

Time (s)	P _{n4} : Evaporator Inlet Pressure	
	Run 1	Run 2
0:00		
15:00		

Testing Schedule at Top of Evaporators: 1 Person

Time (s)	T ₁₁ : Temp. on plates		T ₁₂ : Hot gas outlet Temp		T ₁₇ : Evap inlet Temp.	
	Run 1	Run 2	Run 1	Run 2	Run 1	Run 2
0:00						
15:00						

Table 3.1 and Table 3.2 above summarise the different periods illustrated in the timing diagram and pumping schedule respectively (both are shown in Figure 3.1). All information is based on data obtained from testing at the plant, as well as from Worthington-Smith & Brouwer⁽¹³⁾ and Rankin.⁽¹⁴⁾ Where timed events are uncertain, they are indicated in italics. Those timed processes that are illustrated in the timing diagram and pumping schedule are repeated in Table 3.3. Tables 3.1 and 3.2 are reproduced below and summarise the processes recorded during testing at the plant.

Table A7.2 Definition of periods during the ice making cycle for Unit 5 of the ERPM plant

Elapsed time (s)	Period length (s)	Name of period	Valve operations	Intended events during operation
10	10	Re-cooling sub-period (Depressurizing of evaporator after harvesting period)	Controlled valve between evaporator and accumulator opens fully.	Evaporator returns to ice-building temperature before ice building commences.
820	810	Ice-building period	Different controlled valves opened and closed.	Cold ammonia liquid circulated through module, entering as liquid and leaving as 4 parts liquid and 1 part gas on average (as predicted in Sections 8. and 9.).
830	10	Liquid transfer period	Harvesting gas controlled valve opens.	Hot gas from condenser pushes liquid to accumulator.
900	70	Warming sub-period	Harvesting gas controlled valve opens.	Hot ammonia gas from condenser warms steel module to melt the inner ice layer.

Table A7.3 Pumping schedule for the two pumper drums of Unit 5

Elapsed time (s)	Period length (s)	Name of period	Valve operations	Intended events during operation
20	20	Pumper drum #1 depressurises during changeover period from pumping to filling	Controlled valve open between pumper drum and accumulator.	Pumper drum vents pressurising harvesting gas to accumulator.
150	130	Re-filling period of pumper drum #1	Controlled valve open between pumper drum and accumulator.	Pumper drum receives full charge from, whilst venting displaced gas to, the accumulator.
170	20	Pumper drum #2 pressurises during changeover period from filling to pumping	Expansion valve open between pumper drum and condensed liquid receiver.	Pumper drum is pressurised by flash gas and starts to pump liquid to evaporators.
300	130	Pumping period of pumper drum #2	Expansion valve open between pumper drum and condensed liquid receiver.	Pumper drum pumps liquid to and through evaporators.

APPENDIX A8

Dimensions and Volumes of the Pumper Drum and Accumulator at the ERPM Plant, and Predicting the URD due to the Interaction of Pressurising Gas and Cold Circulating Refrigerant

As the URD due to the interaction of pressurising gas and refrigerant at the pumper drum is dependent on the change in volume of the pumper drum, these dimensions as well as those of the accumulator are presented here. The analysis to predict the URD due to the abovementioned interaction is then presented.

A8.1 Dimensions of the Pumper Drum and Accumulator at the ERPM Plant

All dimensions are obtained from measurements at the ERPM plant and from Worthington-Smith & Brouwer.⁽¹³⁾ Both drums' outer and internal volumes are obtained by idealising the drum as a cylinder and two hemispheres.

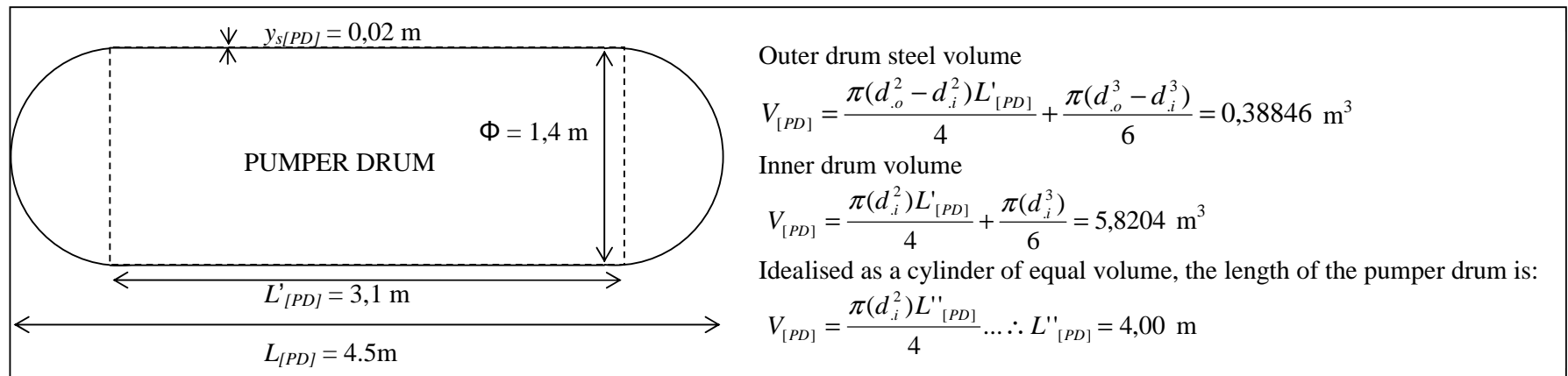


Figure A8.1 Volume of Shell of Pumper Drum showing the actual length, and the idealized length of the tube and hemispheres

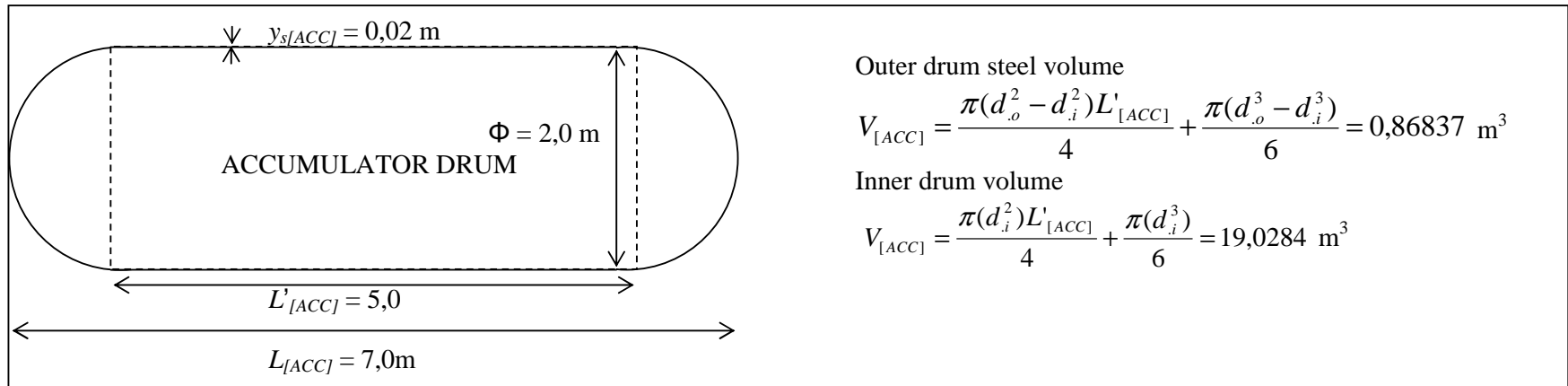


Figure A8.2 Volume of Shell of Accumulator Drum showing the actual length, and the idealized length of the tube and hemispheres

A8.2 Gas Pumping Process: Predicting the URD due to the Interaction of Pressurizing Gas and Cold Liquid Refrigerant Being Pumped

At the start of the pumping process, the level control sensor registers that the liquid level in the pumper drum is at a height of $0.8 \times D_{[PD]}$ and at the end the sensor at the bottom registers that this level is at a height of $0.1 \times D_{[PD]}$ as in Figure 8.9, reproduced below.

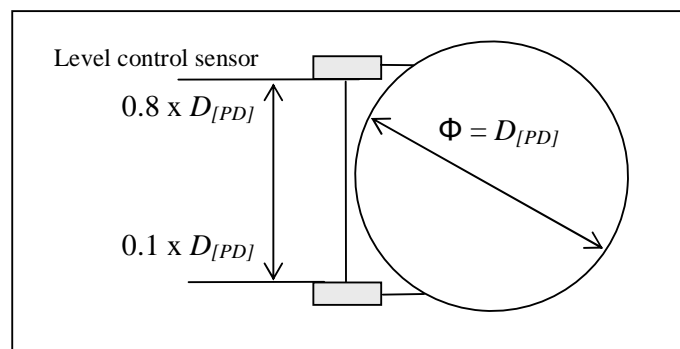


Figure A8.3 Level control sensors of Pumper Drum

The liquid content of the pumper drum at the end of the pumping process is referred to as the Residual Layer or RL. This layer is heated somewhat by the warm pressurizing gas.

If the volume of the pumper drum is idealized as a cylinder, then the change in volume of the liquid therein will be proportional to the change in its cross sectional area occupied by liquid. This idealized length of the cylinder $L''_{[PD]}$, calculated in

Figure A8.1 above, is 4,00 m. All geometric variables of this idealized pumper drum are defined in Figure A8.4 below.

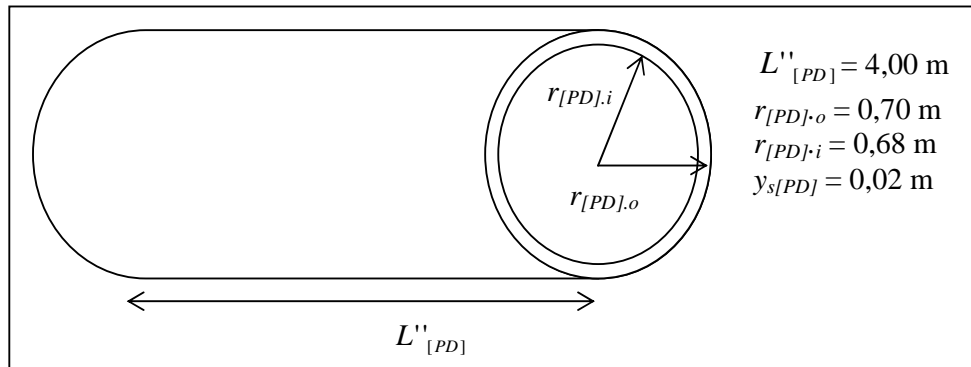


Figure A8.4 Idealised cylindrical pumper drum

Now, the pumping period $t_{[PD+]}$ as defined in Table 3.1 is 130 seconds. In this time, the volumetric flow rate of liquid circulated to and through seven ice building evaporators is¹¹¹:

$$\dot{V}_{r[PD-E]} = \frac{V_{r[PD](t_1)} - V_{r[PD](t_2)}}{t_{[PD+]}}$$

where at (t_2) the final internal volume occupied by liquid in the pumper drum at the end of the pumping period is denoted $V_{r[PD](t_2)}$ and $V_{r[PD](t_1)}$ denotes the initial volume at (t_1) .

A8.2.1 Predicting the Initial Volume of Liquid in the Pumper Drum

Denoting the inner radius of the pumper drum as $r_{[PD].i}$ (0,68 m):

¹¹¹ At any time there are at least seven modules building ice

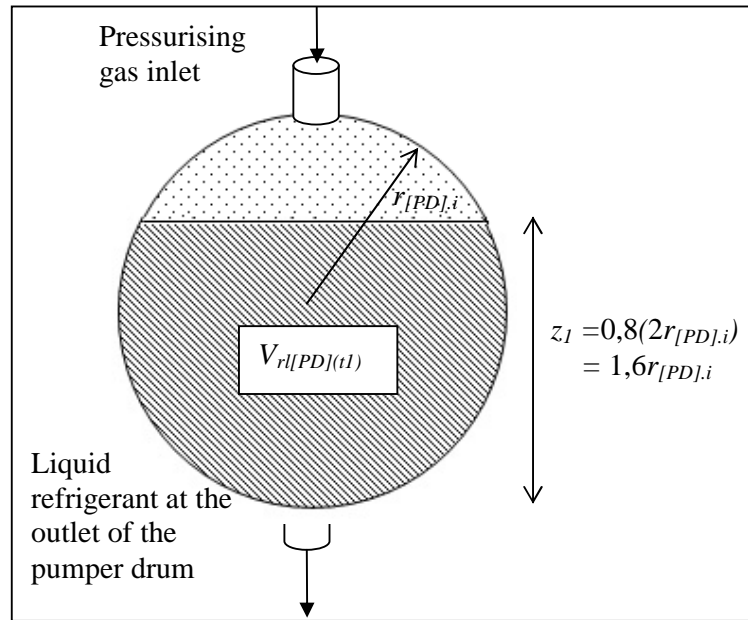


Figure A8.5 Cross-sectional area occupied by the liquid in the pumper drum at the start of pumping

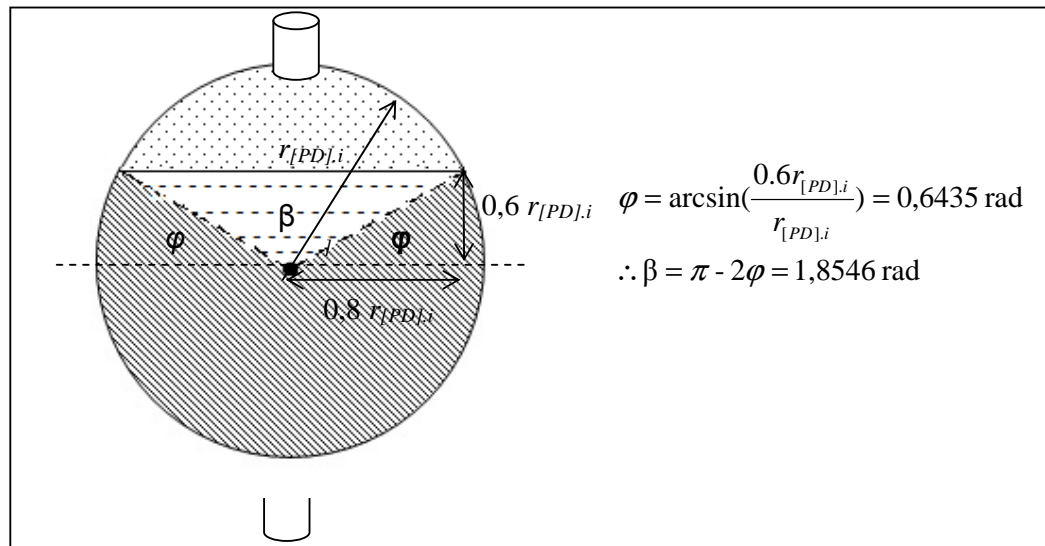


Figure A8.6 Geometrical partitioning of area occupied by the liquid at the start of pumping (denoted by the hatched and dashed areas)

At the beginning of the pumping period, the internal volume of the pumper drum occupied by liquid (hatched and dashed areas of Figure A8.6) is:

$$a_{rl.hatched} = r dr d\theta = \int_0^{r_{[PD],i}} r dr \int_{-\varphi}^{\pi+\varphi} d\theta = \left[\frac{r^2}{2} \right]_0^{r_{[PD],i}} [\theta]_{-\varphi}^{\pi+\varphi} = \frac{r_{[PD],i}^2}{2} (\pi + 2\varphi) = 2.214 r_{[PD],i}^2$$

$$a_{rl.dashed} = \frac{(0.8 r_{[PD],i} \times 2)(0.6 r_{[PD],i})}{2} = 0.48 r_{[PD],i}^2$$

$$V_{rl[PD](t1)} = (a_{rl.hatched} + a_{rl.dashed}) L''_{[PD]} = (2.6943 r_{[PD],i}^2) 4 = 4.9834 \text{ m}^3$$

A8.2.2 Predicting the Final Volume of Liquid in the Pumper Drum

The final volume in the pumper drum at the end of the pumping period is shown in the diagram below.

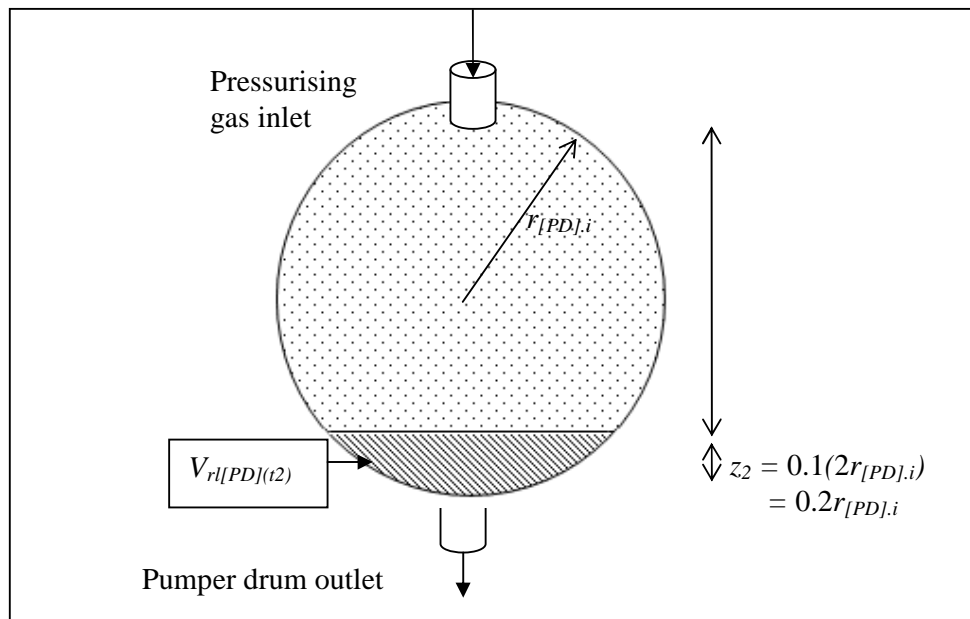


Figure A8.7 Area occupied by the liquid in the pumper drum at the end of pumping

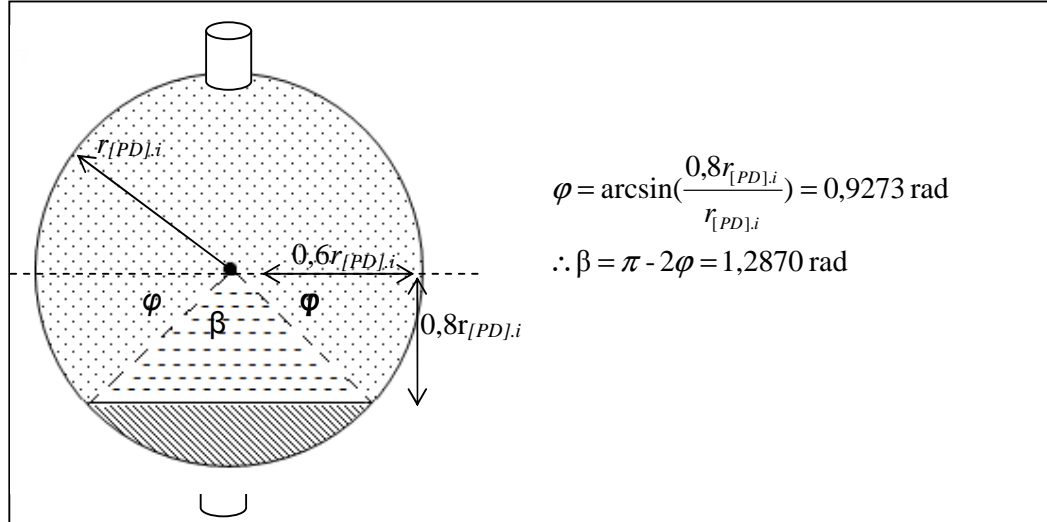


Figure A8.8 Geometrical partitioning of area occupied by the liquid at the end of pumping (denoted by the hatched and dashed areas)

At the end of the pumping period, the internal volume of the pumper drum occupied by liquid (hatched and dashed area of Figure A8.8) is:

$$a_{rv.dotted} = r dr d\theta = \int_0^{r_{[PD].i}} r dr \int_{-\varphi}^{\pi+\varphi} d\theta = \left[\frac{r^2}{2} \right]_0^{r_{[PD].i}} [\theta]_{-\varphi}^{\pi+\varphi} = \frac{r_{[PD].i}^2}{2} (\pi + 2\varphi) = 2,498 r_{[PD].i}^2$$

$$a_{rv.dashed} = \frac{(0,6r_{[PD].i} \times 2)(0,8r_{[PD].i})}{2} = 0,48 r_{[PD].i}^2$$

$$V_{rl[PD](t2)} = (\pi r_{[PD].i}^2 - (a_{rv.dotted} + a_{rv.dashed})) L''_{[PD]} = (0,1635 r_{[PD].i}^2) 4 = 0,3024 \text{ m}^3$$

Therefore the volumetric flow rate of liquid refrigerant to and through the evaporators during the pumping period is:

$$\therefore \dot{V}_{rl[PD-E]} = \frac{4,9834 - 0,3024}{130} = 0,0364 \text{ m}^3/\text{s}$$

The mass flow rate of liquid refrigerant for one module can be predicted from the above equation as:

$$\dot{m}_{r[PD-E]} = \dot{V}_{r[PD-E]} \times \rho_{rl}(T_{r[PD+]}) = 0,0364 \times 645,2 = 23,485 \text{ kg/s}$$

And per module (at least seven modules are building ice at any time)

$$\dot{m}_{r[PD-E]} = 3,354 \text{ kg/s}$$

The mass flow rate required to build an ice layer of 6 mm (5 mm of delivered ice and 1 mm of melted ice) is also predicted from equation (69)¹¹² of Section 8.6.1 above to be 3,363 kg/s (for an average recirculation of 5), and is an independent calculation from that presented above, which is based on the volume of liquid in the pumper drum that is pumped to the evaporators. The mass flow rate predicted in this section is therefore 0,30 % smaller than that predicted by equation (69), if an average recirculation of 5 is input into that equation. However, the required length of the pumper drum based on the mass flow rate predicted in equation (69) is 4 % larger than that of Figure A8.4. This length is obtained from the following formula:

$$L''_{[PD]} = \frac{\Delta m_{r[PD-E]}}{(2,6943 - 0,1635)r_{[PD]i}^2 \rho_{rl}(T_{rl.circ[PD-E]})} \frac{7}{6}$$

where $\Delta m_{r[PD-E]}$ is the mass of liquid flowing through one evaporator module per ice building - as predicted from equation (69) above. The denominator $(2,6943 - 0,1635)r_{[PD]i}^2$ is the change in cross-sectional area of the pumper drum as it empties its contents from 80 % to 10 % of its internal volume. This mass of liquid pumped through the evaporators is then multiplied by 7 ice building modules that the pumper drum feeds at any time, and divided by the six pumping periods in a 15 minute ice building cycle. This equation thus predicts the cylindrical length of the pumper drum required to circulate the mass flow rate predicted in equation (69) through the seven ice building modules. For an average

¹¹² The mass of refrigerant that passes through the evaporator is predicted from equation (69), however, by dividing this mass by the ice building period of 13,5 minutes, the mass flow rate is obtained.

recirculation ratio of 5, the above equation yields a pumper drum length of 4,20 m, which is 4 % larger than the idealized length of the cylindrical drum shown in Figure A8.4 above of 4,00 m.

Therefore, as there is sufficiently accurate agreement between the two methods of predicting the mass flow rate through the evaporator for the cold gas pumped arrangement, the average recirculation ratio is predicted as 5.

A8.2.3 Predicting the Mass and Temperature of the Upper Portion of Pumped Liquid in the Pumping Pumper Drum

During the pumping period at the pumper drum, an upper portion of pumped liquid is warmed due to its interaction with the warmer pressurising gas. As installing temperature sensors inside the pumper drum was prohibited, the change in temperature of this upper portion of pumped liquid was predicted by placing a temperature sensor at the outlet of pumper drum 1 (T7 on Figure A1.1). The temperature peaks of Figure A8.9 below correspond to the temperature rise of the upper portion of liquid refrigerant pumped, which occurs during the last stage of pumping. The temperature reached by this warmed mass of liquid $m_{rl.circ[PD-E]}$ is $T_{rl.circ[PD-E]}$. Both of these variables are predicted in the analysis presented below. The corresponding plot in Appendix A6 is Figure A6.15

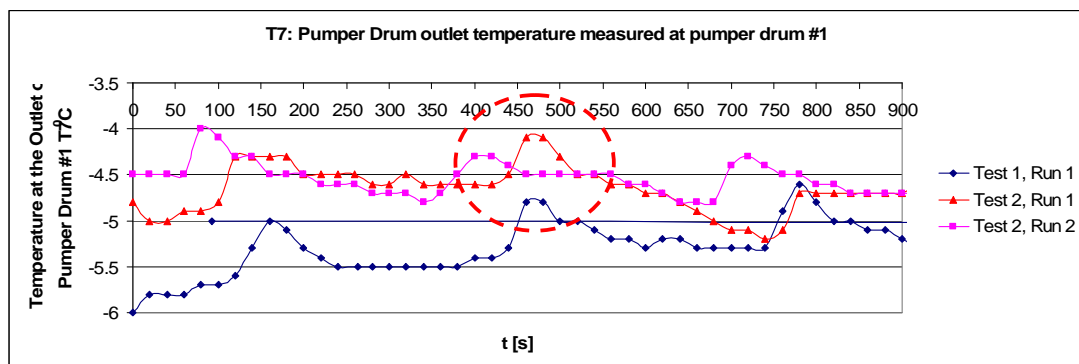


Figure A8.9 Recorded Temperatures at Liquid Outlet of Pumper Drum 1

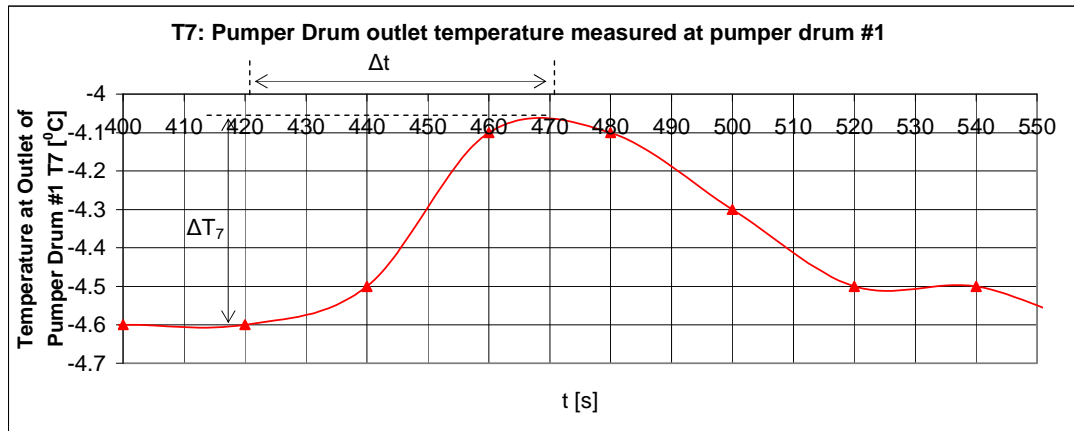


Figure A8.10 Magnification of Figure A8.9 to show one peak temperature of Test 2, Run 1

From Figure A8.9, there are three peaks in a 900 second period (a complete ice-building and harvesting cycle), corresponding with the three pumping periods of pumper drum 1 therein. From Table 3.1, the combined pumping and venting process lasts for 150 seconds, consisting of 130 seconds of pumping and 20 seconds of venting before filling begins. From Figure A8.10, the outlet temperature of the pumper drum reaches its maximum value of $\Delta T_7 = 0,55 \text{ }^\circ\text{C}$ after time $\Delta t = 50$ seconds. Averaging the change in temperature over the three tests performed as well as the peak temperature from Figure A8.10, the upper

pumped layer reaches an average change in temperature of $\frac{\Sigma \Delta T_7}{3 \times 2} = 0,294 \text{ }^\circ\text{C}$.

The volume of liquid pumped over $\Delta t = 50$ seconds to the seven modules building ice at any time is $V_{rl.circ[PD-E]} = 0,0379 \times 50 = 1,895 \text{ m}^3$, based on the volumetric flow rate required to build the required and melted ice layer predicted by equation (69) of Section 8.6.1, as opposed to that predicted in Section A8.2.2 above. As mentioned in Section A8.2.2, this volumetric flow rate is 4 % larger than that predicted in the aforementioned section. The volume predicted above multiplied by the density of the liquid $\rho_{rl.circ[PD-E]}(T_{rl.circ[PD-E]}) = 644,4 \text{ kg/m}^3$, where

$T_{rl.circ[PD-E]} = T_{r[PD-]} + \frac{\Sigma \Delta T_7}{3 \times 2}$, is the mass of the upper pumped layer of liquid

$m_{rl.circ[PD-E]}$ that is warmed by the pressurising gas to $T_{rl.circ[PD-E]}$ over $\Delta t = 50$

seconds. For all seven ice building modules and per pumping period of pumper drum 1, $m_{rl.circ[PD-E]} = 1221,12$ kg, or 174,45 kg per module. Thus, for an ice building period of one module, which lasts 810 seconds, this module will see $\frac{810}{150} = 5,4$ pumping periods. The total mass circulated to one module per ice building period that is warmed to $T_{rl.circ[PD-E]}$ is therefore $174,45 \times 5,4 = 942,02$ kg/module.

Both $m_{rl.circ[PD-E]}$ and $T_{rl.circ[PD-E]}$ are inputs into equation (64) of Section 8.4.2 above, which predicts the URD of re-cooling this warmed upper pumped layer of liquid to filling pumper drum temperature (as the liquid will be re-cooled before it reaches the evaporator inlet, it is assumed that this re-cooling occurs close to the pumper drum).

A8.2.4 Predicting the Temperature of the Upper Pumped Layer for the Hot Gas Pumped Arrangement

This Section outlines the analysis to predict the input variables $m_{rl.circ[PD-E]\{HGPS\}}$ and $T_{rl.circ[PD-E]\{HGPS\}}$ of equation (77) of Section 8.7.3 above, which predicts the URD of re-cooling the upper pumped layer for the HGPS.

In Figure A8.11 below, $y_{r[PD]RL}$ and $y_{r[PD]UPL}$ are the vertical depths that the residual, and upper pumped, liquid layers occupy respectively in the pumping pumper drum during the last stage of the pumping period.

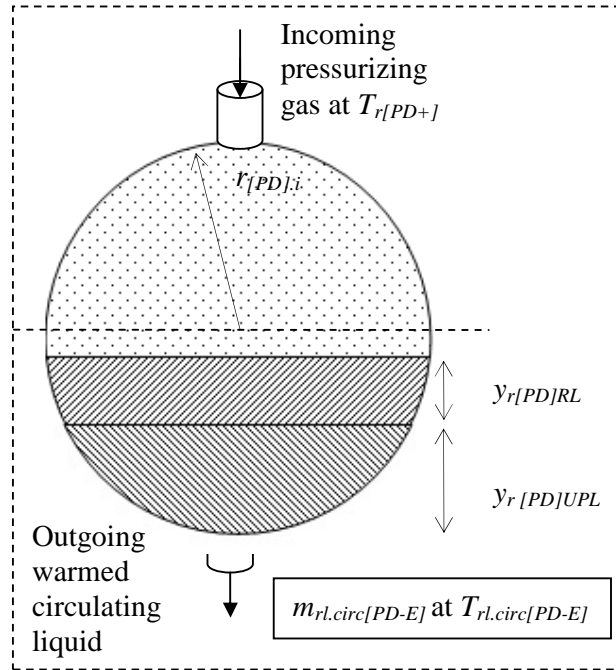


Figure A8.11 Control Volume showing areas occupied by the Residual and Upper Pumped Liquid Layers in the Pumper Drum for the CGPS

By performing a heat transfer analysis for the control volume of Figure A8.11, based on the predicted temperature of the upper portion of pumped liquid, $T_{rl.circ[PD-E]}$, and the mass of this liquid, $m_{rl.circ[PD-E]}$ for the CGPS, these corresponding variables can be predicted for the HGPS. Referring to the control volume of Figure A8.11 above, during the last stage of the pumping period, when the pressurising gas begins to warm the circulated mass of the Upper Pumped Layer, $m_{rl.circ[PD-E]}$, the cross-sectional area of the pumper drum that is occupied by the Residual Layer (RL) above the Upper Pumped Layer (UPL) is defined in Figure A8.8 above as:

$$a_{rl[PD]RL} = (\pi r_{[PD].i}^2 - (a_{rv.dotted} + a_{rv.dashed})) = (0,1635 r_{[PD].i}^2) = 0,0756 \text{ m}^2 \text{ at a vertical depth of } z_2 = 0,2 r_{[PD].i} = 0,136 \text{ m}.$$

The UPL, based on the volume that it occupies initially during the last stage of the pumping period, occupies a cross-sectional area of $a_{rl[PD]UPL} = \frac{V_{rl.circ[PD-E]}}{L''_{[PD]}} = 0,474 \text{ m}^2$. The total area occupied by both layers is therefore $a_{rl[PD]RL} + a_{rl[PD]UPL} = 0,610 \text{ m}^2$.

Now, as pressurising gas at $T_{r[PD+]}$ fills the pumper drum to increase its pressure and to circulate liquid to the evaporator, the liquid refrigerant occupying the UPL for the CGPS is warmed. For the last 50 seconds of the pumping period, this UPL, initially at filling temperature $T_{r[PD-]}$ is warmed by the incoming gas to $T_{r,circ[PD-E]}$. The heat transfer through the control volume defined in Figure A8.8 above is:

$$\dot{q}_{r,circ[PD-E]} = \frac{m_{r,circ[PD-E]} c_{r,circ[PD-E]} (T_{r,circ[PD-E]})(T_{r[PD-]} - T_{r,circ[PD-E]})}{t_{[PD+]}} = \frac{T_{r,circ[PD-E]} - T_{r[PD+]}}{\frac{1}{h'_{r,circ[E-ACC]}} + \frac{y_{r[PD]RL}}{\bar{k}_{r[PD]RL}}}$$

Where $h'_{r,circ[E-ACC]}$ is the condensing heat transfer coefficient of the warm pressurizing gas, $c_{r,circ[PD-E]}$ is the specific heat of ammonia at $T_{r,circ[PD-E]}$ and $\bar{k}_{r[PD]RL}$ is the average conductivity of the Residual Layer at $T = \frac{T_{r[PD+]} + T_{r[PD-]}}{2}$.

Both $m_{r,circ[PD-E]}$ and $T_{r,circ[PD-E]}$ are predicted in Section A8.2.3 above at an average recirculation ratio of 5, and therefore the only unknown variable in the heat transfer equation above is $h'_{r,circ[E-ACC]}$. Substituting the known variables into this equation; $h'_{r,circ[E-ACC]} = 1.433 \text{ W/m}^2 \cdot ^\circ\text{C}$.

Finally, by making the following assumptions for the HGPS, the temperature to which the UPL is warmed by the incoming gas can be predicted:

1. The HGPS circulates liquid to the evaporators at the same volumetric flow rate as the CGPS.
2. The condensing heat transfer coefficient and pumper drum dimensions of the two arrangements are identical.
3. The incoming pressurizing gas is at saturated condensed liquid receiver temperature $T_{sat[REC]}$.

Based on the above assumptions, the heat transfer equation for the HGPS is:

$$\begin{aligned} \dot{q}_{rl.circ[PD-E]\{HGPS\}} &= \frac{m_{rl.circ[PD-E]\{HGPS\}} C_{rl.circ[PD-E]} (T_{rl.circ[PD-E]\{HGPS\}}) (T_{r[PD-]} - T_{rl.circ[PD-E]\{HGPS\}})}{t_{[PD+]}} \\ &= \frac{T_{rl.circ[PD-E]\{HGPS\}} - T_{sat[REC]}}{\frac{1}{h'_{rl.circ[E-ACC]}} + \frac{y_{rl[PD]RL}}{\bar{k}_{rl[PD]RL\{HGPS\}}}} \end{aligned}$$

where $m_{rl.circ[PD-E]\{HGPS\}} =$

$$V_{rl.circ[PD-E]} \rho_{rl.circ[PD-E]} (T_{rl.circ[PD-E]\{HGPS\}}) = (0,0379 \times 50) \times (643,00) = 1218,49 \text{ kg.}$$

With all the other variables determined from the heat transfer equation for the CGPS, $T_{rl.circ[PD-E]\{HGPS\}}$ can be predicted from the above equation for the HGPS.

The final change in temperature of the UPL for the HGPS is $T_{rl.circ[PD-E]\{HGPS\}} - T_{r[PD-]} = 0,80 \text{ }^{\circ}\text{C}$. This change in temperature, as well as the mass of the upper pumped layer that is warmed during the pumping period $m_{rl.circ[PD-E]\{HGPS\}}$, is input into equation (77) of Section 8.7.3 above to predict the URD of re-cooling the upper pumped layer for the HGPS.

APPENDIX A9

Sizing the Mechanical Pump for the Mechanically Pumped System

Table A9.1 Dimensions of piping measured at the ERPM plant

Pipe Position	Pipe Length [m]	Pipe Diameter [m]
Accumulator to Pumper Drum	1.0 m	0.25 m
Pumper Drum to Evaporator Inlet	2.5 m	0.25 m
Floor to Evaporator Inlet	4.5 m	
Accumulator to Floor	3.0 m	

Based on measurements at the ERPM plant as shown in Figure A9. 1 below, an initial static head of 3 metres exists between the outlet at the accumulator and the floor of the plant, where the pump would presumably stand. It is also assumed that the pump would be positioned 4,5 metres below the evaporator inlet (based on the present configuration of the ERPM plant where the bottom level is about 4.5 metres below the evaporator modules).

Applying an energy conservation equation between the outlet of the accumulator and the inlet to the evaporator:

$$\frac{P_{r[ACC]o}}{\rho_{rl}(P_{r[ACC]})g} + \frac{\dot{v}_{r[ACC-P]o}^2}{2g} + z_{[ACC-P]} + H'_{[P]} = \frac{P_{r[E]i}}{\rho_{rl}(P_{r[E]})g} + \frac{\dot{v}_{r[P-E]i}^2}{2g} + z_{[P-E]} + \left(f_{[PI]} \frac{l_{[PI]}}{d_{[PI]o}} + \Sigma K_{[PI]} + f_{[PI]h} \frac{l_{[PI]h}}{d_{[PI]h}} + \Sigma K_{[PI]h} \right) \frac{\dot{v}_{r[P-E]i}^2}{2g}$$

Where $l_{[PI]}$ is the total length of piping, $f_{[PI]}$ is the constant friction factor and $\Sigma K_{[PI]}$ is the sum of the minor loss coefficients, predicted from Sinnott⁽⁸⁾. The subscript h denotes properties of the smaller horizontal pipes and is described below.

$\dot{V}_{r[P-E]} = \dot{m}_{r[P-E]} v_{r(P_{r[PD+]})} \times 7$ where $\dot{m}_{r[ACC-P]} = \dot{m}_{r[P-E]} = \dot{m}_{r[PD-E]}$ for the CGPS.

$$\dot{V}_{r[P-E]} = 3,363(0,001592)7 = 0,0375 \text{ m}^3/\text{s}.$$

$$\dot{v}_{r[P-E]} = \frac{\dot{V}_{r[P-E]}}{\left(\pi \frac{d_{[PI]o}^2}{4}\right)} = \frac{0,0375}{\left(\pi \frac{0,25^2}{4}\right)} = 0,764 \text{ m/s}$$

where $d_{[PI]o}$ is the outlet pipe

diameter based on that of Table A9.1 above.

The Reynolds number at this velocity is:

$$Re_{[PI]} = \dot{v}_{r[P-E]} d_{[PI]o} \frac{\rho_{r(P_{r[PD+]})}}{\mu_{r(P_{r[PD+]})}} = 0,764(0,25) \frac{648,6}{0,0001815} = 682549$$

From the Moody Diagram of Figure A9.3 below, and assuming a relative roughness for refrigeration-grade stainless steel piping from Barber⁽¹⁵⁾ of $e/d = 0,003$, $f_{[PI]} = 0,0285$.

Assuming minor loss coefficients for the exit, a valve and two elbows, from Sinnott⁽⁸⁾:

$$\Sigma K_{[PI]} = (K_{Valve} + 2K_{Elbow} + K_{Exit}) = (5 + 2(1.5) + 1) = 9$$

Once the liquid reaches the inlet to the evaporators, it would enter a splitter manifold and split into 7 pipes of equal diameter (a control valve on the 8th pipe of the harvesting module, as shown in Figure A9.2 below, would ensure that no liquid enters that module) that would carry the liquid through to the ice building modules. As it is difficult to predict the exact length of all these inlet pipes, it is conservatively assumed, based on the configuration of the plant, that each pipe would travel a horizontal distance of 7 metres. If it is assumed that the liquid from the large pump inlet pipe would split into seven horizontal pipes of equal diameter at the manifold, that each horizontal pipe diameter is 1/7th the area of the larger pipe, and that the velocity of the liquid remains constant (i.e. the volumetric flow rate is split evenly between the 7 horizontal pipes), the Reynolds number and frictional head loss coefficient for each horizontal pipe is:

$$Re_{[PI]h} = \dot{v}_{r[P-E]} d_{[PI]h} \frac{\rho_r(P_{r[PD+]})}{\mu_r(P_{r[PD+]})} = 0,764(0,095) \frac{648,6}{0,0001815} = 259369$$

Where, as mentioned above, the subscript h denotes properties of the smaller horizontal pipes. From the Moody Diagram of Figure A9.3 below, and assuming a relative roughness for refrigeration-grade stainless steel piping from Barber⁽¹⁵⁾ of $e/d = 0,003$, $f_{[PI]h} = 0,0285$.

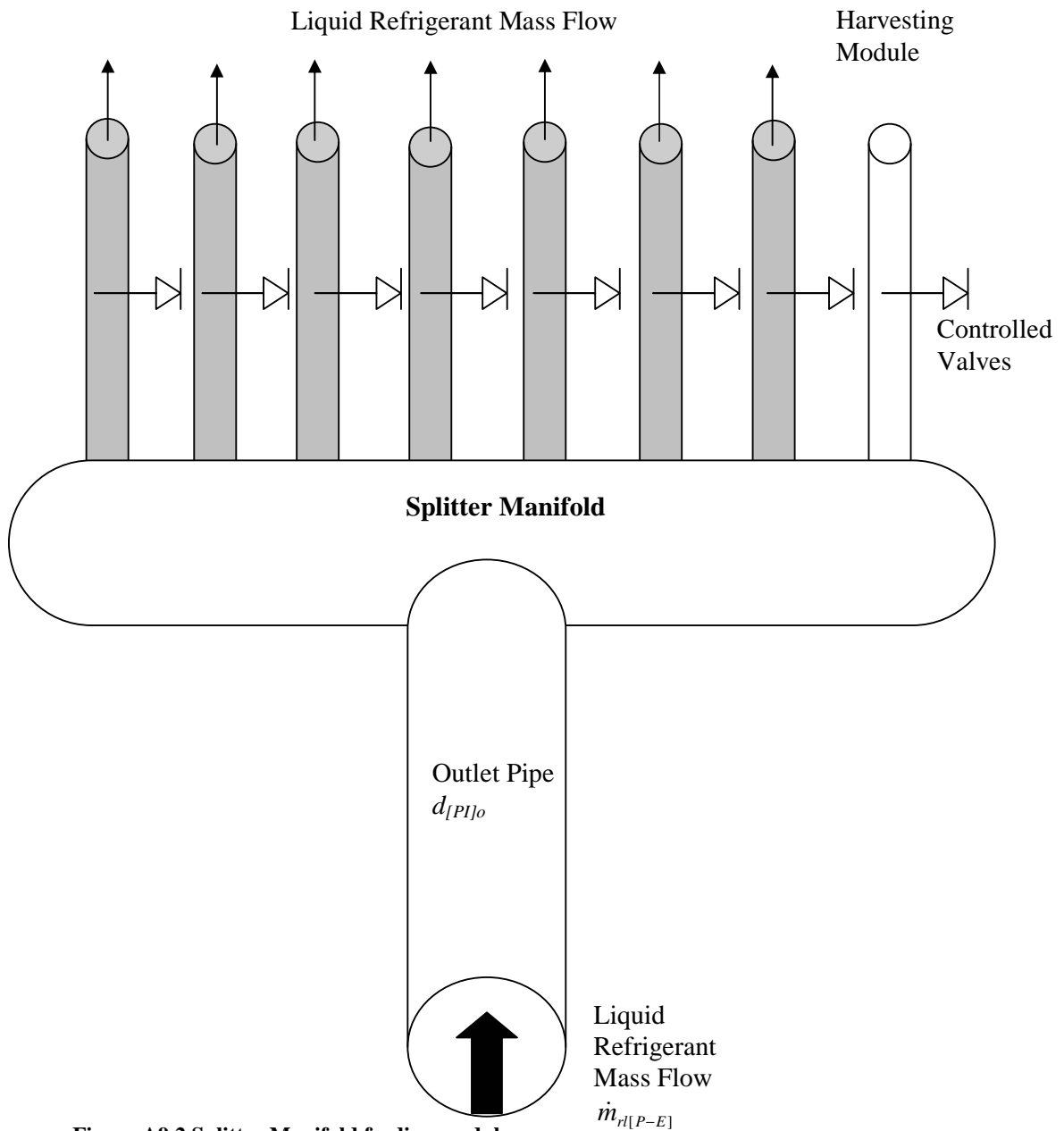


Figure A9.2 Splitter Manifold feeding modules

Now, assuming that there exist two elbows, an exit, and that the splitter manifold acts as a tee threaded branch flow⁽⁴⁴⁾, the minor loss coefficients for the horizontal pipes are:

$$\Sigma K_{[PI]h} = (2K_{Elbow} + K_{Exit} + K_{Manifold}) = (2(1,5) + 1 + 2) = 6$$

Finally, it is assumed that changes in velocity from the accumulator outlet to the evaporator inlet can be neglected. From the energy conservation equation above:

$$\frac{303,5 \times 10^3}{650,7(9,81)} + 3 + H'_{[P]} = \frac{343,5 \times 10^3}{646,6(9,81)} + 4,5 + \left(0,0285 \frac{4,5}{0,25} + 9 + 7 \left(0,0285 \frac{7}{0,095} + 6 \right) \right) \frac{0,764^2}{2(9,81)}$$

$$H'_{[P]} = 10,08 \text{ m}$$

The shaft power needed to drive the pump, assuming a mechanical pump efficiency of 85 % is:

$$\dot{W}_{[P]\{MPS\}mech} = \frac{\rho_r (P_{r[PD+]}) g \dot{V}_{r[P-E]} H'_{[P]}}{1000 \eta_{[P]}} = \frac{628,30 \cdot 9,81 \cdot 0,0375 \cdot 10,08}{1000 \cdot 0,85} = 2,737 \text{ kW}$$

And per module this input power is 0,391 kW.

The work input from the pump increases the enthalpy of the liquid refrigerant as it increases its pressure. The URD of re-cooling the warmed liquid refrigerant per module at the evaporator, over a complete ice building period, is obtained by inputting the mechanical input power predicted in this section into equation (81) of Section 8.8.1 above.

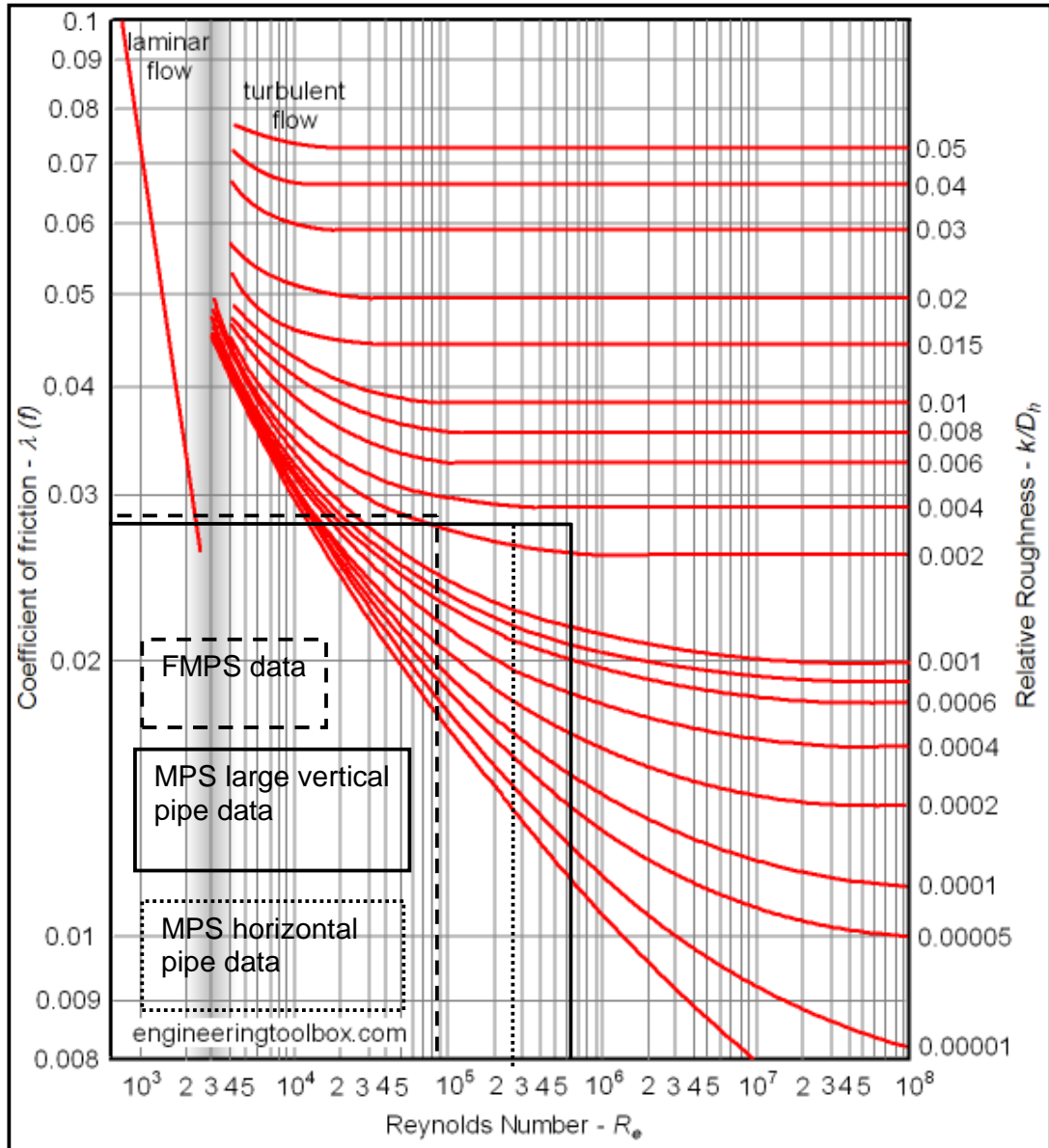


Figure A9.3 Moody Diagram⁽³⁹⁾

APPENDIX A10

Analyses to Support Predictions of the Models of Sections 8 and 9

A10.1 Sensitivity Analysis to Support the Predicted Temperature of Liquid that is Expelled and Warmed by Harvesting Gas at the Beginning of the Warming Sub-Period from Section 8.2.1

As mentioned in Section 8.2.1, at the beginning of the warming sub-period, it is assumed that all the liquid remaining in the module at the end of ice building is expelled to the accumulator within half the harvesting time of 90 seconds. This is a conservative assumption, as from Figure 8.5 above, the longer the warm gas is in contact with the liquid, the warmer that liquid becomes and the larger the URD of re-cooling that liquid at the accumulator. In foot note (18) of Section 8.2.1 above, it is stated that in reality, it would not take the full 45 seconds to expel this liquid, however the total URD for the gas pumped systems are relatively insensitive to this change in temperature, and so a conservative approach is deemed appropriate in this instance. To support this assumption, a sensitivity analysis is performed to predict what effect the expelling time would have on the overall URD of both gas pumped arrangements modeled in Section 8.

The table below presents the values of percentage URD of total refrigeration demand per module over one complete ice-making cycle of 15 minutes, for all four pumping arrangements. The two extreme estimated times required to expel the liquid are input into the model of Section 8. to obtain the percentage URD for each pumping arrangement. From the sensitivity analysis, the difference in percentage total URD per module ranges from 0 – 0.17 %. Thus the conservative assumption that the time required to expel the liquid is 45 seconds does not significantly affect the percentage URD per module.

Table A10 1 Sensitivity analysis: effect on total percentage URD of the assumed time required to expel the remaining refrigerant in the module at the beginning of the warming sub-period

Extremes of estimated time required to expel the remaining refrigerant in the module at the beginning of the warming sub-period, based on a harvesting time of 90 seconds ⁽¹³⁾	Temperature rise due to contact with harvesting gas: ($T_{r[E-ACC]} - T_{r[E]build}$) From Figure 8.4	Perc. Total URD of Total Demand for the CGPS	Perc. Total URD of Total Demand for the HGPS	Perc. Total URD of Total Demand for the MPS	Perc. Total URD of Total Demand for the FMPS
1 second	$\approx 0^{\circ}\text{C}$	20.57 %	22.23 %	20.60 %	20.18 %
45 seconds	2.25°C	20.74 %	22.39 %	20.77 %	20.18 %
Difference in Percentage Total URD of Total Demand		0.17 %	0.16 %	0.17 %	0 %

A10.2 Sensitivity Analysis to Support the Assumed Percentage of Liquid Trapped behind the Level Regulating Valve at the Beginning of the Re-Cooling Sub-Period of Section 8.2.2

The table below shows the sensitivity analysis of the assumption made in Section 8.2.2 where it is assumed that the trapped liquid occupies approximately 5 percent of the internal volume of the module at the beginning of the re-cooling sub-period. Varying this volume of trapped liquid and subsequently trapped vapour, the URDs (from equations (44) and (45) respectively of Section 8.2.2.1) resulting from this trapped liquid and vapour venting to the accumulator are:

$$\Delta H_{rl.trap[E]} = -m_{rl.trap[E](t2)} (h_{rl}(T_{har}) - h_{rl}(T_{r[E]build})) \quad \text{and}$$

$$\Delta H_{rv.trap[E]} = -m_{rv.trap[E](t2)} (h_{rv}(T_{r.har}) - h_{rv}(T_{r[ACC]}))$$

Table A10 2 Sensitivity analysis predicting the change in URD per module as a percentage of total refrigeration demand if the volume of liquid trapped behind the level regulating valve at the beginning of the re-cooling sub-period is varied from 0 – 5 %. Average recirculation ratio is five.

Percentage volume of liquid trapped behind the level regulating valve	$\Delta H_{rl.trap[E]}$ [kJ/kg]	$\Delta H_{rv.trap[E]}$ [kJ/kg]	Percentage total URD of total refrigeration demand CGPS
0 %	0	74,54	20,56 %
5 %	1765,00	67,27	20,74 %

Thus, as the URD as a percentage of total refrigeration demand for the CGPS does not change appreciably (0,18 %), the assumption that the liquid trapped behind the level regulating valve at the beginning of the re-cooling sub-period occupies 5 percent of the total internal volume of the module does not significantly affect predicted total URD. .

A10.3 Mass Rate Balance to Predict the Mass Flow Rate of Refrigerant Built-Up in the Evaporator during Ice Building

The mass flow rate for the control volume of Figure 8.1 of Section 8.1 is

$$\frac{dm_{cv}}{dt} = \dot{m}_{r[PD-E]} - \dot{m}_{r[l,v][E-ACC]}$$

where $\frac{dm_{cv}}{dt}$ is the time rate of change of mass contained within the control volume at time t . From Section 8.2.1 above and based on the analysis presented in Appendix A2, it is conservatively assumed that each plate of the module is filled by 30% of its inner volume with liquid ammonia¹¹⁴ at the end of ice-building and at the beginning of the warming sub-period. If it is further assumed that the mass of liquid occupying the module at the beginning of the ice building period is

¹¹⁴ With the remaining volume occupied by refrigerant vapour at ice building temperature.

negligible, and that the rate of change of mass of the vapour component is also negligible, then the above equation simplifies to:

$$\frac{30na_{[E]chl}L_{[E]}0,3\rho_{rl}(T_{r[E]build})}{13,5 \times 60} = \dot{m}_{r[PD-E]} - \dot{m}_{r[l,v][E-ACC]}$$

$$0,198 = \dot{m}_{r[PD-E]} - \dot{m}_{r[l,v][E-ACC]}$$

From Section A8.2.2 above, based on the dimensions of the pumper drum and the pumping period, the mass flow rate of refrigerant pumped to and through the evaporators is predicted to be

$$\dot{m}_{r[PD-E]} = 3,354 \text{ kg/s}$$

The rate of change of mass contained within the control volume is therefore 5,90% of the predicted mass flow rate at the inlet of the evaporator. As mentioned above, the assumption that the liquid refrigerant occupies 30% is conservative. Therefore, the difference between the mass flow rate at the inlet and the outlet of the evaporator is assumed to be negligible, and $\dot{m}_{r[PD-E]} \approx \dot{m}_{r[l,v][E-ACC]}$.

APPENDIX A11

Sample Calculation to Support the Model of Section 8.

This section outlines a sample calculation for the analysis presented in Section 8. Where relevant, equations are numbered the same as they appear in the main body of the report in straight brackets. The following analysis applies for a recirculation ratio of 5. All property data and calculation results are obtained from EES.⁽⁴⁰⁾

Table A11.1 Variables used in the sample calculation of Section 8.

Variable	Value	Units
$a_{[E]}$	4,445	m ²
$a_{[E]chl}$	0,000224	m ²
c_w	4,186	°C
c_I	2,098	kJ/kg.C
$\bar{c}_{w[PRC]}$	4,183	kJ/kg
$c_s(T_{r[ACC]})$	0,4502	kJ/kg.C
$c_s(T_{r[PD-]})$	0,4533	kJ/kg.C
$c_I(\bar{T}_{r[E]build})$	2,098	kJ/kg.C
h_{sf}	335	kJ/kg
$h_{rl}(T_{r.har})$	241,50	kJ/kg
$h_{rl}(T_{r[E]build})$	173,00	kJ/kg
$h_{rv}(T_{r.har})$	1471,00	kJ/kg
$h_{rv}(T_{r[ACC]})$	1451,00	kJ/kg
$h_{rl}(P_{r[ACC]})$	158,80	kJ/kg
$h_{rl}(P_{r[E]har}, T_{rl[E-ACC]})$	183,30	kJ/kg
$h_{rv}(P_{r[REC]})$	1485,00	kJ/kg
$h_{rv}(P_{r[ACC]})$	1451,00	kJ/kg

Variable	Value	Units
$h_{rl}(P_{r[PD-]}, T_{rl.circ[PD-E]\{HGPS\}})$	181,40	kJ/kg
$h_{rl}(P_{r[PD-]})$	177,80	kJ/kg
$h_{rl}(T_{r[E]})$	173,00	kJ/kg
$h_{rv}(P_{r[PD+]})$	1469,00	kJ/kg
$h_{rv}(P_{r[PD+]})$	1456,00	kJ/kg
$L_{[E]}$	3,5	m
$m_{rl.trap[E]\{t2\}}$	25,78	kg
$m_{s[E]}$	3692,00	kg
$m_{s[PD]}$	2867,00	kg
$m_{s[ACC]}$	6870,00	kg
n	35	
P_{atm}	83,5	kPa
ρ_l	920	kg/m ³
$\rho_{rv}(P_{r[PD-]})$	2,92	kg/m ³
$\rho_{rv}(P_{r[PD+]})$	4,492	kg/m ³
$\rho_{rl}(T_{r[E]build})$	646,60	kg/m ³
$\rho_{rl}(T_{r[E]build})$	2,809	kg/m ³
$\rho_{rv}(P_{r[REC]})$	8,81	kg/m ³
$\rho_{rl}(P_{r[ACC]})$	650,70	kg/m ³
$T_{w[E]i}$	12	kJ/kg
$T_{r[E]build}$	-5,833	⁰ C
$T_{i.o}$	0	⁰ C
$T_{w[PRC]i}$	22,2	⁰ C
$T_{w[PRC]o}$	12	⁰ C

Variable	Value	Units
$T_{\text{sat}}(P_{r[E]build})$	8,959	$^{\circ}\text{C}$
$T_{r[PD+]\{HG\text{PS}\}}$	29,01	$^{\circ}\text{C}$
$T_{r[PD+]}$	7,45	$^{\circ}\text{C}$
$u_{rl}(T_{r[E]build})$	172,50	kJ/kg
$u_{rl}(T_{r[E]build})$	1333,00	kJ/kg
$V_{[E]}$	0,8232	m^3
$v_{rv}(P_{r.har})$	0,2119	m^3/kg
$y_{l.req}$	0,005	m
$y_{l.m}$	0,001	m

A11.1 Productive and Unproductive Refrigeration Demands

Directly Related to Ice Building

Per module, the mass of ice built, $m_{I,b}$, consists of the thickness of ice required, $m_{I.req}$, as well as the thickness of the innermost layer of ice that has to be melted to release the ice from the surface of each plate.

$$m_{I,b} = \rho_I n a_{[E]} (2y_{l.req} + 2y_{l.m}) = 920 \cdot (35) \cdot 4,445 (2(0,005) + 2(0,001)) = 1712,00 \text{ kg} \quad \{1\} (8)$$

Where n is the number of plates per module, $a_{[E]}$ the surface area of one side of the evaporator plate, and $y_{l.req}$ and $y_{l.m}$ are the thicknesses of the particulate ice layer delivered to the screw conveyor below the evaporators and of the subsequently melted innermost layer respectively. The factor of two is to account for the fact that ice is built on both sides of the plate.

The ice thickness built on one side of each plate, based on tests performed at the plant as well as Worthington-Smith & Brouwer,⁽¹³⁾ van der Walt & de Kock⁽¹⁸⁾¹¹⁵ and Rankin⁽¹⁴⁾, is approximately 5-6 mm (refer to Appendix A6 for these results). Taking the upper value of ice *delivered* of 5 mm (with 1 mm of ice subsequently melted) to the screw conveyor below the evaporator module is therefore:

$$m_{I.req} = \rho_i n a_{[E]} (2y_{I.req}) = 1427,00 \text{ kg} \quad \{2\} (9)$$

A11.1.1 URDs and PRDs at the Evaporator during the Ice Building Period

The PRD associated with the evaporator during the ice building period comprises chilling the inlet feed-water from 12° to 0 °C and freezing the required ice layer. From Figure 3.4 above, the mass of water initially at around 22,2 °C⁽¹³⁾ that enters Unit 5 equals, during a complete ice-making batch-cycle, the mass of ice delivered by the evaporator. Therefore, per module, the PRD of chilling this water further to 0 °C is:

$$Q_{PRD[E]} = m_{I.req} (-c_w T_{w[E]i} - h_{sf}) = 1427(-4,186(12) - 335) = -549557,00 \text{ kJ} \quad \{3\} (18)$$

The URDs associated with the evaporator during the ice building period are the freezing of the melted ice layer, as well as the sub-cooling of the entire ice layer.

$$\begin{aligned} Q_{URD[E]} &= m_{I.b} (-c_w T_{w[E]i} - h_{sf} + c_I \frac{(T_{r[E]build} + T_{I.o})}{2}) - Q_{PRD[E]} \\ &= 1712(-4,186(12) - 335 + 2,098 \frac{((-5.833) + 0)}{2}) - 549557 = -120435,60 \text{ kJ} \end{aligned} \quad \{4\}(19)$$

¹¹⁵ Who, as mentioned above, merely *state typical figures* and therefore offer no experimental validation for the thickness of ice built.

Per module, the PRD associated with the chilling of make-up water at the pre-chiller is:

$$Q_{PRD[PRC]} = -m_{I.req} \bar{c}_{w[PRC]} (T_{w[PRC]i} - T_{w[PRC]o}) = 1427(4,183)(22,2 - 12) = -60869,00 \text{ kJ} \quad \{5\}(20)$$

where $\bar{c}_{w[PRC]}$ is an averaged specific heat based on the inlet and outlet water temperatures, and the outlet water temperature $T_{w[PRC]o}$ is the same as the inlet temperature at the evaporator $T_{w[E]i}$.

A11.1.2 The Warming Sub-Period

Predicting the Mass of Liquid Condensed during the Warming Sub-Period

Harvesting gas condenses to liquid throughout the warming sub-period and is expelled to the accumulator. The re-cooling of this condensed liquid $m_{rl\{c\}}$, which is assumed to be at harvesting temperature for the purpose of this investigation, constitutes a URD at the accumulator where it is re-cooled. The value of $m_{rl\{c\}}$ is predicted as follows:

1. Incoming harvesting gas condenses to warm up the steel plates and the manifolds as per equation (25)

$$\begin{aligned} \Delta H_{r.har.1} &= m_{s[E]} c_s (T_{r[E]build} - T_{sat}(P_{r[E]har}) - T_{sat}(P_{r[E]build})) = 3692 \cdot 0,4525 [8,959 - (-5,833)] \\ &= 24713,00 \text{ kJ} \end{aligned} \quad \{6\}(29)$$

2. Incoming harvesting gas condenses to reverse the sub-cooling effect in the built up ice layer. As mentioned in Section 8.1 the relatively small thickness of the ice sheet justifies the use of an arithmetic mean to represent the sub-cooled ice temperature.⁽¹²⁾

$$\Delta H_{r.har.2} = -m_{I,b} c_I \left(\frac{T_{r[E]build} + T_{I.o}}{2} \right) = 1712(2,098 \frac{((-5.833) + 0)}{2}) = 10473,00 \text{ kJ}$$

{7} (30)

3. Incoming harvesting gas condenses to melt the innermost ice layer.

$$\Delta H_{r.har.3} = 2n\rho_I a_{[E]} y_{I,m} h_{sf} = 2 \cdot 35 \cdot 920 \cdot 4,445 \cdot 0,001 \cdot 335 = 95896,00 \text{ kJ}$$

{8} (31)

URDs 2. and 3. above are heat transfers across the control volume and comprise Q_{cv} in equation (21) above.

As all the condensed liquid must be re-cooled to the temperature in the accumulator, the mass of condensed liquid can be predicted as follows:

$$m_{rl\{c\}} [h_{rv}(P_{r[E]har}) - h_{rl}(P_{r[E]har})] = \Sigma \Delta H_{r.har} = \Delta H_{r.har.1} + \Delta H_{r.har.2} + \Delta H_{r.har.3}$$

$$\therefore m_{rl\{c\}} = \frac{131082}{(1471,00 - 241,50)} = 106,60 \text{ kg} \quad \{9\}(32)$$

Predicting the Mass and Temperature of Liquid Expelled and Warmed by Harvesting Gas at the Beginning of the Warming Sub-Period

Predicting the Mass

$\Delta m_{rl.cont[E-ACC]}$ in equation (21) is predicted by estimating the ratio of gas and liquid in the evaporator at the end of the ice building period, and is based on the following assumptions:⁽¹²⁾

1. "The nature of the boiling of two-phase flow is extremely complex"⁽¹²⁾ and can be simplified by assuming that the "temperature of the boiling ammonia is constant along the plate length."⁽¹²⁾
2. The heat flux is uniform along the entire length of the plate.
3. The ratio of vapour to liquid velocity is constant along the entire length of the plate.

Thus the total internal volume of each plate consists of the volume of gas and the volume of liquid, all at evaporating pressure, and based on the area of the individual channels along the length of the plate. From observations at the plant, there are 30 such channels per plate. Therefore, the internal volume of the plates is:

$$30a_{[E]chl}L_{[E]} = V_{rl[E]} + V_{rv[E]} = 30 \cdot 0,000224 \cdot 3,5 = 0,02352 \quad \{10\} \quad (33)$$

Where $a_{[E]chl}$ is the internal cross sectional area of the refrigerant channels of one evaporator plate, $L_{[E]}$ is the vertical length of the plate and $V_{rl[E]}$ and $V_{rv[E]}$ are the volumes of the refrigerant liquid and vapour occupying this internal volume at the beginning of the warming sub-period. In modelling, a conservative approach is taken when analysing this transferred mass, and it is predicted, based on the analysis presented in Appendix A2, that each plate is filled by 30% of its inner volume with liquid ammonia at the beginning of the warming sub-period. Therefore the mass of liquid transferred out of the module¹¹⁶ at the beginning of the warming sub-period, assuming all densities are at evaporating pressure, is

$$\begin{aligned} \Delta m_{rl,cont[E-ACC]} &= 30na_{[E]chl}L_{[E]}(0,3\rho_{rl}(P_{r[E]build}) + 0,7\rho_{rv}(P_{r[E]build})) \\ &= 30 \cdot 35 \cdot 0,000224 \cdot 3,5(0,3 \cdot 646,60 + 0,7 \cdot 2,809) = 161,30 \text{ kg} \end{aligned} \quad \{11\} \quad (34)$$

A11.1.3 The Re-Cooling Sub-Period

Predicting the URD of Re-cooling the Mass of Liquid Trapped behind the Level Regulating Valve at the Beginning of the Re-Cooling Sub-Period

The level-regulating valve at the bottom of the evaporator allows condensed liquid refrigerant during the warming sub-period to return to the accumulator. However, at the end of the warming sub-period some warm ammonia (refrigerant) liquid

¹¹⁶ $n = 35$ plates per module; each plate has 30 channels.

will be trapped behind the level-regulating valve and must be re-cooled to ice building temperature $T_{r[E]build}$.

After discussion with Rankin⁽¹⁴⁾, who confirmed that most if not all the liquid is vented to the accumulator prior to harvesting, it is assumed that the trapped liquid occupies approximately 5 percent of the internal volume of the module.¹¹⁷ This assumption is based on the investigation of Bailey-McEwan⁽¹²⁾ (his page 63).

$$m_{rl.trap[E](t2)} = \rho_{rl}(T_{r.har}) 30na_{[E]chl} L_{[E]} \cdot 0,05 = 626,3 \cdot 30 \cdot 35 \cdot 0,000224 \cdot 3,5 \cdot 0,05 = 25,78 \text{ kg} \quad \{12\}$$

This trapped liquid is denoted as $m_{rl.trap[E](t2)}$ in equation (26) above, and the demand of re-cooling this liquid at the evaporator is:

$$\Delta H_{rl.trap[E]} = -m_{rl.trap[E](t2)} (h_{rl}(T_{r.har}) - h_{rl}(T_{r[E]build})) = 25,78(241,50 - 173,00) = -1765,00 \text{ kJ} \quad \{13\} \quad (40)$$

Predicting the URD of Re-cooling the Mass of Vapour Vented to the Accumulator at the Beginning of the Re-Cooling Sub-Period

At the beginning of the re-cooling sub-period, the warm harvesting vapour that is trapped in the evaporator is vented, through the liquid-vapour path, to the accumulator and must be re-cooled to accumulator temperature. This URD is also in the investigation of Lorentzen and Baglo⁽⁶⁾ and is the ‘loss’ of gas due to venting to the accumulator. This vapour occupies 95 percent of the internal volume of the evaporator, due to the assumption made above that the liquid trapped behind the level regulating control valve occupies the remaining 5 percent¹¹⁸. The mass of vapour remaining inside the plates, $m_{rv.trap[E](t2)}$ (from

¹¹⁷ The sensitivity analysis that justifies this assumption is shown in Appendix A10.2, where varying the volume occupied by liquid at the beginning of the re-cooling sub-period from 0-5 % of the internal volume of the module results in a change in total percentage URD of total refrigeration demand for the CGPS of 0.18 %.

¹¹⁸ Based on the sensitivity analysis of Appendix A10.2 mentioned in the previous footnote.

equation (27) of Section 8.2.2) at the beginning of the re-cooling sub-period is predicted as follows:

$$m_{rv.trap[E](t2)} = \frac{0,95V_{[E]}}{v_{rv}(P_{r.har})} = \frac{0,95(0,8232)}{0,2119} = 3,69 \text{ kg} \quad \{14\} (41)$$

The trapped gas is vented to the accumulator, and therefore the URD associated with re-cooling this warm gas should strictly be seen at the accumulator. However $m_{rv.trap[E](t2)}$ returns to the accumulator via the liquid-vapour path and therefore mixes with the return liquid-vapour mixture from the other seven modules that are building ice. In re-cooling this trapped gas, a slight amount of the returning liquid will boil before it enters the accumulator. Nonetheless, the re-cooling of the trapped vapour takes place simultaneously with that of the trapped liquid, so it is convenient to consider them simultaneously. This URD is therefore assumed to be seen where it originates i.e. at the evaporator during the re-cooling sub-period and is predicted as:

$$\Delta H_{rv.trap[E]} = -m_{rv.trap[E](t2)} (h_{rv}(T_{r.har}) - h_{rv}(T_{r[ACC]})) = -3,69(1471,00 - 1451,00) = 67,30 \text{ kJ} \quad \{15\} (42)$$

URDs at the Evaporator During the Re-Cooling Sub-Period

The URDs seen by the evaporator during the re-cooling sub-period are:

(iv) The re-cooling of the evaporator plates and its manifolds, the same as

$\Delta H_{r.har.1}$ above :

$$\begin{aligned} \Delta H_{r.s[E]} = \\ -\Delta U_{s[E]} = -m_{s[E]} c_s (T_{r[E]build}) [T_{sat}(P_{r[E]har}) - T_{sat}(P_{r[E]build})] = -24713,00 \text{ kJ} \end{aligned} \quad \{16\} (43)$$

(v) The re-cooling of the liquid trapped behind the level regulating control valve:

$$\Delta H_{rl.trap[E]} = -m_{rl.trap[E](t2)} (h_{rl}(T_{r[E]har}) - h_{rl}(T_{r[E]build})) = -1765,00 \text{ kJ} \quad \{17\} (44)$$

- (vi) The re-cooling of the vapour trapped inside the evaporator modules at the beginning of the re-cooling sub-period:

$$\Delta H_{rv.trap[E]} = -m_{rv.trap[E](t2)} (h_{rv}(T_{r[E]har}) - h_{rv}(T_{r[ACC]})) = -67,30 \text{ kJ} \quad \{18\} \quad (45)$$

A11.2 URDs at the Accumulator during the Transient Period

The URDs specific to the “transient period” are that of re-cooling the steel of the accumulator and the vented pressurising gas after each venting period at the [pumping] pumper drum. However, as described in Section 7.2.3, both these URDs are *inherent* in that they would have been generated had the minor flow of refrigerant required to pressurise the pumper drum expanded, in one step, all the way from condensed liquid receiver pressure to accumulator pressure. These URDs are nonetheless addressed here, because predicting them using test data from the CGPS allows for the same URDs to be predicted for the HGPS - where they become *avoidable* URDs¹¹⁹. Re-cooling the vapour trapped inside the evaporator modules at the beginning of the re-cooling sub-period as well as re-cooling the liquid refrigerant expelled to the accumulator at the beginning of the warming sub-period are not specific to the “transient” period (i.e. they occur continuously throughout the ice making cycle) and are addressed in equations (45) and (54) respectively.

During a complete ice building and shedding period of one module (15 minutes), each pumper drum is pressurised 3 times and therefore vents 3 times, as shown in the pumping schedule of the timing diagram of Figure 3.1.

From Figure 8.8 above, the maximum measured temperature change is 0,9 °C. Therefore for the two pumper drums of Unit 5, the *inherent* URD of re-cooling the accumulator per ice building and shedding cycle is:

¹¹⁹ Due to the extra mass flow rate of hot gas required to pressurize the pumper drum, as shown in Figure 7.1 above.

$$\begin{aligned}\Delta\hat{H}_{r.s[ACC]} &= -m_{s[ACC]}c_s(T_{r[ACC]})(T_{heat[ACC]} - T_{r[ACC]}) \times 3 \times 2 = -6870,00 \cdot 0,4502(0,9) \times 3 \times 2 \\ &= -16699,00 \text{ kJ} \end{aligned} \quad \{19\}(52)$$

where $T_{heat[ACC]} - T_{r[ACC]}$ is equal to $0.9 \text{ } ^\circ\text{C}$ for the CGPS.

A11.2.1 URDs at the Accumulator during the Complete Ice Building and Shedding Cycle of One Module

Unavoidable URDs at the accumulator over the entire ice building and shedding period of one module include¹²⁰:

1. Re-cooling the liquid condensed during the warming sub-period of the module:

$$\begin{aligned}\Delta H_{rl\{c\}} &= -m_{rl\{c\}}(h_{rl}(P_{r[E].har}, \bar{T}_{rl\{c\}}) - h_{rl}(P_{r[ACC]})) = -106,60(241,50 - 158,80) \\ &= -8823,00 \text{ kJ} \end{aligned} \quad \{20\}(53)$$

As mentioned above, for the purposes of this investigation the mean temperature of the condensed liquid $\bar{T}_{rl\{c\}}$ is assumed to be saturation temperature at harvesting pressure $T_{sat}(P_{r[E]har})$.

2. Re-cooling the liquid refrigerant expelled to the accumulator at the beginning of the warming sub-period of the module:

$$\begin{aligned}\Delta H_{rl.cont[E-ACC]} &= -\Delta m_{rl.cont[E-ACC]}(h_{rl}(P_{r[E]har}, T_{rl[E-ACC]}) - h_{rl}(P_{r[ACC]})) \\ &= -161,30(183,30 - 158,80) = -3963,00 \text{ kJ} \end{aligned} \quad \{21\}(54)$$

Inherent URDs at the accumulator over the entire ice building and shedding period of one module include

3. Re-cooling the gas vented from the pumping pumper drum. Each pumper drum has level control sensors near its top and bottom as shown in Figure 8.9 above.

¹²⁰ As these URDs are for one module, over the entire ice building and shedding period of one module (15 minutes) the accumulator sees eight times the URDs listed in 1. and 2. below.

During the filling period, the drum is filled with liquid refrigerant by the accumulator to $0.8 \times D_{[PD]}$, and during the pumping period, pumps its contents out until the liquid level sensor registers a depth of liquid at $0.1 \times D_{[PD]}$. The remainder of the volume of the pumper drum is filled with pressurizing gas, which must be vented to the accumulator at the end of its pumping period. The volume occupied by this gas is predicted in Figure A8.8 of Appendix A8 to be

$$V_{rv[PD](t2)} = ((a_{rv.dotted} + a_{rv.dashed}))L''_{[PD]} = (2,978r_{[PD],i}^2)4,2 = 5,784 \text{ m}^3 \quad \{22\}$$

Where as mentioned in Section A8.2.2 the required length of the pumper drum based on the mass flow rate predicted in equation (69) of Section 8.6.1 is 4 % larger than that of Figure A8.4. The mass of gas is therefore

$$m_{rv.vent[(PD+)-ACC]} = 5,784 \cdot \rho_{rv}(P_{r[PD+]}) = 26,07 \text{ kg} \quad \{23\}$$

and the *inherent* URD of re-cooling this mass of gas is:

$$\begin{aligned} \Delta H_{rv.vent[(PD+)-ACC]} &= -m_{rv.vent[(PD+)-ACC]}(h_{rv}(P_{r[PD+]}) - h_{rv}(P_{r[ACC]})) \times 3 \times 2 \\ &= -26,07(1469,00 - 1451,00) \times 3 \times 2 = -2783,00 \text{ kJ} \end{aligned} \quad \{24\} \quad (55)$$

where the subscript $[PD+]$ denotes pressurised [pumping] pumper drum conditions, the mass flow of gas is denoted $\dot{m}_{rv.vent[(PD+)-ACC]}$, and it is conservatively assumed that the vapour is at saturated conditions at the pumping pressure¹²¹ $h_{rv}(P_{r[PD+]})$. From the timing diagram and pumping schedule of Figure 3.1, this URD occurs 3 times per pumper drum over the entire ice building and shedding cycle of one module.

4. Re-cooling the gas vented from the filling pumper drum. During the filling period, vapour is continuously vented from the filling pumper drum to the

¹²¹ Measured at the plant as 200 kPa above filling pumper drum pressure.

accumulator. The minor difference in pressure results in the *inherent* URD of re-cooling this vapour to accumulator temperature.

The mass of gas vented is

$$m_{rv.vent[(PD-)-ACC]} = 5,784 \cdot \rho_{rv}(P_{r[PD-]}) = 16,94 \text{ kg} \quad \{26\}$$

$$\begin{aligned} \Delta \hat{H}_{rv.vent[(PD-)-ACC]} &= -m_{rv.vent[(PD-)-ACC]} (h_{rv}(P_{r[PD-]}) - h_{rv}(P_{r[ACC]})) \times 3 \times 2 \\ &= 16,94(1456,00 - 1451,00) \times 3 \times 2 = -496,50 \text{ kJ/kg} \end{aligned} \quad \{27\} \text{ (56)}$$

where the subscript $[PD-]$ denotes [filling] pumper drum conditions, the mass flow of gas is denoted $\dot{m}_{rv.vent[(PD-)-ACC]}$, and it is justifiably assumed that the vapour is at saturated conditions at the filling pressure $h_{rv}(P_{r[PD-]})$. This URD occurs 3 times per pumper drum over the entire ice building and shedding cycle of one module.

A11.2.2 URDs at the Filling Pumper Drum

The only URD at the pumper drum seen during the filling process is the re-cooling of the steel of the pumper drum, which is warmed during its pumping period. The rest of the URDs are seen at the accumulator and listed in Section 8.3.2 above. However, as described in Sections 7.2.3 and 8.3.1, for the CGPS, this URD is *inherent* in that it would have been generated had the minor flow of refrigerant required to pressurise the pumper drum expanded, in one step, all the way from condensed liquid receiver pressure to accumulator pressure. This URD is nonetheless addressed here as it can be predicted using test data from the CGPS, and allows for the same URD to be predicted for the HGPS - where it is an *avoidable* URD¹²². The temperature at the pumper drum wall was measured at the

¹²² Due to the extra mass flow rate of hot gas required to pressurize the pumper drum, as shown in Figure 7.1 above.

ERPM plant (sensor T6 of Figure A1.1) and is plotted in Figure 8-11 above. From the timing diagram of Figure 3.1, pumper drum 1 undergoes 3 pumping periods every 15 minutes, and from Figure 8.11 above, the maximum temperature rise during pumping is 1°C above filling temperature.

The *inherent* URD of re-cooling the steel of the two pumper drums during the filling period, and for a complete ice making cycle of 15 minutes which comprises three filling periods per pumper drum, is:

$$\begin{aligned}\Delta\hat{H}_{r.s[PD]} &= -m_{s[PD]}c_s(T_{r[PD-]})(T_{heat[PD]} - T_{r[PD-]}) \times 3 \times 2 = -2867,00 \cdot 0,4533 \cdot 1 \times 3 \times 2 \\ &= - 7798,00 \text{ kJ} \qquad \qquad \qquad \{28\} \text{ (63)}\end{aligned}$$

A11.2.3 URD of Re-Cooling the Upper Portion of Circulating Liquid at the Pumping Pumper Drum

The final *inherent* URD for the CGPS is that of re-cooling the upper portion of warmed liquid in the pumper drum. During the ice making period, cold flash gas throttled down from the expansion valve feeding the pumper drum (as well as a small portion of warm gas from the condensed liquid receiver to boost the pressure in the pumper drum to circulate a sufficient flow of liquid) is used to pump the liquid ammonia through the evaporator. The interaction of pressurising gas and colder liquid refrigerant in the pumper drum results in a major URD for any *hot* gas pumped system (HGPS), and is the first ‘loss’, or URD in the terminology of this investigation, included in predicting the total ‘refrigeration loss’ of the system by Lorentzen and Baglo⁽⁶⁾.

From Figure 8-9 above, and based on test data collected from the ERPM plant, the pumping pumper drum expels 95% of its volume of liquid to the evaporator in a time of 130 seconds. The upper portion of this liquid is heated by the incoming pressurising gas to $T_{r.circ[PD-E]}$ (based on temperature measurements at sensing point T7 of Figure A1.1). This URD is not seen at the pumper drum, rather it is

seen at the entrance to the evaporator. However, seeing that this URD arises at the pumper drum, it is presented here rather than in Section 8.2 above. Predicting $T_{rl.circ[PD-E]}$ from test data as well as the mass of liquid heated to this temperature $m_{rl.circ[PD-E]}$ is performed in Appendix A8.2.3. The final *inherent* URD of re-cooling this portion of liquid, per module (there are seven modules building ice at any time - each ice building period lasting 810 seconds and each pumping period lasting 150 seconds), and for the $\frac{810}{150} = 5,4$ pumping periods that the module sees per ice building period, is:

$$\begin{aligned} \Delta \widehat{H}_{rl.circ[PD-E]} &= -m_{rl.circ[PD-E]} (h_{rl}(T_{rl.circ[PD-E]}) - h_{rl}(T_{r[PD-]})) = \\ &= -1221,12 \left(\frac{5,4}{7}\right) (179,10 - 177,80) = -1274,00 \text{ kJ} \end{aligned} \quad \{29\} (64)$$

Where it is assumed that the enthalpy of the upper portion of circulated liquid is initially at [filling] pumper drum temperature.

A11.3 Total PRD and URD for the Cold Gas Pumped

Arrangement Per Module

A11.3.1 Total PRD Per Module for all Pumping Arrangements

The total PRD per module is identical for all pumping arrangements, and from equations (18) and (20) of Section 8.1.1 and 8.1.2, is:

$$\Sigma Q_{PRD} = Q_{PRD[E]} + Q_{PRD[PRC]} = 610425,50 \text{ kJ} \quad \{30\}(65)$$

A11.3.2 Total URD Per Module for the Cold Gas Pumped Arrangement

All the URDs for the CGPS are *unavoidable* and/or *inherent*. Summing these URDs the total URD *per module*, from equations (19), (40), (42), (43), (53), (54), and (56) is:

$$\begin{aligned}\Sigma\Delta H_{URD\{CGPS\}} &= Q_{URD[E]} + \Delta H_{r.s[E]} + \Delta H_{rl.trap[E]} + \Delta H_{rv.trap[E]} + \Delta H_{rl\{c\}} + \Delta H_{rl.cont[E-ACC]} \\ &= -(120435,60 + 24713,00 + 1765,00 + 67,30 + 8823,00 + 3963,00) \\ &= -159715,27 \text{ kJ}\end{aligned}$$

{31}(66)

A11.4 Predicting the Average Recirculation Ratio and Compressor Work Input for the Operating Cold Gas Pumped System Per Module

A11.4.1 Predicting the Average Recirculation Ratio for the Operating CGPS

From the control volume energy balance at the evaporators during ice building (Section 8.1 above), the enthalpy at the outlet of the evaporator is based on the average recirculation ratio, $\bar{x}_{r[E]o}$, which is the inverse of the quality of refrigerant. From equation (17) above:

$$\begin{aligned}& (m_{r[E](t2)} - m_{r[E](t1)})\mu_{rl}(T_{r[E]build}) + (m_{rv[E](t2)} - m_{rv[E](t1)})\mu_{rv}(T_{r[E]build}) \\ & - m_{I.b}(-c_w T_{w[E]i} - h_{sf} + c_l \frac{(T_{r[E]build} + T_{I.o})}{2}) \\ & = |\Delta m_{rl[PD-E]} h_{rl}(T_{r[E]}) - \Delta m_{r(l,v)[E-ACC]} h_{r(l,v)}(T_{r[E]}, \bar{x}_{r[E]o})_{build}\end{aligned}\quad \{32\}(17)$$

The first four terms of equation (17) above comprise the change in internal energy of the refrigerant. As mentioned in Section 8.2.1 above and based on the analysis presented in Appendix A2, it is conservatively assumed that each plate is filled by

30% of its inner volume with liquid ammonia¹²³ at the end of ice-building and at the beginning of the warming sub-period. If it is further assumed that the mass of liquid occupying the module at the beginning of the ice building period is negligible, then equation (17) simplifies to:

$$\begin{aligned}
& (m_{r[E](t2)} \mu_{rl}(T_{r[E]build}) + (m_{rv[E](t2)} - m_{rv[E](t1)}) \mu_{rv}(T_{r[E]build})) \\
& - m_{I,b} (-c_w T_{w[E]i} - h_{sf} + c_l \frac{(T_{r[E]build} + T_{I,o})}{2}) \\
& = \left| \Delta m_{r[PD-E]} h_{rl}(T_{r[E]}) - \Delta m_{r(l,v)[E-ACC]} h_{r(l,v)}(T_{r[E]}, \bar{x}_{r[E]o}) \right|_{build} \quad \{33\}(67)
\end{aligned}$$

Representing the masses of the liquid and vapour in the module at the end of ice-building, equation (67) becomes:

$$\begin{aligned}
& 30na_{[E]chl} L_{[E]} (0,3\rho_{rl}(T_{r[E]build}) \mu_{rl}(T_{r[E]build}) + 0,3\rho_{rv}(T_{r[E]build}) \mu_{rv}(T_{r[E]build})) \\
& - m_{I,b} (-c_w T_{w[E]i} - h_{sf} + c_l \frac{(T_{r[E]build} + T_{I,o})}{2}) \\
& = \left| \Delta m_{r[PD-E]} h_{rl}(T_{r[E]}) - \Delta m_{r(l,v)[E-ACC]} h_{r(l,v)}(T_{r[E]}, \bar{x}_{r[E]o}) \right|_{build} \quad \{34\}(68)
\end{aligned}$$

The changes in internal energy, represented by the masses of liquid and vapour in the module at the end of ice building, are accounted for in equation (68). The mass flow rate at the inlet to the evaporator $\dot{m}_{r[PD-E]}$ remains constant throughout the ice building period, and therefore the difference between the inlet and outlet ($\dot{m}_{r(l,v)[E-ACC]}$) mass flow rates is the rate of change of mass in the evaporator. This mass flow rate is predicted from a mass rate balance in Appendix A10.3 to be negligible compared to the inlet mass flow rate¹²⁴. Based on this assumption, and since the evaporating temperature is assumed to remain constant throughout the ice building period¹²⁵, the mass flow of refrigerant at the inlet and outlet of the evaporator are assumed to be identical, and consequently $\Delta m_{r[PD-E]} \approx \Delta m_{r(l,v)[E-ACC]}$. Equation (68) thus simplifies to

¹²³ With the remaining volume occupied by refrigerant vapour at ice building temperature.

¹²⁴ Appendix A10.3 predicts that the rate of change of mass contained within the control volume is 5,90% of the predicted mass flow rate at the inlet of the evaporator.

¹²⁵ i.e. After the re-cooling sub-period the evaporator returns to ice building temperature.

$$30na_{[E]chl}L_{[E]}(0,3\rho_{rl}(T_{r[E]build})\mu_{rl}(T_{r[E]build})+0,3\rho_{rv}(T_{r[E]build})\mu_{rv}(T_{r[E]build})) - m_{l,b}(-c_w T_{w[E]i} - h_{sf} + c_I \frac{(T_{r[E]build} + T_{l,o})}{2}) = |\Delta m_{r[PD-E]}(h_{rl}(T_{r[E]}) - h_{r(l,v)}(T_{r[E]}, \bar{x}_{r[E]o}))|_{build} \quad \{35\} \quad (69)$$

Substituting values into equation (69) yields:

$$35 \cdot 30 \cdot (0,000224)3,5(0,3 \cdot 646,60 \cdot 172,50 + 0,3 \cdot 2,809 \cdot 1333,00) - 1712,00(-4,186 \cdot 12 - 335,00 + 2,098 \frac{((-5,833) + 0)}{2}) = |\Delta m_{r[PD-E]}(h_{r(l,v)}(T_{r[E]}, \bar{x}_{r[E]o}) - 173,00)|_{build} \\ \therefore |\Delta m_{r[PD-E]}(h_{r(l,v)}(T_{r[E]}, \bar{x}_{r[E]o}) - 173,00)|_{build} = 698407,00 \text{ kJ} \quad \{36\}$$

The thickness of ice sheet delivered, from measurements at the ERPM plant, is approximately 5 mm (from Table A6.3 of Appendix A6). The thickness of ice built however includes a layer of ice that is subsequently melted during the warming sub-period. Both the thickness of the built ice layer and the melted ice layer are predicted from the heat transfer models during ice building and harvesting presented in Section 9. below.¹²⁶ An average built ice layer thickness of 6 mm is input into equation (8) of Section 8.1 above to obtain the mass of ice built during the ice building period $m_{l,b}$. Thus the only unknowns in equation (69) of Section 8.6.1 above are the enthalpy of the two-phase mixture at the outlet of the evaporator, which is based on the average recirculation ratio, and the mass of liquid pumped to and through the evaporator. By varying the average recirculation ratio $\bar{x}_{r[E]o}$ in equation (69) above between realistic limits, the mass flow rate of liquid refrigerant through the evaporators can therefore be predicted.

Based on Figure 8.9 and the analysis performed in Appendix A8, the mass flow rate of liquid pumped through to seven modules (with one module harvesting) can also be predicted from the change in liquid volume of the [pumping] pumper drum over the pumping period. For an average recirculation ratio of 5:

¹²⁶ From Table 9.2, the built ice sheet thickness varies from 5,84 – 6,67 mm based on the different convective boiling heat transfer coefficients. From Table 9.3, the melted ice sheet thickness varies from 0,786 – 1,149 mm based on the different convective condensing heat transfer coefficients.

$$h_{r(l,v)}(T_{r[E]}, \bar{x}_{r[E]o} = 5) = 429,40 \text{ kJ/kg} \quad \{37\}$$

$$\therefore \left| \Delta m_{r[PD-E]} (429,40 - 173,00) \right|_{build} = 698407,00 \text{ kJ} \quad \{38\}$$

$$\Delta m_{r[PD-E]} = 2724,00 \text{ kg} \quad \{39\}$$

$$\therefore \dot{m}_{r[PD-E]} = \frac{\Delta m_{r[PD-E]}}{13,5 \times 60} = 3,363 \text{ kg/s} \quad \{40\}$$

This predicted mass flow rate from Section A8.2.2 is 3,354 kg/s, and subsequently, the mass pumped to and through the evaporators during ice building, is 0,30 % smaller than $\Delta m_{r[PD-E]}$ predicted from equation (69) of Section 8.6.1 above- based on an average recirculation ratio $\bar{x}_{r[E]o}$ of approximately 5.

Therefore, as there is sufficiently accurate agreement between the two methods of predicting the mass flow rate through the evaporator for the cold gas pumped arrangement, the average recirculation ratio is predicted as 5. Hereafter, for simplicity, the average recirculation ratio will be denoted as x_1 .

A11.4.2 Predicting the Average Electrical and Mechanical Compressor Work Input for the Operating CGPS

Based on test data obtained from the ERPM plant and from Appendix A6 (Section A6.1), the electrical and mechanical work input into the compressor per module can be predicted:

$$\dot{W}_{[CR]\{CGPS\}elec} = 180 \text{ kW/module} \quad \{41\}(70)$$

Assuming a compressor motor efficiency η_m of 96%, the mechanical power input of the compressor for the CGPS is:

$$\dot{W}_{[CR]\{CGPS\}mech} = \dot{W}_{[CR]\{CGPS\}elec} \eta_m = 172.8 \text{ kW/module} \quad \{42\}(70b)$$

A11.5 Total URD for the Hot Gas Pumped Arrangement Per Module

A11.5.1 URDs at the Accumulator for the HGPS

As mentioned in Section 8.3.1 above, the URD specific to the “transient period” is that of re-cooling the steel of the accumulator after each venting period at the pumping pumper drum. For the HGPS, this is an *avoidable* URD. During a complete ice building and shedding cycle of one module (15 minutes), each pumper drum is pressurised 3 times and therefore vents 3 times, as shown in the pumping schedule of Figure 3.1. On the basis of the predicted *inherent* URDs at the accumulator for the CGPS, the corresponding *avoidable* ones of the HGPS, and hence the temperature rise at the accumulator for this arrangement, can be predicted. It is recalled from Section 8.3.2 that the URDs seen at the accumulator for the CGPS over the entire ice building and shedding cycle of one module comprise of:

$$\Sigma \Delta H_{URD[ACC]\{CGPS\}} = \Delta H_{rl\{c\}} + \Delta H_{rl.cont[E-ACC]} + \frac{\Delta \hat{H}_{rv.vent[(PD+)-ACC]}}{8} + \frac{\Delta \hat{H}_{rv.vent[(PD-)-ACC]}}{8} \quad \{43\}(71)$$

Now, since the pumping pumper drum is filled with gas from the condensed liquid receiver, the venting gas will be at a higher temperature than that of the CGPS. Assuming that the level control sensors at the pumper drum regulate the mass of liquid pumped in the same manner and within the same time as the CGPS, the volume that the pressurizing gas occupies (from Section A8.2.2 above) is 5,784 m³. The corresponding mass of this gas is:

$$m_{rv.vent[(PD+)-ACC]\{HGPS\}} = 5,784 \cdot \rho_{rv}(P_{r[REC]}) = 51,09 \text{ kg} \quad \{44\}$$

and the URD of re-cooling this mass of gas is:

temperature at the accumulator for the HGPS, $T_{heat[ACC]\{HGPS\}} - T_{r[ACC]}$, is assumed to be predicted by the ratio of the URDs of re-cooling this vented pressurizing gas for the HGPS and CGPS, multiplied by the change in temperature measured for the cold gas pumped arrangement, $T_{heat[ACC]} - T_{r[ACC]}$:

$$\begin{aligned} [T_{heat[ACC]\{HGPS\}} - T_{r[ACC]}] &= [T_{heat[ACC]} - T_{r[ACC]}] \left[\frac{\Delta H_{rv.vent[(PD+)-ACC]\{HGPS\}}}{\Delta \hat{H}_{rv.vent[(PD+)-ACC]}} \right] \\ &= 0,90 \frac{10436,00}{2783,00} = 3,38 \text{ } ^\circ\text{C} \end{aligned} \quad \{46\} (73)$$

Finally, the URD of re-cooling the accumulator for the hot gas pumped arrangement is:

$$\begin{aligned} \Delta H_{r.s[ACC]\{HGPS\}} &= -m_{s[ACC]} c_s (T_{r[ACC]})(T_{heat[ACC]\{HGPS\}} - T_{r[ACC]}) \times 3 \times 2 \\ &= -6870,00 \cdot 0,4502(3,38) = -62621,00 \text{ kJ} \end{aligned} \quad \{47\} (74)$$

A11.5.2 URDs at the Filling Pumper Drum for the HGPS

As mentioned in Section 8.4.1 above, the only URD at the pumper drum seen during the filling process is the re-cooling of the steel of this drum at the end of its pumping period¹²⁸. It is assumed that the URD of re-cooling the residual liquid that is left in the pumper drum at the end of its pumping process is included in the URD of re-cooling the vented pressurising gas to the accumulator (equation (72)), as well as that of re-cooling the steel of the pumper drum.

The URD of re-cooling the steel of the pumper drum during the filling period is:

peaks of Figure 8.8 are regarded as accurately measuring the change in temperature at the accumulator during the venting period of the [pumping] pumper drum

¹²⁸ From the timing diagram of Figure 3.1, this occurs six times per ice building and shedding cycle of one module (15 minutes).

$$\begin{aligned}\Delta H_{r,s[PD]\{HGPS\}} &= -m_{s[PD]}c_s(T_{r[PD-]})(T_{heat[PD]\{HGPS\}} - T_{r[PD-]}) \times 3 \times 2 \\ &= -2867,00 \cdot 0,4533(3,88) \times 3 \times 2 = -30255,00 \text{ kJ}\end{aligned}\quad \{48\}(75)$$

The pumping period for the HGPS is assumed to be identical to that of the CGPS, except that now gas at pressurized liquid receiver temperature is introduced into the [pumping] pumper drum. It is therefore assumed that the maximum temperature difference reached by the pumper drum $T_{heat[PD]\{HGPS\}} - T_{r[PD-]}$ is predicted by the ratio of pressurizing inlet gas temperatures for the HGPS and the CGPS multiplied by the temperature difference measured at pumper drum 1 (Figure 8.11 above) for the cold gas operating plant. As the change in temperature is a measure of the energy gained by the pumper drum by sensible heat, it is justifiably assumed to be proportional to this ratio of pressurizing gas temperatures.

$$T_{heat[PD]\{HGPS\}} - T_{r[PD-]} = (T_{heat[PD]} - T_{r[PD-]}) \left[\frac{T_{r[PD+]\{HGPS\}}}{T_{r[PD+]}} \right] = 1,00 \frac{29,01}{7,45} = 3,88 \text{ } ^\circ\text{C}^{129}\quad \{49\}(76)$$

A11.5.3 URD of Re-Cooling the Upper Portion of Circulating Liquid at the Pumping Pumper Drum for the HGPS

From Figure 8.9 above, and based on test data collected from the ERPM plant, the pumping pumper drum expels 95% of its volume of liquid to the evaporator in a time of 130 seconds. The upper portion of this liquid is heated by the incoming gas to $T_{r.circ[PD-E]\{HGPS\}}$ which is predicted based on test data for the circulating temperature of the cold gas pumped arrangement $T_{r.circ[PD-E]}$. Predicting the increased temperature for the HGPS as well as the mass of liquid heated to this temperature $m_{r.circ[PD-E]\{HGPS\}}$ is performed in Appendix A8.2.4. The final URD of

¹²⁹ $T_{r[PD+]}$ is saturated temperature at 200 kPa above filling pumper drum pressure for the CGPS, and $T_{r[PD+]\{HGPS\}}$ is saturated temperature at condensed liquid receiver pressure.

re-cooling this portion of liquid, per module (there are seven modules building ice at any time - each ice building period lasting 810 seconds and each pumping period lasting 150 seconds), and for the $\frac{810}{150} = 5,4$ pumping periods that the module sees per ice building period, is:

$$\begin{aligned}\Delta H_{rl.circ[PD-E]\{HGPS\}} &= -m_{rl.circ[PD-E]\{HGPS\}} \frac{5,4}{7} (h_{rl}(P_{r[PD-]}, T_{rl.circ[PD-E]\{HGPS\}}) - h_{rl}(P_{r[PD-]})) \\ &= -1218,49 \frac{5,4}{7} (181,40 - 177,80) = -3453,00 \text{ kJ}\end{aligned}$$

{50} (77)

A11.5.4 Total URD for the HGPS

Summing the URDs for the HGPS, and assuming that the URDs of re-cooling the steel of the accumulator and pumper drums, plus all gas vented from both drums to the accumulator, are shared equally amongst the eight modules, the total URD per module from equations (19), (40), (42), (43), (53), (54), (56), (72), (74), (75), and (77) is:

$$\begin{aligned}\Sigma \Delta H_{URD\{HGPS\}} &= Q_{URD[E]} + \Delta H_{r.s[E]} + \Delta H_{rl.trap[E]} + \Delta H_{rv.trap[E]} + \frac{\Delta H_{r.s[ACC]\{HGPS\}}}{8} \\ &+ \Delta H_{rl\{c\}} + \Delta H_{rl.cont[E-ACC]} + \frac{\Delta H_{rv.vent[(PD+)-ACC]\{HGPS\}}}{8} \\ &+ \frac{\Delta H_{rv.vent[(PD-)-ACC]}}{8} + \frac{\Delta H_{r.s[PD]\{HGPS\}}}{8} + \Delta H_{rl.circ[PD-E]\{HGPS\}}\end{aligned}$$

{51} (78)

$$\begin{aligned}\Sigma \Delta H_{URD\{HGPS\}} &= - \left(120435,60 + 24713,00 + 1765,00 + 67,30 + \frac{62621,00}{8} \right. \\ &\quad \left. + 8823,00 + 3963,00 + \frac{10436,00}{8} + \frac{496,50}{8} + \frac{30255,00}{8} + 3453,00 \right) \\ &= -176144,00 \text{ kJ}\end{aligned}$$

A11.6 Total URD for the Mechanically Pumped Arrangement Per Module

For the mechanically pumped arrangement, the avoidable URDs due to pressurizing gas circulating the liquid in the pumper drum to the evaporators for the gas pumped arrangements are essentially replaced by the avoidable URD of increasing the pressure of the same amount of liquid refrigerant across the mechanical pump. As there is no pressurizing gas vented to the accumulator for this arrangement, it is assumed that the accumulator temperature remains constant throughout the ice building and shedding cycle. Therefore there is no URD of re-cooling the accumulator for this mechanically pumped system (MPS). To obtain the mechanical work input of the pump, an energy balance analysis is performed in Appendix A9. The final mechanical work input from the pump assuming a mechanical pump efficiency of 85 % is:

$$\dot{W}_{[P]\{MPS\}mech} = \frac{\rho_{rl} (P_{r\{PD+\}}) g \dot{V}_{rl\{P-E\}} H'_{[P]}}{1000 \eta_{[P]}} = \frac{628,30 \cdot 9,81 \cdot 0,0375 \cdot 10,08}{1000 \cdot 0,85} = 2,737 \text{ kW} \quad \{52\}$$

And per module this input power is 0,391 kW.

The work input from the pump increases the enthalpy of the liquid refrigerant as it increases its pressure. The URD of re-cooling the warmed liquid refrigerant per module at the evaporator, over a complete ice building period of $(t_2 - t_1)$, is simply the integral of the mechanical work input over this time divided by 7 ice building modules.

$$\Delta H_{rl\{P\}} = - \int_{t_1}^{t_2} \dot{W}_{[P]\{MPS\}mech} dt = 0,391(13,5 \times 60) = -316,71 \text{ kJ} \quad \{53\}(81)$$

A11.6.1 Total URD for the MPS

From equations (19), (40), (42), (43), (53), (54) and (81) the URDs for the MPS are:

$$\begin{aligned} \Sigma \Delta H_{URD\{MPS\}} = & Q_{URD[E]} + \Delta H_{r.s[E]} + \Delta H_{rl.trap[E]} + \Delta H_{rv.trap[E]} + \Delta H_{rl\{c\}} \\ & + \Delta H_{rl.com[E-ACC]} + \Delta H_{rl\{P\}} \end{aligned} \quad \{54\}(82)$$

$$\begin{aligned} \Sigma \Delta H_{URD\{MPS\}} = & -(120435,60 + 24713,00 + 1765,00 + 67,30 + 8823,00 + 3963,00 + 316,71) \\ = & -160032,00 \text{ kJ} \end{aligned} \quad \{54\}$$

A11.7 Total URD for a Fully Mechanically Pumped Arrangement Per Module

A theoretical model for a completely mechanically pumped system, based on a suggestion by Bailey-McEwan,⁽¹⁶⁾ is developed. The system, utilising two pumps – a pump to circulate the refrigerant through the evaporators and one to discharge/recharge the evaporators with liquid before and after harvesting – would eliminate the URD associated with harvesting gas expelling cold ammonia liquid to the accumulator at the beginning of the warming sub-period, $\Delta H_{rl.com[E-ACC]}$. It would also eliminate the URD due to the warm ammonia (refrigerant) liquid that is trapped behind the level-regulating valve at the end of the warming sub-period, $\Delta H_{rl.trap[E]}$.

Appendix A4 outlines the analysis to determine the mechanical power required by the recharge pump, as well as the basic design of the vessels and piping.

The final mechanical work input for the recharge pump is:

$$\dot{W}_{[P]\{FMPS\}mech} = \frac{\rho_{rl}(P_{r[ACC]})g\dot{V}_{rl[DV-RV]}H'_{[P]\{FMPS\}}}{1000\eta_{[P]}} = \frac{650,70 \cdot 9,81 \cdot 0,0011 \cdot 5,71}{1000 \cdot 0,85} = 0,045 \text{ kW} \quad \{55\}(83)$$

The work input from the pump increases the enthalpy of the liquid refrigerant as it increases its pressure. The URD of re-cooling the warmed liquid refrigerant per module at the evaporator, over a complete recharge time of 13 minutes, denoted $(t_2 - t_1)$, is simply the integral of the mechanical work input over this time.

$$\Delta H_{rl[P]\{FMPS\}} = \int_{t_1}^{t_2} \dot{W}_{[P]\{FMPS\}mech} dt = 0,045(13 \times 60) = 35,27 \text{ kJ} \quad \{56\}(84)$$

A11.7.1 Total URD for the FMPS

From equations (19), (43), (53), (54), (81) and (84) the URDs for the MPS are:

$$\Sigma \Delta H_{URD\{FMPS\}} = Q_{URD[E]} + \Delta H_{r.s[E]} + \Delta H_{rl[c]} + \Delta H_{rl.cont[E-ACC]} + \Delta H_{rl[P]} + \Delta H_{rl[P]\{FMPS\}} \quad \{57\}(85)$$

$$\begin{aligned} \Sigma \Delta H_{URD\{MPS\}} &= -(120435,60 + 24713,00 + 8823,00 + 67,30 + 316,71 + 35,27) \\ &= -154339,00 \text{ kJ} \end{aligned} \quad \{58\}$$

A11.8 Comparison of Results for the Pumping Arrangements

A11.8.1 Total PRD and URD for the Four Pumping Arrangements

Graphs based on the model described in Section 8. comparing the different pumping arrangements at various performance quantities and operating parameters are presented in Section 8.10 above. The sample calculation presented above is based on an average recirculation ratio of five. Therefore the following tables summarise the information that is presented in the graphs of Section 8.10,

for an average recirculation ratio of five. First, the total refrigeration demand per module for each pumping arrangement is calculated as follows:

$$\Sigma\Delta H = \Sigma Q_{PRD} + \Sigma\Delta H_{URD} \quad \{59\}$$

Where ΣQ_{PRD} is the sum of the PRDs at the evaporator and pre-chiller, which is identical for all four pumping arrangements, and is predicted above to be:

$$\Sigma Q_{PRD} = Q_{PRD[E]} + Q_{PRD[PRC]} = -549557,00 - 60869,00 = -610426,00 \text{ kJ} \quad \{60\}$$

The sum of the URDs for each system is added to the above PRDs to obtain the total refrigeration demand per module. The percentage URD of total refrigeration demand is then predicted to be:

$$\%URD = \frac{\Sigma\Delta H_{URD}}{\Sigma\Delta H} \quad \{61\}$$

The table below, based on the calculation presented above for an average recirculation ratio of five, summarises the total URD, and subsequently, the percentage URD of total refrigeration demand per module for the four pumping arrangements.

Table A11.2 Comparison of the results for the four pumping arrangements

Variable	CGPS	HGPS	MPS	FMPS
$\Sigma\Delta H_{URD}$ [kJ]	-159715,00	-176144,00	-160032,00	-154339,00
ΣQ_{PRD} [kJ]	-610426,00	-610426,00	-610426,00	-610426,00
$\Sigma\Delta H$ [kJ]	-770141,00	-786570,00	-770458,00	-764765,00
$\%URD$	20,74 %	22,39 %	20,77	20,18 %

A11.8.2 COP for the Four Pumping Arrangements

Based on test data obtained from the ERPM plant and from Appendix A6 (Section 6.1), the electrical and mechanical work input into the compressor per module can be predicted:

$$\dot{W}_{[CR]\{CGPS\}elec} = 180,00 \text{ kW/module} \quad \{62\} (70)$$

Assuming a compressor motor efficiency η_m of 96%, the mechanical power input of the compressor for the CGPS is:

$$\dot{W}_{[CR]\{CGPS\}mech} = \dot{W}_{[CR]\{CGPS\}elec} \eta_m = 172,80 \text{ kW/module} \quad \{64\} (70b)$$

The energy input per module over a complete ice building and shedding period of 15 minutes is therefore:

$$\begin{aligned} W_{[CR]\{CGPS\}mech} &= \int_{t_1}^{t_2} \dot{W}_{[CR]\{CGPS\}mech} \\ &= \dot{W}_{[CR]\{CGPS\}mech} (t_2 - t_1) = 172.8(15 \times 60) = 155520,00 \text{ kJ} \end{aligned}$$

$$COP_{\{CGPS\}} = \frac{\Sigma Q_{PRD}}{\Sigma W_{[CR]\{CGPS\}mech}} = \frac{610426,00}{155520,00} = 3,925$$

From equation (5a) of Section 7.2, the mechanical work input for the HGPS is predicted as follows:

$$COP_{\{HGPS\}} = \frac{\Sigma Q_{PRD}}{\Sigma W_{[CR]\{HGPS\}mech}} \quad \{65\} (5a)$$

where

$$\Sigma W_{[CR]\{HGPS\}mech} = \Sigma W_{[CR]\{CGPS\}mech} \frac{\Sigma \Delta H_{\{HGPS\}}}{\Sigma \Delta H_{\{CGPS\}}} \quad \{66\} (5b)$$

The ratio of the total refrigeration demands in the above equation allows for the mechanical and electrical work input into the compressor to be predicted for all arrangements, based on the assumption of negligible changes in compressor isentropic efficiency mentioned on Section 7.2.

For the mechanically pumped system, the COP is:

$$COP_{\{MPS\}} = \frac{\Sigma Q_{PRD}}{\Sigma W_{\{CR\}\{MPS\}mech} + \Sigma W_{\{P\}\{MPS\}mech}} \quad \{67\}(6a)$$

where

$$\Sigma W_{\{CR\}\{MPS\}mech} = \Sigma W_{\{CR\}\{CGPS\}mech} \frac{\Sigma \Delta H_{\{MPS\}}}{\Sigma \Delta H_{\{CGPS\}}} \quad \{68\}(6b)$$

Similarly for the fully mechanically pumped system, the COP is:

$$COP_{\{FMPS\}} = \frac{\Sigma Q_{PRD}}{\Sigma W_{\{CR\}\{FMPS\}mech} + \Sigma W_{\{P\}\{FMPS\}mech}} \quad \{69\}$$

where

$$\Sigma W_{\{CR\}\{FMPS\}mech} = \Sigma W_{\{CR\}\{CGPS\}mech} \frac{\Sigma \Delta H_{\{FMPS\}}}{\Sigma \Delta H_{\{CGPS\}}} \quad \{70\}$$

The table below summarises the COP for each pumping arrangement at an average recirculation ratio of 5:

Table 11. 3 Comparison of the COP for the four pumping arrangements

Variable	CGPS	HGPS	MPS	FMPS
$\Sigma \Delta H$ [kJ]	-770141,00	-786570,00	-770458,00	-764765,00
$W_{\{CR\}\{CGPS\}mech}$ [kW]	172,80	176,49	172,87	171,59
COP	3,925	3,843	3,915	3,943

A11.9 Operating Cost Analysis for the Different Pumping Arrangements

The annual operating cost for the different pumping arrangements can then be predicted from equation (7) above as follows:

$$\text{Electrical Operating Cost per Year} = (\Sigma \dot{W}_{[CR]elec} + \Sigma \dot{W}_{[P]elec}) \times \frac{\text{Cents}}{\text{kWh}} \times \frac{\text{hr}}{\text{year}} \{71\} (7)$$

As opposed to Section 8.10 above, where a comparison of the energy efficiency of the different pumping arrangements is performed per module, for the annual electrical cost analysis presented below, the comparison is performed per unit.¹³⁰

The average industrial rate per kWh is presented in Table A6.2 of Appendix A6. The results of the annual electrical operating cost per arrangement for an average recirculation ratio of 5, and based on operating parameters measured at the ERPM plant, are summarized in the table below.

Table 11.4 Annual electrical power consumption and cost for the different pumping arrangements, at an average recirculation ratio of 5. Annual cost rounded to nearest R1,000.

Pumping Arrangement	$\dot{W}_{[CR]elec}$ [kW]	$\Sigma \dot{W}_{[P]elec}$ [kW]	Cents/kW/year	Electrical Operating Cost / Year	Difference Compared to Operating CGPS of ERPM plant
CGPS	1440,00	-	315871	R4,549,000	-
HGPS	1470,40	-	315871	R4,646,000	+ R97,000
MPS	1440,80	3,26	315871	R4,561,000	+ R12,000
FMPS	1429,60	3.64	315871	R4,528,000	- R21,000

¹³⁰ Each unit consists of eight modules.

APPENDIX A12

Sample Calculation to Support the Model of Section 9.

This section outlines a sample calculation for the analysis presented in Section 9. Where relevant, equations are numbered the same as they appear in the main body of the report in straight brackets. All property data and calculation results are obtained from EES.⁽⁴⁰⁾

Table A12.1 Variables used in the sample calculation of Section 9.

Variable	Value	Units
$c_{s[E]}(T_{r[E]build})$	452,50	J/kg.C
$c_{s[E]}(T_{r[E]har})$	7906,00	J/kg.C
$c_w(P_{atm})$	4228,00	J/kg.C
$c_l(0^\circ)$	2,041	kJ/kg.C
h_{sf}	335	kJ/kg
$h_{fg}(T_{r[E]har})$	1229000,00	J/kg
$k_{s[E]}(T_{r[E]build})$	14,31	W/m.C
$k_l(T_{r[E]build})$	1,901	W/m.C
$k_{rl}(T_{r[E]build})$	0,5773	W/m.C
$k_{rl}(T_{r[E]har})$	0,5325	W/m.C
$k_{s[E]}(T_{r[E]har})$	14,49	W/m.C
$L_{c.s[E]}$	0,00075	m
P_{atm}	83,5	kPa
$Pr_{rl}(T_{r[E]har})$	1,357	Prandtl Number
$Pr_{rl}(T_{r[E]build})$	1,442	Prandtl Number
$\rho_{rv}(T_{r[E]har})$	4,720	kg/m ³
$\rho_{rl}(T_{r[E]har})$	626,30	kg/m ³
$\rho_w(P_{atm})$	1000,00	kg/m ³

Variable	Value	Units
$\rho_{s[E]}(T_{r[E]build})$	7911,00	kg/m ³
ρ_l	920,00	kg/m ³
$\rho_{rv}(T_{r[E]build})$	2,809	kg/m ³
$\rho_{rl}(T_{r[E]build})$	646,60	kg/m ³
$\rho_{s[E]}(T_{r[E]har})$	7911,00	kg/m ³
$T_{r[E]build}$	-5.833	⁰ C
$t_{l,b}$	810	s
$T_{l,o}$	0	⁰ C
$T_{r[E]har}$	8,959	⁰ C
t_{har}	90	s
$\bar{T}_{I\{sc\}}$	2,917	⁰ C
$T_{w,i}$	1,50	kJ/kg
$\mu_{rv}(T_{r[E]build})$	0,000008877	kg/m-s
$\mu_{rl}(T_{r[E]har})$	0,0001549	kg/m-s
$\mu_{rl}(T_{r[E]build})$	0,0001815	kg/m-s
$y_{s[E]}$	1,50	mm

A12.1 Heat Transfer Model during Ice Building

Section 9. presents two heat transfer models that have been developed to predict the thickness of ice built and shed during the ice building and harvesting cycle of one module. The inputs to the models are the operating parameters measured at the ERPM plant, as well as the mass flow rate and average recirculation ratio predicted in Section 8.6.1 above.

Applying the principle of energy conservation to the control volume of Figure 9.1 above, and assuming that all thermophysical properties are independent of temperature, the heat flux from the water/ice interface to the refrigerant is

$$\dot{q}_1 = \frac{T_{I,o} - T_{r[E]build}}{\frac{1}{h'_{r[E]}} + \frac{y_{s[E]}}{k_{s[E]}(T_{r[E]build})} + \frac{y_I}{k_I(T_{r[E]build})}} \quad \{1\} (86)$$

And heat flux at the ice/water interface, based on the average external convection heat transfer coefficient for free-falling water \bar{h}'_w is

$$\dot{q}_2 = \frac{T_{w,i} - T_{I,o}}{\frac{1}{\bar{h}'_w}} \quad \{2\}(87)$$

The difference between \dot{q}_1 and \dot{q}_2 is equal to the rate at which latent heat is removed from the water per unit area, and is predicted as

$$\rho_I h_{sf} \frac{\partial y_I}{\partial t} = \dot{q}_1 - \dot{q}_2 \quad \{3\}(88)$$

To predict the average external heat transfer coefficient of water flowing over the plate, the External_Flow_Plate procedure of the EES external library is used.⁽³¹⁾ Inputs to the procedure include the free stream fluid temperature (determined from tests performed at the ERPM ice plant and shown in Appendix A6 Table A6.3), the outer ice surface temperature and pressure, as well as the free stream velocity, which is predicted to be 0,274 m/s based on tests performed at the plant (refer to Appendix A3 for this calculation). From EES⁽³¹⁾, $\bar{h}'_w = 213,70 \text{ W/m}^2.C$.

The different correlations used to predict the thickness of ice built during the ice building period is presented below, based on an average recirculation ratio of five and the mass flow rate predicted in the sample calculation for Section 8. presented above.

The mass flow rate per channel (30 channels per plate) feeding one side of one plate (35 plates per module) is:

$$\dot{m}_{r[PD-E]chl} = \frac{\dot{m}_{r[PD-E]}}{35 \times 30 \times 2} = \frac{3,363}{2100} = 0,0016 \text{ kg/s} \quad \{4\}$$

Each channel through which the refrigerant flows feeds both sides of one plate; therefore the cross sectional area of one channel feeding both sides of the plate, based on Figure 9.2 is:

$a_{[E]chl} = (0,035 - 2 \times 0,0015)(0,01 - 2 \times 0,0015) = 0,000224 \text{ m}^2$. For the purpose of this analysis, even though the shape of the channels of the plate through which refrigerant flows is elliptical, they are modelled as a vertical tube with the same cross sectional area, and serving both sides of the plate. It is recalled that there are 35 plates per module and 30 channels per plate. If it is assumed that the refrigerant flows uniformly through each channel, each channel is in effect two sub channels - serving opposite sides of the plate. Thus the refrigerant mass flow can be considered as being split among sixty channels. This assumption facilitates the analysis presented in equations (86), (87), (88) and (96) where it is assumed in these equations that ice is built on one side of the plate.

The results presented below therefore apply for one sub-channel feeding one side of the plate.

$$\frac{\pi D^2}{4} = \frac{a_{[E]chl}}{2} \quad \therefore D = 0,012 \text{ m.} \quad \{5\}$$

The mean mass flux, G , is therefore:

$$G = \frac{\dot{m}_{r[PD-E]}}{\frac{\pi D^2}{4}} = 14,16 \text{ kg/m}^2 \cdot \text{s} \quad \{6\}$$

A12.1.1 The Shah Correlation

The Shah coefficient employs four dimensionless coefficients. The ratio of the heat transfer coefficients of the two-phase flow $h'_{2ph[Sh]}$ and the superficial liquid flow h'_l is denoted as:

$$\psi = h'_{2ph[Sh]} / h'_l \quad \{7\}(89)$$

Where the superficial heat transfer coefficient of the liquid phase h'_l is calculated by the Dittus-Boelter equation as:

$$\begin{aligned} h'_l &= 0,023 \left(\frac{G(1-x')D}{\mu_{rl}(T_{r[E]build})} \right)^{0,8} Pr_{rl}^{0,4}(T_{r[E]build}) \frac{k_{rl}(T_{r[E]build})}{D} \\ &= 0,023 \left(\frac{14,16(1-0,2)0,012}{0,0001815} \right)^{0,8} 1,442^{0,4} \frac{0,5773}{0,012} = 255,20 \text{ W/m}^2 \cdot \text{C} \end{aligned} \quad \{8\}(90)$$

where G is the mean mass flux on the cross-section of the tube, D is the internal diameter of the tube, μ_{rl} is the dynamic viscosity liquid ammonia at $T_{r[E]build}$, x' is the vapour quality, k_{rl} is the thermal conductivity of the liquid, and Pr_{rl} is the Prandtl number, both at $T_{r[E]build}$. The ratio ψ is dependent on the convection number Co , and the boiling number Bo :

$$\begin{aligned} Co &= \left(\frac{1}{x'} - 1 \right)^{0,8} \left(\frac{\rho_{rv}(T_{r[E]build})}{\rho_{rl}(T_{r[E]build})} \right)^{0,5} = 4^{0,8} \left(\frac{2,809}{646,6} \right)^{0,5} = 0,1998 \\ Bo &= \frac{\dot{q}_1}{Gh_{fg}(T_{r[E]build})} = \left(\frac{T_{I.o} - T_{r[E]build}}{\frac{1}{h'_{2ph[Sh]} + \frac{y_{s[E]}}{k_{s[E]}(T_{r[E]build})} + \frac{y_I}{k_I(T_{r[E]build})}} \right) \frac{1}{14,16 \times 1282} = 0,00008503 \end{aligned} \quad \{9\}(91)$$

Where \dot{q}_1 is the heat flux from the water/ice interface to the refrigerant and is predicted by substituting the Shah correlation $h'_{2ph[Sh]}$ into $h'_{r[E]}$ of equation (86) above.

Finally, the value of ψ in the bubble suppression regime based on, and at various values of Co is:

$$\psi_{bs} = 15,43Bo^{0,5} \exp(2,47Co^{-0,15}) = 3,557 \quad \{10\}(92)$$

And in the convective boiling regime:

$$\psi_{cb} = \frac{1,8}{Co^{0,8}} \quad \{11\}(92b)$$

The larger of ψ_{bs} or ψ_{cb} is substituted into equation (89) to obtain $h'_{2ph[Sh]}$.

Therefore $h'_{2ph[Sh]} = 1666,00 \text{ W/m}^2 \cdot \text{C}$.

This model is compared to the flow boiling in a vertical tube procedure in EES⁽³⁴⁾, which is based on the Shah⁽²⁶⁾ correlation and considers both nucleate and convective boiling conditions. The governing equations of the EES⁽³⁴⁾ procedure are not provided, however it is used as a comparison to the Shah correlation as well as to the Gungor-Winterton model developed below. The final correlation predicted by EES⁽³⁴⁾ is $h'_{2ph[EES]} = 221,00 \text{ W/m}^2 \cdot \text{C}$.

A12.1.2 The Gungor-Winterton Correlation

A third model used to predict the refrigerant side convective boiling heat transfer coefficient is that of Gungor & Winterton,⁽²⁸⁾ who calculated the boiling heat transfer coefficient for various fluids at saturated and subcooled boiling conditions.

Gungor & Winterton⁽²⁸⁾ divided the heat transfer into two parts, a microconvective (nucleate boiling) contribution based on pool boiling, and a macroconvective contribution (non-boiling forced convection), based on the famous Dittus-Boelter equation (equation (90) above). The following is the form of the correlation to predict the convective boiling heat transfer coefficient of ammonia and other refrigerants in vertical tubes:

$$h'_{2ph[G]} = Eh'_l + Sh'_p \quad \{12\} (93)$$

where

$$\begin{aligned} h'_l &= 0,023 \left(\frac{G(1-x')D}{\mu_{rl}(T_{r[E]build})} \right)^{0,8} Pr_{rl}^{0,4} (T_{r[E]build}) \frac{k_{rl}(T_{r[E]build})}{D} \\ &= 0,023 \left(\frac{14,16(1-0,2)0,012}{0,0001815} \right)^{0,8} 1,442^{0,4} \frac{0,5773}{0,012} = 255,20 \text{ W/m}^2 \cdot \text{C} \end{aligned}$$

$$\begin{aligned}
 h'_p &= 55 Pr_{rl}^{0.12} (T_{r[E]build}) [\log_{10} Pr_{rl} (T_{r[E]build})]^{-0.55} m_m^{-0.5} \dot{q}_1^{0.67} \\
 &= 55 \cdot 1,442^{0.12} [\log_{10} 1,442]^{-0.55} 17,03^{-0.5} \dot{q}_1^{0.67} = 5242,00 \text{ W/m}^2 \cdot \text{C}
 \end{aligned}
 \tag{13}(94)$$

Here, m_m is the molecular weight of the fluid, which in the case of ammonia, is 17.03.⁽³⁾ \dot{q}_1 of equation (86) is predicted using the Gungor-Winterton correlation. In equation (93) above, the enhancement factor, E , takes into account the two-phase nature of the refrigerant. The final values for E and S (suppression factor) make use of the boiling number, Bo from Shah⁽²⁶⁾ and the Lockhart-Martinelli parameter X_{tt} in equation (95b) below:

$$\begin{aligned}
 E &= 1 + 24000 * Bo^{1.16} + 1,37 * (1 / X_{tt})^{0.86} = 1 + 24000 \cdot 0,00008503^{1.16} + 1,37 \cdot \left(\frac{1}{0,3104}\right)^{0.86} = 5,203 \\
 S &= \frac{1}{1 + 1.15 * 10^{-6} E^2 \left(\frac{G(1-x')D}{\mu_{rl}(P_{r[E]build})}\right)^{1.17}} = \frac{1}{1 + 1.15 * 10^{-6} 5,203^2 \left(\frac{14,16(1-0,2)0,012}{0,0001815}\right)^{1.17}} = 0,933
 \end{aligned}
 \tag{14}(95)$$

where

$$X_{tt} = \left| \left(\frac{\rho_{rv}}{\rho_{rl}}\right)^{0.5} \left(\frac{\mu_{rl}}{\mu_{rv}}\right)^{0.1} \left(\frac{1-x'}{x'}\right)^{0.9} \right|_{T_{r[E]build}} = \left(\frac{2,809}{646,6}\right)^{0.5} \left(\frac{0,0001815}{0,000008877}\right)^{0.1} \left(\frac{1-0,2}{0,2}\right)^{0.9} = 0,3104
 \tag{15}(95b)$$

Finally, $h'_{2ph[G]} = Eh'_l + Sh'_p = 5,203 \cdot 255,20 + 0,933 \cdot 5242,00 = 6219,00 \text{ W/m}^2 \cdot \text{C}$

The three correlations described above¹³¹ are used to predict the refrigerant side convective boiling heat transfer coefficient h'_r in equation (86) above.

¹³¹ That of Shah, EES and Gungor-Winterton.

A12.1.3 Predicting the Layer of Ice Built during the Ice Building Period

Predicting the Time Required for the Steel Wall to reach Ice Building Temperature during the Re-Cooling Sub-Period¹³²

Before the heat transfer model during ice building can be presented, the time required to re-cool the outer wall of the evaporator plate to evaporating temperature, which occurs at the beginning of the re-cooling sub-period of the harvesting period - before feed water is introduced and ice starts to build - is predicted. Three predictions of the convective boiling heat transfer coefficient are used, based on Shah (equation (89)), Gungor & Winterton (equation (91)) and EES.⁽³⁴⁾ It is assumed (and validated below from predictions of the model during the warming sub-period of the harvesting period) that at the end of the warming sub-period, the inner steel wall reaches saturated harvesting temperature $T_{r[E]har}$.

Using the one-term approximation of the Fourier series for transient heat conduction⁽²⁴⁾, and verifying the results with the corresponding one-term procedure in EES⁽⁴⁰⁾, the transient response of a semi-infinite plate with the inner wall exposed to convection and the outer wall adiabatic is predicted. Assuming all steel properties (density, specific heat etc) are uniform and constant at evaporating temperature, the mid-point temperature of the evaporator's steel wall is predicted based on the Fourier and Biot numbers as follows:

$$\begin{aligned}
 B_i &= \frac{h'_r L_{c.s[E]}}{k_{s[E]} (T_{r[E]build})} \\
 \alpha_s &= \left[\frac{k_{s[E]}}{\rho_{s[E]} c_{s[E]}} \right]_{(T_{r[E]build})} \\
 F_o &= \frac{\alpha_s t_{I.b}}{L_{c.s[E]}} \\
 \frac{(T_{s[E]} - T_{r[E]build})}{(T_{r[E]har} - T_{r[E]build})} &= C e^{-\xi^2 F_o}
 \end{aligned}
 \tag{16}(96)$$

¹³² This period is defined in Section 8.2.2 and by the dashed rectangle between $(t_3 - t_2)$ in the timing diagram of Figure 3.2

Where for a plane wall, the values of C and ξ are functions of Biot number only:

$$\begin{aligned} (\xi) \tan(\xi) &= B_i \\ C &= \frac{4 \sin(\xi)}{2(\xi) + \sin(2(\xi))} \end{aligned} \quad \{17\}(97)$$

Inputting the known variables into equations (96) and (97) above and solving for the mid-point steel wall temperature $T_{s[E]}$, the change in temperature over time at the mid-point of the steel wall can be predicted. The results from the EES⁽⁴⁰⁾ procedure mentioned above for the different heat transfer correlations, and for an ice building period $t_{l,b}$ of 810 seconds, are summarised in the table below.

Table A12.2 Mid-point steel wall temperatures

Heat Transfer Coefficient Used [W/m ² .C]	B_i	F_o	$T_{s[E]}$ [°C]
$h'_{2ph[G]}$	0,6593	1423,00	-5,833
$h'_{2ph[Sh]}$	0,1766	1423,00	-5,833
$h'_{2ph[EES]}$	0,0234	1423,00	-5,833

Referring to Figure 9.3 of Section 9.1 above, both the Shah and Gungor-Winterton correlations predict that the mid-point of the steel wall reaches evaporating temperature within 20 seconds from the beginning of the re-cooling sub-period. The EES correlation predicts that the mid-point of the wall approaches $T_{r[E]build}$ only after 150 seconds.

The values of the convective boiling heat transfer coefficient, together with the thickness of ice built that is predicted from equation (88) by inputting these coefficients into equation (86) above, is shown in the table below (Table 9.2 of Section 9.1 above). Equation (88) is then solved numerically in EES.

Table A12.3 Parameters predicted from the heat transfer model during ice building

h'_r [W/m ² .C]	$h'_{2,ph[G]}$ [W/m ² .C]	$h'_{2,ph[Sh]}$ [W/m ² .C]	$h'_{2,ph[EES]}$ [W/m ² .C]
Final values	6219,00	1666,00	221,00
Final predicted thickness of ice built $y_{L,b}$	6,67 mm	5,84 mm	2,11 mm
% Difference: $y_{L,b}$	0%	12,37 %	68,37 %

A12.2 Heat Transfer Model during the Warming Sub-Period of the Harvesting Period

As with the ice building period, predicting the refrigerant side convective condensing heat transfer coefficient during the warming sub-period of the harvesting period¹³³ is complex. The transient nature of the warming sub-period makes it difficult to model accurately, as well as to corroborate with experimental data. Nonetheless, the following model attempts to predict the thickness of ice melted $y_{L,m}$ over the warming sub-period based on fundamental heat transfer analysis, assuming that the ice sheet falls off the plate only at the end of the this period.

“Harvesting” or ice shedding is achieved by passing hot refrigerant gas at harvesting pressure $P_{r,har}$ through the channels in the plate. As the ice layer is sub-cooled, the assumptions listed in Section 9.2 above are made in order to develop the fundamental equations.

A12.2.1 Predicting the Evaporator Steel Temperature Distribution during the Warming Sub-Period

Assuming that the steel wall can be modelled as a semi-infinite plate, is insulated adiabatically on one side (outer wall) by the ice layer, and exposed to the refrigerant at harvesting pressure and temperature on the inside, the one-term approximation of the Fourier series for transient heat conduction⁽²⁴⁾ can be used to

¹³³ This period is defined in Section 8.2.1 and by the hatched rectangle between $(t_2 - t_1)$ in the timing diagram of Figure 3.2 above.

predict the time required for the outer wall to reach 0°C. All steel properties (density, specific heat etc) are assumed uniform and constant at harvesting temperature $T_{r[E]har}$. As for the transient conduction model during ice building of Section 9.1 above, results are compared to and verified with the one-term procedure in EES.⁽⁴⁰⁾ The Biot and Fourier numbers during harvesting are predicted as:

$$\begin{aligned}
 B_i &= \frac{h'_{r.har} L_{c.s[E]}}{k_{s[E]} (T_{r[E]har})} \\
 \alpha_s &= \left[\frac{k_{s[E]}}{\rho_{s[E]} c_{s[E]} (T_{r[E]har})} \right] \\
 F_o &= \frac{\alpha_s t_{har}}{L_{c.s[E]}^2} \\
 \frac{(T_{s[E]har} - T_{r[E]har})}{(T_{r[E]build} - T_{r[E]har})} &= C e^{-\xi^2 F_o}
 \end{aligned}
 \tag{18}(98)$$

Where for a plane wall, the values of C and ξ are functions of Biot number only:

$$\begin{aligned}
 (\xi) \tan(\xi) &= B_i \\
 C &= \frac{4 \sin(\xi)}{2(\xi) + \sin(2(\xi))}
 \end{aligned}
 \tag{19}(99)$$

The refrigerant side convection condensing heat transfer coefficient $h'_{r.har}$ is derived below. Inputting the known variables into equations (98) and (99) above ($h'_{2ph[Nu]\{c\}}$ is substituted into equation (99)), the results for the inner and outer steel wall temperature, from the EES⁽⁴⁰⁾ procedure mentioned above and for a harvesting period t_{har} of 90 seconds, are summarised in the table below.

Table A12.4 Inner and outer wall temperatures at the end of the harvesting period

Heat Transfer Coefficient Used [W/m ² .C]	B_i	F_o	$T_{s[E]}$ At Inner Wall [°C]	$T_{s[E]}$ At Outer Wall [°C]
$h'_{2ph[Nu]\{c\}}$	0,436	158,10	8,895	2,450

A12.2.2 Predicting the Temperature reached by the Melted Ice Layer at the end of the Warming Sub-Period

Now, based on a suggestion of Bailey-McEwan⁽³⁵⁾, the above assumption is disregarded¹³⁴, and it is assumed that only the melted ice layer loses its sub-cooling prior to melting, whilst the remaining ice layer retains all of its sub-cooling. This melted ice layer which has turned to water (reaching temperatures of $T_{I.m.har}$ (initially at zero degrees) at the end of the warming sub-period), would now act as an additional conductive resistance to heat flow, absorbing heat from the wall at one end, whilst being cooled by the remaining ice layer at the other, as illustrated in Figure 9.10 above. Thus it must be assumed that even though a layer of water is stationary between the remaining ice layer and the wall, only at the end of the warming sub-period does the ice sheet detach itself from the wall. As mentioned above, this assumption is based on Senatore⁽⁴⁾ who predicted that the ice sheet would remain in position due to “stiction” between the sheet and the steel evaporator wall.

Modifying the heat balance equation of the control volume shown in Figure 9.10 to include conduction from the plate wall through the melted ice layer to the remaining ice sheet, the temperature change of the melted ice layer ($T_{I.m.har}$) at the end of the warming sub-period can be predicted by solving the following equation:

$$-\left[\rho_w c_w\right]_{T_{I.o}} y_{I.m} \frac{\partial T_{I.m.har}}{\partial t} = -k_s (T_{r\{E\}har}) (\bar{T}_{s\{E\}har} - T_{I.m.har}) + k_I (\bar{T}_{I\{sc\}}) (T_{I.m.har} - \bar{T}_{I\{sc\}}) \quad \{20\}(100)$$

Where $\bar{T}_{I\{sc\}}$ and $\bar{T}_{s\{E\}har}$ is the average temperatures of the linearly sub-cooled ice layer, and the wall temperature during harvesting $\bar{T}_{s\{E\}har}$ is assumed to be the average of the inner and outer wall temperatures as shown in the table above.

¹³⁴ That the inner ice layer only begins melting once the entire ice sheet has lost its sub-cooling.

As the melted ice layer's thickness $y_{I,m}(t)$ is a function of time, the equation above is solved simultaneously with equations (98), (104) and (105) below. The solution of equation (100) over the entire warming sub-period of 90 seconds, is shown in the Figure 9.11 of Section 9.2.2 above.

Applying the principle of energy conservation to the control volume of Figure 9.10 of Section 9.2.2 above, and assuming that all thermophysical properties are independent of temperature, the heat flux from the refrigerant to the melted ice layer is

$$\dot{q}_1 = \frac{(T_{r[E]har} - T_{I,m.har})}{\frac{1}{h'_{r.har}} + \frac{y_{s[E]}}{k_{s[E]}(T_{r[E]har})} + \frac{y_{I,m}}{k_w(T_{I,m.har})}} \quad \{21\}(101)$$

And the heat flux at the melted / remaining ice layer interface, based on the average sub-cooled temperature of the remaining layer is

$$\dot{q}_2 = \frac{(T_{I,m.har} - \bar{T}_{I\{sc\}})}{\frac{y_{I,b} - y_{I,m}}{k_I(\bar{T}_{I\{sc\}})}} \quad \{22\} (102)$$

The difference between \dot{q}_1 and \dot{q}_2 is equal to the rate at which ice is melted and warmed per unit area, and is predicted as

$$\rho_I h_{sf} \frac{\partial y_{I,m}}{\partial t} = \dot{q}_1 - \dot{q}_2 \quad \{23\}(103)$$

The final heat transfer equation during the warming sub-period of the harvesting process, including the melted ice layer at $T_{I,m.har}$, and the ice layer at $\bar{T}_{I\{sc\}}$ is

$$\rho_I h_{sf} \frac{\partial y_{I,m}}{\partial t} = \frac{(T_{r[E]har} - T_{I,m.har})}{\frac{1}{h'_{r.har}} + \frac{y_{s[E]}}{k_{s[E]}(T_{r[E]har})} + \frac{y_{I,m}}{k_w(T_{I,m.har})}} - \frac{(T_{I,m.har} - \bar{T}_{I\{sc\}})}{\frac{y_{I,b} - y_{I,m}}{k_I(\bar{T}_{I\{sc\}})}} \quad \{24\}(104)$$

Where $y_{l,b}$ is the thickness of the ice sheet that is built during the ice building period and is predicted in Table 9.2 of Section 9.1 above to be 6,31 mm (which is the average thickness of ice built from the Gungor-Winterton and Shah correlations). Equation (104) is integrated over the 90 second harvesting period and solved numerically in EES, simultaneously with equations (98), (100) and (105). The various convective condensation vertical-tube heat transfer coefficients predicted in the above models are substituted into $h'_{r,har}$ of equation (104) above, and the results are shown in Figure 9.13 of Section 9.2.5. Table 9.3 of the same section, summarising the thickness of ice melted based on the different correlations, is reproduced below.

A12.2.3 Predicting the Mass Flow Rate of Harvesting Gas during the Warming Sub-Period

To predict the convective condensing heat transfer coefficients described below, it is first necessary to predict the mass flow rate of harvesting gas during the warming sub-period. It is recalled from equation (28) of Section 8.2.1 above that the final energy rate balance equation for the control volume of Figure 8.3 is:

$$\begin{aligned} \Delta U_{s[E]} + \Delta U_{rl,trap[E]} + \Delta U_{rv,trap[E]} = Q_{cv} + \Delta m_{rv[REC-E]} h_{rv}(P_{r,har}, T_{r,har}) \\ - \Delta m_{rl,cont[E-ACC]} h_{rl}(P_{r[E]har}, T_{rl[E-ACC]}) \quad \{25\} (28) \\ - m_{rl\{c\}} h_{rl}(P_{r[E]har}, \bar{T}_{r\{c\}}) \end{aligned}$$

where the internal energy gains on the left-hand side of the equation are:

$\Delta U_{s[E]}$: of the steel of the evaporator plates and their inlet and outlet manifolds;

$\Delta U_{rl,trap[E]}$: of the refrigerant liquid in the plates and manifolds; and

$\Delta U_{rv,trap[E]}$: of the refrigerant vapour confined in the plates between the beginning and the end of harvesting.

The heat transfer across the control volume Q_{cv} is that required to melt the innermost layer of ice and to release its sub-cooling. As the additional heat transfer

required to warm this melted ice layer to $T_{I,m.har}$ is an assumption and could not be verified by testing at the operating plant, it is not considered in Q_{cv} . Furthermore, the specific heat of water is considered negligible when compared to the latent heat of fusion of ice formation (4,186 kJ/kg.C and 335,0 kJ/kg respectively). Therefore, to retain consistency between the models of Section 8. and Section 9.1, and *only* for the purpose of predicting the mass flow rate of harvesting gas, it is assumed that the ice detaches from the steel wall once it reaches 0 °C as opposed to $T_{I,m.har}$.

The remaining variables are defined in Section 8.2.1 above. The final form of equation (28) over the warming sub-period of 90 seconds is:

$$\begin{aligned}
& m_{s[E]} c_s (P_{r[E]}) [T_{sat}(P_{r[E]har}) - T_{sat}(P_{r[E]build})] \\
& + (0,05V_{[E]} \rho_{rl}(P_{r[E]har}))_{(t2)} u_{rl}(P_{r[E]har}) - (0,30V_{[E]} \rho_{rl}(P_{r[E]build}))_{(t1)} u_{rl}(P_{r[E]build}) \\
& + (0,95V_{[E]} \rho_{rv}(P_{r[E]har}))_{(t2)} u_{rv}(P_{r[E]har}) - (0,70V_{[E]} \rho_{rv}(P_{r[E]build}))_{(t1)} u_{rv}(P_{r[E]build}) \\
& = -2n \rho_I a_{[E]} y_{I,m} (h_{sf} - c_I (\frac{T_{r[E]build} + T_{I,o}}{2}) + \Delta m_{rv[REC-E]} h_{rv}(P_{r.har}, T_{r.har}) \\
& - \Delta m_{rl.cont[E-ACC]} h_{rl}(P_{r[E]har}, T_{r[E-ACC]}) - m_{rl\{c\}} h_{rl}(P_{r[E]har}, \bar{T}_{r\{c\}})
\end{aligned} \tag{26}(105)$$

where the number of plates per module denoted n is 35. The variables in the above equation are all defined in the sample calculation presented above and therefore only the solution to the equation is presented below. As the melted ice layer $y_{I,m}(t)$ is a function of time, the equation above is solved simultaneously with equations (98), (100) and (104) by substituting $h'_{2ph[Nu]\{c\}}$ (presented below) into the relevant equations.

Solving the above equation into yields the mass of gas from the condensed liquid receiver introduced at the inlet of the evaporator during the warming sub-period $\Delta m_{rv[REC-E]}$. The mass flow rate of the harvesting gas per module is therefore:

$$\dot{m}_{rv[REC-E]} = \frac{\Delta m_{rv[REC-E]}}{t_{har}} = 117,90 \text{ kg/s} \tag{27}(106)$$

And per channel (there are 30 channels per plate) feeding one side of the plate, the mass flow rate is:

$$\dot{m}_{rv[REC-E]chl} = \frac{\Delta m_{rv[REC-E]}}{t_{har} \times n \times 30 \times 2} = 0,0006235 \text{ kg/s} \quad \{28\}(107)$$

Recall that the equivalent diameter of the tube, D , based on half the cross sectional area of the channel, is:

$$\frac{\pi D^2}{4} = \frac{a_{[E]chl}}{2} \quad \therefore D = 0,012 \text{ m.}$$

Therefore, the mean mass flux, G , is:

$$G = \frac{\dot{m}_{rv[REC-E]chl}}{\frac{\pi D^2}{4}} = 5,513 \text{ kg/m}^2 \cdot \text{s}$$

A12.2.4 Predicting the Refrigerant Side Convective Condensing Heat Transfer Coefficient

The Shah Correlation for Film Condensation inside Vertical Pipes

Shah⁽²⁹⁾ modified his two phase convective boiling heat transfer coefficient⁽²⁶⁾ model developed in Section 9.1 above to apply to film condensation inside vertical pipes.

$$\psi_{har} = \frac{h'_{2ph[Sh]\{c\}}}{h'_1} \quad \{29\} (108)$$

Here, $h'_{2ph[Sh]\{c\}}$ is the Shah⁽²⁹⁾ two phase convective condensing heat transfer coefficient, and the superficial heat transfer coefficient of the liquid phase only h'_1 is calculated by the Dittus-Boelter equation to predict the heat transfer coefficient

- assuming all the mass flowing as a liquid. The mass flow rate, predicted from equation (105), depends on the thickness of ice melted. Therefore, different coefficients will yield different mass flow rates, and different mass fluxes. The Shah correlation presented below is therefore obtained by substituting $h'_{2ph[Sh]\{c\}}$ into equations (98), (100), (104) and (105).

The mean mass flux for the Shah correlation is:

$$G = \frac{\dot{m}_{rl[REC-E]chl}}{\frac{\pi D^2}{4}} = 4,387 \text{ kg/m}^2 \cdot \text{s} \quad \{30\}$$

$$\begin{aligned} h'_{l\{c\}} &= 0,023 \left(\frac{GD}{\mu_{rl}(T_{r[E]har})} \right)^{0,8} Pr_{rl}^{0,4} (T_{r[E]har}) \frac{k_{rl}(T_{r[E]har})}{D} \\ &= 0,023 \left(\frac{4,387 \cdot 0,012}{0,0001549} \right)^{0,8} 1,357^{0,4} \frac{0,5325}{0,012} = 122,20 \end{aligned} \quad \{31\} \{109\}$$

$$h'_1 = h'_{l\{c\}} (1 - x'_{har})^{0,8} = 70,19 \text{ W/m}^2 \cdot \text{C} \quad \{32\} \{110\}$$

where x'_{har} is the thermodynamic vapour quality of the harvesting gas, assumed to be an average value of 0,5 as per Shah⁽²⁹⁾. The ratio ψ_{har} is dependent on the condensing convection number Co_{har} :

$$Co_{har} = \left(\frac{1}{x'_{har}} - 1 \right)^{0,8} \left| \frac{\rho_{rv}}{\rho_{rl}} \right|_{T_{r,har}}^{0,5} = 0,08681 \quad \{33\} \{111\}$$

$$\psi_{har} = \frac{1,8}{Co_{har}^{0,8}} = 12,72 \quad \{34\} \{112\}$$

$h'_{2ph[Sh]\{c\}}$ is predicted by substituting equation (108) into equation (112), yielding

$$h'_{2ph[Sh]\{c\}} = 892,60 \text{ W/m}^2 \cdot \text{C}.$$

Shah further states that “in the process of condensation, liquid will be formed whenever vapour contacts the pipe surface and thus the pipe circumference will always be wetted at all flow rates and in all flow orientations. Hence (the above) equation may be expected to apply to condensation in all flow orientations with

minimum modification.”⁽²⁹⁾ A major assumption of this model is that vapour quality variation is linear with channel length, $L_{[E]chl}$. Shah⁽²⁹⁾ simplifies equation (108) where saturated vapour enters the tube and saturated liquid exits the tube to one term if the arithmetic mean quality, x'_{har} of 0,5 is used:

$$\bar{h}'_{2ph[Sh]\{c\}} = h'_{l\{c\}} \left(0,55 + \frac{2,09}{Pr_{rl}^{0,38} (T_{r[E]har})} \right) \quad \{35\} \quad (113)$$

As mentioned above, all equations must be solved based on the correlation used, and therefore values of the previously predicted variables will differ somewhat for the different correlations.

$$\bar{h}'_{2ph[Sh]\{c\}} = h'_{l\{c\}} \left(0,55 + \frac{2,09}{Pr_{rl}^{0,38} (T_{r[E]har})} \right) = 75,41 \left(0,55 + \frac{2,09}{1,357^{0,38}} \right) = 181,80 \text{ W/m}^2 \cdot \text{C} \quad \{36\}$$

The Nusselt Equation for Flow in Vertical Tubes

A theoretical correlation for flow in vertical tubes, based on Nusselt's equation for film condensation⁽²⁷⁾ is developed as a comparison to both Shah⁽²⁹⁾ correlations presented above. This correlation can be used for film condensation at the inner or outer walls of vertical tubes if the tube diameter is large compared to the film thickness (which in this case is true). The average steel wall temperature $\bar{T}_{s[E]har}$, predicted from equation (98) above, is used in this correlation.

$$\begin{aligned} h'_{2ph[Nu]\{c\}} &= 0,943 \left[\frac{h_{fg} g (\rho_{rl} - \rho_{rv}) k_{rl}^3}{L_{[E]chl} (T_{r[E]har} - \bar{T}_{s[E]har}) \frac{\mu_{rl}}{\rho_{rl}}} \right]_{T_{r[E]har}}^{\frac{1}{4}} \\ &= 0,943 \left[\frac{1229000,00 \cdot 9,81(626,30 - 4,720)0,5325^3}{3,5(8,959 - 5,673) \frac{0,0001549}{626,30}} \right]^{\frac{1}{4}} = 4211,43 \text{ W/m}^2 \cdot \text{C} \end{aligned} \quad \{37\} \quad (114)$$

The melted ice layer over time is plotted in Figure 9.13 by inputting the three vertical tube convective condensing heat transfer coefficients into equation (104) above. The values of ice melted at the end of 90 seconds is summarised in the table below.

Table A12.6 Convection condensing heat transfer coefficients and corresponding thickness of melted ice layer

$h'_{r.har}$ [W/m ² .C]	$h'_{2ph\{Nu\}\{c\}}$ [W/m ² .C]	$h'_{2ph\{Sh\}\{c\}}$ [W/m ² .C]	$\bar{h}'_{2ph\{Sh\}\{c\}}$ [W/m ² .C]
Final values	4211	893	182
Final predicted thickness of melted ice layer $y_{L,m}$ [mm]	1,149	0,786	0,143
% Difference: $y_{L,m}$	0 %	31,63 %	87,54 %

Figure 9.13 of Section 9.2.5 above is based on the assumption that the ice melts for the entire harvesting period of 90 seconds. Therefore, if it is assumed conservatively¹³⁵, based on observations of the harvesting process at the plant, that the valve change-over time, plus the time required to expel the liquid to the accumulator and the time required to heat up the steel wall to zero degrees at its outer surface takes up half of the warming sub-period of 90 seconds, the final melted ice thickness on one side of the plate is summarised in the table below (reproduced from Table 9.4 above).

Table A12.7 Convective condensing heat transfer coefficients thickness of melted ice for a harvesting time of 45 seconds

$h'_{r.har}$ [W/m ² .C]	$h'_{2ph\{Nu\}\{c\}}$ [W/m ² .C]	$h'_{2ph\{Sh\}\{c\}}$ [W/m ² .C]	$\bar{h}'_{2ph\{Sh\}\{c\}}$ [W/m ² .C]
Final values	4179	1435	343
Final predicted thickness of melted ice layer $y_{L,m}$ [mm]	0,877	0,651	0,226
% Difference: $y_{L,m}$	0 %	25,82%	74,20 %

From Section 9.2.5: From Table 9.3 and Table 9.4 (of Section 9.2) above, if the harvesting time is halved, the thickness of ice melted decreases by only 17 % for $h'_{2ph\{Sh\}\{c\}}$, and increases by 58 % for $\bar{h}'_{2ph\{Sh\}\{c\}}$. Although this seems counter-

¹³⁵ This assumption should be considered a lower limit of the thickness of ice melted, with the predictions shown in Table A12.6 above considered as an upper limit.

intuitive, as mentioned above, the Shah⁽²⁹⁾ correlations are dependent on the mass flow rate of harvesting gas, which increases as harvesting time decreases. Therefore the decreased harvesting period that the warm gas is in contact with the steel evaporator wall is offset by the increased convective condensing heat transfer coefficients for these correlations. The Nusselt correlation $h'_{2ph[Nu]\{c\}}$ however is not as dependent on mass flow rate, although it is solved simultaneously with the mass flow rate during the warming sub-period of equation (105). Based on this correlation, the upper and lower limit of thickness of ice melted is 1,149 and 0,877 mm respectively, which constitutes a 24 % difference. For the model developed in Section 8. above, a mean value for the thickness of ice melted of 1,00 mm is assumed when predicting the URD associated with the building of the subsequently melted ice layer. Thus this assumption of melted ice layer thickness is substantiated and is further corroboration of the mass flow rate and average recirculation ratio required to build the entire ice layer that is predicted in Sections 8. and 9.1.

APPENDIX A13

Analysis to Prove the Simplified Control-Volume Thermodynamic Analysis of Gas and Mechanically Pumped Arrangements in Section 7.2.3

The analysis presented below proves that any URDs generated at the pumper drum during the pumping and filling periods of the CGPS can be considered *inherent* URDs.

Table A13.1 Variables used in the analysis presented below

Variable	Value	Units
$c_s(T_{r[PD-]})$	0,4533	kJ/kg.C
$h_{rv}(T_{r[ACC]})$	1451,00	kJ/kg
$h_{rl}(T_{r[ACC]})$	158,80	kJ/kg
$h_{r[REC]o}(T_{r[REC]})$	336,8	kJ/kg
$h_{rv}(P_{r[REC]})$	1485,00	kJ/kg
$h_{rv}(P_{r[ACC]})$	1451,00	kJ/kg
$h_{rl}(T_{r[PD-]})$	177,80	kJ/kg
$h_{rl[PD+]i}(T_{r[PD+]})$	234,60	kJ/kg
$h_{rv[PD+]i}(T_{r[PD+]})$	1469,00	kJ/kg
$h_{rl}(T_{r[E]})$	173,00	kJ/kg
$h_{rv}(P_{r[PD+]})$	1469,00	kJ/kg
$h_{rv}(P_{r[PD+]})$	1456,00	kJ/kg
$L''_{[PD]}$	4,2	m
$m_{s[PD]}$	2867	kg
P_{atm}	83,5	kPa
$\rho_{rv}(T_{r[PD+]})$	4,492	kg/m ³
$\rho_{rl}(P_{r[ACC]})$	650,70	kg/m ³

Consider the modified pressure-enthalpy diagram, from Figure A1.2, of the CGPS which depicts the processes in Figure 7.2 during pumping in the pumper drum.

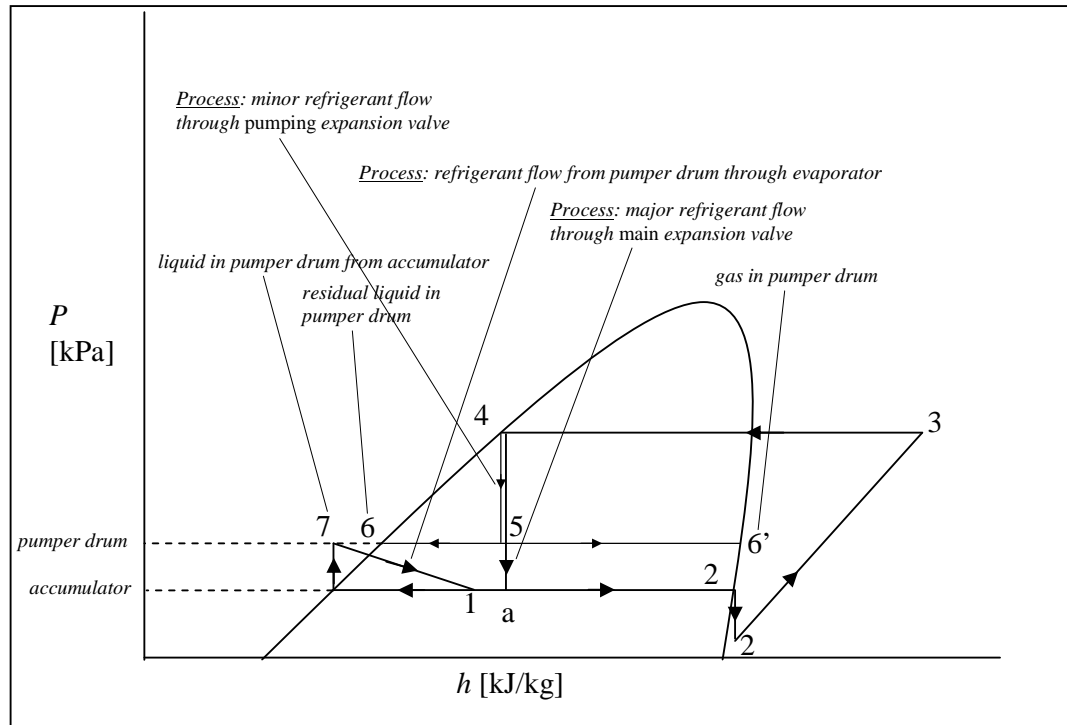


Figure A13.1 Cold Gas Pumped System: Processes during Pumping in the Pumper Drum

In Figure A13.1, the process through the *pumping* expansion valve has small arrows – denoting the *minor* flow of condensed liquid through this expansion valve to the pumper drum. In this figure, it is seen that:

- the major refrigerant flow through the main expansion valve drops (as for the mechanically pumped system) all the way from condensed liquid pressure to accumulator pressure;
- the minor refrigerant flow through the pumping expansion valve drops from condensed liquid pressure to pumping pressure.

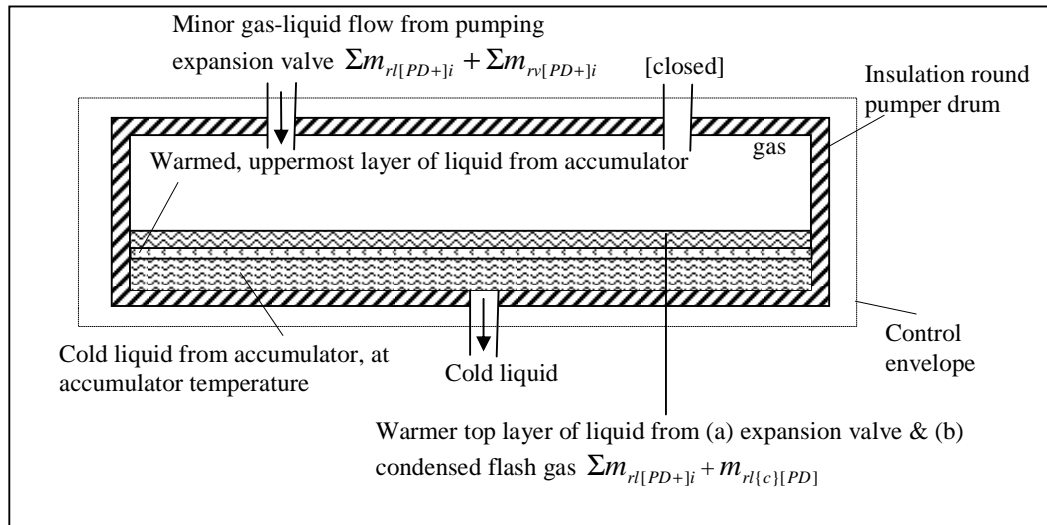


Figure A13. 2 Interior of pumper drum during pumping

Now, for the control envelope around the pumper drum of the CGPS as shown in Figure 7.1 above, the following analysis is performed to prove that all the URDs generated over a complete pressurising and venting period of one pumper drum amount to (add up to) the *inherent* URD of needing to compress the flash gas generated in expanding liquid down from the condensed liquid receiver to accumulator pressure (4 – a in Figure 1.).

From Figure A8.7 of Appendix A8, and Figure A13.2 above, at the end of the pumping period, the liquid in the pumper drum occupies a volume of the pumper drum referred to as the residual layer, which contains:

- (a) flash gas at pumping pressure;
- (b) a warmer, top layer of liquid, comprising:
 - (i) the unflashed liquid from the expansion valve, plus;
 - (ii) the liquid from flash gas condensing on the surface of the cold liquid from the accumulator, and on the pumper drum walls;
- (c) the uppermost layer of cold liquid from the accumulator – warmed due to condensation of flash gas on top of it;
- (d) underneath, the remaining cold liquid from the accumulator.

At the end of the pumping period, it is assumed that both portions of liquid of (b)(i) and (b)(ii) above are at saturated pumping temperature $T_{r[PD+]}$. Performing a control volume energy analysis at the pumper drum's pumping expansion valve during the pumping period:

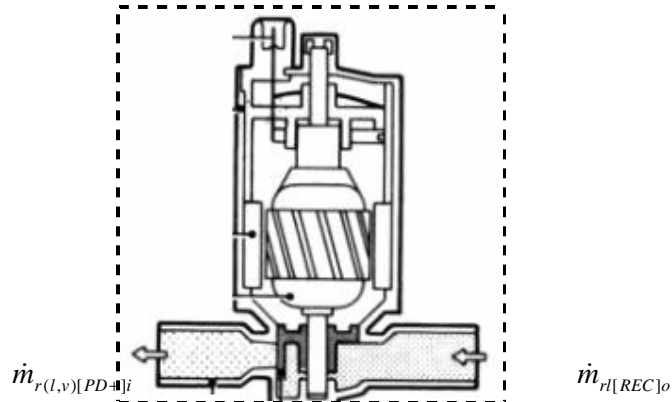


Figure A13.3 Control Volume: Pumping expansion valve at the entrance to the pumper drum ⁽⁴⁵⁾

$$dE_{cv}/dt = \dot{Q}_{cv} - \dot{W}_{cv} + \sum_i \dot{m}_i (h_i + V_i^2/2 + gz_i) - \sum_o \dot{m}_o (h_o + V_o^2/2 + gz_o)$$

Which simplifies to

$$h_{r[REC]o}(T_{r[REC]}) = h_{r(l,v)[PD+]i}(T_{r[PD+]})$$

where $h_{r[REC]o}$ is the enthalpy of the liquid at the entrance to the pumping expansion valve from the condensed liquid receiver, and $h_{r(l,v)[PD+]i}$ is the enthalpy of the two-phase mixture at the inlet to the pumper drum.

From the tests performed at the plant, from Table 8.1 above, the pressures at the receiver and (pumping) pumper drum are 1133,5 kPa and 563,5 kPa (absolute) respectively. The quality of the refrigerant $x'_{r[PD+]i}$ at the pumper drum inlet is therefore:

$$\begin{aligned}
h_{r[REC]o}(T_{r[REC]}) &= h_{r[PD+]i}(T_{r[PD+]}) + x'_{r[PD+]i} (h_{rv[PD+]i}(T_{r[PD+]}) - h_{r[PD+]i}(T_{r[PD+]})) \\
336,8 &= 234,6 + x'_{r[PD+]i} (1469 - 234,6) \\
x'_{r[PD+]i} &= 0,0828
\end{aligned}$$

Now, from Section 7.2.3 above, over the pumping period, the minor refrigerant mass inflow (across the control envelope) from the liquid receiver is more than that needed just to pressurise the drum. The balance is the additional mass inflow needed to maintain that pressure as some flash gas condenses on top of the cold liquid, and on the pumper drum's shell. Therefore from Figure 8.9 above, as the liquid control sensors switch the pumper drum to filling once it reaches 10 % of its drum height, it must be assumed that a portion of the residual layer includes a portion of the gas that is condensed $m_{r\{c\}[PD]}$.

Denoting the initial liquid-vapour mixture required to pressurise the pumper drum before any gas condenses in the process denoted by the subscript 1, the mass of liquid and vapour resulting from this two-phase mixture that enters into the pumper drum over the initial pumping period (i.e. the mass due to (a) and (b)(i) above), based on the analysis performed in Appendix A8 above, is:

$$\begin{aligned}
x'_{r[PD+]i} &= \frac{m_{rv[PD+]i1}}{m_{rv[PD+]i1} + m_{r[PD+]i1}} \\
x'_{r[PD+]i} &= \frac{2,9781R_{[PD]}^2 L_{[PD]} \rho_{rv}(T_{r[PD+]})}{2,9781R_{[PD]}^2 L_{[PD]} \rho_{rv}(T_{r[PD+]}) + m_{r[PD+]i1}} \\
0,0828 &= \frac{26,07}{26,07 + m_{r[PD+]i1}} \\
\therefore m_{r[PD+]i1} &= 288,79 \text{ kg}
\end{aligned}$$

where $m_{r[PD+]i1}$ is the corresponding mass of liquid that accompanies the two-phase mixture at the outlet of the expansion valve.

Processes at the pumper drum during the pumping period

From data recorded at the ERPM plant, the temperature of the pumper drum's outer shell during the pumping period is shown in Figure 8.11 above. The maximum temperature rise at the pumper drum is measured as 1° C above filling temperature. From equation (61) of Section 8.4.1, the internal energy temporarily stored in the steel of the pumper drum during the pumping period is:

$$\Delta\widehat{U}_{s[PD+]} = m_{s[PD]} c_s (T_{r[PD-]})(T_{heat[PD]} - T_{r[PD-]}) = 2867,00 \cdot 0,4533 \cdot 1 = 1299,61 \text{ kJ}$$

In Section 8.4.2 above, the warming of the upper portion of pumped liquid is assumed, in equation (61), to result from a further portion of pressurising gas that condenses on the surface of liquid. Predicting the temperature rise of the upper pumped layer $T_{rl,circ[PD-E]}$ from test data, as well as the mass of liquid warmed to this temperature $m_{rl,circ[PD-E]}$ is performed in Appendix A8.2.3. The internal energy temporarily gained by this upper portion of liquid from the accumulator is:

$$\Delta\widehat{U}_{rl,circ[PD-E]} = m_{rl,circ[PD-E]} (h_{rl}(T_{rl,circ[PD-E]}) - h_{rl}(T_{r[PD-]}))$$

where from Appendix A8.2.3:

$$m_{rl,circ[PD-E]} = 1221,12 \text{ kg}$$

$$\therefore \Delta\widehat{U}_{rl,circ[PD-E]} = 1221,12(179,10 - 177,80) = 1587,47 \text{ kJ}$$

where it is assumed that the enthalpy of the upper portion of circulated liquid is initially at [filling] pumper drum temperature.

If it is assumed that first the pumper drum is fully pressurized before any gas condenses, the mass of gas that must condense $m_{rv\{c\}[PD]}$ during the pumping period to account for the “warming” of the pumper drum walls and the upper surface of the liquid is:

$$m_{rv\{c\}[PD]} (h_{rv[PD+i]}(T_{r[PD+]}) - h_{rl[PD+i]}(T_{r[PD+]})) = \Delta H_{rl,circ[PD-E]} + \Delta H_{r.s[PD]}$$

$$m_{rv\{c\}[PD]} = \frac{1587,47 + 1299,61}{(1469 - 234,6)} = 2,34 \text{ kg}$$

$$\therefore m_{rl\{c\}[PD]} = 2,34 \text{ kg}$$

From Figure A13.2, the residual layer in the pumper drum now consists of (b) – (d) above. If it is assumed that the liquid condensed from the gas $m_{rv\{c\}}$ takes up an inconsiderable amount of volume in the pumper drum, then to maintain pumping pressure, a commensurate mass of vapour must enter, together with its accompanying mass of unflashed liquid (denoted by the subscript 2). Since the quality at the outlet of the pumping expansion valve is predicted above, as well as the mass of gas required to compensate for that condensed, the extra mass of unflashed liquid at the outlet of the valve $m_{rl[PD+]i2}$ can be predicted:

$$0,0828 = \frac{2,34}{2,34 + m_{rl[PD+]i2}}$$

$$m_{rl[PD+]i2} = 25,92 \text{ kg}$$

Total mass of liquid and vapour entering the control volume during the pumping period

The total mass of liquid and vapour that expands across the pumping expansion valve therefore includes the following:

- (iii) unflashed liquid if no flash gas were to condense;
- (iv) accompanying flash gas if none were to condense;
- (v) extra unflashed liquid entering with the extra flash gas to maintain pressure;
- (vi) extra flash gas to replace that condensed:

$$\Sigma m_{rl[REC]o} = \Sigma m_{rl[PD+]i} + \Sigma m_{rv[PD+]i} = 288,79 + 26,07 + 25,92 + 2,34 = 343,12 \text{ kg}$$

The total mass of liquid contained in the residual layer of the pumper drum at pumping pressure is:

$$\Sigma m_{r[PD+]i} = m_{r[PD+]i1} + m_{r[PD+]i2} + m_{r\{c\}} = 288,79 + 25,92 + 2,34 = 317,05 \text{ kg}$$

The total mass of vapour contained in the pumper drum at pumping pressure is:

$$\Sigma m_{rv[PD+]i} = m_{rv[PD+]i1} - m_{rv\{c\}} + m_{rv[PD+]i2} = 26,07 - 2,34 + 2,34 = 26,07 \text{ kg}$$

Processes during the depressurisation of the pumper drum

If the outer control volume shown in Figure 7.2 above is now considered, at the end of the pumping period, the liquid that entered the pumper drum during the pumping period $\Sigma m_{r[PD+]i}$ is allowed to expand to accumulator pressure through the gas return valve.

The quality of the mixture at the inlet of the accumulator and after depressurization is:

$$\begin{aligned} h_{r[PD+]i}(T_{r[PD+]i}) &= h_{r[ACC]i}(T_{r[ACC]}) + x'_{r[ACC]i} (h_{rv[ACC]i}(T_{r[ACC]}) - h_{r[ACC]i}(T_{r[ACC]})) \\ 234,6 &= 158,8 + x'_{r[ACC]i} (1451 - 158,8) \\ x'_{r[ACC]i} &= 0,05866 \end{aligned}$$

$\Sigma m_{r[PD+]i}$ flash cools down to accumulator temperature by evaporating a portion of the liquid:

$$\begin{aligned} x'_{r[ACC]i} &= \frac{m_{rv[PD-]i}}{m_{rv[PD-]i} + m_{r[PD-]i}} \\ 0,05866 &= \frac{m_{rv[PD-]i}}{317,05} \end{aligned}$$

$$\therefore m_{rv[PD-]i} = 18,60 \text{ kg}$$

$$\therefore m_{r[PD-]i} = 298,45 \text{ kg}$$

Of the remaining liquid in the pumper drum now at accumulator pressure, a portion must evaporate to re-cool both the steel of the pumper drum and the uppermost layer of liquid from the accumulator that was “warmed” temporarily during the pumping period. Some liquid in the accumulator must also evaporate to

re-cool the vented pressurising gas to accumulator pressure. At the accumulator, from equation (55):

$$\Delta\widehat{H}_{rv.vent[(PD+)-ACC]} = m_{rv.vent[(PD+)-ACC]} (h_{rv}(P_{r[PD+]}) - h_{rv}(P_{r[ACC]}))$$

$$\Delta\widehat{H}_{rv.vent[(PD+)-ACC]} = 26,07(1469,00 - 1451,00) = 463,83 \text{ kJ}$$

The mass of liquid $m_{rl\{e\}[PD]}$ at accumulator pressure, both in the pumper drum and in the accumulator, that evaporates at the end of the pumping period is therefore:

$$m_{rl\{e\}[PD]} (h_{rv[ACC]}(T_{r[ACC]}) - h_{rl[ACC]}(T_{r[ACC]})) = \Delta\widehat{U}_{rl.circ[PD-E]} + \Delta\widehat{U}_{s[PD+]} + \Delta\widehat{H}_{rv.vent[(PD+)-ACC]}$$

$$m_{rl\{e\}[PD]} = \frac{1587,47 + 1299,61 + 463,38}{(1451 - 158,8)} = 2,59 \text{ kg}$$

Therefore, at the end of one pumping and venting period, the mass of liquid remaining in the pumper drum (at filling / accumulator pressure - but before filling recommences) that can be used, during the next pumping period, to build ice at the evaporators is:

$$\Sigma m_{rl[PD-]} = m_{rl[PD-]} - m_{rl\{e\}[PD]} = 298,45 - 2,59 = 295,86 \text{ kg}$$

The mass of vapour arriving at the accumulator inlet during the venting period is:

$$\Sigma m_{rv[ACC]i} = m_{rv[PD-]} + m_{rl\{e\}[PD]} + m_{rv[PD+]i} = 26,07 + 18,60 + 2,592 = 47,26 \text{ kg}$$

And finally, the mass of liquid that enters from the condensed liquid receiver to supply this liquid and vapour is (again):

$$\Sigma m_{rl[REC]o} = \Sigma m_{rl[PD+]i} + \Sigma m_{rv[PD+]i} = 288,79 + 26,07 + 25,92 + 2,34 = 343,12 \text{ kg}$$

Had $\Sigma m_{rl[REC]o}$ expanded across the major expansion valve of Figure 7.1 directly down to accumulator pressure together with the major refrigerant flow, the following masses of vapour and liquid would be seen at the inlet of the accumulator:

$$h_{r[REC]o}(T_{r[REC]}) = h_{r[ACC]i}(T_{r[ACC]}) + x'_{r[ACC]i} (h_{rv[ACC]i}(T_{r[ACC]}) - h_{r[ACC]i}(T_{r[ACC]}))$$

$$336,8 = 158,8 + x'_{r[ACC]i} (1451 - 158,8)$$

$$x'_{r[ACC]i} = 0,13775$$

The mass of vapour thus produced for a liquid inlet mass of 343,12 kg is:

$$x'_{r[ACC]i} = \frac{m_{rv[ACC]i}}{m_{rv[ACC]i} + m_{r[ACC]i}}$$

$$0,13775 = \frac{m_{rv[ACC]i}}{343,12}$$

$$m_{rv[ACC]i} = 47,26 \text{ kg}$$

$$m_{r[ACC]i} = 295,86 \text{ kg}$$

Therefore, all the URDs generated over a complete pressurising and venting period of one pumper drum amount to (add up to) the *inherent* URD of needing to compress the flash gas generated in expanding liquid down liquid from the condensed liquid receiver to accumulator pressure (4 – a in Figure A13.1 above).